DEVELOPMENT OF A HEATED MULTILAYER SHEAR SENSOR

by

Todd Jerard Barber

B.S. Aero. Eng., Massachusetts Institute of Technology
(1988)

SUBMITTED TO THE DEPARTMENT OF
AERONAUTICS & ASTRONAUTICS
IN PARTIAL FULFILLMENT OF THE REQUIREMENTS
FOR THE DEGREE OF

MASTER OF SCIENCE
in Aeronautics & Astronautics

at the

MASSACHUSETTS INSTITUTE OF TECHNOLOGY
February 1991

Signature of Author.....
Department of Aeronautics & Astronautics
October 1990

Certified by.....
Alan H. Epstein
Professor, Aeronautics & Astronautics

Accepted by.....
Harold Y. Wachman, Chairman
Departmental Graduate Committee
Department of Aeronautics & Astronautics

DEVELOPMENT OF A HEATED MULTILAYER SHEAR SENSOR

by

TODD JERARD BARBER

Submitted to the Department of Aeronautics & Astronautics
February, 1991 in partial fulfillment of the
requirements for the Degree of Master of Science in
Aerospace Engineering

ABSTRACT

An experimental study was carried out to test the feasibility of using a double-layer heat transfer gauge for ultimate application in determining the time-resolved behavior of the boundary layer, passage shock, and possible separation point on a transonic compressor rotor blade. In particular, a gauge with equivalent heater and sensor temperatures was tested, to see the effect of cancelling the steady-state heat conduction into the substrate. Tests were performed in a subsonic wind tunnel for steady calibrations and in a shock tube for an unsteady step response.

For the steady flow case, the use of a controlled gauge allowed for the calculation of the skin friction over a flat plate. Experimental results agreed with theory within the accuracy of the experiment at all but the lowest sensor overheat ratios. Shock tube predictions for the voltage change of the sensor across the shock were generally good, except for one case tested. In both scenarios, the theoretical model overpredicted the actual sensitivity of the gauge to Mach number.

A new gauge geometry was designed for future compressor testing, with tradeoff studies being performed for the parameters under the control of the experimentalist. In particular, both four-element and ten-element gauges were designed specifically with compressor testing as the ultimate application.

Thesis Supervisor: Dr. Alan H. Epstein

Title: Professor of Aeronautics & Astronautics

ACKNOWLEDGEMENTS

The list of people who share this accomplishment with me is truly enormous and it is my pleasure to recognize their efforts. First and foremost, I would like to extend my deepest thanks to Professor Alan Epstein for his uncanny experimental talents, his extreme friendliness and approachability, and his faith in my abilities through all the trials and tribulations of an experimental thesis. His patience, understanding, and expertise will not be soon forgotten.

The GTL support staff has eased my journey through graduate life beyond comprehension. The efforts of Viktor Dubrowski, Roy Andrew, Jim Nash, Bob Haimes, and Jerry Guenette have literally saved months of aimless wandering. Karen Hemmick, Holly Rathbun, Nancy Clark, and Diana Park all have been indispensable for the completion of this project. It is with a twinge of sadness that I leave you all.

My fellow students in GTL have truly been an inspiration for over two years now. There are so many who have helped me through, not just in a technical sense. I would like to formally thank Sasi Digavalli, Judy Pinsley, and Pete Silkowski for brightening the interior of 31-256 with their friendship. To Martin Graf, my new friend and successor, I wish to extend a special welcome and a heartfelt thank you for making my last weeks at MIT as pleasant as possible. I offer my deepest respect and thanks to Charlie Haldeman, the one student in GTL who was never too busy to drop his work and solve my problems. To my best friend in the GTL, Tonghuo Shang, I send a mixed message--a happy 'thank you for everything and best wishes for you and your wife' and a sad 'goodbye, buddy....'

The faculty in GTL, both permanent and visiting members, have provided many useful technical hints throughout this project. In particular, I greatly appreciate the efforts of Dr. Edward Greitzer, Dr. Choon S. Tan, Dr. Mike Giles, and Dr. Peter Bryanston-Cross for their timely advice.

Without the wonderful friendships I've enjoyed outside of GTL, my journey through a master's degree would have been much

more difficult. I give a special thanks to Al, Aric, Ella, Emily, Glenn, Greg, Gus, Iman, Jamie, John, Sam, Steve A., Thomas, Tricia, Venkat, and Will. You are all the best. Notice I listed these alphabetically, absolutely devoid of any favoritism. I'm no dummy--I want to keep my friends. I shall miss all of you so very, very much.

I want to express my deepest gratitude to my family in Kansas. To Mom, Dad, and Lea--thanks for being there for me for eighteen years, helping me to grow into a (more or less) well-adjusted adult. It's too bad MIT has taken all of that away. Just kidding. I love you all very much. Whatever my successes, I take along a part of you.

Finally, I want to send my love across the miles to Lisa, the most special person in my life. Your caring and support through the darkest of days were the one thing that always kept me going. I treasure all of our wonderful memories. Soon we will begin a lifetime of memories together. Oh, and one more thing: Psyche, silly willy...your sugar booger will be there soon!

TABLE OF CONTENTS

LIST OF FIGURES

CHAPTER 2

CHAPTER 3

CHAPTER 4

CHAPTER 5

CHAPTER 6

APPENDIX B

APPENDIX D

Figure D.3: Unsteady voltage traces vs. time: double-layer gauge, high Mach number trials, heater passive, #2

Figure D.4: Unsteady voltage traces vs. time: double-layer gauge, low Mach number trials, heater active, brass support

Figure D.5: Unsteady voltage traces vs. time: double-layer gauge, intermediate Mach number trials, heater active, brass support

Figure D.6: Unsteady voltage traces vs. time: double-layer gauge, high Mach number trials, heater active, brass support

Figure D.7: Unsteady voltage traces vs. time: double-layer gauge, low Mach number trials, heater active, anodized aluminum support, $a_{rs} = 1.06$

Figure D.8: Unsteady voltage traces vs. time: double-layer gauge, intermediate Mach number trials, heater active, anodized aluminum support, $a_{rs} = 1.06$

Figure D.9: Unsteady voltage traces vs. time: double-layer gauge, high Mach number trials, heater active, anodized aluminum support, $a_{rs} = 1.06$

Figure D.10: Unsteady voltage traces vs. time: double-layer gauge, low Mach number trials, heater active, anodized aluminum support, $a_{rs} = 1.08$

Figure D.11: Unsteady voltage traces vs. time: double-layer gauge, intermediate Mach number trials, heater active, anodized aluminum support, $a_{rs} = 1.08$

Figure D.12: Unsteady voltage traces vs. time: double-layer gauge, high Mach number trials, heater active, anodized aluminum support, $a_{rs} = 1.08$

Figure D.13: Unsteady voltage traces vs. time: double-layer gauge, low Mach number trials, heater active, anodized aluminum support, $a_{rs} = 1.11$

Figure D.14: Unsteady voltage traces vs. time: double-layer gauge, intermediate Mach number trials, heater active, anodized aluminum support, $a_{rs} = 1.11$

Figure D.15: Unsteady voltage traces vs. time: double-layer gauge, high Mach number trials, heater active, anodized aluminum support, a_{rs} = 1.11

LIST OF TABLES

Table C.10: Comparison of predicted and measured shock speeds for the shock tube: heat transfer data recorded for a turbine double-layer gauge on anodized aluminum with the heater run actively; $a_{rs} = 1.11$

CHAPTER 1

BACKGROUND AND INTRODUCTION

A hot-film or hot-wire probe is a useful diagnostic tool for making steady or time-resolved measurements in a given flow. The hot-film seems particularly well-suited for making measurements in the boundary layer of a rotating compressor (as in a modern gas turbine axial-flow machine) due to its proven technology, ability to withstand centrifugal stresses, absence of interaction with the flow field, high frequency response, and its capacity for spatial resolution. The structure of the boundary layer, possible separation point, and the oblique passage shock on a compressor rotor blade is largely unknown, particularly in an unsteady sense. A correctly designed and calibrated thin-film gauge may be able to be used to directly verify and measure these phenomena in a compressor test rig. This dictates the design of a thin-film heat flux gauge specifically for that purpose.

In particular, it is postulated [Epstein, Gertz, Owen, and Giles] that vortex shedding in upstream compressor blade wakes drives an observed 15 kHz oscillation of the oblique passage shock. This was inferred from a bimodal velocity histogram from experimental laser anemometry data. A shock oscillation amplitude of 0.5 mm was proposed to explain the observations. It is desired to verify this amplitude and frequency of oscillation for the passage shock directly. The thin-film heat transfer gauge offers the experimentalist a means to do so.

In addition, a low frequency (350 Hz) oscillation is inferred in the experimental measurements as well. It is postulated that this is due to an oscillation of a separation point on the suction surface of the rotor blade. Again , thin-film heat transfer technology may offer a direct measurement of this phenomenon, confirming the

indirect observations previously made. Also of interest is the location of a possible transition point in the boundary layer on the compressor blade. The success of a computational code (CFD model) for a turbomachine component hinges on knowledge of the correct location of the transition point from laminar to turbulent flow. In short, a well-designed thin-film heat transfer gauge may provide the mean and time-resolved flow structure in a transonic compressor rotor passage.

Such a thin-film gauge would need to be designed with all of the above criteria in mind. In particular, a double-layer multi-element heat transfer gauge has been developed [Epstein, Guenette, Norton, and Yuzhang] that satisfies many of the requirements above. Proof of concept testing and preliminary calibrations may be performed on these readily available gauges. Ultimately, a gauge with a geometry tailored to the application (mapping the unsteady flow structure on a compressor rotor blade) should be designed, calibrated, and tested on a compressor simulation rig. It is the aim of this work to perform experiments on readily available thin-film gauges to obtain predictions for the sensor voltage changes as a function of the flow properties in the test. In particular, steady-state and time-resolved testing should both be performed for a wide variety of flow Mach numbers, controlled gauge temperatures, and operating modes (described subsequently). Theoretical predictions for these output voltage changes should be compared with the actual experimental observations for consistency. In addition, a candidate gauge design for the compressor testing should be presented, after a tradeoff study is performed for the various gauge parameters that are determined by the designer.

CHAPTER 2

THIN-FILM HEAT TRANSFER GAUGES: INTRODUCTION AND OPERATION

2.1 INTRODUCTION TO THIN-FILM HEAT TRANSFER GAUGES

The use of single thin-film heat transfer gauges as a flow sensor, via constant temperature anemometry, is a familiar concept [Blackwelder]. The principle of operation is identical to that of a hot-wire anemometer, which is a very popular diagnostic tool. A constant temperature anemometer is an electronic feedback loop that will maintain a resistor (called the "probe" or "gauge") at a certain resistance value set by the operator. There exists an approximately linear relationship between resistance and temperature:

$$R_h = R_c\,[1 + \alpha(T_g - T_0)] \qquad (2.1)$$

where R_h is the hot resistance (equal to the control resistance), R_c is the cold resistance (the resistance of the gauge at T_0), T_g is the gauge operating temperature, T_0 is the ambient or reference temperature, and α is the coefficient of thermal resistivity of the thin-film material. The ratio of the hot to the cold resistance R_h/R_c is known as the resistive overheat ratio (a_r), or the overheat ratio for short. Therefore, a constant temperature anemometer loop fixes a gauge to be at a temperature T_g which is higher than ambient temperature (since $a_r>1$). See Figure 2.1 for a schematic of the anemometer bridge loop employed.

A standard TSI anemometer unit, model 1050A, was throughout testing. In a hot-wire anemometer, the heat provided (via a current) to the gauge is dissipated into the surrounding flow via the heat transfer process of forced convection. As the flow speed

is increased, for example, the convection of heat away from the hot-wire to the flow is increased; therefore, more current needs to be provided to the gauge to maintain it at the elevated temperature T_g. This change can be seen by monitoring the voltage value across the gauge. Since the temperature (and hence resistance) of the gauge is a constant and the current has increased, the voltage value across the gauge will increase accordingly. In fact, if a reasonable relation can be obtained for the forced convection as a function of velocity, it is possible to use the hot-wire anemometer as a velocity meter, since the temperature of the hot wire is known.

The arguments of the preceding paragraph hold for a hot-film anemometer as well, but additional complications exist. In particular, due to the geometric nature of thin-film gauges, forced convection is not the only heat transfer mechanism of importance. A thin-film gauge consists of a thin (approximately 1000 Å) film of metal (in this case, pure nickel) mounted on an insulating layer of kapton (a polyimide material) called a substrate. The kapton thickness is many times greater than that of the thin nickel film. Figure 2.2 represents a schematic of a cross section of a typical gauge (not to scale). Heat conduction into the substrate allows for another means for heat to be transferred from the heated film, and has indeed been observed in practice.

2.2 OPERATING MODES OF THIN-FILM GAUGES

A comparison of the gauges used (in cross-section) and their operating modes can be seen in Figure 2.3. In the case of the shock tube, the test article represents the shock tube probe support. For the single-layer gauge, the kapton is bonded directly to the test article. For the double-layer gauge, the lower resistor (which acts as a heater) is bonded between the kapton and the test article. Since the heater is bonded intimately with the probe support, it is imperative that the probe support be a non-conducting material. This lead to the requirement that the

aluminum probe support be anodized. In the heater passive mode, the bottom thin-film resistor is not controlled in a constant temperature anemometer loop. This is in contrast to the heater active mode, in which both the sensor and the heater are controlled in separate anemometer loops. Experimental results utilizing these three operating modes will be presented later.

The off-design condition of balancing both the heater and the sensor to different constant temperatures was not investigated. It was determined that such a configuration was not stable, due to the fact that the resistor operating at lower temperature by the anemometer loop would have its temperature increased beyond its operating temperature due to heat conduction from the resistor operating at higher temperature. Once this elevated temperature is realized in the lower temperature resistor, no means can be provided to reduce the temperature of this resistor back to its operating point (i.e., no mechanism exploiting the Peltier effect exists for these standard anemometer units and probes). This is due to the fact that positive current can only be injected into the gauges by the anemometer unit and increases in current correspond to increases in temperature of the resistor.

Control resistances were set on the anemometer unit using both an external 5:1 bridge and the resistance decades, depending on the resistance value of the probe used. Control resistances less than 50 ohms may be set directly with the resistance decades on a 1:1 bridge, while control resistances greater than 50 ohms must be set using the external control resistor feature on the 5:1 bridge. A simple internal rewiring procedure described in the TSI operating manual allows a toggle between these two methods of setting the control resistances. External control resistors are constructed from potentiometers and standard circuit resistors in series. With this design, the overheat ratio can be changed by adjusting the potentiometer. A circuit resistor is used in series with the potentiometer to allow the use of a lower resistance

potentiometer, which gives better controllability on setting the overheat ratio.

CHAPTER 3

THEORETICAL PREDICTIONS FOR UNSTEADY HEAT TRANSFER AND MULTI-ELEMENT GAUGE DESIGN

3.1 MODELLING THE UNSTEADY SUBSTRATE HEAT CONDUCTION

Various models were tried for the cases of non-zero heat conduction into the substrate. A first attempt at modelling this problem was made by assuming that the support was a good thermal conductor and the temperature at the junction between the substrate and probe support was ambient temperature. This lead to substrate conduction values well over three orders of magnitude higher than the convection changes seen across the shock. From this model, the theoretical voltage output change across the shock was predicted to be no more than 20 mV. Actual output voltage changes across the shock were typically 200-300 mV. Clearly, this model is not sufficient to explain the operation of the device. Rather, an unsteady model must be formulated. It is hoped that this model could demonstrate a much lower value for the conduction into the substrate at the time of data acquisition. In all models employed here, it is assumed that the thermal properties within the thin-film gauge itself can be ignored without substantially affecting the output. This is presumed to be a good assumption due to the low thickness of the nickel film (i.e., the film appears thermally transparent due to its size). This is shown to be the case in Appendix A, which solves the steady conduction solution for the case where the thermal properties of the thin-film are not ignored.

The following unsteady heat transfer problem was solved to investigate the time-dependant behavior of the substrate heat conduction:

$$\kappa_1 \frac{\partial^2 T_1}{\partial x^2} = \frac{\partial T_1}{\partial t} \tag{3.1}$$

$$\kappa_2 \frac{\partial^2 T_2}{\partial x^2} = \frac{\partial T_2}{\partial t} \tag{3.2}$$

subject to the following boundary conditions:

1. $T_1(0,t) = T^* \; [= T_s - T_0] = \text{constant}$
2. $T_1(\delta,t) = T_2(\delta,t)$
3. $k_1 \frac{\partial T_1}{\partial x}(\delta,t) = k_2 \frac{\partial T_2}{\partial x}(\delta,t)$
4. $T_2(\infty, t) = 0$
5. $T_1(x,0) = 0$
6. $T_2(x,0) = 0$

Here, k is the thermal conductivity, δ is the thickness of the substrate, and κ is the thermal diffusivity. The subscript 1 refers to the kapton layer and the subscript 2 refers to the brass probe support. This readily solved via Laplace transform techniques. In particular, it is found that the temperature in the brass support is represented by:

$$T_2(x,t) = T^*(1-\beta)\, \pounds^{-1} \left[\left(\frac{e^{-q_2(x+2i\delta)}\, e^{-(q_1-q_2)\delta}}{s} \sum_{i=0}^{\infty} \beta^i\, e^{-2iq_1\delta} \right) \right] \tag{3.3}$$

where q_2 and β are defined as follows:

$$q_2 = \sqrt{\frac{s}{\kappa_2}} \tag{3.4}$$

$$\beta = \frac{1 - \gamma}{1 + \gamma} \tag{3.5}$$

with γ defined below as:

$$\gamma = \sqrt{\frac{\rho_1 c_1 k_1}{\rho_2 c_2 k_2}} \qquad (3.6)$$

In (3.6), ρ represents the material density and c represents the material specific heat. The individual terms in (3.3) may be evaluated [Carslaw and Jaeger] using the following relation:

$$\mathcal{L}^{-1}\left[\frac{e^{-q_2 \chi}}{s}\right] = \text{erfc}\left[\frac{\chi}{2\sqrt{\kappa_2 t}}\right] \qquad (3.7)$$

where erfc( ) denotes the complimentary error function defined as follows:

$$\text{erfc}(z) = 1 - \text{erf}(z) = 1 - \frac{2}{\sqrt{\pi}} \int_0^z e^{-t^2} d\,t \qquad (3.8)$$

This is a common function in unsteady heat transfer problems and is rather well tabulated. Applying (3.7) to (3.8), the following is obtained for the final solution for the temperature in the brass layer:

$$T_2(x,t) = T^*(1-\beta) \sum_{i=0}^{\infty} \beta^i \, \text{erfc}\left[\frac{x + 2.9\delta\,[2.69i + 1]}{2\sqrt{\kappa_2 t}}\right] \qquad (3.9)$$

From this, it is possible to obtain the conduction by differentiation, since in general:

$$q_{cond} = -k \frac{\partial T}{\partial x} \qquad (3.10)$$

Since differentiation is a linear operator, the derivative may be moved under the summation sign when applying (3.10) to (3.9). As a final result:

$$q_{cond} = \frac{k_2 T^* (1-\beta)}{\sqrt{\pi \kappa_2 t}} \sum_{i=0}^{\infty} \beta^i \, e^{-(2i+1)^2/197t} \qquad (3.11)$$

This expression was evaluated numerically by computer. This unsteady conduction, normalized by the steady conduction that would occur if the brass support were at ambient temperature (the previously mentioned steady model conduction), is plotted as a function of time in Figures 3.1 and 3.2. Figure 3.1 represents a plot with a linear time scale, and Figure 3.2 depicts the same plot with the time axis on a $\log_{10}$ scale. Several features may be noted in these two figures (particularly Figure 3.2). This time axis represents the time since the anemometers were turned on. Since it is generally many thousands of seconds following this process that the shock tube runs were made, the reduction of the substrate conduction is seen to be striking. This gives much more consistent results when attempting to predict the theoretical voltage jump across a shock, due to the fact that the probe is now much more sensitive to changes in the flow. The peak that occurs after 10 ms in the conduction implies that a thermal wave is propagating from the sensor through the substrate. It is only on time scales of this order that the conduction would severely limit the operation of the heater-passive or single-sensor gauge.

The effect of a finite thickness glue layer on the results presented in Figures 3.1 and 3.2 was numerically investigated. Assuming that the thermal properties of the glue are similar to that of the kapton (a much more realistic assumption than assuming equivalence with brass), this just increases the value of δ in the previous calculation. In particular, a 5 μm glue layer was assumed and the results were recalculated. Presented in Figures 3.3 and Figures 3.4 are the same plots as in Figures 3.1 and 3.2,

except now the curve representing the scenario with a glue layer are offered for comparison. As can be seen from the graphs, the effect of the glue layer is to slightly move the peak of the conduction graph to the right, towards increased time. This gives slightly higher conduction values after the peak and slightly lower values before the peak for the glue case, consistent with predictions. Since the glue layer thickness is somewhat beyond the control of the experimentalist, it is important to demonstrate that the effect of a glue layer is not a significant contribution to the heat transfer process as modelled here.

3.2 PARALLEL VS. SERIES GAUGES

To completely determine the processes that take place in the boundary layer on a flat plate or compressor blade, spatial resolution of the candidate sensor is an important criterion. In particular, the single resistance bar (such as a DISA sensor) would not allow for good spatial resolution in such an environment, except with a large number of sensors placed in close proximity. Therefore, a multiple-element gauge is desirable for spatial resolution. However, this may adversely effect the signal to noise ratio of the output voltage across the gauge. Two types of multiple-element geometries were investigated; in particular, a parallel (or ladder) geometry and a series (or serpentine) gauge. See Figure 3.5. The use of a series gauge as a hot-film probe has been demonstrated [Epstein, Guenette, Norton, and Yuzhang]. It is desired to compare the voltage across a ladder gauge with that of a serpentine gauge with exactly the same properties. Figure 3.6 represents this relationship, graphing the ladder to serpentine gauge output ratio as a function of the number of resistance elements. This basically scales as the inverse square of the number of resistance elements. Clearly, this dictates that a serpentine pattern be used in the design of a mulitple-element gauge.

3.3 VOLTAGE PREDICTIONS FOR A MULTI-ELEMENT GAUGE

It is desired to know the expected voltage change as a shock wave crosses one element of an n element gauge. This allows the experimentalist to determine, by simply examining the voltage trace from a thin-film heat flux sensor, the presence and the motion of a shock. This is important for attempting to decipher the flow structure on the surface of a transonic compressor blade. Unfortunately, the absolute changes predicted by these models are not physically relevant, since these models were derived using the constant conduction into the substrate model, which has been shown not to be a realistic assumption. However, the shape of the plots will remain unchanged if the unsteady conduction model derived previously is incorporated into the present model. Figures 3.7-3.10 present the sensor voltage as a function of shock position divided by gauge length. Therefore, the leftmost points represent a shock just at one boundary of the gauge and the rightmost points represent the shock after crossing the entire length of the gauge. Two different sensor gauge overheat ratios are presented for both laminar and turbulent flow. Although the change in voltage as the shock propagates is larger in magnitude than is shown here, the nearly linear profile of sensor voltage with shock position over gauge length is expected to be seen, even taking into account the unsteady heat transfer term derived last chapter. Notice that in all cases that higher Mach numbers give larger voltage changes as the shock propagates over the gauge, consistent with intuition. Note also that the predicted value of the absolute voltage level is an increasing function of the overheat ratio, as is expected.

For the case where the heater and sensor are controlled to be at the same temperature in a double-layer gauge (note the distinction between multi-element and multi-layer), the conduction into the substrate can only equal zero if the heater and sensor temperature are balanced exactly. Therefore, it is useful to estimate the decrease in sensor voltage as the temperature difference between the sensor and the heater is increased.

Figures 3.11-3.14 present the sensor output voltage change across a shock (across all elements of the gauge) as a function of temperature ratio, where the temperature ratio is defined to be the temperature difference between the sensor and the heater normalized by the ambient air temperature. Again, results are presented for both laminar and turbulent flows, with two overheats and three Mach numbers investigated. As before, the absolute voltage level presented here is not correct due to the fact that this model incorporates a steady substrate conduction term. However, the shape of the curve with temperature ratio is consistent with the correct substrate conduction model. In all cases, there is a severe penalty for temperature mismatch between the sensor and the heater. Many of the parameters that determine the proximity of the heater and sensor temperatures are beyond the control of the experimentalist. Good calibrations for α are a necessity, as are carefully prepared control resistors or carefully dialed resistance decade values, depending on the mode of operation of the anemometer units.

3.4 MULTI-LAYER MULTI-ELEMENT GAUGE DESIGN TRADEOFFS

3.4.1 Element spacing

As mentioned above, the spatial resolution of a candidate heat transfer gauge is an important criterion for gauge design. The physical shock oscillation on a transonic compressor blade has been measured to have an amplitude of 0.5 mm. This, however, does not represent the true supersonic interaction length, due to shock wave/boundary layer interactions. In particular, it is desired to know whether the amplitude of shock oscillation is larger or smaller than this supersonic interaction length. Figure 3.15 represents a schematic of this scenario. Correlations can be found for scaling laws for the supersonic interaction domain. It is found that many experimental data points collapse onto one curve, described below:

$$L^* \approx 70\ \delta_0^*\ (H_i - 1) \qquad (3.12)$$

where L^* is the interaction length, δ_0^* is the displacement thickness of the boundary layer, and H_i is the incompressible shape factor, which is a strong function of the Reynolds number and a rather weak function of the shock Mach number (at least until M_s becomes greater than 1.3, when separation may occur). For this geometry, it is found that, for the Reynolds numbers encountered on the compressor rotor blade, the supersonic interaction length is roughly 2 mm, or about four times the shock oscillation amplitude. Therefore, the boundaries of the oscillating shock are smeared by the larger interaction region between the oblique shock and the turbulent boundary layer. Hence, providing a spatial resolution less than the shock oscillation amplitude is futile. A design value of 1.00 mm, or 1000 μm was chosen as the distance between adjacent gauge elements (denoted by ε). Therefore, the width of the gauge depends only on the the width of the individual resistance elements (δ) and the number of resistance elements (n).

3.4.2 Power considerations in gauge sizing

It is an important design criterion that the power supplied by the anemometer be equivalent to the power dissipated in the thin-film gauge. This depends not only on the surface area of the resistance elements, but on the surface area of the tags and leads as well. Tags are the electrical connections between resistance elements (i.e., they are part of the serpentine pattern) and leads are two electrical connections from one side of the heat-flux gauge. In general, the leads for these thin-film gauges are gold-plated to lower their resistance. There is usually no need to plate the tags, as their total resistance is typically small in a serpentine pattern. However, due to the fact that ε is so large and that the cold resistance of the gauge is being designed to have a value of 15 Ω (to allow standard use on DISA or TSI anemometer units), as well as the power limitations of the anemometer, the tags have a

substantial resistance in the geometry employed here, so they will need to be gold-plated as well. It was desired to have a gauge that would work even with the failure of the gold-plating, but it was demonstrated that such a gauge cannot be constructed. Therefore, the successful operation of this multi-layer serpentine gauge hinges on the success of the plating process. For a completely non-plated gauge, there is an optimum (i.e., lowest) total tag and lead resistance for a given total resistance. This is demonstrated in Appendix B.

It was decided to select the total tag resistance to be no more than 20% of the total element resistance, since higher tag resistances will reduce the sensitivity of the gauge to flow changes. The effect of changing the parameter δ is seen in Figures 3.16-3.18, which depict the dissipated electric power as a function of the number of resistance elements. The three graphs represent three different σ values for the gauges, where σ is the ohms per square of the gauge. Due to power limitations of the anemometer, a value of $\delta = 20\ \mu m$ was selected. This is physically realizable with vacuum sputtering technology. Figure 3.19 presents the correlation for dissipated heat flux as a function of overheat ratio for various materials. For a given overheat ratio and support material for the bonded gauge, this fixes the allowed surface area for the gauge. In particular, Figures 3.20 and 3.21 plot the dissipated to supplied power ratio as a function of gauge cold resistance for different values of n. The horizontal line at one represents the design point. Figure 3.20 shows the effect of the number of resistance elements for a fixed tag to element resistance ratio of 0.1. Figure 3.21 shows the effect of changing the tag to element resistance ratio for a fixed ten-element gauge. However, this is academic, as a value of 0.2 for the tag to element resistance ratio may be too large to assure a sensitive thin-film gauge.

3.4.3 Tag resistance tradeoffs: effects of 2D electrical conduction and plating

As mentioned before, the resistance of a material is a function of the geometry of the material and a material property known as the resistivity. In particular, for a rectangular conductor of width W, length L, and thickness t [t << W,L], the resistance of the plate along its length can be written as:

$$R = \frac{L\rho}{Wt} \tag{3.13}$$

where ρ is the resistivity of the material. However, this is only true for the case where current is distributed evenly over each of the sides of width W. The geometry for the thin-film resistance tag is much different than this. Current is injected at one corner of the rectangle and is lead off at an adjacent corner, the length of the side between these two corners being L. Therefore, arbitrarily increasing the width W of a tag element to lower the tag resistance will not work according to (3.13), since the current lines will thin out and therefore less resistance is offered to the total flow of current than would be expected. The analytical solution of the effective resistance of this 2D plate is extremely complex, and numerous attempts at an analytical solution failed. A numerical solution technique, though, can be readily applied. A computer smoothing algorithm was used to solve Laplace's equation for this geometry. Results were obtained for a case with four times fewer grid points, with no noticeable change of the output. This demonstrates that the smoothing algorithm has converged. Presented in Figure 3.22 is a plot of this true resistance, normalized by the resistance expected using (3.13), as a function of the width to length ratio of the tag. This effect clearly demonstrates that the current density rapidly decreases with increasing W, so this is a substantial effect. This model was incorporated into the gauge design model with a noticeable shift in the results. It is clear that this effect is more crucial for higher values of the tag/element resistance ratio. It is also clear that the solution to this problem is a strong function of the ratio of the

width of the element to the width of the tag (i.e., how much of the rectangle has current entering it and leaving it) This analysis was performed for a tag to element width ratio of 52, but may be performed for an arbitrary tag to element width ratio as well.

The effect of the thickness of the plating material, as well as the choice of plating material, on the resistance of the plating material for different values of n is presented in Figures 3.23-3.25. Figures 3.23 and 3.24 show that there is a severe (i.e., greater than linear) penalty for choosing higher values of n. However, there is also a sharp decrease in the plate resistance for thicker plates, which may allow for a gauge to be designed with more elements. The desired limit of $(R_{tag}/R_{element}) < 0.1$ may be difficult to obtain in practice for gauges with more than a few elements. Figure 3.25 compares gold and copper as candidates for a plating material, with the plate and thin-film thicknesses set equal. Although copper offers superior performance, the corrosion properties and stability of gold make it a more attractive candidate for plating. There is a practical limit on the thickness of plating that may be allowed. Certainly, a plate thickness of 6000 Å is reasonable, with no significant boundary layer interaction phenomena.

A four-element and a ten-element gauge were designed meeting all the above criteria. Table 3.1 presents the design specifications and the system parameters for both gauges, allowing for either gold or copper plating. The symbols used are defined as follows:

1. δ = width of the individual gauge element
2. L = length of the individual gauge element
3. ϵ = distance between adjacent gauge elements
4. x = width of individual tag
5. l = total length of gauge
6. w = total width of gauge
7. t_{Ni} = thickness of thin nickel film
8. t_p= thickness of plate material

9. (ρ_p/ρ_{Ni}) = ratio of resistivities for plate and nickel
10. $(R_T)_{cold}$ = total cold gauge resistance
11. $(R_e)_{cold}$ = total cold resistance of n elements
12. $(R_t)_{cold}$ = total cold resistance of (n-1) tags
13. (R_t/R_T) = ratio of tag to total resistance

Figure 3.26 shows a scale drawing of the four-element gauge, while Figure 3.27 depicts the ten-element gauge. The length of the ten-element gauge is nearly one centimeter, so a spatial map of the surface of a compressor rotor blade may be provided with a minimum amount of difficult and complex instrumentation. These gauges were designed with a stringent requirement that the cold resistance be no more than 15 Ω. Very different gauge geometries are possible if the cold resistance of the gauge is allowed to be hundreds or thousands of ohms. This requirement is largely one of familiarity, as this is a typical cold resistance value for a hot wire probe. In addition, with this design, the resistance decades control on the anemometer can be used exclusively to set the overheat ratio, thus eliminating the need for cumbersome homemade control resistors.

CHAPTER 4

DESCRIPTION OF EXPERIMENTAL APPARATUS AND TEST GAUGES

4.1 EXPERIMENTAL APPARATUS FOR THE SHOCK TUBE

4.1.1 Introduction and principle of operation

The use of a shock tube offers the experimentalist a relatively simple way to provide a step function in temperature or velocity. This is useful in measuring the unsteady frequency response of a wide variety of flow probes, in this case for a thin-film heat transfer probe. Unsteady flow probe calibrations are also provided via the shock tube. A schematic representation of the GTL shock tube facility is presented in Figure 4.1. This device was constructed with simplicity of operation as the most important criterion. To this end, it was decided to use over-pressure to burst the diaphragm rather than a complex bursting device. This has the disadvantage, of course, of not being able to select the shock Mach number (which is a function of the break pressure) for a given test.

Oil-free air is supplied from the GTL compressor and is controlled via a supply valve. A pressure relief valve (50 psi) is provided for safety purposes. The region to the right of the diaphragm (the "driver" side) in Figure 4.1 is pressurized gradually, to allow for a quasi-equilibrium break of the diaphragm. At this point, the gauge pressure in the driver side is recorded. Upon bursting, a shock wave propagates to the left, into the "driven" side of the shock tube. The action of the shock wave on the pressure transducers will be described subsequently.

At the moment of rupture, the pressure profile along the length of the shock tube is a step function. Figure 4.2 depicts this configuration, with the moment of rupture arbitrarily called time zero. This facility has the capacity to allow for an evacuation of the driven side of the shock tube, to allow for greater pressure ratios between the driver and driven sides. This allows for arbitrary increases in the shock Mach number, since the Mach number is an increasing function of the break pressure ratio (p_4/p_1). However, for these sets of experiments, this vacuum scenario was not employed. Rather, a range of shock Mach numbers were obtained through the use of different diaphragm materials, as explained later.

The physical state of the shock tube somewhat after the burst can best be described with the use of an x-t diagram (see Figure 4.3). All relevant features of the problem can be seen here. At the far left, the shock wave is seen propagating to the left with speed c_s. To the immediate right of the shock is the contact surface, which is moving to the left at speed u_2. Physically, the contact surface represents the discontinuity between the two fluids of different entropy. At the far left is an expansion wave, which propagates to the right into the driver side of the shock tube. The leading expansion wave moves at speed a_4, the speed of sound in the driver gas at burst. The nomenclature for regions (1)-(4) in Figure 4.3 is standard for the shock tube and shall be used extensively here. At the instant in time cited in Figure 4.3, the pressure and temperature profiles along the shock tube are presented in Figure 4.4. The relation between break pressure ratio and Mach number is derived through standard non-stationary shock relations, with the requirement that the pressure and the velocity are continuous between regions (2) and (3). Notice the gradual change of flow properties through the expansion wave, as compared with the (ideally) discontinuous change between regions (1) and (2) and (2) and (3).

4.1.2 Data Acquisition and Triggering Mechanism

Since the data acquisition time is limited to less than 10 milliseconds for this shock tube (as explained presently), a high-frequency triggering device is clearly an important requirement. High-frequency response static pressure transducers are an excellent choice for a triggering mechanism. Since the pressure increases across a normal shock, as the shock in the shock tube propagates to the left and reaches the rightmost pressure transducer, a step increase in pressure is recorded. This step can be used to trigger a digital oscilloscope to begin recording data from the thin-film heat transfer probe (see Figure 4.1). The thin-film heat transfer probe is located between the two pressure tranducers. By adjusting the time scale on the oscilloscope, the response of the heat transfer probe to a step in velocity and temperature can be obtained.

Since the distance between the two pressure transducers is known, an experimental value for the shock speed can be obtained by measuring the time delay on the oscilloscope. This experimental shock speed can then be compared to the shock speed predicted by knowing the break pressure ratio, which is also a measured quantity. This gives an internal consistency check. It was found that experimental and predicted shock speeds agreed very well (typically within 1-2 %), but only if the break pressure was approached in a quasi-equilibrium fashion. This is due to the fact that if the pressure is still increasing significantly while the membrane breaks, a well-defined shock front is not established by the time the shock has propagated to the first pressure transducer.

From Figure 4.3, we can see that the data acquisition time is limited by three different constraints. First, the shock wave may reflect from the far left wall and pass over the heat transfer gauge (again). This is called the driven reflection. Second, the contact surface may pass over the heat transfer gauge as it moves left. Finally, the expansion wave may reflect off of the far right wall

and may interact with the thin-film gauge. This is a driver reflection. The maximum data acquisition time for these three constraints is a function of the shock Mach number, and any one of them may be the important constraint for a given M_s. Plotted in Figure 2.5 is the maximum data acquisition time as a function of M_s for the three different constraints mentioned above. It is seen that the driven reflection is limiting for $M_s<1.21$, whereas the contact surface is the constraint for $M_s>1.21$. This is significant, because the Mach number range encountered in testing was $M_s=1.07-1.30$.

4.1.3 Selection of diaphragm materials

As mentioned previously, to obtain a range of shock Mach numbers, at least two options are available. The use of vacuum in the driven side was not used due to the difficulty encountered in sealing the driven side from small leaks, particularly at the heat transfer probe attachment junction. Therefore, another option was needed to provide a reasonable Mach number range over which to test the thin-film probes. For a shock tube activated by over-pressure and not a manual bursting device, the only way to obtain a variety of Mach numbers is to use different diaphragm materials. Many possible candidates for diaphragm materials were tested. In particular, four types of Flexel cellophane products were tested, along with two thicknesses of common aluminum foil. Standard aluminum foil, although an attractive diaphragm candidate due to its low burst pressure, was found not to break cleanly enough to allow for a well-defined shock wave to form. This was determined by examining the shape of the pressure pulse as it passed the first pressure transducer. A sharp rise in pressure signals a well-defined shock wave, whereas a gradual ramp in pressure indicates a shock wave that is getting steeper and is still being formed.

Having eliminated standard aluminum foil, heavy duty aluminum foil was tested. It was found to be an excellent

diaphragm material, with an intermediate average Mach number (1.21) with very little variance. The four cellophanes tested were Flexel products, with the following Flexel catalog numbers: "K" HB-20, MST, 123 "V" 58P, and 118 "V" 58F. A variety of trials were made with all five of the candidate diaphragm materials. Presented in Figure 4.6 is a plot of the mean break pressure for each of the five diaphragm materials, with one standard deviation shown. Notice that the most repeatable results are obtained with heavy duty aluminum foil. This is a Stop 'n' Shop brand name product, with a thickness of 1.5 mils. Figure 4.7 presents the same data, except now the more physically relevant parameter of shock Mach number is plotted rather than break pressure. It is intended that Figure 4.7 aid future users of the shock tube by offering a standard database for diaphragm material selection. In particular, an experimentalist may choose the membrane that provides the Mach number of interest or may use a variety of materials to obtain a reasonable Mach number range.

The ultimate proof of concept test for the shock tube comes by comparing the experimental and the theoretical shock speeds. The theoretical shock speed is not truly analytical in an absolute sense because it relies on the measurement of break pressure. However, by comparing the speed implied by the pressure ratio at burst with the speed measured between the two pressure transducers, the degree of applicability of the standard one-dimensional shock tube equations can be determined. Figure 4.8 presents the percentage error in theoretical and experimental shock speeds as a function of Mach number for each shock tube test run. No distinction is made between the different heat transfer gauge conditions utilized, since we are only verifying the correct operation of the shock tube. The excellent agreement between theoretical and experimental shock speeds is clearly seen.

4.2 EXPERIMENTAL APPARATUS FOR THE SUBSONIC WIND TUNNEL

The shock tube is an ideal diagnostic tool to obtain the unsteady response (at least to a step function) of a thin-film heat transfer gauge. However, it cannot be of assistance in determining the steady response of one of these probes, nor in obtaining steady calibrations. The ideal test situation would consist of a subsonic wind tunnel, with provisions for changing the velocity and total temperature of the air stream. Such a facility is readily available and is sketched in Figure 4.9. The test section is split into two separate sections. Both flow speed and total temperature of the flow can be controlled, with a Mach number range for the tunnel from 0.0-0.2 and temperature increase over ambient of up to 40 K possible (for low speeds). Heating of the flow is accomplished through resistive (ohmic) power dissipation far upstream of the test section. The temperature of the airstream was not varied in the experiments performed here.

Flow speed is readily obtained from the manometer board. The static and total pressure at the test section are measured in inches of oil. From Bernoulli's equation, the difference in these two readings reflects the dynamic head of the system. The flow velocity is obtained as follows:

$$v = \sqrt{\frac{2\,\rho_o\,g\,h\,\sin\theta}{\rho_a}} \qquad (4.1)$$

where v is the speed of the flow, ρ_o is the density of the oil, h is the height difference between the two relevant manometer columns, g is the acceleration due to gravity, θ is the angle of inclination of the manometer board, and ρ_a is the density of the airstream. A compressible model is used to reduce the data, however, as in the future these concepts may be tested on a steady flow device capable of compressible flow speeds.

4.3 DESCRIPTION OF TEST GAUGES

4.3.1 Probe supports for the thin film gauges

Several probe supports were constructed to allow the thin-film gauges to be used in the shock tube. A flush-mounting system is used with these gauges, to give minimum disturbance to the flow field of interest. Bonding is accomplished through standard strain-gauge bonding techniques. Both single-layer and double-layer gauges were tested. A double-layer gauge consists of a top thin-film resistor called the sensor, an insulating layer of kapton, and a bottom thin-film resistor called the heater. Figure 4.10 shows a schematic of the single-layer gauge used in shock tube testing. The radius of curvature r_c of the right end of the probe support was machined to match the radius of the inner wall of the shock tube (for flush-mounting). An external BNC plug was used for ease of electrical connection with the anemometer units. The probe support was constructed of brass for its desirable thermal and electrical properties. Additionally, a gauge support constructed of anodized aluminum was used for the final set of tests. It was desired to have the same material supporting the gauge, and hence the same thermal properties, as for the flat plate probe support. Figure 4.11 depicts the gauge support for the double-layer gauge. Clearly, four leads are now necessary for the circuitry. An aluminum minibox was used (far left) to facilitate two BNC connectors. For both types of probe supports, the external groove was filled with epoxy to strain-relieve the leads attached to the gauge itself.

The flat plate probe support sketched in the tunnel in Figure 4.9 is shown in detail in Figure 4.12, to scale. The thickness of the anodized aluminum plate is 32 mils. The four square tags in each corner of the flat plate each are equipped with a centered 0.25 inch diameter hole. This is for ease of mounting in the subsonic tunnel as well as for providing a non-critical point of attachment during the anodizing process. As for the shock tube, standard strain-gauge bonding techniques are used to mount the heat transfer gauge to the flat plate. The leads are strain-relieved

via a connection to the underside of the plate to a kapton soldering terminal. External connectors then connect the soldering terminals to BNC cables. The location of the gauge on the flat plate was dictated by boundary layer considerations. It was discovered that there was a way to obtain both laminar and turbulent flow depending on whether the flow came from the left or from the right (as seen in Figure 4.12).

To assure a well-behaved boundary layer on the flat plate, the leading edge was smoothed to give an approximately elliptic profile, with the requirements that it be symmetric, blunt at the leading edge, and have a major to minor axis ratio of the ellipse of at least five. Shown in Figure 4.13 is a 3D sketch of the leading edge approximately elliptical geometry. Naturally, this profile was produced on the other side of the flat plate (the side not drawn, downstream in Figure 4.13) since it is meant to be interchangeable. The turbulent flow configuration is shown in Figure 4.13. If the flow direction were from the right, this diagram would represent the laminar flow configuration. Without this leading edge profile tailoring, the boundary layer will differ substantially from a simplistic model, due to the discontinuity in slope at the leading edge.

4.3.2 The calibration of α

Before a heat transfer probe may be tested in the shock tube, the thermal coefficient of resistivity (α) of each thin film element must be calibrated. For sensors provided by a manufacturer (a single sensor from DISA, in this case), the α is calibrated at the company and its value is provided. Otherwise, a calibration must be performed by the experimentalist. This would not be so except for the fact that the thermal coefficient of resistivity of a material is substantially different from the bulk value as the thickness of the material decreases. In particular, for the sensors tested here, the value of α obtained from calibration is between two and eight times smaller than the bulk value for pure nickel.

A facility is available for the calibration of α for these devices. It consists of a well-insulated temperature bath accurate to 0.1 K, with operator temperature control. The bath fluid is Fluorinert, a non-reacting liquid with well-known thermal properties and stability. Initial attempts at calibration in distilled water were unsuccessful, demonstrating that the distilled water sample was more ionic than expected. The calibration procedure is simply to measure the resistance of the thin-film gauge as a function of bath temperature while the thin-film is completely immersed in the fluid. The thin film must be tested after being mounted to the probe support, as the bonding process might change the value of α. From Equation (2.1), it is expected that the data from such a calibration would fall on a straight line. Therefore, once the experimental points were obtained, a linear regression procedure was used to determine the best fit line for resistance vs. temperature. Figure 4.14 presents such a calibration for a thin nickel film with thickness 2600 Å. This thin film was used as a heater with a DISA single sensor, model number 55R47 providing a homemade double-layer probe. Figures 4.15-4.18 show calibrations for ready-made double-layered probes, one mounted on a brass support and the other mounted on an anodized aluminum support. Notice that the heater and sensor must be calibrated separately, and in fact that the value of α is substantially different between the heater and the sensor for each case. This is not surprising, as the heater and sensor for a given gauge are constructed separately by a vacuum sputtering technique. In all cases, the data fits a straight line relatively well. The approximately parabolic shape of the data points in Figure 4.17 represents a non-equilibrium heating process. This usually may be avoided by carefully stabilizing the bath temperature before taking a resistance measurement.

Unlike the shock tube, the only experiments performed in the subsonic tunnel facility were experiments using double-layer gauges with the heater and sensor temperatures actively

controlled to be identical. Ready-made, turbine heat transfer gauges were employed exclusively, due to their proven technology and their availability. As for the shock tube, TSI anemometer units were used to control the gauge sensor and heater at constant temperature. The sensor and the heater were calibrated, after flat plate mounting, in the Fluorinert temperature bath described previously. The calibrations for the first flat plate gauge are presented in Figures 4.19 and 4.20, while those for the second flat plate gauge are presented in Figures 4.21 and 4.22. In Figure 4.21 particularly, notice again the slight parabolic nature of the data points, due to non-equilibrium heating of the gauge in the temperature bath. As it will be demonstrated later, the largest error source encountered in the subsonic wind tunnel experiments is due to calibration errors for the coefficient of thermal resistivity for the heater and the sensor. Tests would have been performed exclusively on the the first flat plate gauge, but a sensor failure lead to the construction of the replacement gauge.

4.3.3 Feasibility of balancing non-standard resistors

The anemometer units from TSI are typically used to balance probes in a resistance range of 5-50 ohms. The so-called turbine gauges typically have a cold resistance of between 500 and 1000 ohms for both the sensor and the heater. When these gauges were used in the MIT Blowdown Turbine Facility, homemade bridge balance units specifically designed for these large gauge resistances were employed. According to the manufacturer, no data exists on the ability of TSI anemometer units to balance gauges in the centi-ohm to kilo-ohm range. Figure 4.23 represents the data from a simple test to determine if these anemometers can be used for this non-standard application. The anemometer output voltage is plotted as a function of the sensor cold resistance, holding the control (hot) resistance constant at 522.4 ohms. All three anemometer bridges (each one is a 5:1 bridge, with different current levels) were tested. Since saturation for these anemometers occurs at an output voltage of

approximately 22.6 volts, the sensitivity to overheat ratio is seen to be represented. However, due to the large values of the sensor output voltage, a forced flow over a gauge with this resistance may cause saturation (these tests were performed at zero flow). No saturation occurred in any of the actual heat flux measurements performed. Figure 4.24 represents a similar test, with now the cold resistance held constant and the overheat ratio varied. Plotted is the output voltage vs. overheat ratio for a cold resistance of 1510 ohms. There appears to be a tradeoff between sensitivity and possible saturation for the different bridges. Bridge #1, the standard bridge for most anemometry work, offers the best sensitivity but may saturate at high flow velocities. This bridge was used exclusively with no saturation occurring. Notice, however, that the curve for bridge #1 is incomplete. At higher overheat ratios, it became impossible to set the standby voltage of the anemometer within the desired range of 2-5 volts for this bridge.

One possible test of a double-layer gauge consists of running the heater actively in a control loop and allowing the sensor to be passive. In this case, it is expected that the temperature of the sensor would rise until it approximately equalled the temperature of the heater (in zero flow). Since resistance is a known function of temperature for the sensor, if we measure the resistance of the sensor in this configuration, we can calculate the implied temperature of the sensor. Plotted in Figure 4.25 is the sensor temperature vs. the heater temperature for such a test, with both temperatures being non-dimensionalized by the ambient temperature. Again, all three bridges were tested. Bridge #1 offers superior performance, as the expected curve is a line of slope one through the origin and the curve for bridge #1 closely approximates this. Bridge #3 is not acceptable, because with low overheat ratios for the heater, the sensor temperature is too large. Notice that beyond a heater to ambient temperature ratio of 1.11, the sensor temperature remains roughly constant. It appears that increasing the heater temperature beyond this point only

increases the heat conduction into the probe support. This therefore may provide a limit on the overheat ratio that can be employed. Figure 4.26 shows the voltage output for a double-layer gauge operated so that $T_s=T_h$ versus the sensor overheat ratio. To an overheat ratio of 1.08, the voltage value for this heater-controlled gauge is sensitive to overheat ratio (again, for zero flow). This does represent a much lower overheat than is typically run for a hot-film probe (generally, a_r=1.4-1.5 in air). At higher overheat ratios, the voltage value for the double- layer gauge will certainly saturate, at least for these high cold resistance gauges. Therefore, overheat ratios were limited somewhat severely in the tests performed. This may have affected the results adversely, because over the overheat ratio range tested here, higher overheat ratios generally provided better results than lower ones.

CHAPTER 5

DATA REDUCTION AND ERROR ANALYSIS

5.1 DATA REDUCTION FOR THE SHOCK TUBE

A simplistic quasi-steady model for the heat transfer effects of a propagating shock were examined in this study. It was assumed in this scenario that an ideal, non-separating turbulent Blasius boundary layer grew in thickness at the gauge location following the passage of the shock. The Reynolds number for this configuration can be written as follows:

$$Re = \frac{\phi_m (c_s t)}{\mu} \tag{5.1}$$

where ϕ_m is the mass flux in the shock tube, μ is the viscosity of the air, c_s is the shock speed and t is the time since shock passage. The quantity $(c_s t)$ replaces the characteristic length in the Reynolds number equation. By examining the heat transfer coefficient h, the effect of the propagating shock on the convective heat transfer can be determined. In general:

$$h \sim \frac{Re^{0.8}}{x} \sim x^{-0.2} \tag{5.2}$$

but, since $x = c_s t$:

$$h \sim \frac{1}{t^{1/5}} \tag{5.3}$$

Therefore, as the shock propagates away from the heat transfer gauge, the value of h (and hence q_{conv} and V_0) decrease after an initial infinite spike. In particular, since the output voltage scales

as the square root of the convected heat transfer, for a zero conduction case:

$$V_0 \sim \frac{1}{t^{1/10}}$$

(5.4)

showing that the decay in voltage with time following shock passage should be very slight.

The output voltage as a function of time shall be derived for the case of no substrate heat conduction. The case of constant heat conduction can be treated similarly. The impedance of any resistive element is a function of geometry and a material property known as the resistivity. In particular, the resistivity of a material divided by its thickness gives a quantity called the ohms/square, denoted here by σ. For a resistor of length L and width W, the resistance can be expressed as follows:

$$R = \sigma \left(\frac{L}{W} \right) \tag{5.5}$$

The measurement of the thickness or the resistivity of the thin-film gauge is not a trivial process. As for the thermal coefficient of resistivity, the resistivity of a thin-film material is a strong function of the thickness of the material. However, this presents no difficulty since the thickness and resistivity of the thin-film material appear only in the form of σ, and σ is readily calculated by dividing the measured resistance of the gauge by the length to width ratio.

It can be shown [Blackwelder] that the voltage output from a hot-wire or hot-film anemometer can be written as follows:

$$V_0 = \left(1 + \frac{R_1}{R_s} \right) \sqrt{R_s \, q_{conv} \, S} \tag{5.6}$$

for a case with no heat conduction (again, this is just a power balance). The parameter S is the area over which heat transfer takes place. The bridge ratio (R_1/R_s) is five in all cases tested. Notice that R_s is the hot resistance of the gauge sensor. Combining (5.5) with (5.6) and the definition of h, with the realization that S= LW:

$$V_0 = L\left(1 + \frac{R_1}{R_s}\right)\sqrt{a_{rs}\,\sigma\,h\,[T_s - T]} \qquad (5.7)$$

Therefore, the voltage output per unit length of sensor is independent of the surface geometry of the sensor, as is expected. The heat transfer coefficient h can be expressed:

$$h = 0.0296\ Pr^{1/3}\ k_f\left[\frac{\rho u}{\mu(T_f)}\right]^{0.8}(c_s t)^{-0.2}\ (T_s - T) \qquad (5.8)$$

where T_f is the film temperature as before and T is the fluid temperature (before or after the shock, as the case may be). Combining (5.7) and (5.8) gives the basic quasi-steady voltage output relation:

$$V_0=L\left(1 + \frac{R_1}{R_s}\right)\sqrt{a_{rs}\sigma[T_s - T]0.0296\ Pr^{1/3}\ k_f\left[\frac{\rho u}{\mu(T_f)}\right]^{0.8}(c_s t)^{-0.2}} \qquad (5.9)$$

This has the correct scaling, in agreement with (5.4). All shock tube runs utilizing a zero conduction condition were analyzed with (5.9), with an arbitrary time being chosen after the shock passage to compare the change in the voltage output observed experimentally at that same time. This result is affected by conduction into the substrate, which occurs when the heater is not controlled to match the sensor temperature. The unsteady

modelling of this problem is presented later, with a companion equation to (4.26) derived for these sets of shock tube runs.

5.2 DATA REDUCTION FOR THE SUBSONIC WIND TUNNEL

The problem that is needed to be solved in general is to calculate the skin friction in a given flow when the velocity of the stream (or mass flux, in compressible flow) and the total temperature of the stream are unknown. This clearly represents the situation of interest in a modern transonic compressor. A calculation procedure based on steady flow is proposed here. Therefore, the validity of the analytical model can be ascertained by examining the true skin friction in a nominally steady flow and comparing it to the skin friction predicted by the model. Indeed, that is what has been done in the steady testing performed. The analytical model for predicting the skin friction is derived in this section. For all heat transfer modelling presented here, steady, quasi-steady, or unsteady, the heat transfer process of radiation was ignored because the emissivity of pure nickel is extremely low (ε_{Ni}= 0.03). In addition, the fourth power dependance of the radiative heat transfer on temperature allows the radiation to be ignored, since low overheat ratios were used throughout testing.

The Nusselt number is a non-dimensional heat transfer coefficient useful for demonstrating heat transfer correlations. It can be shown [Incropera and DeWitt] that the Nusselt number, for a flat plate in parallel flow with an unheated starting length, can be correlated as follows:

$$Nu_x = \frac{Nu_0}{\left[1 - \left(\frac{x'}{x}\right)^{m_1}\right]^{m_2}} \qquad (5.10)$$

where Nu_x is the Nusselt number at a given streamwise location, Nu_0 is the Nusselt number at the leading edge of the flat plate, x' is the distance from the leading edge to the heated location (the

thin-film gauge, in this case), x is the streamwise coordinate, and m_1 and m_2 are, respectively, 3/4 and 1/3 for laminar flow and 9/10 and 1/9 for turbulent flow. To obtain the average Nusselt numbers over the region of interest, these expressions would have to be numerically integrated, for

$$\int x^m (a + bx^n)^p \, dx \tag{5.11}$$

is only solvable when p is an integer, (m+1)/n is an integer, or p + (m+1)/ n is an integer. However, for the situation of interest here, a good approximation to the integral can be obtained by expanding the integrand in a Taylor series and retaining the first few terms only. This is possible because the width of the gauge (Δx) is small compared to the length from the flat plate leading edge to the gauge (x'). By performing the above mentioned Taylor series expansion, the following expressions are obtained for the average Nusselt numbers across the gauge width:

$$Nu_l = \frac{3a_l}{2}\left(\frac{4}{3}\right)^{1/3}\left(\frac{x'}{\Delta x}\right)^{1/3} \tag{5.12}$$

$$Nu_t = \frac{9a_t}{8}\left(\frac{10}{9}\right)^{1/9}\left(\frac{x'}{\Delta x}\right)^{1/9} \tag{5.13}$$

where equations (5.13) and (5.14) represent the laminar and turbulent subcases, respectively, and the coefficients a_l and a_t are defined as follows:

$$a_l = 0.332\ Pr^{1/3}\ Re_{x'}^{1/2} \tag{5.14}$$

$$a_t = 0.0296\ Pr^{1/3}\ Re_{x'}^{4/5} \tag{5.15}$$

with Pr representing the Prandtl number for air (0.72) and $Re_{x'}$ denoting the Reynolds number based on the unheated starting length.

To obtain the skin friction, the modified form of Reynold's analogy is employed:

$$C_f = 2\ St\ Pr^{2/3} \tag{5.16}$$

where C_f is the skin friction and St is the Stanton number, another non-dimensional heat transfer coefficient defined as follows:

$$St = \frac{Nu}{Pr \cdot Re} \tag{5.17}$$

To relate the heat transfer coefficients to the sensor voltage, a power balance must be performed. In general, the heat lost to convection and conduction is balanced by the power input to the sensor, or equivalently:

$$\frac{V_0^2}{R_s} = \frac{k_s}{\delta_s}\ (T_s - T_h) + q_{conv} \tag{5.18}$$

where the first term on the right is the conduction and the term on the left is the power dissipated in the sensor. In this expression, k_s is the thermal conductivity of the substrate, δ_s is the thickness of the substrate, T_s is the controlled temperature of the sensor, T_h is the controlled temperature of the heater, V_0 is the output voltage of the sensor, and R_s is the controlled (hot) resistance of the sensor. In general, the convection cannot be explicitly calculated from this expression, due to the fact that temperature at the substrate/support bonding site is unknown. For a heater passive case, it may be calculated by measuring the resistance of the heater. If the sensor and heater are controlled to be at an identical temperature, however, the steady conduction term goes to zero and the convection can be calculated since the voltage output and hot resistance of the sensor are known. The convection can be related to heat transfer coefficients as follows:

$$q_{conv} = h\,[T_s - Pr^{1/3}T_t] \tag{5.19}$$

where T_t is the unknown total temperature of the airstream and h is the heat transfer coefficient, which may be calculated as follows:

$$h_x = \frac{Nu_x\, k_f}{x} \tag{5.20}$$

where k_f is the thermal conductivity of the fluid. The only fundamental unknowns in equations (5.10) and (5.12) to (5.20) are the total temperature of the airstream T_t and the mass flux of the airstream ρv, which appears in the expression for the Reynolds number as follows:

$$Re_{x'} = \frac{\rho v\, x'}{\mu(T_f)} \tag{5.21}$$

where $\mu(T_f)$ is the viscosity calculated at the film temperature T_f, defined as the average of T_s and T_t.

The procedure used to predict the skin friction is as follows:

1. Select an overheat ratio and calculate the sensor temperature from eq. (2.1).
2. Balance the anemometer so that no heat ideally is conducted through the kapton substrate (i.e., set $T_s = T_h$ using the control resistors). In actuality, this alignment process is approximate only.
3. Measure the output voltage in a given total temperature and mass flux.
4. Calculate the convected heat transfer from eq. (5.19).
5. Combine equations (5.19), (5.20), (5.21), (5.10), (5.12) or (5.13), and (5.14) or (5.15) to obtain one equation for the two unknowns T_t and ρv, utilizing (5.12) and (5.14) for laminar flow and (5.13) and (5.15) for turbulent flow.

6. At the same flow conditions, choose another overheat ratio and repeat steps (2)- (5).

This will give two equations in the two unknowns T_t and ρv, which may be solved numerically. It is imperative that different overheat ratios be run for the two trials, or the same equation will be produced from steps (2) to (5). Once the total temperature and the mass flux of the stream are known, the skin friction can be calculated as follows:

$$C_f = \frac{2\ Pr^{2/3}\ h}{\rho v\ C_p} \tag{5.22}$$

where C_p is the specific heat of the flow in question. Assuming the boundary layer is well-behaved, the theoretical skin friction can be calculated from the same formula, with the true total temperature and mass flux replacing the calculated T_t and ρv. In particular, it may be shown that the experimental to actual skin friction ratio may be calculated as follows:

$$\frac{(Cf)_e}{(Cf)_a} = \left[\frac{(\rho v)_e}{(\rho v)_a}\right]^{m-1} \left[\frac{T_s + (T_t)_a}{T_s + (T_t)_e}\right]^{3(m-1)/2} \left[\frac{T_s + T' + (T_t)_e}{T_s + T' + (T_t)_a}\right]^{m-1} \tag{5.23}$$

where the subscript e denotes experimental, the subscript a denotes actual, T' is a constant (221.2 K), and m is 0.8 or 0.5, depending on whether or not the flow is turbulent or laminar, respectively. It is through the use of equation (4.14) that the graphs of subsequent chapters were prepared.

5.3 ERROR ANALYSIS

Many possible sources of error exist that will cause a discrepancy between the theoretical and experimental values of skin friction. A standard error analysis was performed to investigate the relative importance of the error terms to the

calculation of the skin friction ratio. For a typical test case, the most important error-producing sources are the thermal coefficients of resistivity of the sensor and the heater (α_s and α_h, respectively). This is not due to the inherent error encountered when attempting to calibrate the value of α, but is due rather to the very large coefficient multiplying α that occurs in the error analysis. The next most important source of error comes from the drift of the sensor or heater cold resistance or the error encountered when setting the overheat ratio. The output voltage measurements represent the next most important source of error. All other errors, including those due to Prandtl number (Pr), distance from leading edge of flat plate to the gauge location (x), angle of inclination of the manometer board (θ), width of gauge (Δx), ambient pressure (P_0), total pressure (P_t), and ambient temperature (T_0) are negligible. This is depicted graphically in Figure 5.1, for a typical case of turbulent flow, a_{rs1}= 1.04, and a_{rs2}=1.08. This has important ramifications for the thin-film heat transfer gauge designer. The calculation of α is seen to be one of the most critical steps in the entire skin friction measurement process. Since the coefficient of the α error term cannot be altered significantly, the only way to lower this error source is to reduce the error in α itself during the calibration procedure.

The error analysis proceeds as follows: for a given measured quantity ϕ, which is a function of the n variables a_1, a_2, a_3, ..., a_n such that a_i is independent of a_j when i,j= 1 to n and i and j are not equal, the error in ϕ can be calculated from the chain rule to be as follows:

$$\frac{\delta \phi}{\phi} = \sqrt{\sum_{i=1}^{n} \left(\frac{\partial \phi}{\partial a_i} \cdot \frac{a_i}{\phi} \cdot \frac{\partial a_i}{a_i} \right)^2} \qquad (5.24)$$

This is a classic Gaussian distribution on the possible error sources in the problem. For this case, equation (5.23) was used to describe the ϕ function, with the ratio of experimental to actual skin friction being ϕ. The error terms evaluated were α_s and α_h, V_1 and V_2, R_{cs1}, R_{cs2}, R_{ch1}, and R_{ch2}, Pr, θ, Δx, x', T_t , P_t, and P_0. By far the most influential of the error terms evaluated above are the coefficients of thermal resistivity. This may be explained by looking at the how the coefficient of the α error term scales in this error analysis. It was found that the variation in ϕ with respect to α is directly proportional to the variation in T_g with respect to α:

$$\frac{\partial \phi}{\partial \alpha} \sim \frac{\partial T_g}{\partial \alpha} \tag{5.25}$$

However, the variation of T_g with respect to α can be readily calculated:

$$\frac{\partial T_g}{\partial \alpha} = \frac{\partial}{\partial \alpha}\left[\frac{a_r - 1}{\alpha} + T_0\right] = -\left[\frac{a_r - 1}{\alpha^2}\right] \tag{5.26}$$

Even for low overheats, this quantity is large due to the fact that the value of α is small and α appears to the negative two power. This mandates a very careful calibration for the value of α, for the only way to reduce the error due to α in (5.24) is to reduce the variation in α divided by α term. The accuracy in calculating α, i.e. $\frac{\partial \alpha}{\alpha}$, is assumed to be 5%. The total error term for α_s or α_h is on the order of 30-35%.

The reason that the gas temperature or the wall to gas temperature ratio is not included in the error analysis is because it is not independent of the fifteen variables selected above. Indeed, it is desired to know the error associated with the drift of the tunnel temperature, which could be as much as 5 K. A standard error analysis shows that the effect may indeed be substantial, with the error in ϕ found to 5.5% and 22 % for

turbulent and laminar flows, respectively, for a low overheat ratio of around 1.04. It is also seen that the error increases as the wall to gas temperature ratio approaches one , as is expected. Experiments need to be performed with various gas temperatures and wall temperatures to discover how the experimental error scales with the wall to gas temperature ratio. In these sets of tests, only the wall temperature was varied, and the experimental errors observed were indeed more substantial for lower wall to gas temperature ratios (lower overheats).

CHAPTER 6

EXPERIMENTAL DATA AND COMPARISON OF DATA WITH THEORY

6.1 SHOCK TUBE EXPERIMENTAL RESULTS

Ten separate shock tube runs were performed. The parameters that characterized these runs are listed below:

Run #1: Shock tube familiarity testing; no heat transfer data recorded; heavy duty aluminum foil diaphragms only; brass support

Run #2: Shock tube familiarity testing; no heat transfer data recorded; heavy duty aluminum foil diaphragms only; brass support

Run #3: Range of diaphragm materials testing: standard aluminum foil, heavy duty aluminum foil, and 118 "V" 58F cellophane; no heat transfer data recorded; brass support

Run #4: Single DISA sensor testing; heat transfer data recorded; brass support; a_{rs}= 1.23

Run #5: Double-layer gauge testing; DISA sensor; DISA heater; heater passive; heat transfer data recorded; brass support; a_{rs}= 1.20

Run #6: Double-layer gauge testing; DISA sensor; 2600 Å nickel thin-film heater; heater passive; heat transfer data recorded; brass support; a_{rs}= 1.20

Run #7: Double-layer gauge testing; DISA sensor; 2600 Å nickel thin-film heater; heater active; $T_s=T_h$; heat transfer data recorded; brass support; a_{rs}= 1.20

Run #8: Double-layer gauge testing; turbine gauges; heater active; $T_s=T_h$; heat transfer data recorded; anodized aluminum support; a_{rs}= 1.06

Run #9: Double-layer gauge testing; turbine gauges; heater active; $T_s=T_h$; heat transfer data recorded; anodized aluminum support; a_{rs}= 1.08

Run #10: Double-layer gauge testing; turbine gauges; heater active; $T_s=T_h$; heat transfer data recorded; anodized aluminum support; a_{rs}= 1.11

Tables C.1 through C.10 represent these ten shock tube runs, presented in Appendix C. Each of these tables provide supplementary information to the heat transfer plots that shall appear presently. The turbine gauges mentioned above are readily available, double-layer heat flux gauges that are so labelled for their extensive application in the MIT Blowdown Turbine Facility.

Figures 6.1-6.6 and Figures D.1-D.15 represent the unsteady voltage trace from the gauge sensor as a function of time for runs #4-#10 above. The point of zero time represents the interaction of the shock with the first pressure transducer. As mentioned previously, the sensor voltage is expected to rise as the shock passes the heat transfer gauge, since heat is now being transferred downstream by forced convection. Indeed, this is observed in nearly every voltage trace.

Figures 6.1-6.3 represent the six data points taken during Run #4. The voltage (and hence heat transfer) closely approximates a

step. After shock passage, the voltage level remains roughly constant, in contrast with later runs. The voltage jump across the shock increases with shock Mach number, as expected..

Figures 6.4-6.6 are the voltage traces for Run #5. Again, the voltage traces generally reflect the classic step response. The highest Mach number traces, in Figure 3.14, exhibit a gradual rise in voltage after the passage of the shock. All traces exhibit a greater voltage discontinuity for higher Mach numbers, as before. The second trace in Figure 6.5 unfortunately has been shifted on the time axis, so time zero no longer corresponds to the passage of the shock by the first pressure transducer. Comparing traces in Run #5 vs. Run # 4 demonstrates that, for a given Mach number, the voltage jump is less for the lower overheat ratio case. Again , this is predicted by theory. Appendix D contains the remaining voltage traces and their description, representing Runs #6-10.

6.2 SUBSONIC WIND TUNNEL PROOF OF CONCEPT TESTING AND EXPERIMENTAL RESULTS:

The use of the subsonic wind tunnel facility has been demonstrated in various experiments since its completion. A well-defined steady flow is assumed to be provided, with reasonable flow calibrations having been performed for previous experiments to verify the operation of the infra-red camera and the manometer board for measuring flow temperature and velocity, respectively. No independent sensing devices were employed in these experiments to verify the accuracy of the pressure probes in the test section and the manometer board.

The ambient temperature during subsonic tunnel testing maintained a constant value of 300 K, with less than 1 K variation. However, the temperature of the tunnel was not recorded during testing. To verify the sensitivity of the gauge to velocity (or mass flux), a calibration curve is needed. Figures 6.7-6.10 represent the voltage across the sensor and the heater for laminar and

turbulent flow as a function of the mass flux for the overheat ratios a_{rs}= 1.02, 1.04, 1.06, and 1.08. Due to the scale of these plots, they do not truly represent a calibration curve. On a much more expanded voltage scale, these would resemble classic hot-film calibration curves. Notice the increase in voltage level as a function of the overheat ratio, as is predicted by theory. These plots basically confirm that the anemometer is operating favorably under these atypical large gauge resistance conditions. The sensor curves are more sensitive to mass flux at lower mass flux values, as is expected from the approximately one-quarter power relation between voltage and mass flux.

6.3 SHOCK TUBE COMPARISON OF THEORY AND EXPERIMENT

Figure 6.11 shows a comparison of the theoretical and experimental voltage output for a single sensor at an overheat ratio of 1.23 as a function of Mach number [Run #4]. This represents a test for the analytical model employed. It is seen that the analytical model predicts the output voltage very well, including the trend with Mach number. As the two widely spaced data points at M_s= 1.21 indicate, the error on the output voltage may well encompass the theoretical curve comfortably. To define a voltage after the shock in each trace, an arbitrary time is agreed upon after the shock passage to take the data. In this case, that time difference is 0.2 ms.

For Run #5, which is a double-layer gauge with the heater not controlled (passive), Figure 6.12 shows the output voltage versus Mach number for the experimental data and the analytical model. In this case, the analytical model does a reasonably good job of predicting the level of the voltage change, except that the trend with Mach number is reversed. As before, the time delay is 0.2 ms for the measurement of the voltage change. For Run #6, the equivalent plot is presented in Figure 6.13. The analytical model in this scenario represents an unsteady heat conduction model.

The fact that the experimental points remain roughly constant with Mach number suggests that a thermal equilibrium is being set up, with unmodelled heat transfer processes driving the phenomenon. With a steady, no conduction model, the theoretical curve in Figure 6.13 would appear roughly constant, but at a level over twice the experimental values. If all unsteady heat processes could be properly modelled, a theoretical curve would predict the experimental data points to a much higher degree of accuracy. However, the decrease in sensor voltage change with Mach number would still not be expected, even in that scenario. As before, the voltage after the shock was recorded at 0.2 ms.

For Run #7, which is identical to Run #6 except for the fact that the heater is now controlled so that there is no steady-state conduction into the substrate, Figure 6.14 offers the comparison between theory and experiment for the voltage output as a function of M_s. Although the trend with Mach number is again reversed, the voltage levels between the theoretical and experimental curves are reasonably similar. Hence, in this case, the use of an actively controlled heater has allowed for a better prediction of the experimental voltage output. This is demonstrated more strikingly in Figure 6.15, which gives the percentage error in voltage change across the shock (theoretical vs. experimental) as a function of Mach number for both the heater passive and heater active cases [Run #6 and Run #7, respectively]. The heater active case predicts the experimental voltage output far better than the heater passive case. Data is recorded after the shock passage at a time difference of 0.2 ms.

Figures 6.16-6.18 represent the runs #8-#10, respectively, with the time after shock passage when voltage data was recorded being 0.8 ms. Figures 6.19-6.21 represent the runs #8-#10, respectively, with the time after shock passage when voltage was recorded being 1.27 ms. The extreme disagreement between the theoretical and the experimental values as compared with

previous runs can be observed. Clearly, the large voltage dips present account for some of the discrepancy, but not nearly enough to explain the much larger theoretical prediction for the voltage output. Notice that the results are improved somewhat for the 1.27 ms case. It is postulated that the reason for the large discrepancy in both cases may be due to a non-standard operation of the anemometer unit.

As mentioned previously, there may exist two possible drivers for the large voltage dips seen following shock passage; namely, separation of the boundary layer or an unmodelled heat transfer process. By examining a greatly expanded trace of the pressure pulse recorded by the first pressure transducer after a shock passage, it may be possible to estimate whether or not the boundary layer has separated. Figure 6.22 shows such a pressure pulse. If the boundary layer were not separated, a smooth rise in pressure would be seen, even at this time scale magnification. However, the existence of an inflection point (even a small horizontal region) around a time of 0.03 ms suggests the possibility that the boundary layer is indeed separating. More extensive tests would need to be performed to see what the true state of the boundary layer is at the heat transfer gauge location. The severity of the voltage dip is an increasing function of the shock Mach number and a decreasing function of the overheat ratio (or physically the temperature of the sensor). The increase in the voltage dip with increasing shock Mach number is perfectly consistent with a separation model. The decrease of the size of the voltage dip with increasing sensor temperature cannot be explained with a simple separation model, so some unmodelled heat transfer effect must be dominate in this instance.

6.4 SUBSONIC WIND TUNNEL COMPARISON OF THEORY AND EXPERIMENT

Presented in Figures 6.23 and 6.24 are the experimental to theoretical skin friction values as a function of the measured mass

flux. Ideally, all curves should fall on a horizontal line of value one. For each mass flux, four overheat ratios were run, for both laminar and turbulent flow. By using any two overheat ratios and the measured sensor output voltages, the experimental skin friction can be obtained. The trends seen in Figure 6.23 and 6.24 are clear: (1) results are better for higher overheat ratio combinations; (2) results are better for two overheat ratios that are not adjacent (i.e, 1.02 and 1.04, 1.04 and 1.06, and 1.06 and 1.08); (3) theoretical skin friction tends to overpredict the experimental value at low mass flux values and underpredict the value at higher mass fluxes; and (4) turbulent results are better than laminar, consistent with error analysis predictions. Figures 6.25 and 6.26 graph the actual values of the theoretical and experimental skin friction as a function of the test section Mach number, a more useful parameter for scaling. Similar to the shock tube, it may be said that the theoretical curve is overpredicting the change due to Mach number.

Figures 6.27-6.32 show the theoretical to experimental skin friction ratio as a function of mass flux, with calculated error bars on each data point. Basically, Figures 6.23 and 6.24 represent a composite of all of the curves in Figures 6.27-6.32, albeit without the error bars. A composite curve was not utilized here for the sake of clarity. The laminar error bars consistently extend beyond the boundaries of the graph, comfortably enclosing the expected output curve. It should be mentioned, though, that the largest error bars occur for the case of laminar flow, a_{rs1}= 1.04, and a_{rs2}=1.06, which represents the largest experimental deviation as well (see Figure 6.30). Turbulent error bars are much smaller, and typically do encompass the predicted line except at the lowest overheat ratios. The laminar error bars are much larger than the turbulent ones due to the fact that the exponent in heat transfer/boundary layer correlations for laminar flow is 0.5, while it is 0.8 for turbulent flow. It is seen that the use of the double-layer heat transfer gauge with $T_s=T_h$ does a

reasonable job of predicting the experimental skin friction values in a steady flow of unknown mass flux and total temperature. Whether or not the agreement will hold in an unsteady flow situation remains to be seen.

CHAPTER 7

CONCLUSIONS AND RECOMMENDATIONS FOR FURTHER STUDY

An experimental feasibility study for a new mode of operation for a double-layer heat transfer gauge has been performed. In particular, three operating modes were tested: a single-sensor mode, a heater-passive mode, and a heater-active mode. Experiments were performed to verify predicted models of gauge output in these modes for both unsteady and steady flow.

Unsteady flow results were generally in good agreement with the analytical model, except that the model tended to overpredict the change in output due to Mach number. In addition, unsteady flow results for the anodized aluminum support were substantially different than those predicted by theory. The model correctly predicted the observed increase in voltage jump for an increase in the overheat ratio. Voltage dips following the passage of the shock in the shock tube were observed, and may be explained by a local separation of the boundary layer coupled with unmodelled heat transfer effects. An expanded view of a typical pressure profile during shock passage demonstrates that separation is probably present. The magnitude of the dip in voltage increased with increasing shock Mach number and decreased with increasing sensor temperature. It is found that the agreement between theory and experiment for all modes tested is better for higher overheat ratios than for lower ones. For a fixed overheat ratio and Mach number, the heater-active experimental output of the double-layer sensor was found to be better predicted than the heater-passive experimental output, showing some justification for the concept of a controlled heater. It was found that the calibration of α, the coefficient of thermal

resistivity, and the accuracy of setting the operating resistance of a gauge are important to realize the heater-active mode, for small differences in the heater and sensor temperature can adversely effect the sensitivity of the gauge. In addition, the use of TSI anemometers on non-standard centi-ohm and kilo-ohm probes has been demonstrated via anemometer testing.

Steady-state experimental results attest to the ability of the heater-controlled multi-layer heat flux gauge to be used as a skin friction measurement device in a flow of unknown mass flux and total temperature. In particular, for the varieties of overheat ratios, mass fluxes, and flow types (laminar, attached and turbulent, attached) tested here, the experimental and theoretical skin friction values were in agreement within the accuracy of the measurement, except at the lowest overheat ratios. Again, the analytical model overpredicted the effect of the Mach number. The theoretical value of the skin friction is obtained via a simplified assumption about the velocity boundary layer over the gauge and the thermal boundary layer incident at the gauge, increasing downstream of the gauge. It was noted that the largest errors occurred during the flow situation which allowed for the largest error bars. Turbulent results were generally better than laminar ones, consistent also with the error analysis. Larger gaps between the two overheat ratios used to experimentally calculate the skin friction offered better results, as did higher overheat ratios in general. Again, this is in agreement with the error analysis. The calibration of the thermal coefficients of resistivity of the heater and sensor is the major source of error in the steady experiments, due to the large coefficient on the error term corresponding to α (it is not due to the inherent error in calculating α itself).

A simplistic steady model of the heat conduction into the substrate by assuming that the gauge support is a good thermal conductor is not adequate. For a case where there is no heater or it is run passively, an unsteady model was developed to estimate

the conduction into the substrate as a function of time. This model predicts the sensor output voltage far more accurately than a simplified steady model.

A new gauge was designed to meet the criteria previously mentioned, specifically suited for use on a transonic compressor rotor blade. It was found that a serpentine gauge is preferable to a ladder gauge for sensitivity. The shock wave/boundary layer "smear" was calculated to be roughly four times the expected shock oscillation amplitude, dictating the choice for the element spacing. The 2D electrical conduction in the tags of the thin-film gauge was found to be significantly different than a simplistic model of the conduction through that region. This was incorporated into the gauge design. It was shown that optimally the total tag resistance and the total lead resistance should be the same, and also that the thin-film nickel resistor is thermally transparent for a steady heat conduction calculation. Both a four-element and a ten-element gauge were designed after a parameter trade-off study.

It is recommended that the double-layer heat transfer gauge designed here, or one similar, be tested in a transonic compressor facility to understand the time-resolved boundary layer, shock wave, and separation point structure in that environment. Also, an unsteady heat transfer problem accounting for the dynamics of the anemometer feedback loop and the heat generated within the thin-film must be solved, with periodic as well as step boundary conditions on convection. Additionally, it is recommended that an error analysis be performed for the thermal coefficient of resistivity as it is presently calibrated. In this way, methods of reducing the inherent error in calculating α may be discovered, which will greatly reduce the experimental error encountered in steady testing, due to the dominance of this source of error.

BIBLIOGRAPHY

1. Berry, Robert W., Hall, Peter M., Harris, Murry T., "Thin Film Technology,", Van Nostrand, Princeton, N. J., 1968.

2. Blackwelder, Ron F., "Hot-Wire and Hot-Film Anemometers," Academic Press, Inc., New York - London, 1981.

3. Carslaw, H. S. and Jaeger, J. C., "Conduction of Heat in Solids," Clarendon Press, Oxford [Eng.], 1947.

4. Eckert, Ernst R. G. and Drake, Robert M., Jr., "Analysis of Heat and Mass Transfer," McGraw-Hill, New York, 1972.

5. Epstein, A. H., Gertz, J. B., Owen, P. R. and Giles, M. B., "Vortex Shedding in High-Speed Compressor Blade Wakes," Journal of Propulsion and Power, Vol. 4, No. 3, pp. 236-244, May-June 1988.

6. Epstein, A. H., Guenette, G. R., Norton, R. J. G. and Yuzhang, Cao, "High-frequency response heat-flux gauge," Review of Scientific Instruments, Vol. 57, No. 4, pp. 639-649, April 1986.

7. Hayashi, Masanori, Sakurai, Akira and Aso, Shigeru, "A Study of a Multi-Layered Thin Film Heat Transfer Gauge and a New Method of Measuring Heat Transfer Rate with It," Transactions of the Japan Society for Aeronautical and Space Sciences, Vol. 30, No. 88, pp. 91-101, 1987.

8. Hayashi, Masanori, Sakurai, Akira and Aso, Shigeru, "Measurements of Heat-Transfer Coefficients in the Interaction Regions between Oblique Shock Waves and Turbulent Boundary Layers with a Multi-Layered Thin Film Heat Transfer Gauge," Transactions of the Japan Society for Aeronautical and Space Sciences, Vol. 30, No. 88, pp. 102-110, 1987.

9. Hildebrand, Francis B., "Advanced Calculus for Applications," Prentice-Hall, Englewood Cliffs, N. J., 1976.

10. Incropera, Frank P. and DeWitt, David P., "Fundamentals of Heat Transfer," Wiley, New York, 1981.

11.. Leipmann, H. W. and Roshko, A., "Elements of Gasdynamics," Wiley, New York, 1957.

12. Rohsenow, Warren M. and Choi, Harry Y., "Heat, Mass, and Momentum Transfer," Prentice-Hall, Englewood Cliffs, N. J., 1961.

13. Sabjen, M., Morris, M., Bogar, T. and Kroutil, J., "Confined Normal-Shock Turbulent Boundary-Layer Interaction followed by an Adverse Pressure Gradient," American Institute of Aeronautics and Astronautics, No. AIAA-89-0354, 1989.

14. Shapiro, Ascher H., "The Dynamics and Thermodynamics of Compressible Fluid Flow: Vol. I," Ronald Press Co., New York, 1953-4.

15. Schlicting, Hermann S., "Boundary-Layer Theory," McGraw-Hill, New York, 1979.

16. Strang, Gilbert , "Introduction to Applied Mathematics," Wellesley, Mass., Wellesley-Cambridge Press, 1986.

17. White, Frank M., "Viscous Fluid Flow," McGraw-Hill, New York, 1974.

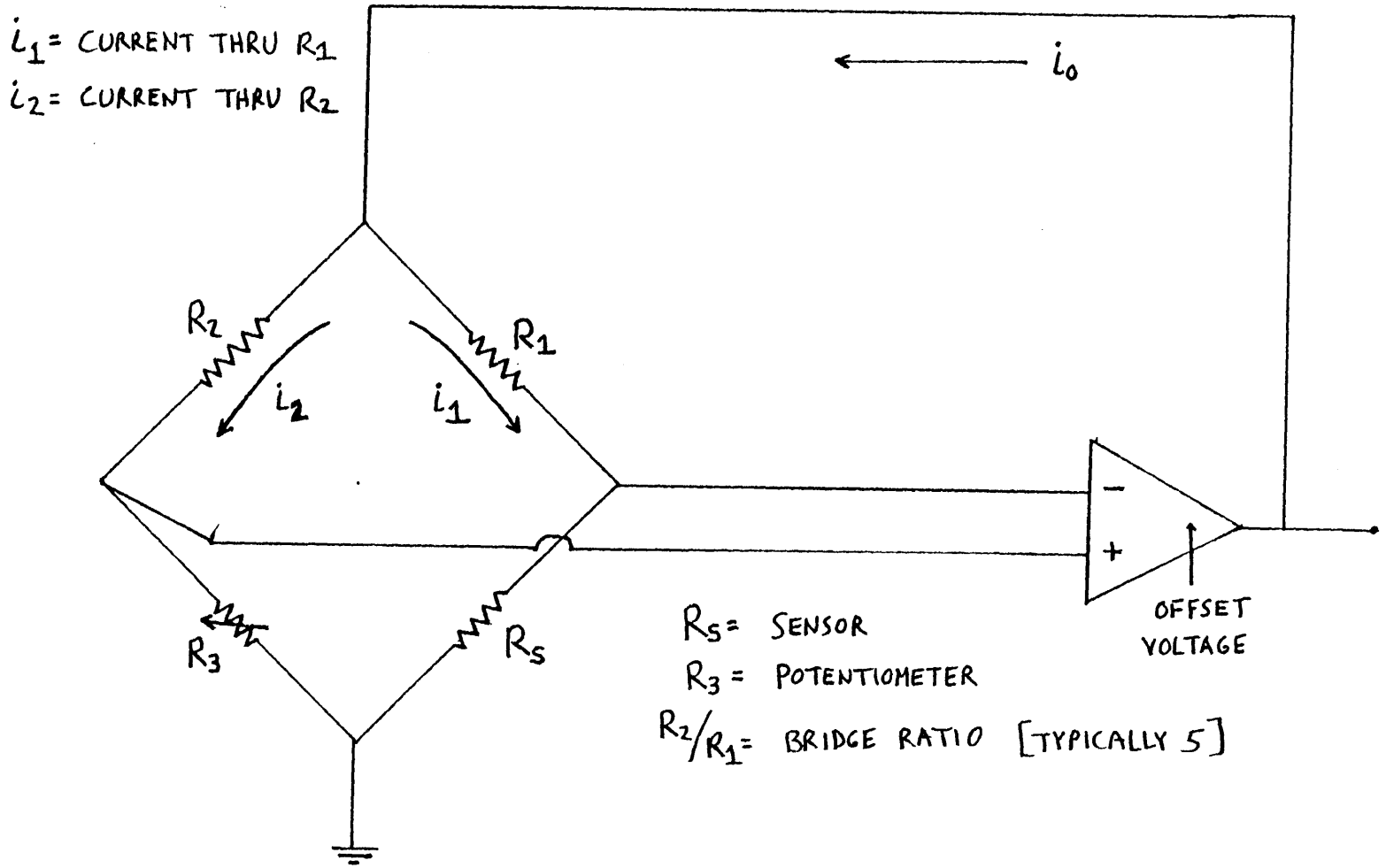

FIGURE 2.1: CONSTANT TEMPERATURE ANEMOMETER FEEDBACK LOOP

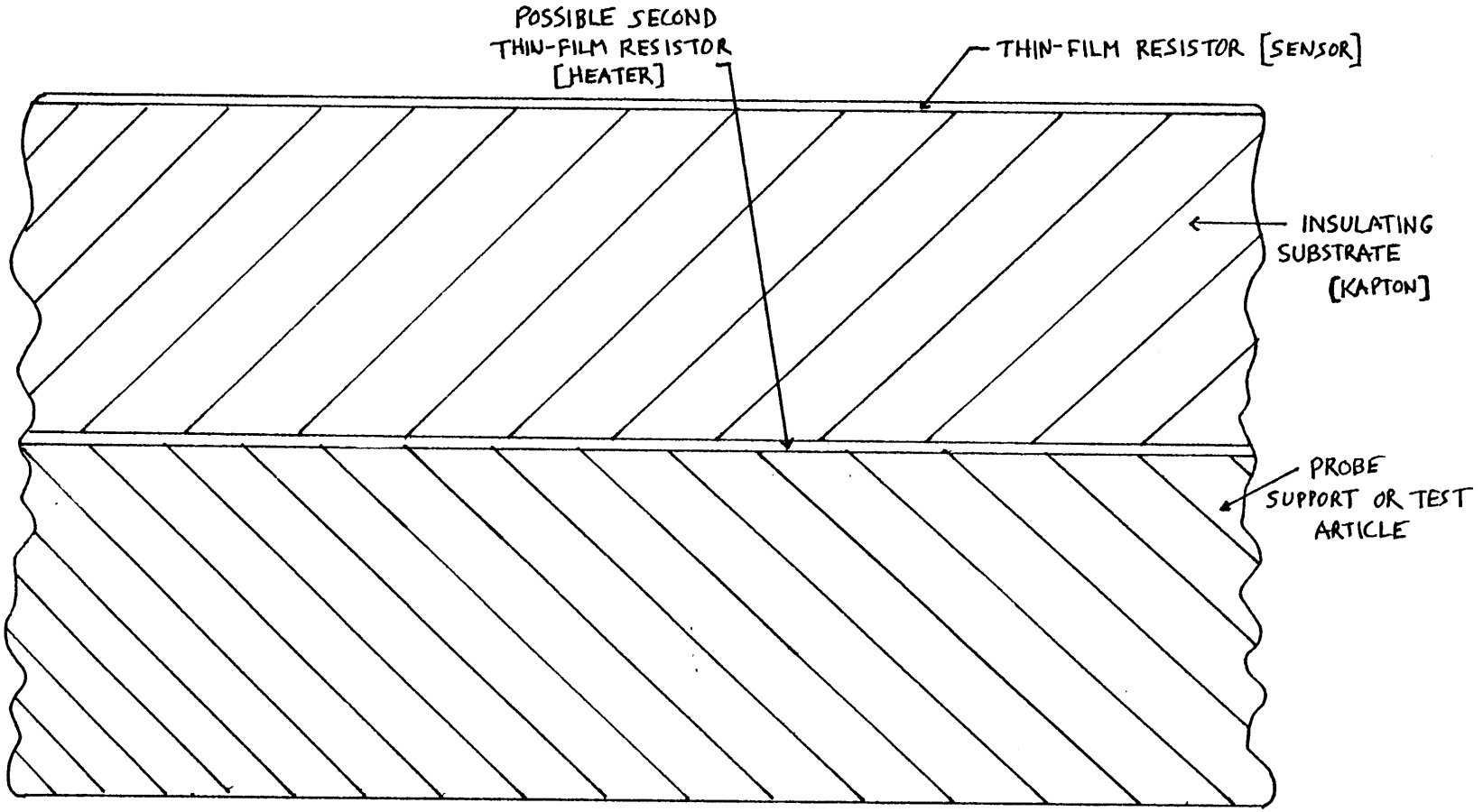

FIGURE 2.2 : THIN-FILM HEAT TRANSFER GAUGE CROSS-SECTION

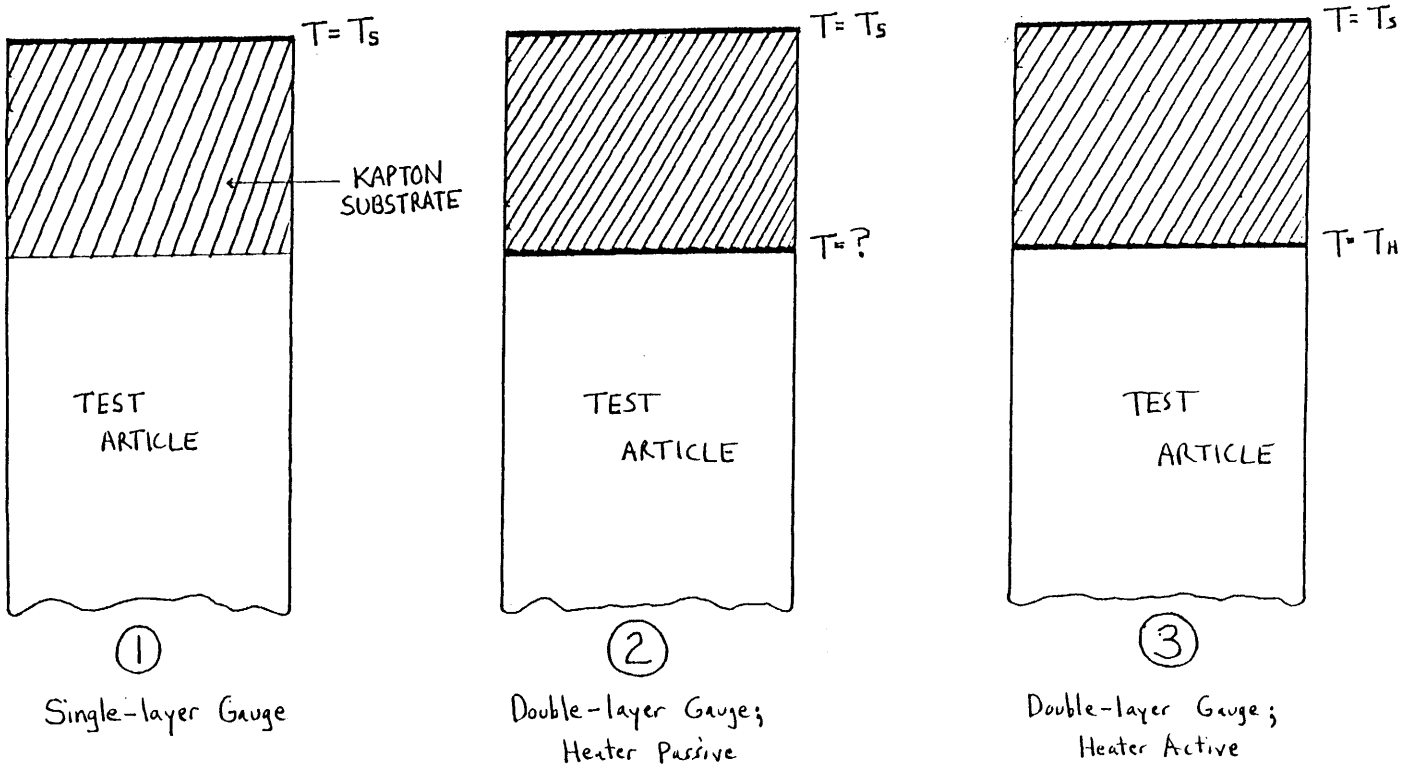

FIGURE 2.3: COMPARISON OF GAUGES AND OPERATING MODES

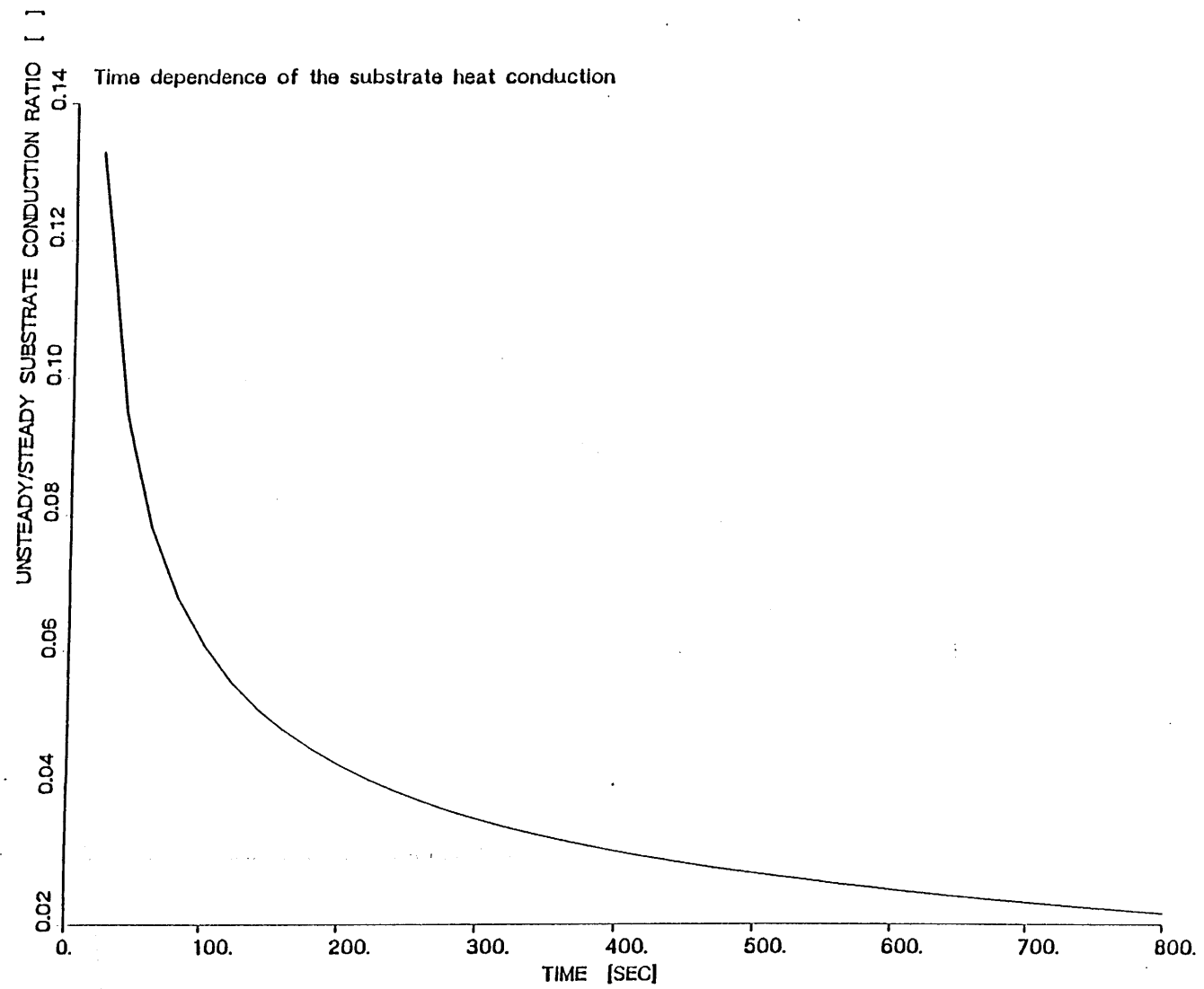

FIGURE 3.1: NORMALIZED UNSTEADY SUBSTRATE CONDUCTION VS. TIME

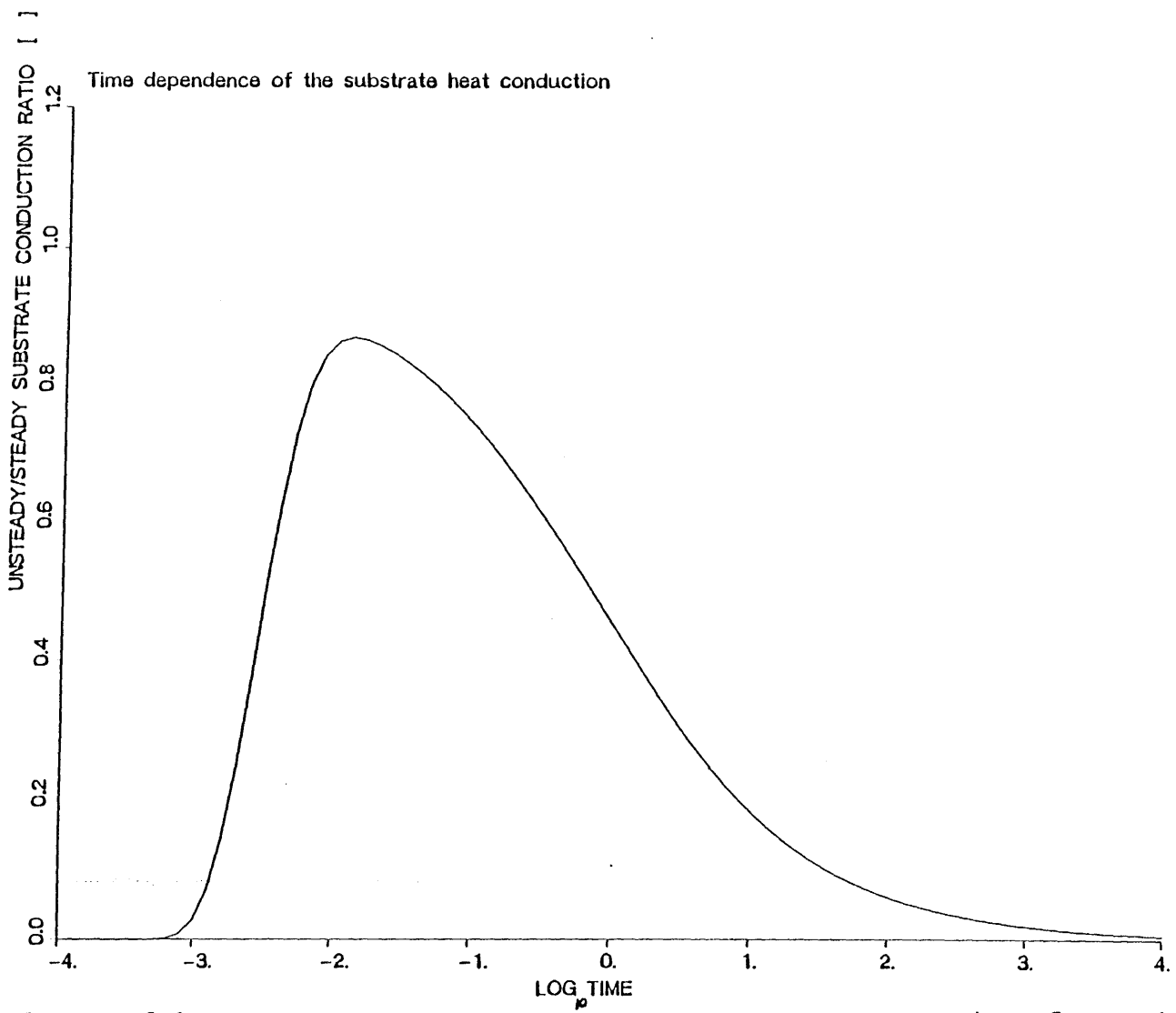

FIGURE 3.2: NORMALIZED UNSTEADY SUBSTRATE CONDUCTION VS. LOG_{10} [TIME]

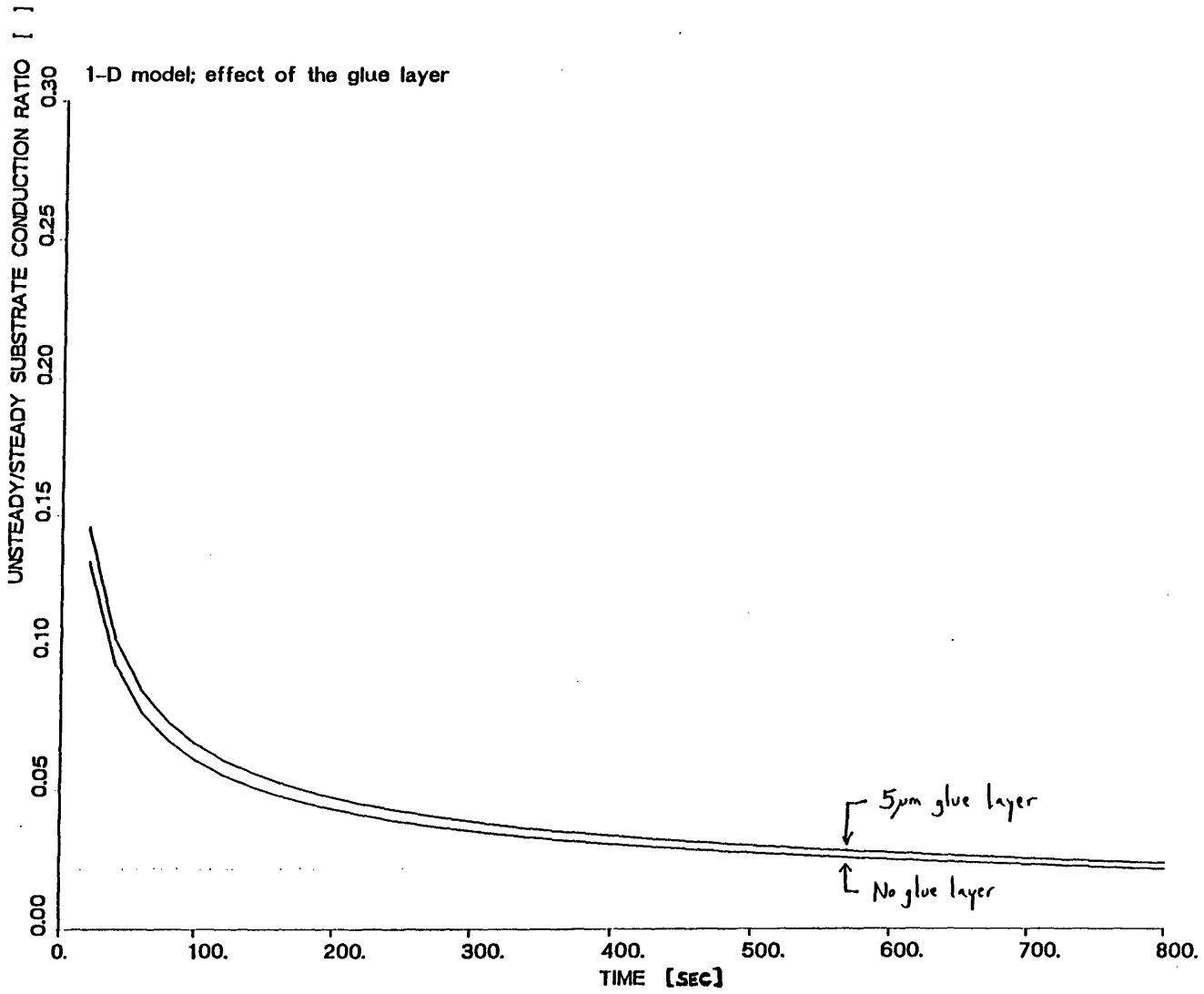

FIGURE 3.3: NORMALIZED UNSTEADY SUBSTRATE CONDUCTION VS. TIME

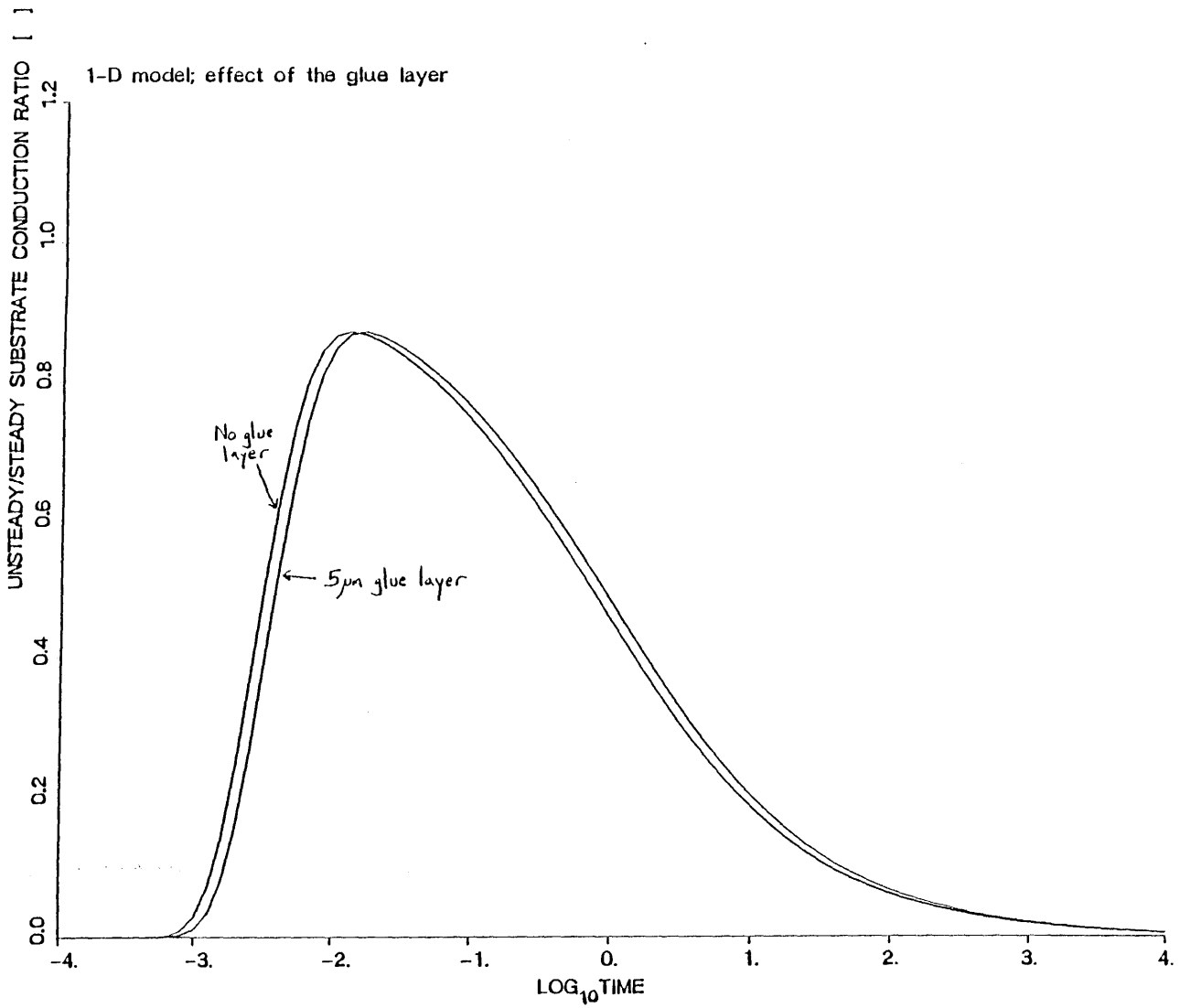

FIGURE 3.4: NORMALIZED UNSTEADY SUBSTRATE CONDUCTION VS. LOG_{10}[TIME]

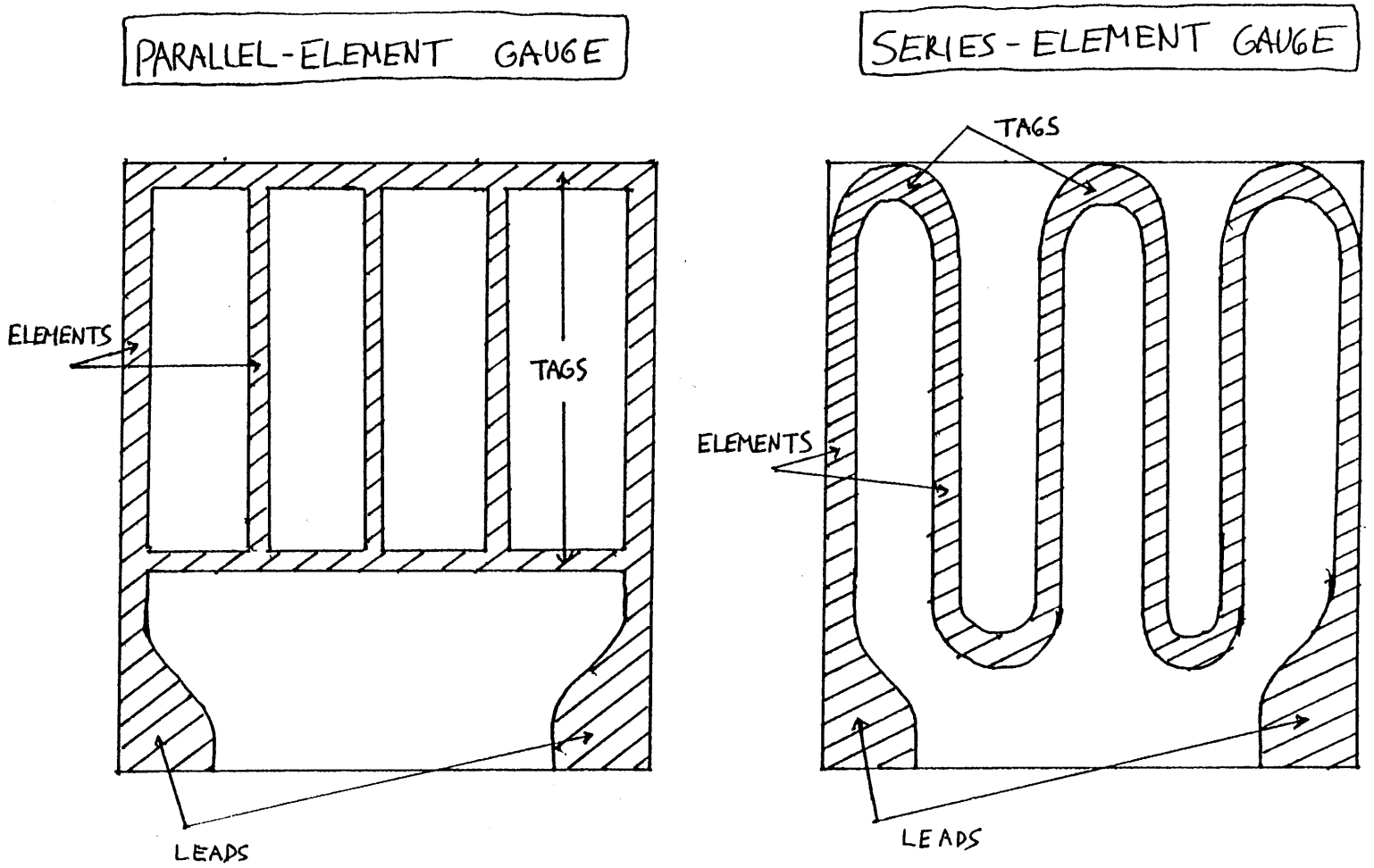

FIGURE 3.5: COMPARISON OF PARALLEL AND SERIES GAUGE GEOMETRIES

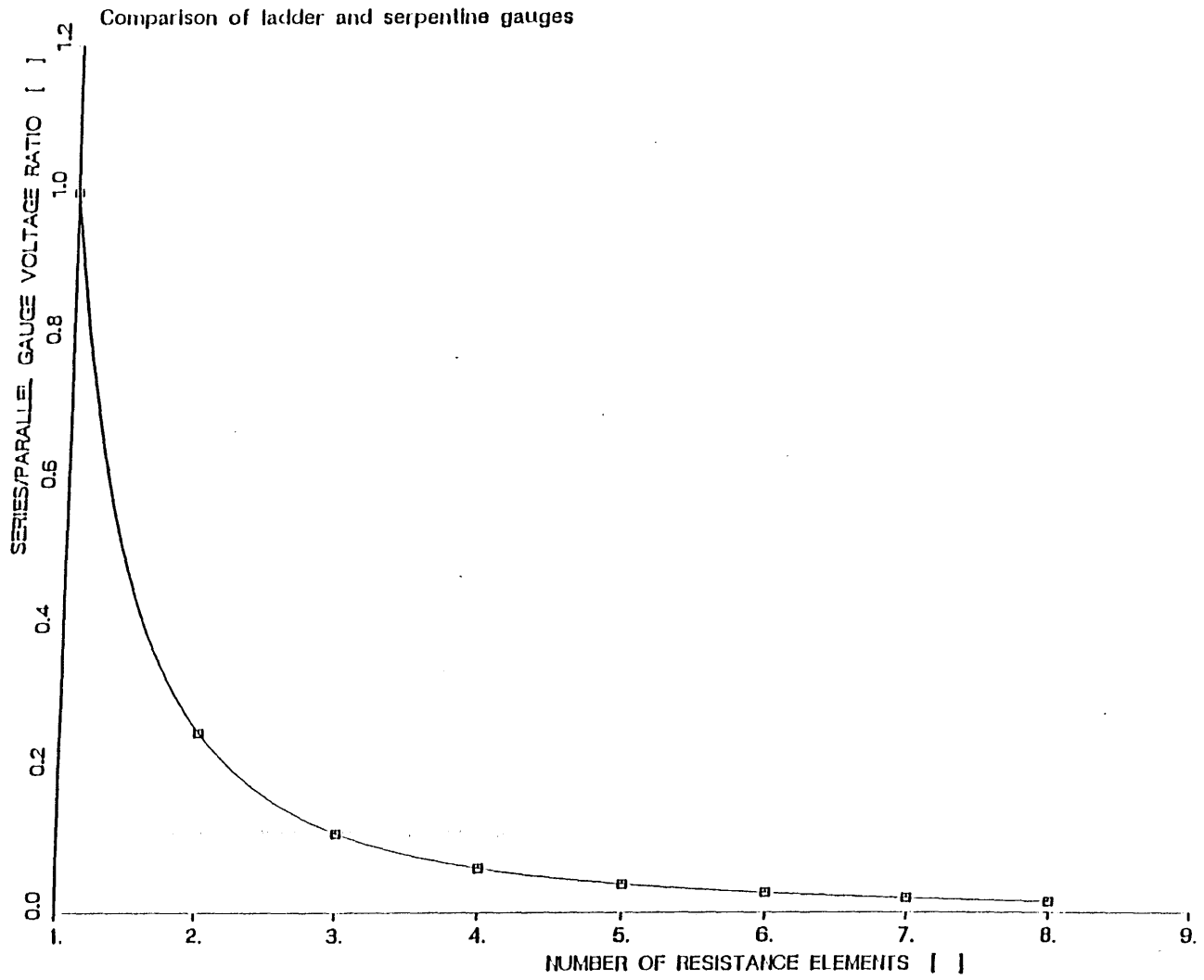

FIGURE 3.6: SERIES/PARALLEL GAUGE VOLTAGE RATIO VS. N

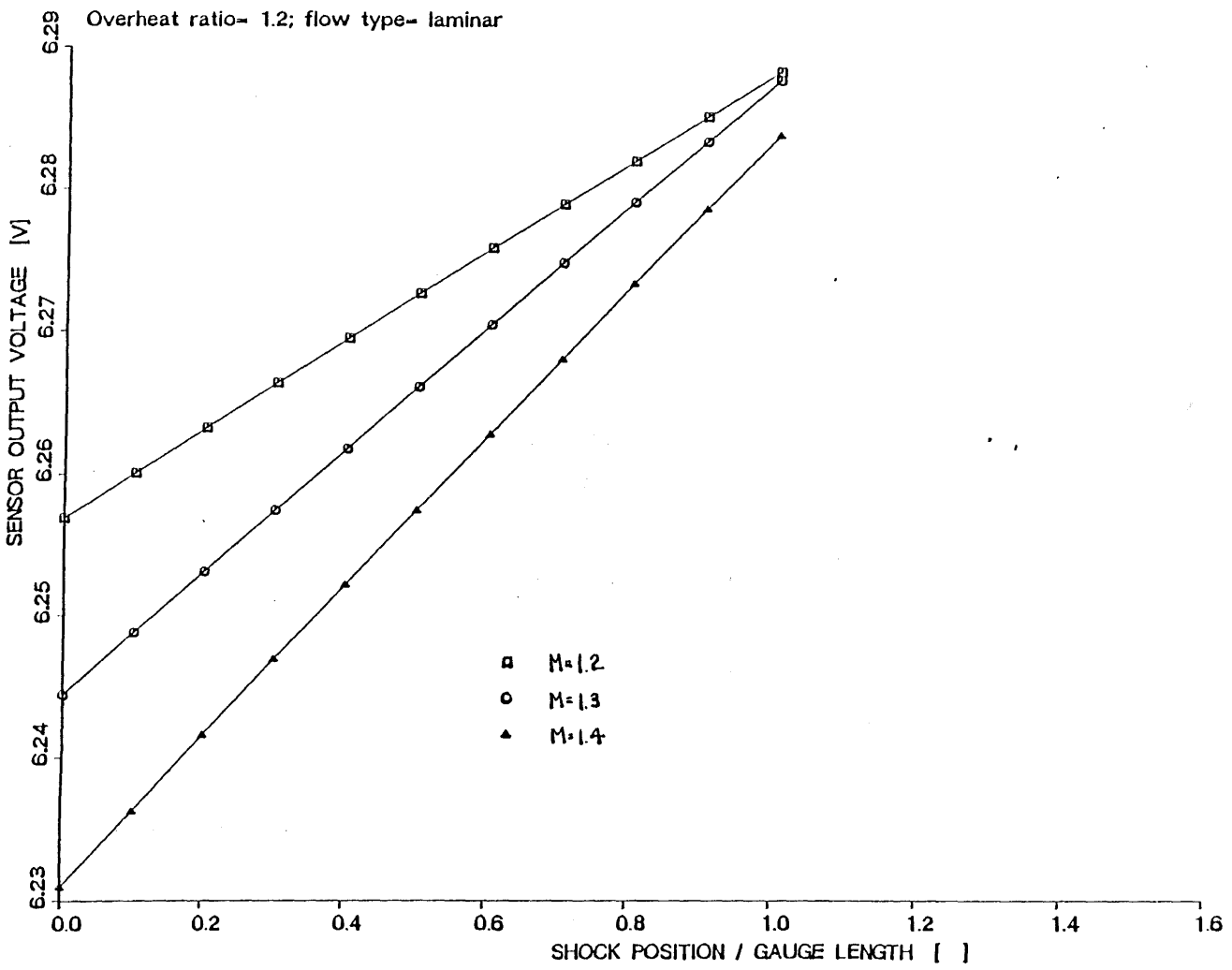

FIGURE 3.7: SENSOR VOLTAGE VS. NORMALIZED SHOCK POSITION

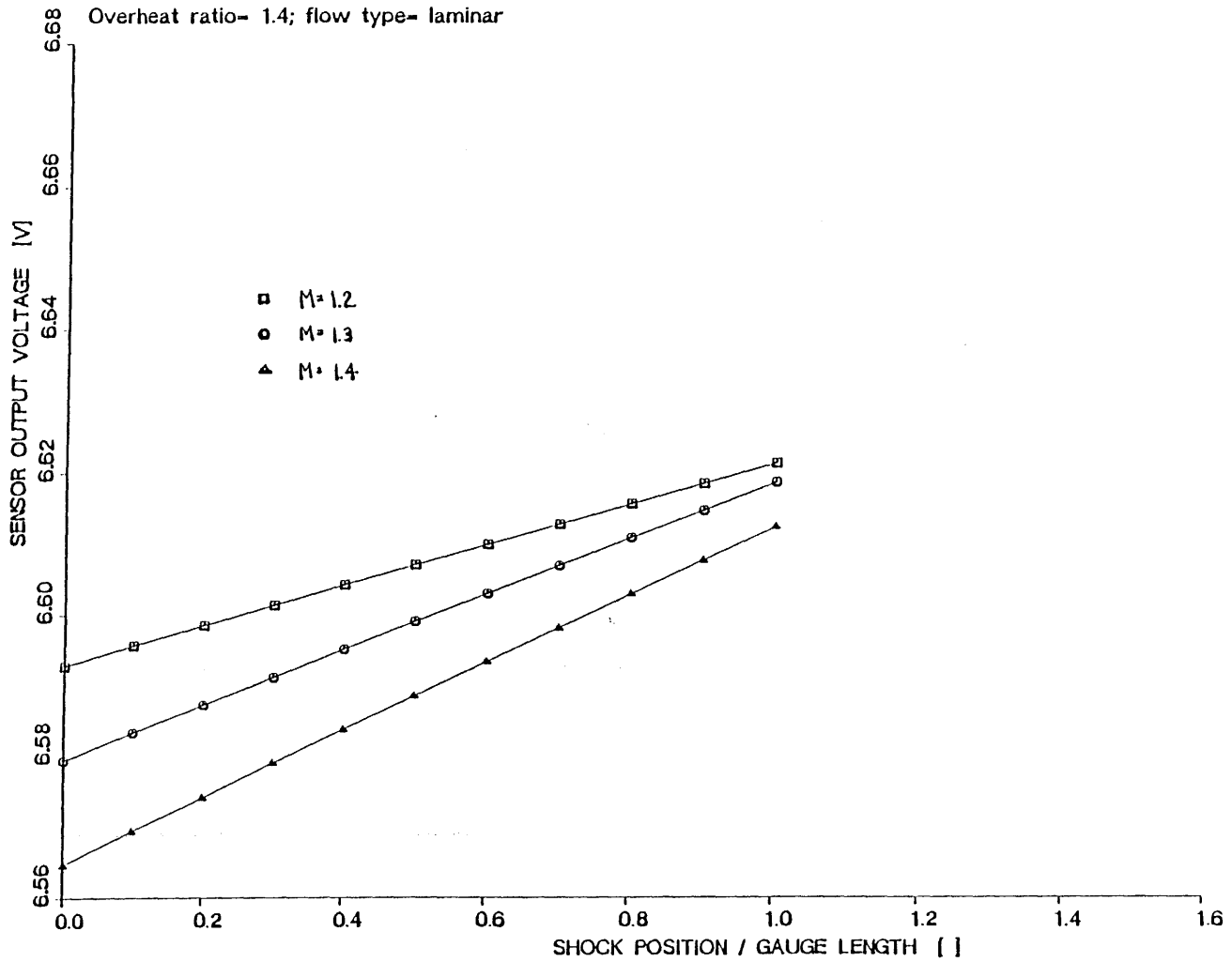

FIGURE 3.8: SENSOR VOLTAGE VS. NORMALIZED SHOCK POSITION

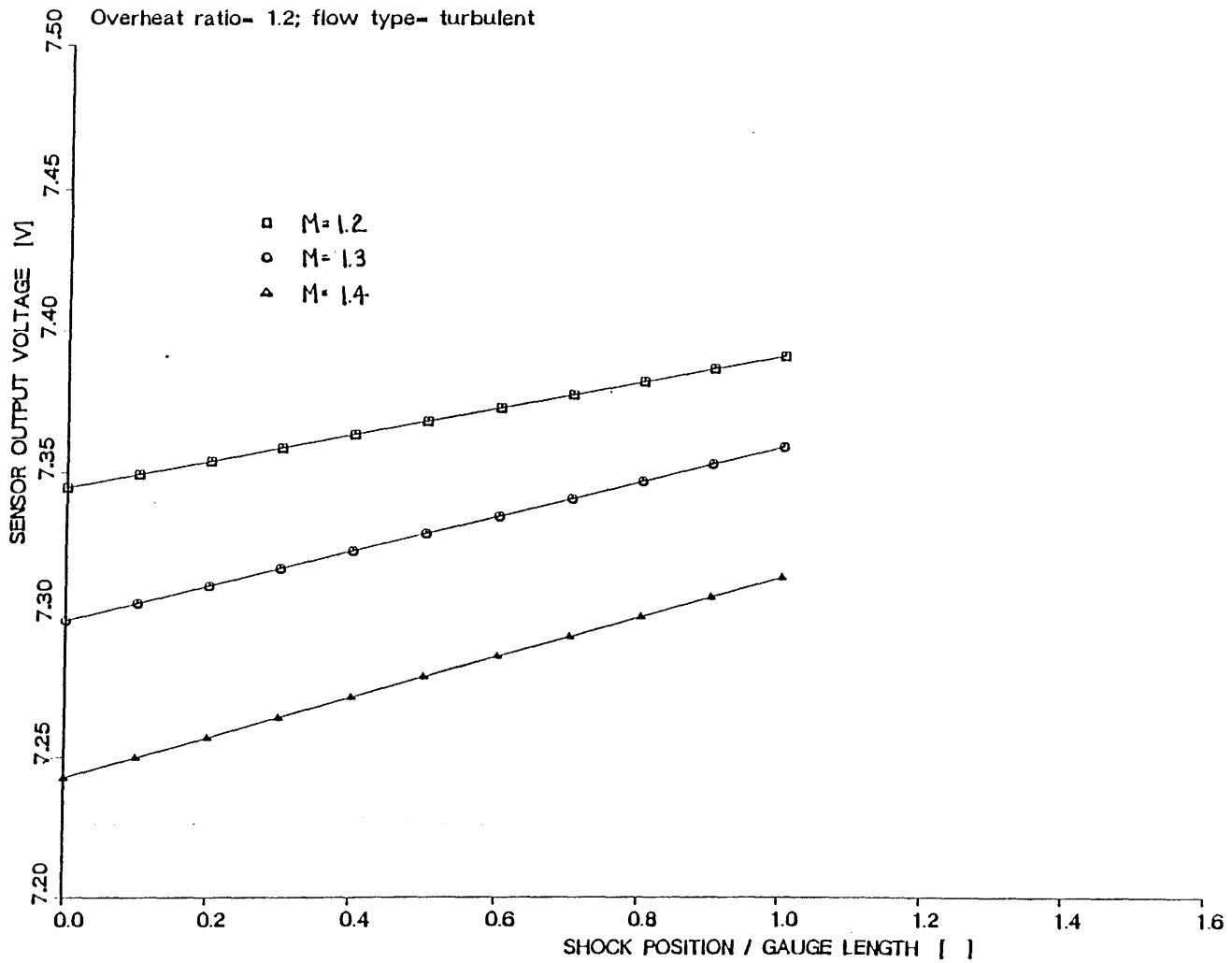

FIGURE 3.9: SENSOR VOLTAGE VS. NORMALIZED SHOCK POSITION

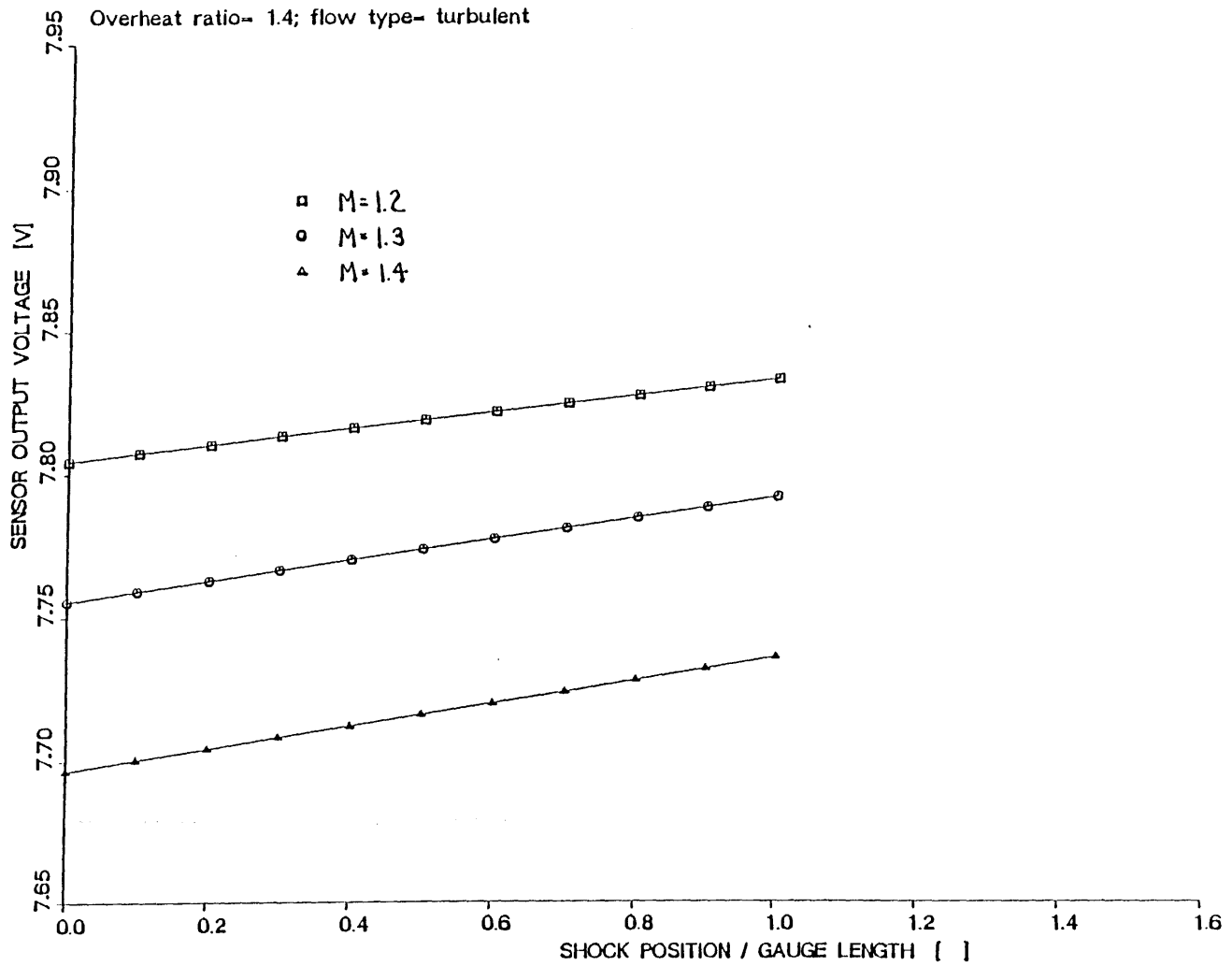

FIGURE 3.10: SENSOR VOLTAGE VS. NORMALIZED SHOCK POSITION

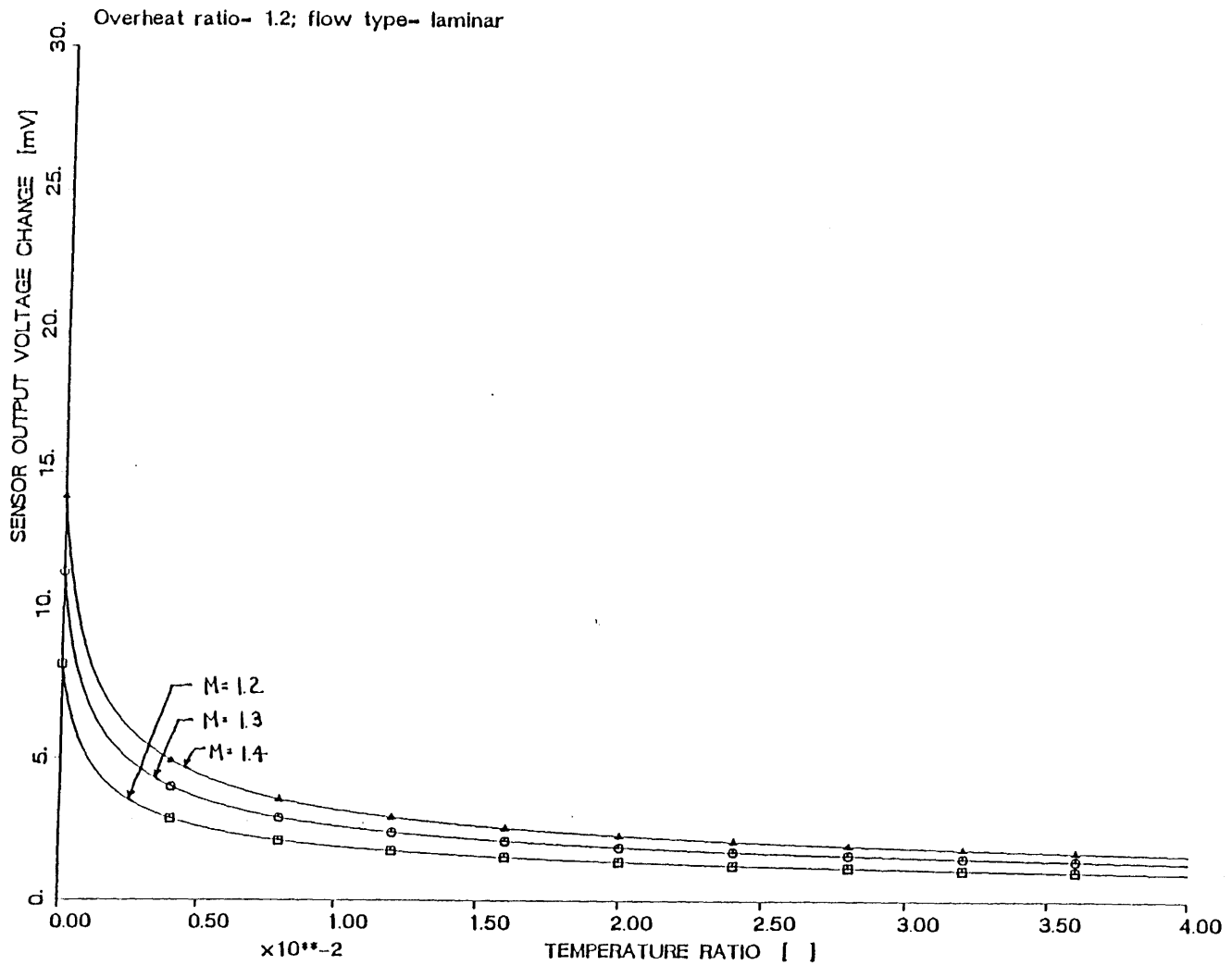

FIGURE 3.11: SENSOR VOLTAGE CHANGE VS. TEMPERATURE RATIO

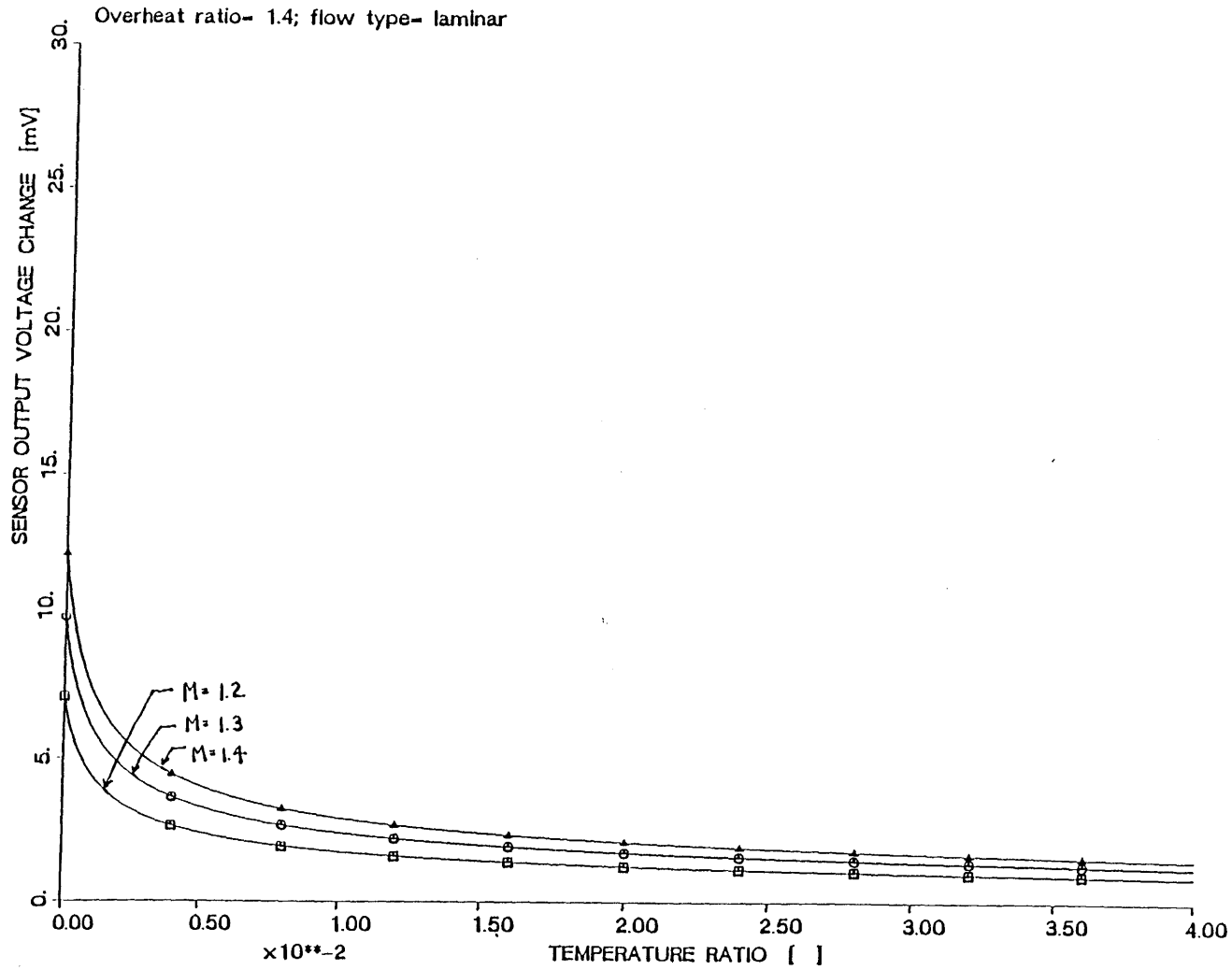

FIGURE 3.12: SENSOR VOLTAGE CHANGE VS. TEMPERATURE RATIO

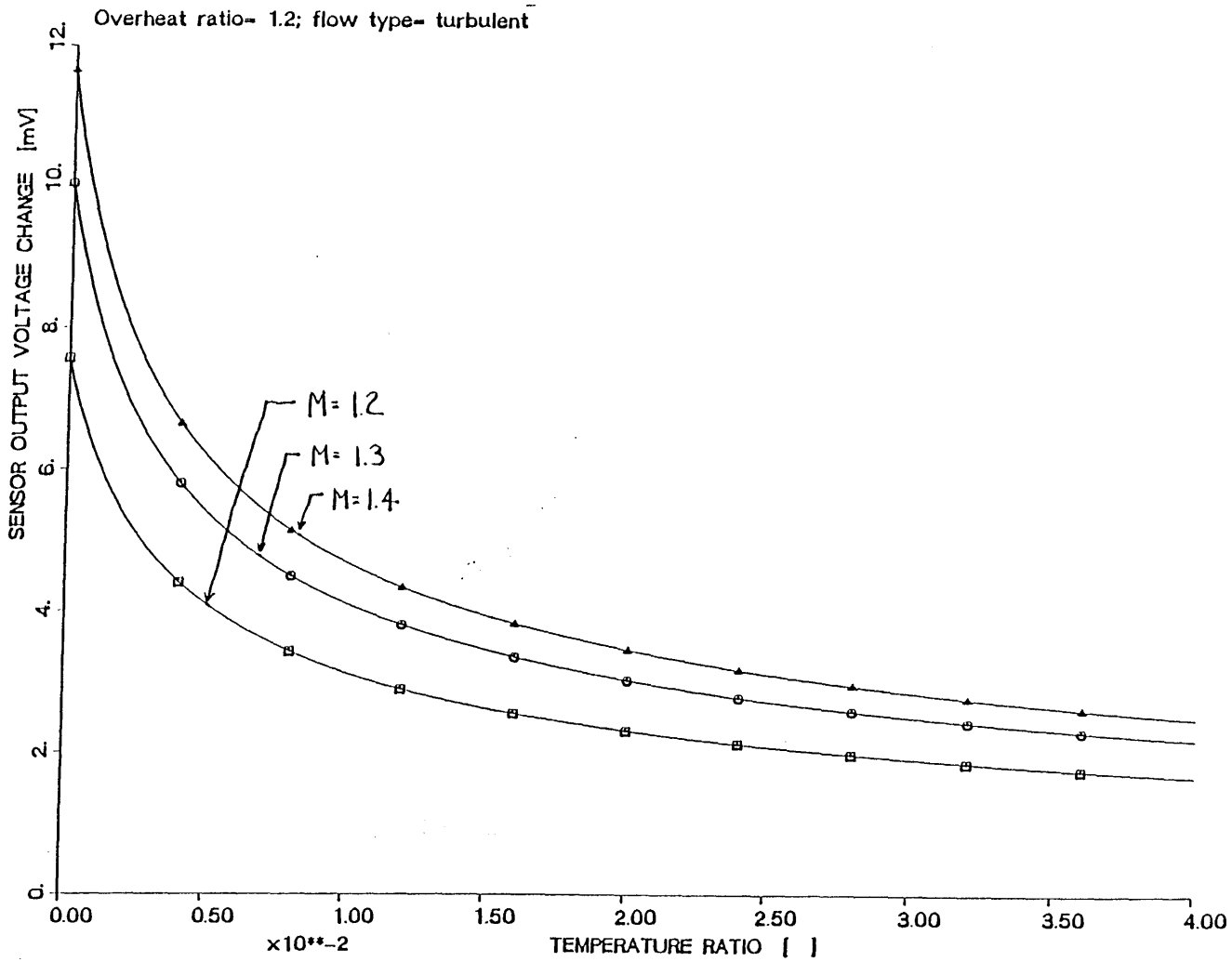

FIGURE 3.13: SENSOR VOLTAGE CHANGE VS. TEMPERATURE RATIO

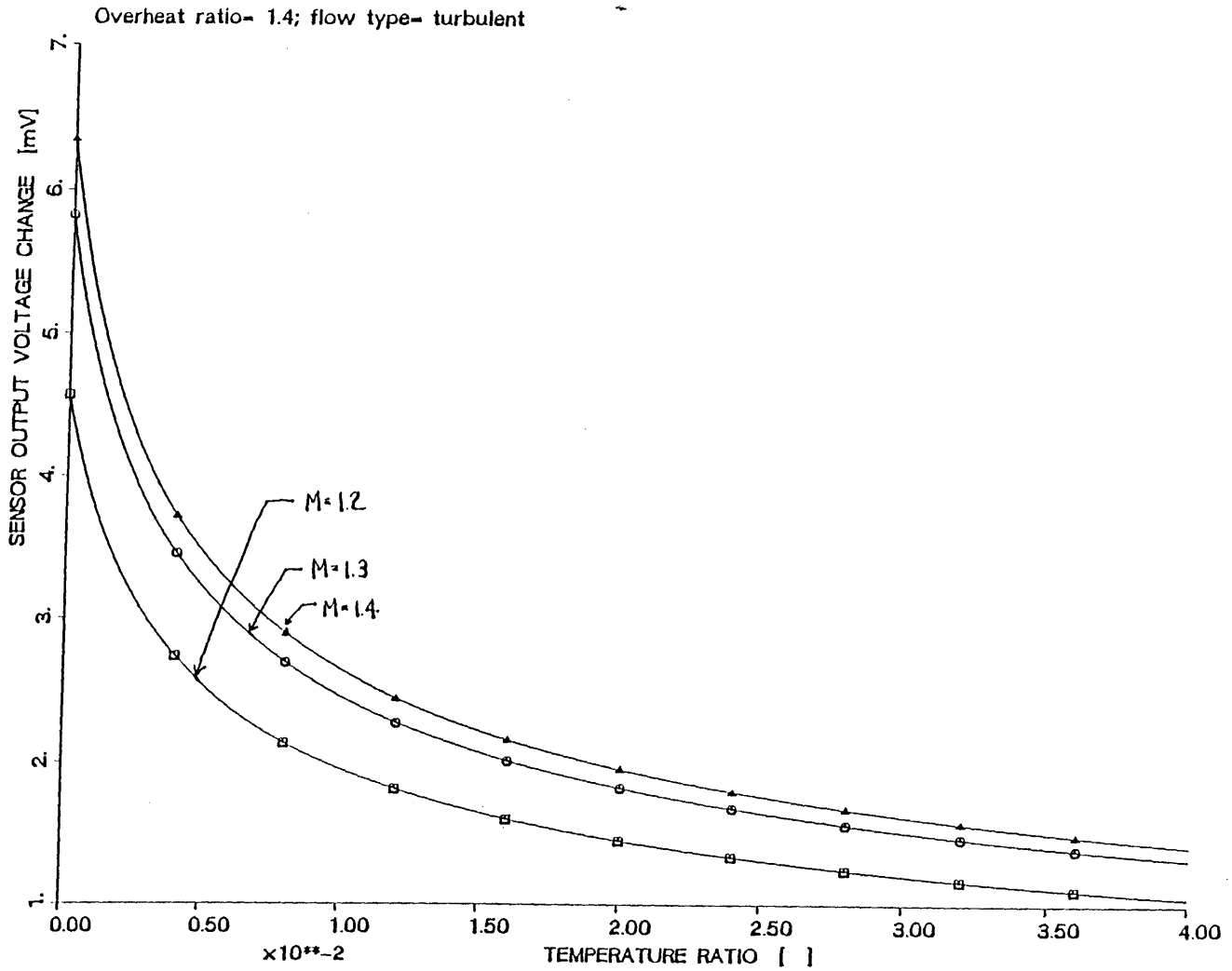

FIGURE 3.14: SENSOR VOLTAGE CHANGE VS. TEMPERATURE RATIO

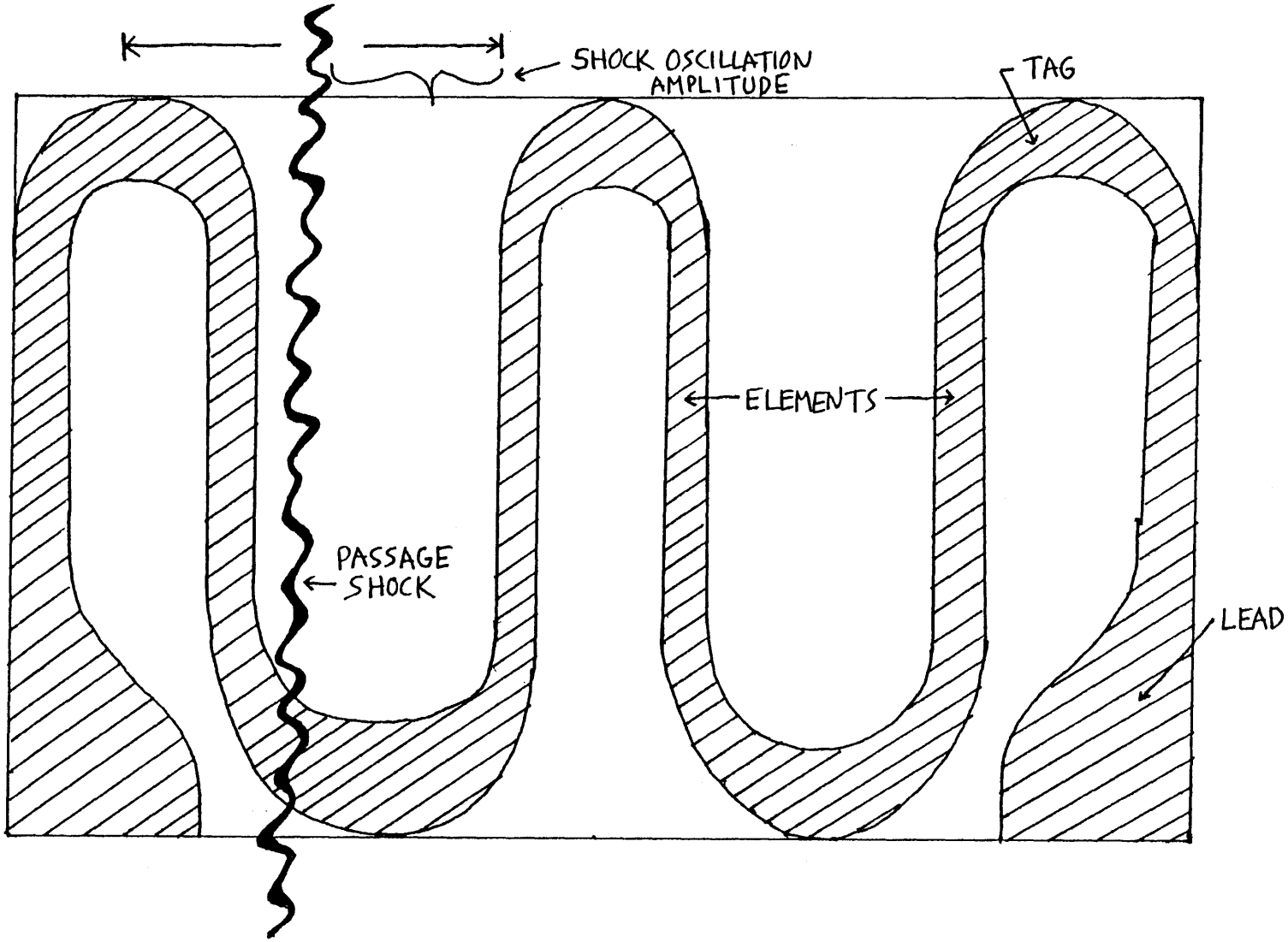

FIGURE 3.15: OSCILLATING SHOCK ON A MULTI-ELEMENT GAUGE

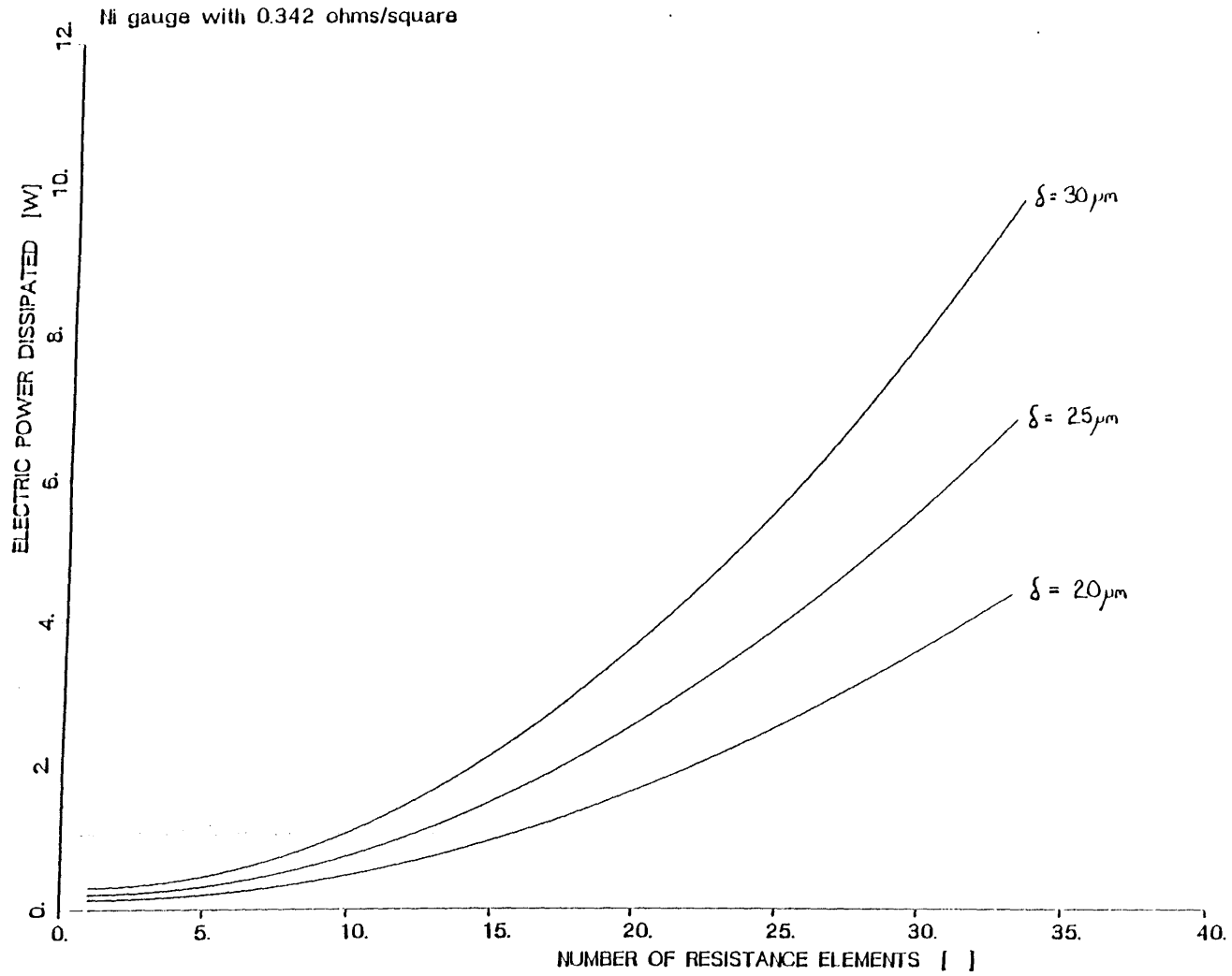

FIGURE 3.16: ELECTRIC POWER DISSIPATED VS. NUMBER OF ELEMENTS

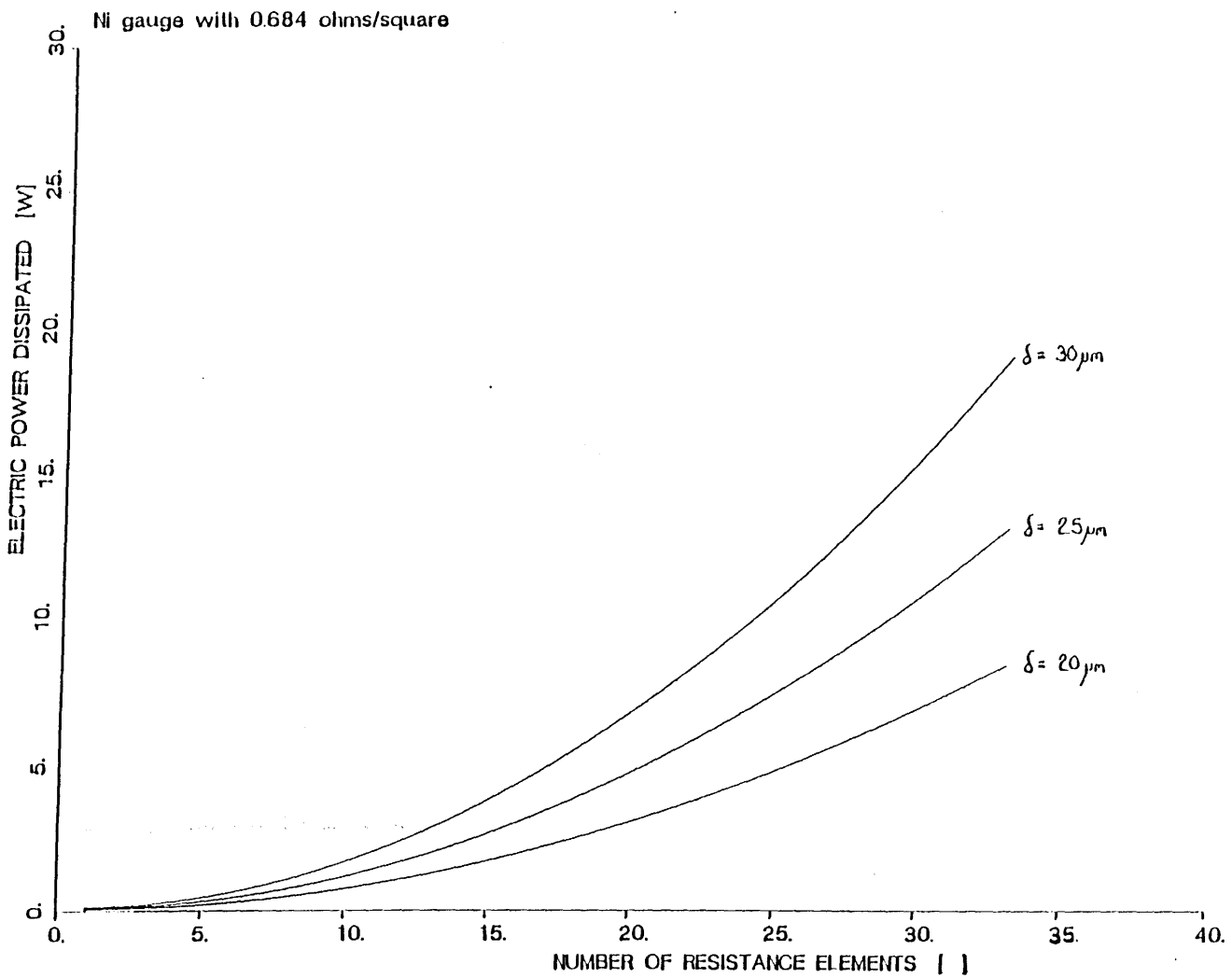

FIGURE 3.17: ELECTRIC POWER DISSIPATED VS. NUMBER OF ELEMENTS

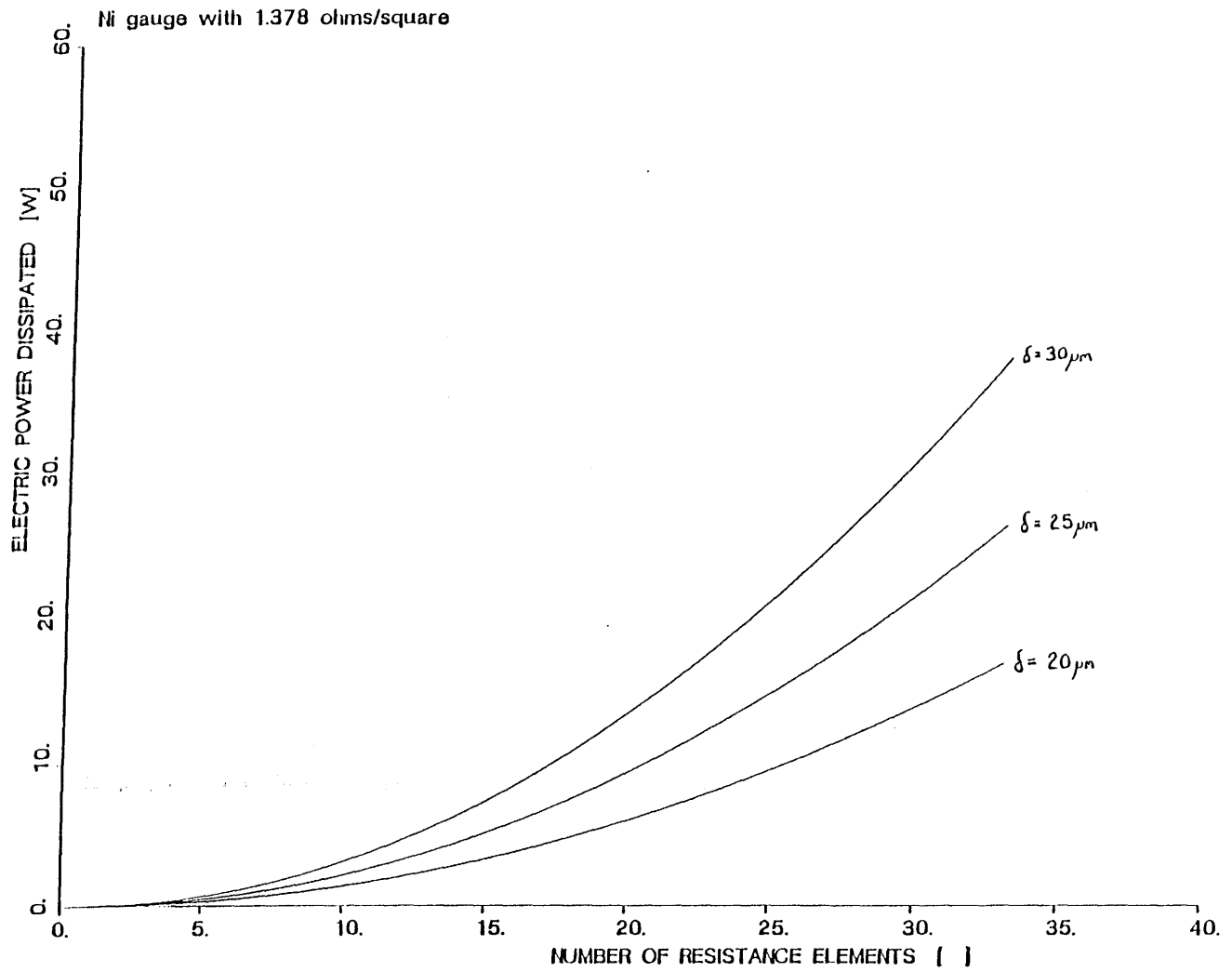

FIGURE 3.18: ELECTRIC POWER DISSIPATED VS. NUMBER OF ELEMENTS

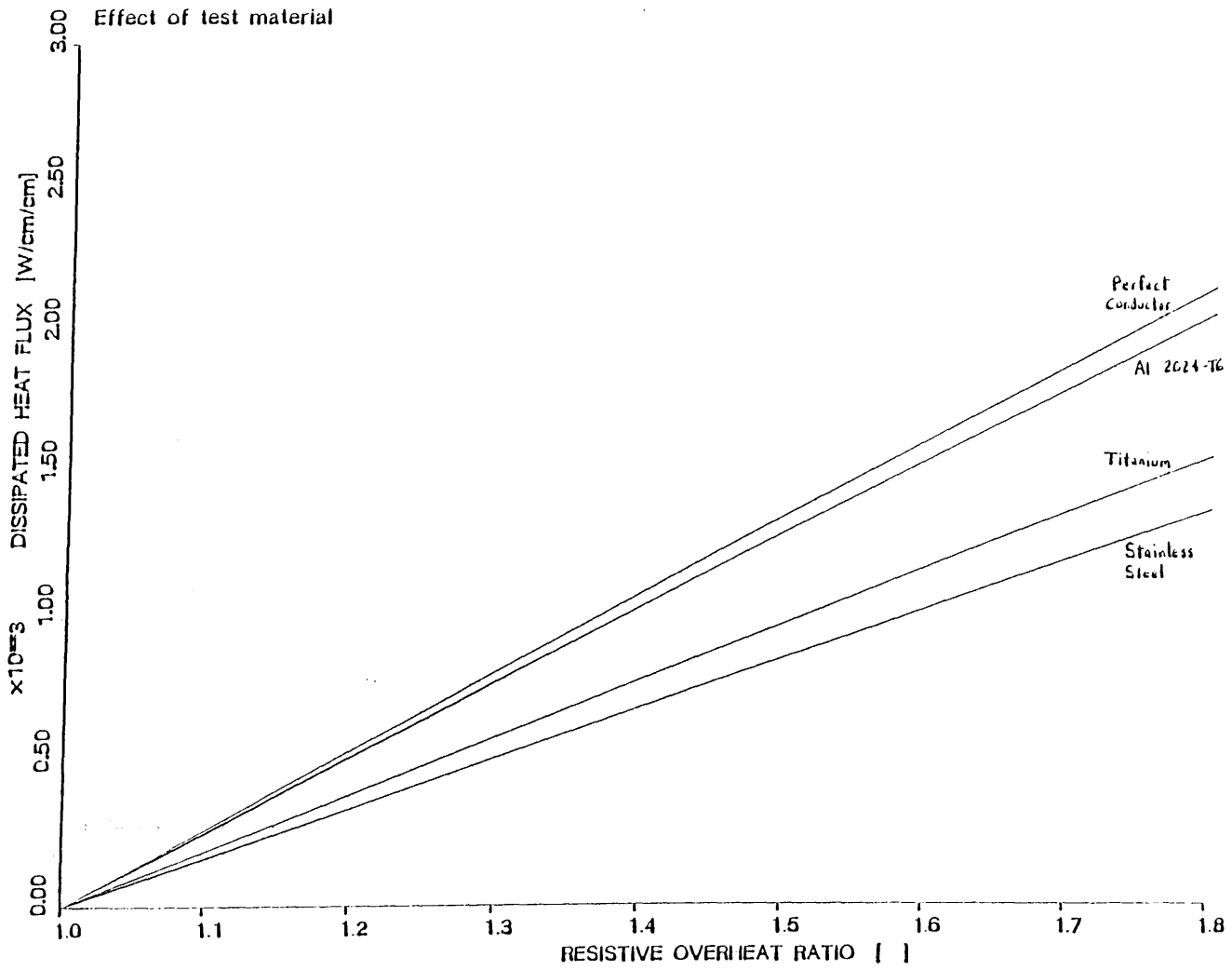

FIGURE 3.19: DISSIPATED HEAT FLUX VS. OVERHEAT RATIO

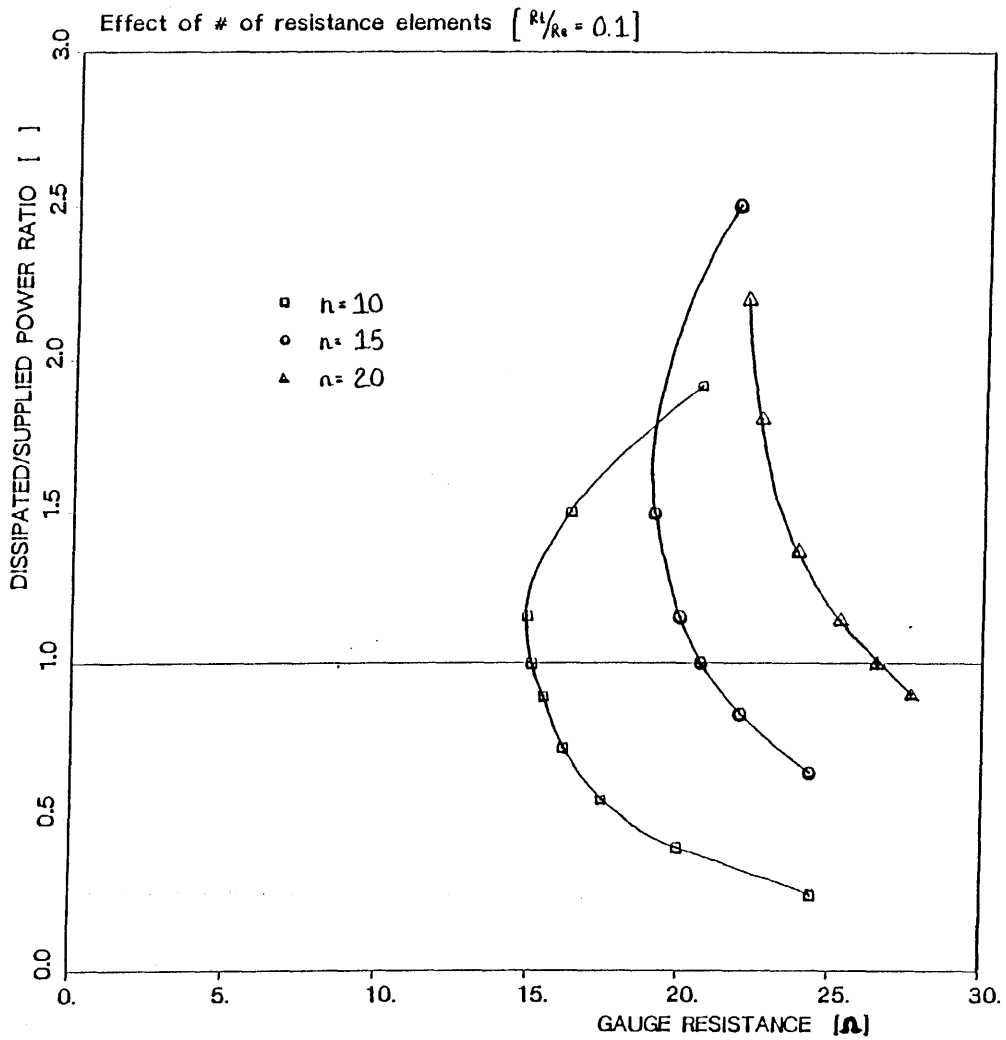

FIGURE 3.20: DISSIPATED/SUPPLIED POWER RATIO VS. GAUGE RESISTANCE

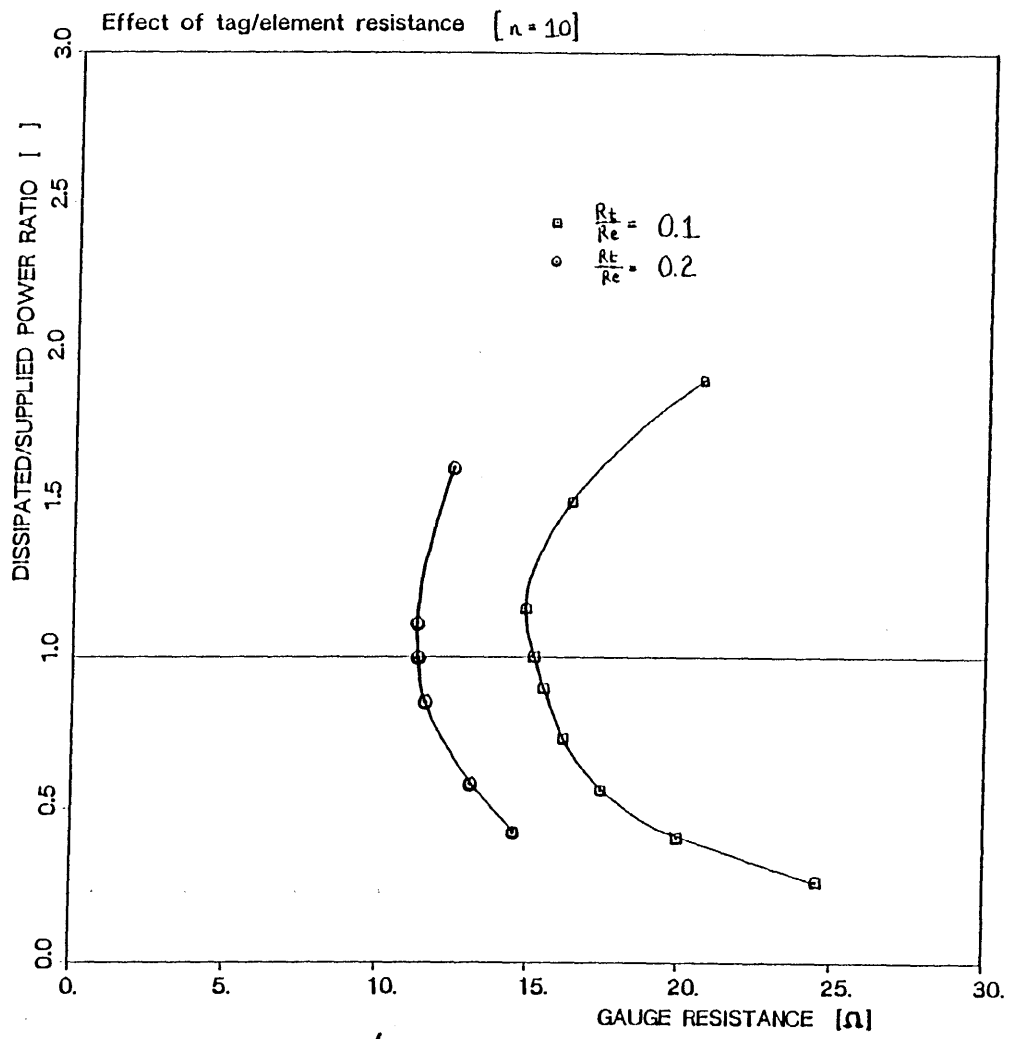

FIGURE 3.21: DISSIPATED/SUPPLIED POWER RATIO VS. GAUGE RESISTANCE

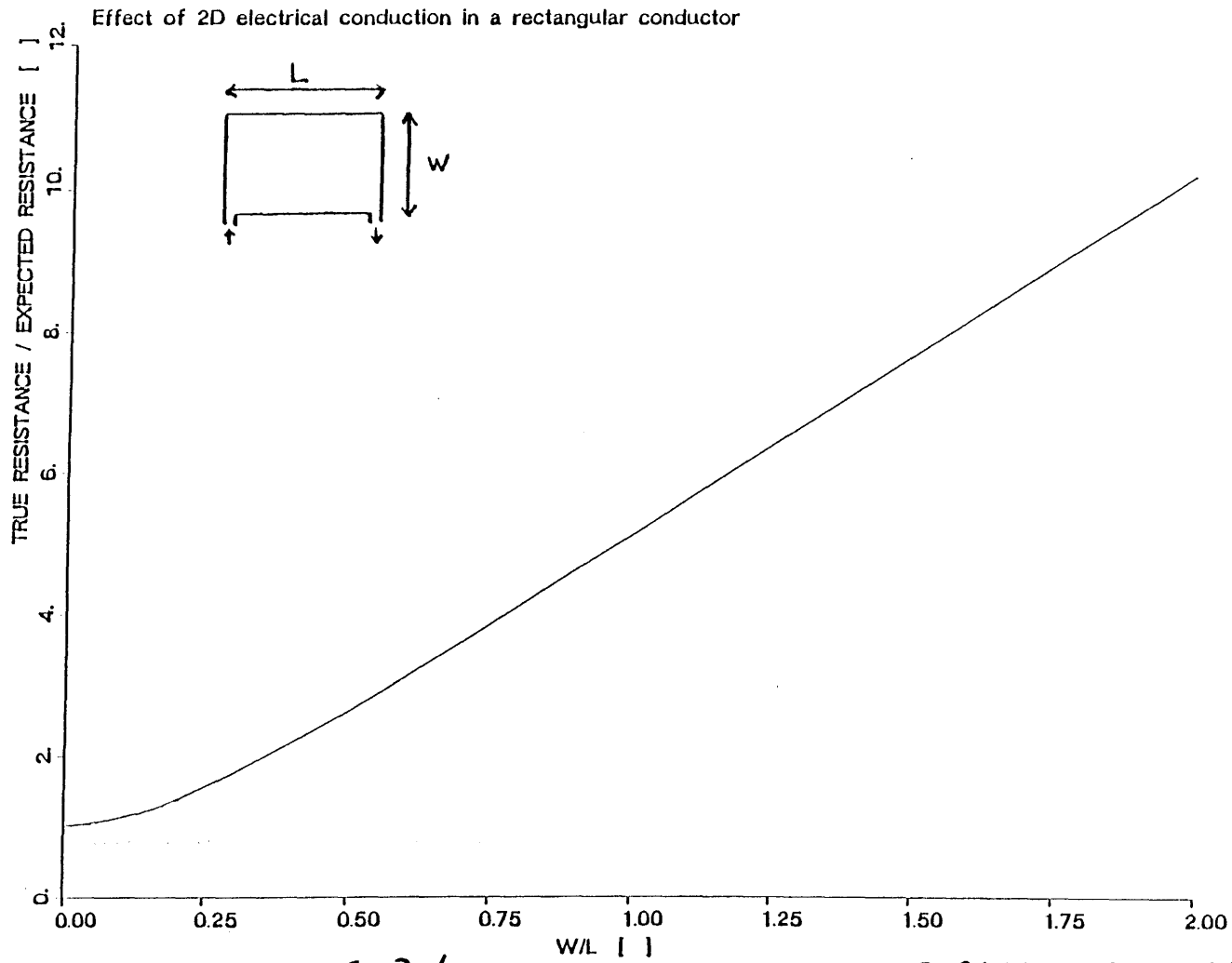

FIGURE 3.22: ACTUAL [2D] / EXPECTED [1D] RESISTANCE RATIO VS. W/L

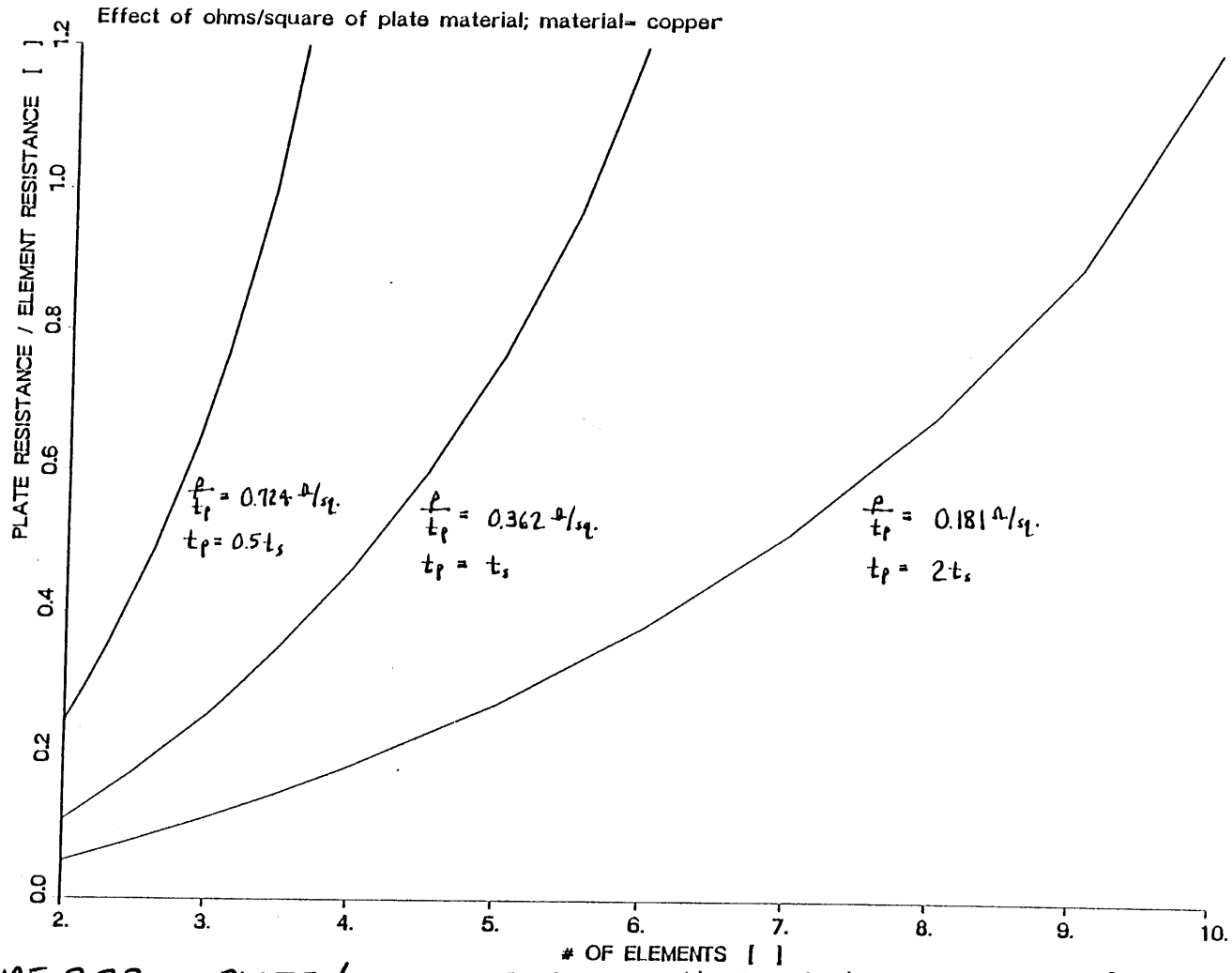

FIGURE 3.23: PLATE / ELEMENT RESISTANCE RATIO VS. NUMBER OF ELEMENTS

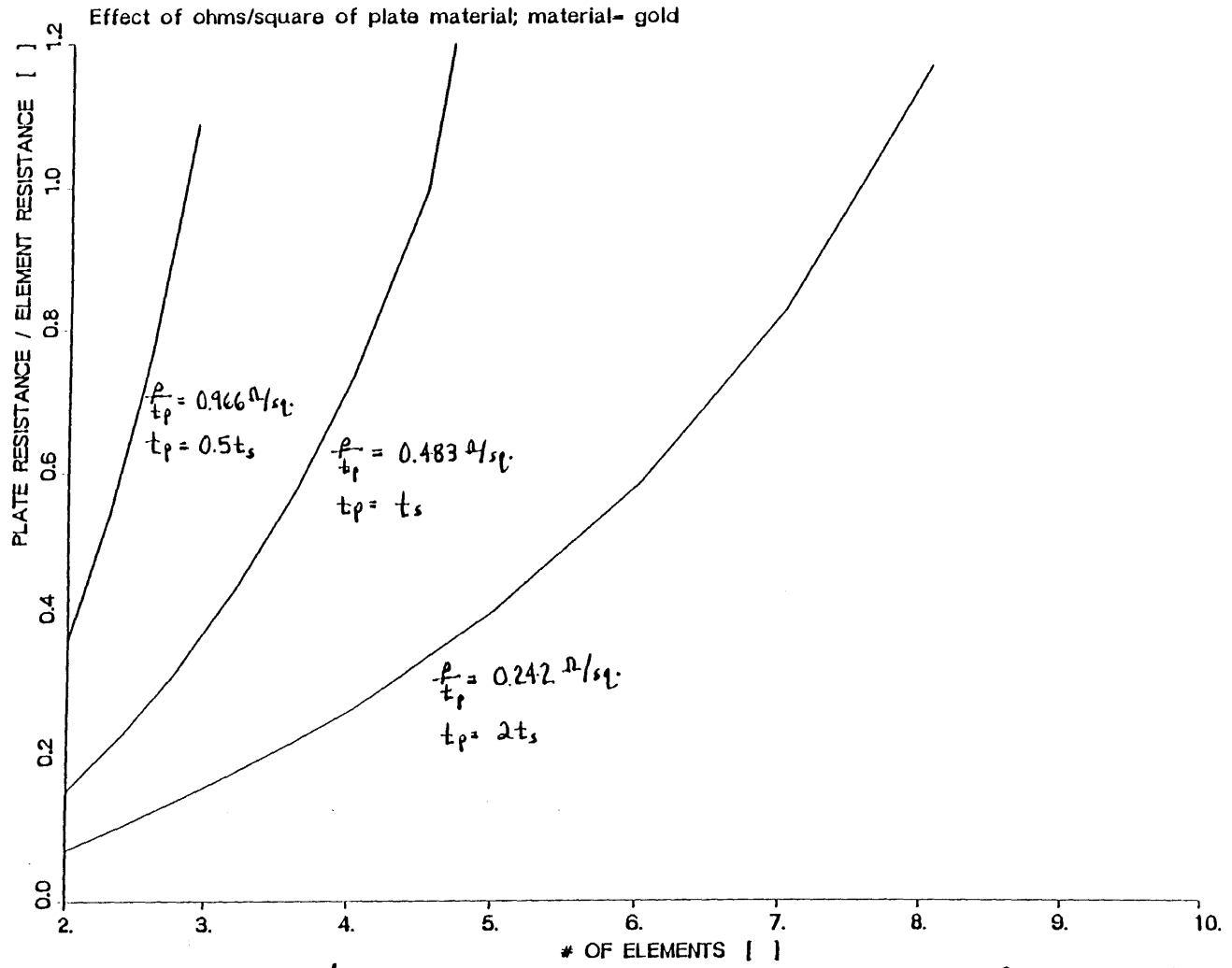

FIGURE 3.24: PLATE/ELEMENT RESISTANCE RATIO VS. NUMBER OF ELEMENTS

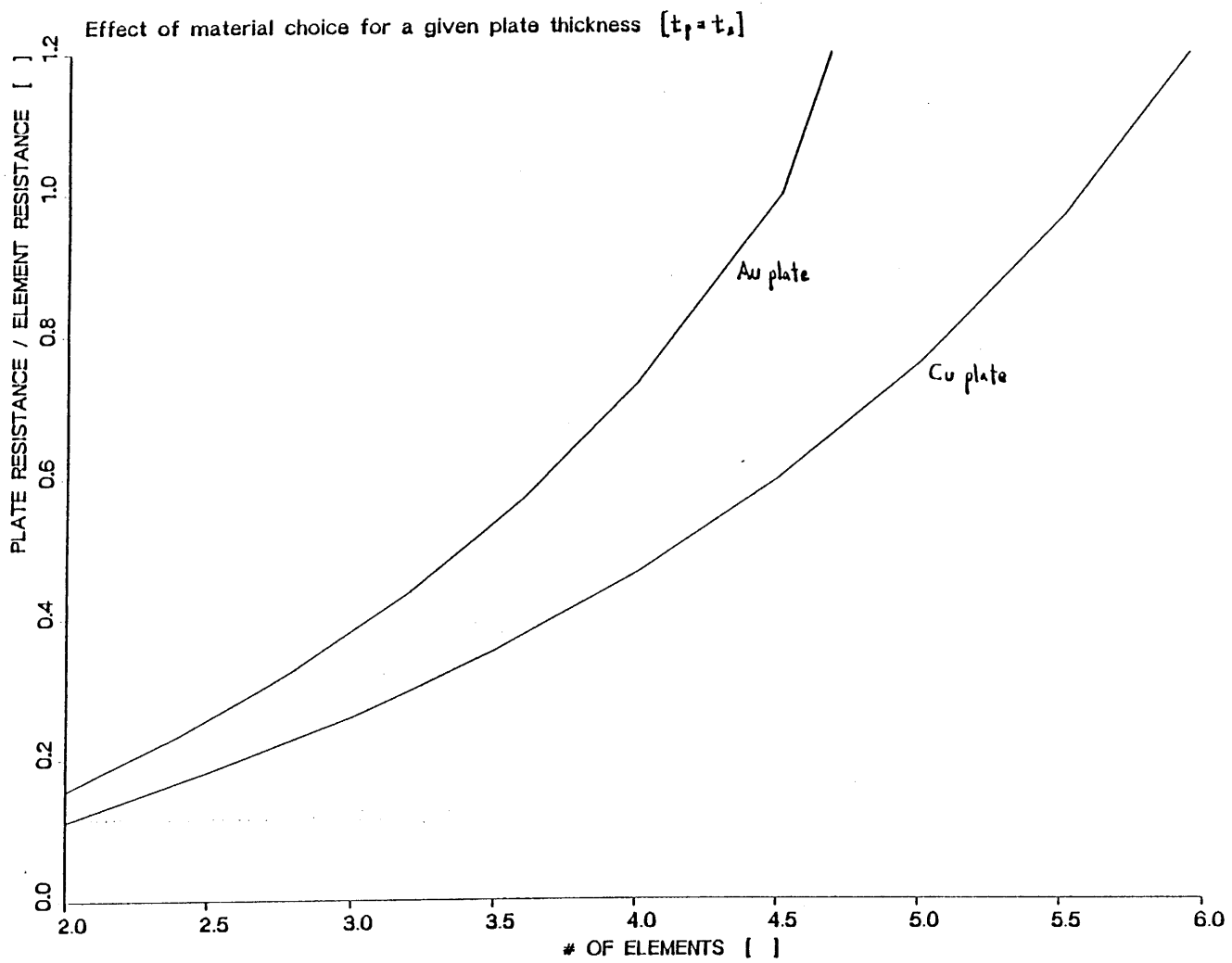

FIGURE 3.25: PLATE/ELEMENT RESISTANCE RATIO VS. NUMBER OF ELEMENTS

TABLE 3.1

GAUGE DESIGN: SYSTEM PARAMETERS

4 ELEMENT GAUGE		10 ELEMENT GAUGE	
Cu tag	Au tag	Cu tag	Au tag
δ = 20 μm	20	20	20
L = 126 μm	124	45.4	43.0
$\mathcal{E}$ = 1000 μm	1000	1000	1000
x = 654 μm	654	218	218
ℓ = 3080 μm	3080	9200	9200
w = 1434 μm	1432	481.4	479
t_{Ni} = 1500 Å	1500	1500	1500
t_p = 6000 Å	6000	6000	6000
$\frac{\rho_e}{\rho_{Ni}}$ = 0.246	0.327	0.246	0.327
$R_{T_{cold}}$ = 15.0 Ω	15.0	15.0	15.0
$R_{e_{cold}}$ = 14.41 Ω	14.22	12.95	12.29
$R_{t_{cold}}$ = 0.59 Ω	0.78	2.05	2.71
$\frac{R_t}{R_T}$ = 4.09 %	5.51 %	15.8 %	22.1 %

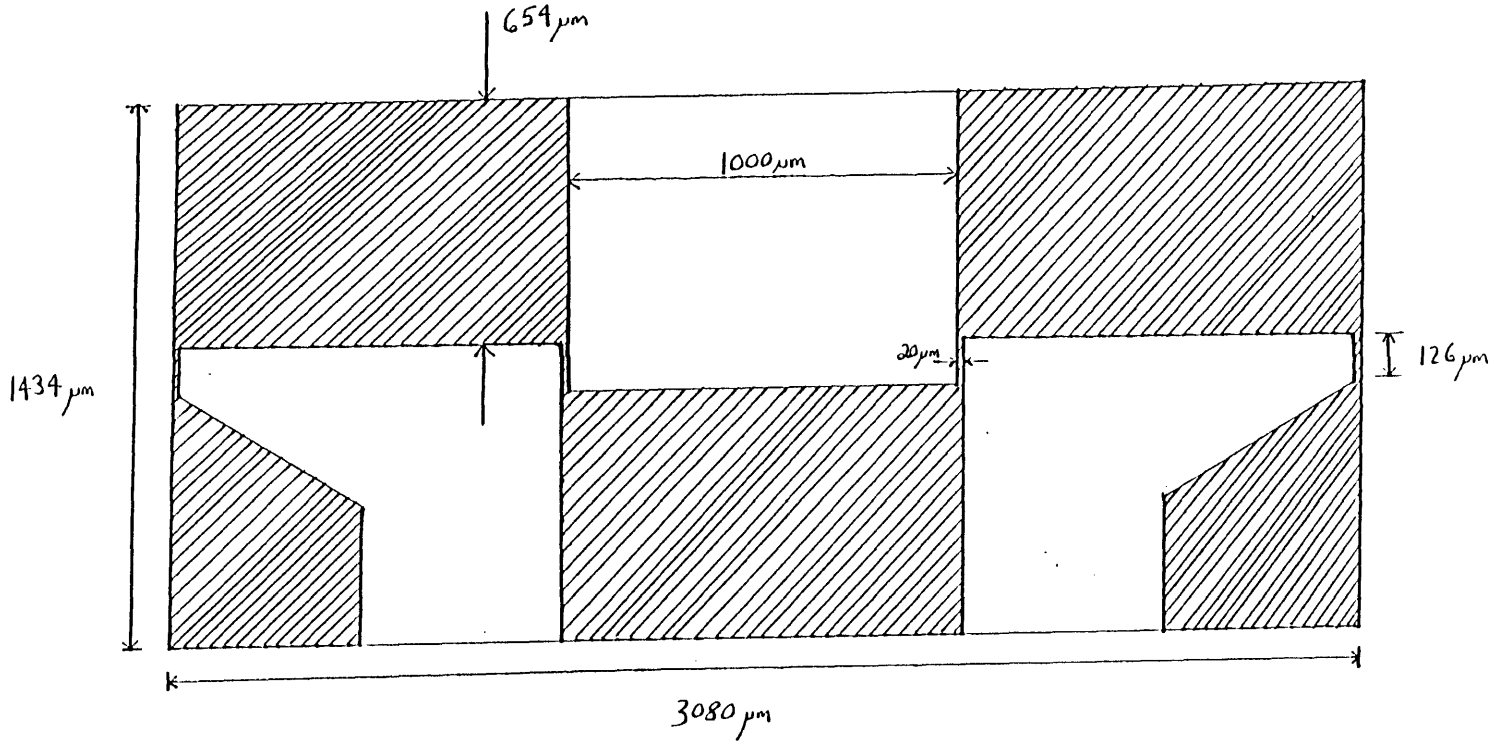

SCALE = 63.5 : 1

FIGURE 3.26 : FOUR-ELEMENT GAUGE DESIGN

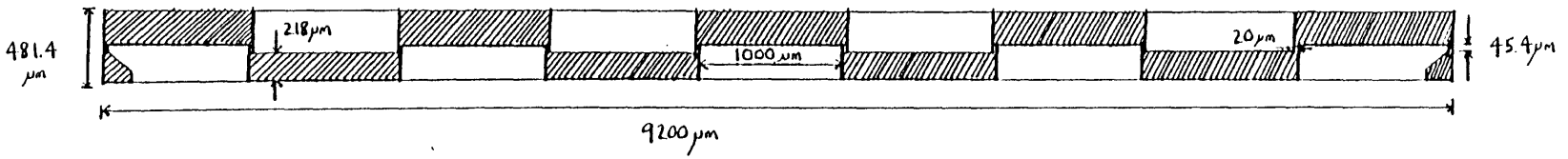

SCALE = 25.4 : 1

FIGURE 3.27: TEN-ELEMENT GAUGE DESIGN

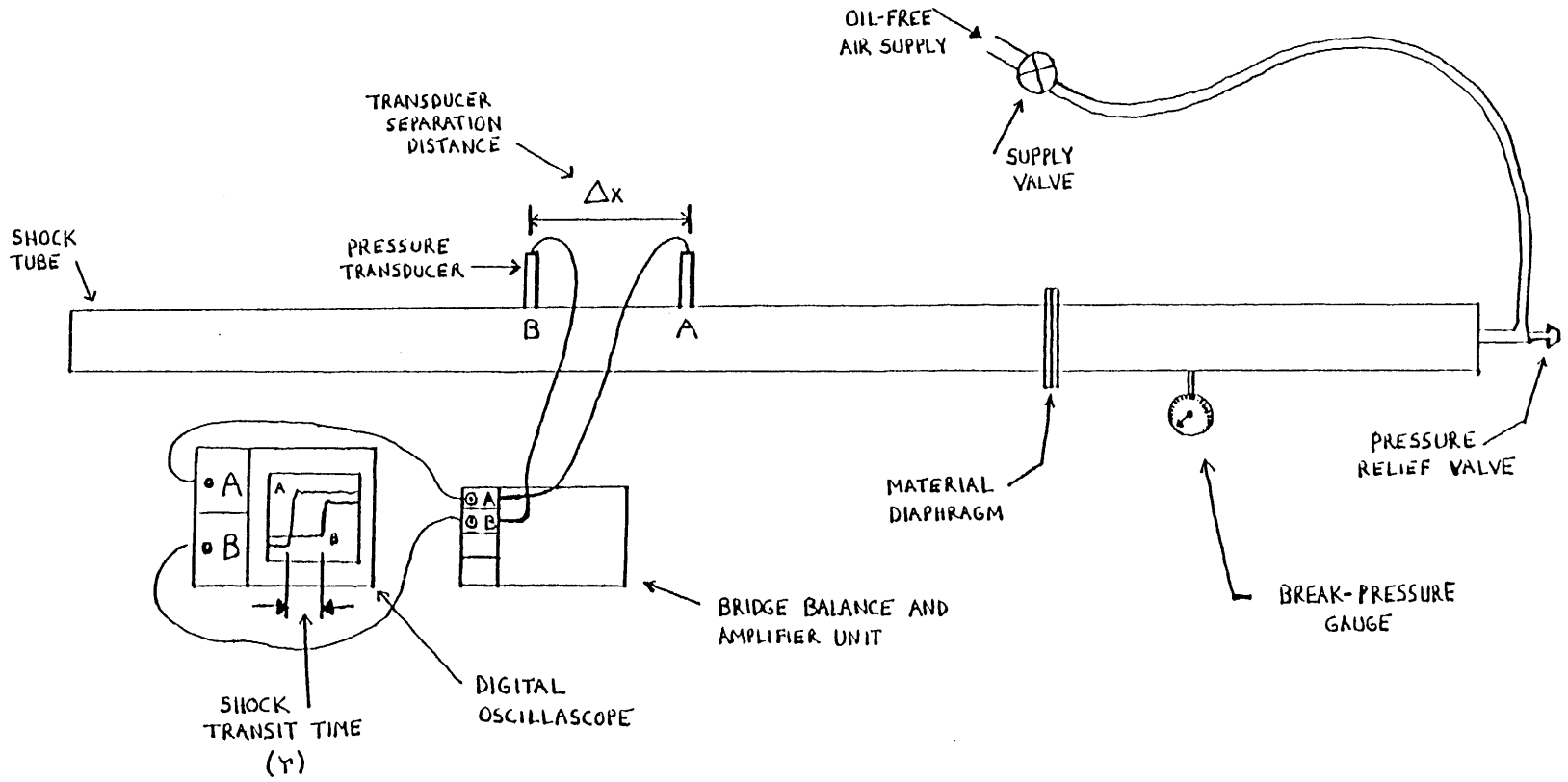

FIGURE 4.1: SHOCK TUBE EXPERIMENTAL APPARATUS

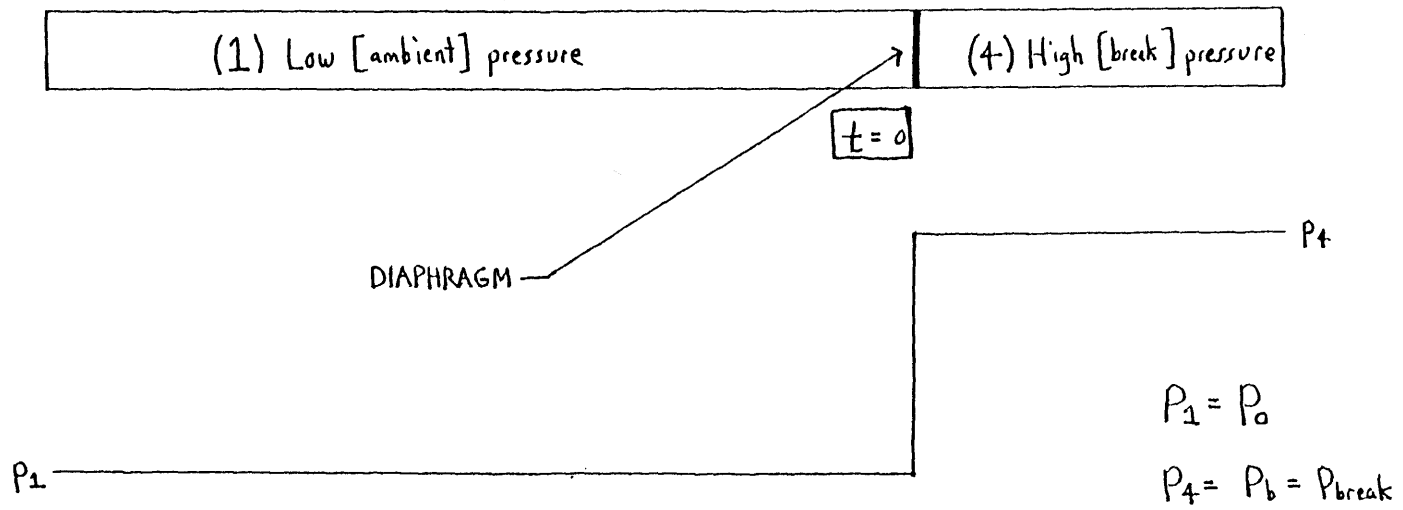

FIGURE 4.2: SHOCK TUBE CONFIGURATION: BEFORE BURST

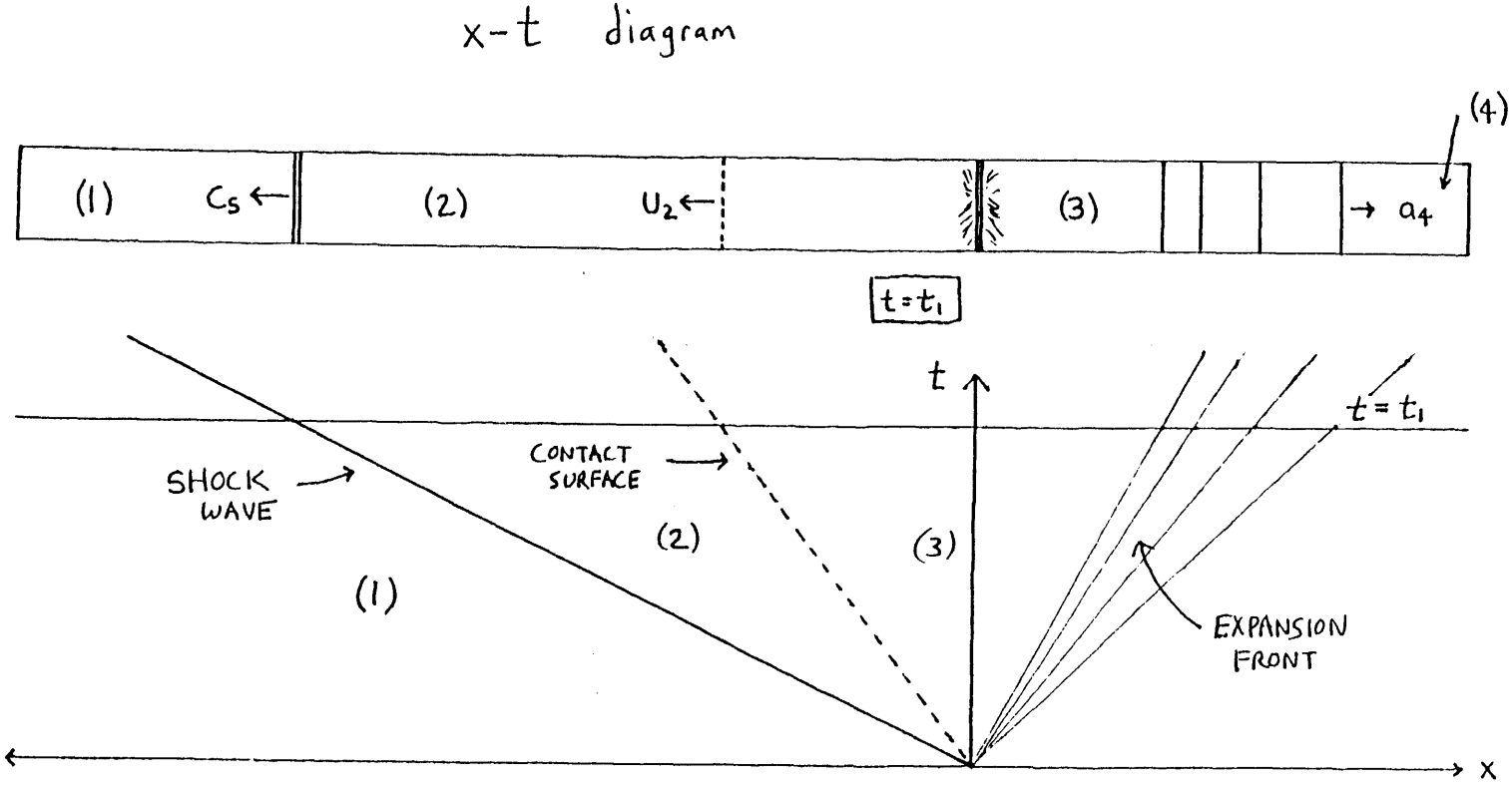

FIGURE 4.3: SHOCK TUBE CONFIGURATION: AFTER BURST

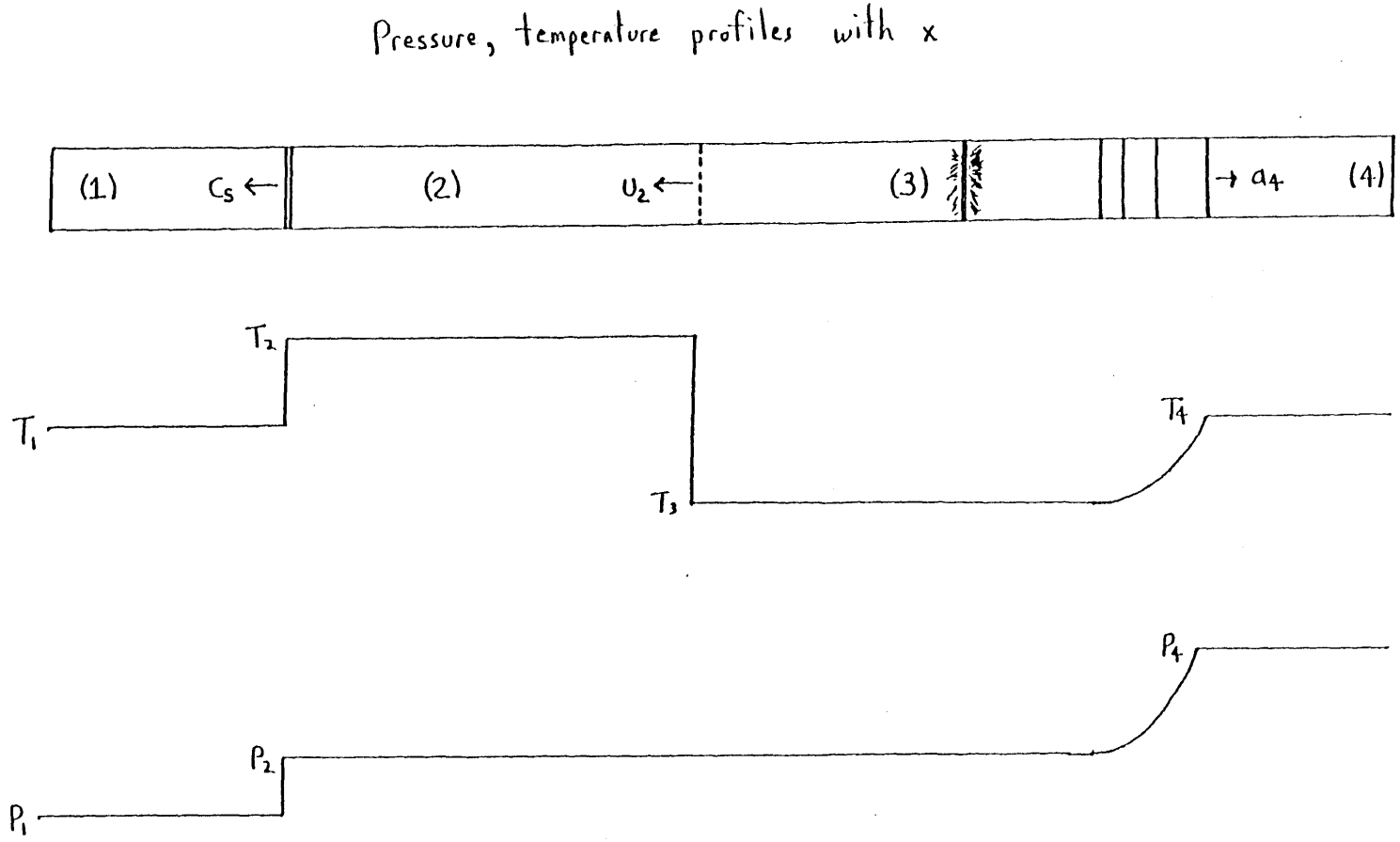

FIGURE 4.4: SHOCK TUBE CONFIGURATION: AFTER BURST

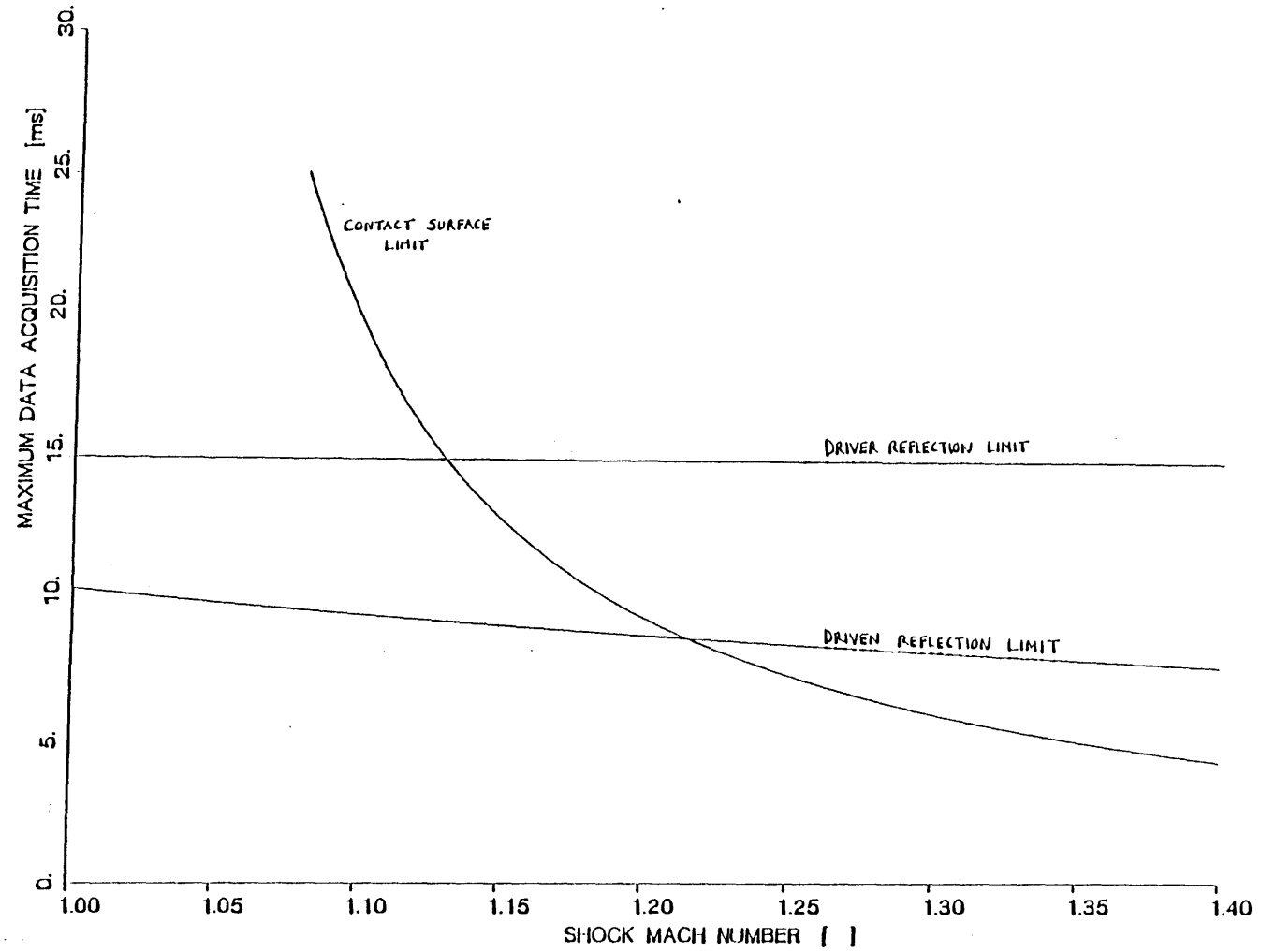

FIGURE 4.5: MAXIMUM DATA ACQUISITION TIME VS. MACH NUMBER

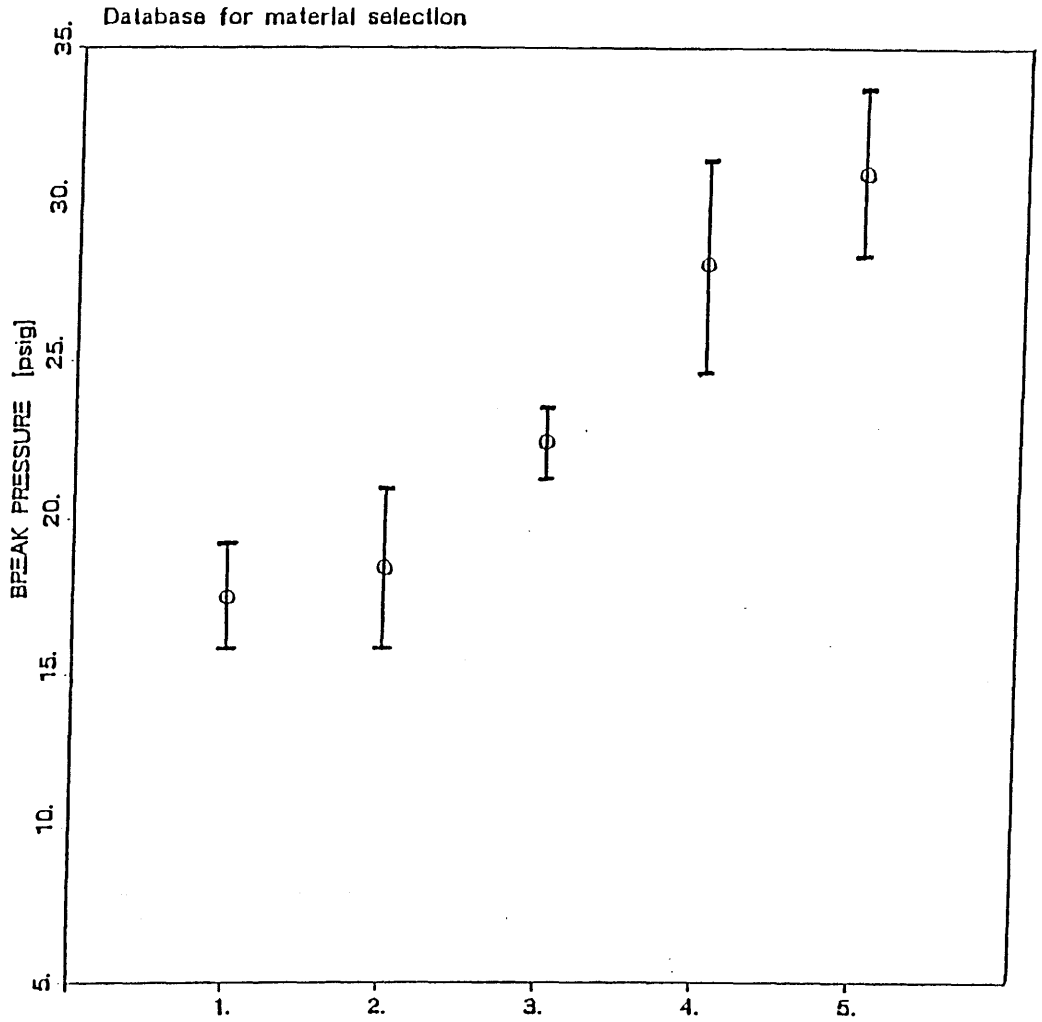

REPRESENTS AVERAGE
± 1 STANDARD DEVIATION

POSITION #	MATERIAL
1	"K" HB-20 CELLOPHANE
2	MST CELLOPHANE
3	HEAVY-DUTY (1.5 mil) ALUMINUM FOIL
4	123 "V" 58P CELLOPHANE
5	118 "V" 58F CELLOPHANE

FIGURE 4.6: MEAN AND DEVIATION BREAK PRESSURES FOR DIAPHRAGM MATERIALS

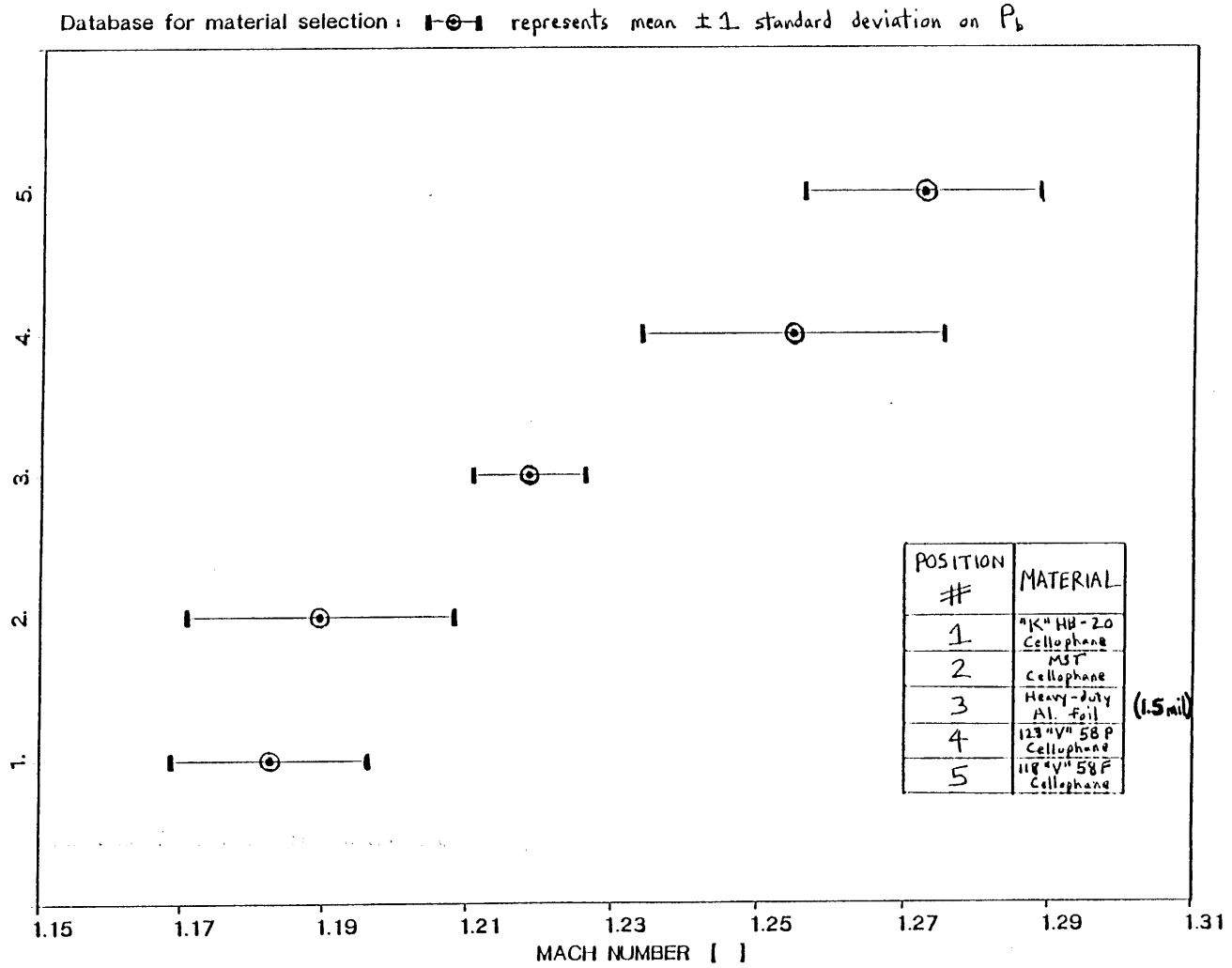

FIGURE 4.7: MEAN AND DEVIATION MACH NUMBERS FOR DIAPHRAGM MATERIALS

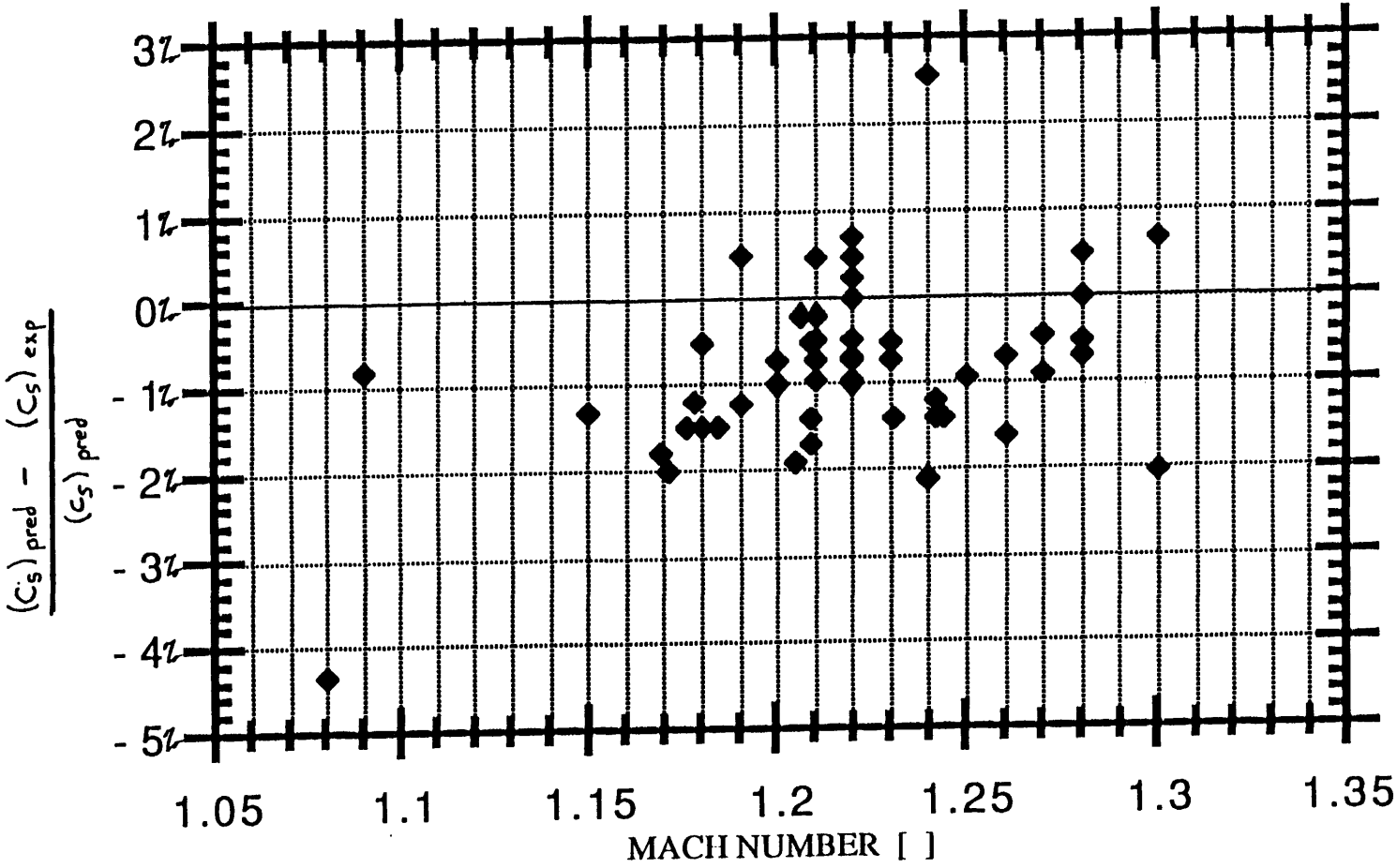

FIGURE 4.8: SHOCK SPEED PERCENTAGE ERROR VS. MACH NUMBER

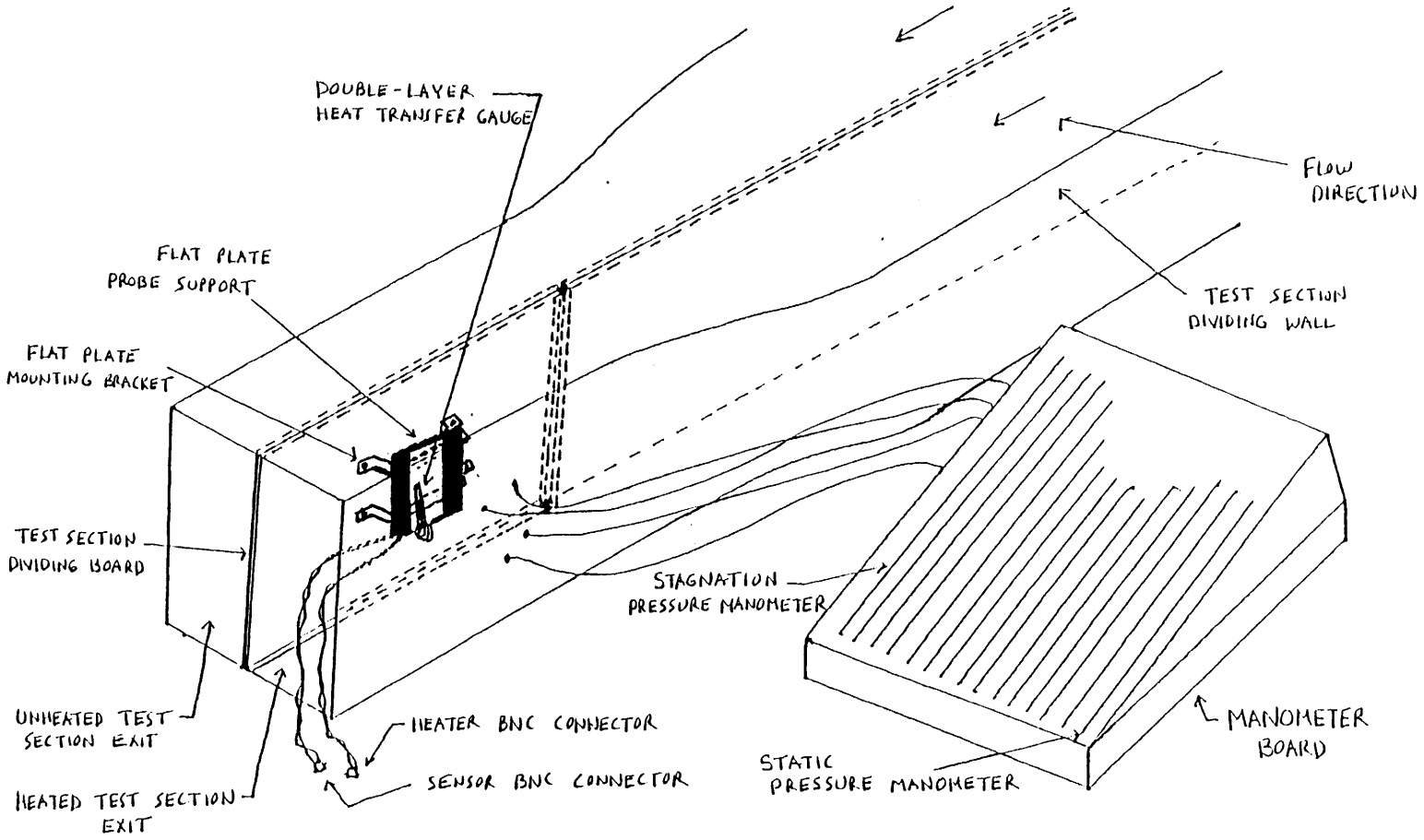

FIGURE 4.9: SUBSONIC WIND TUNNEL EXPERIMENTAL APPARATUS

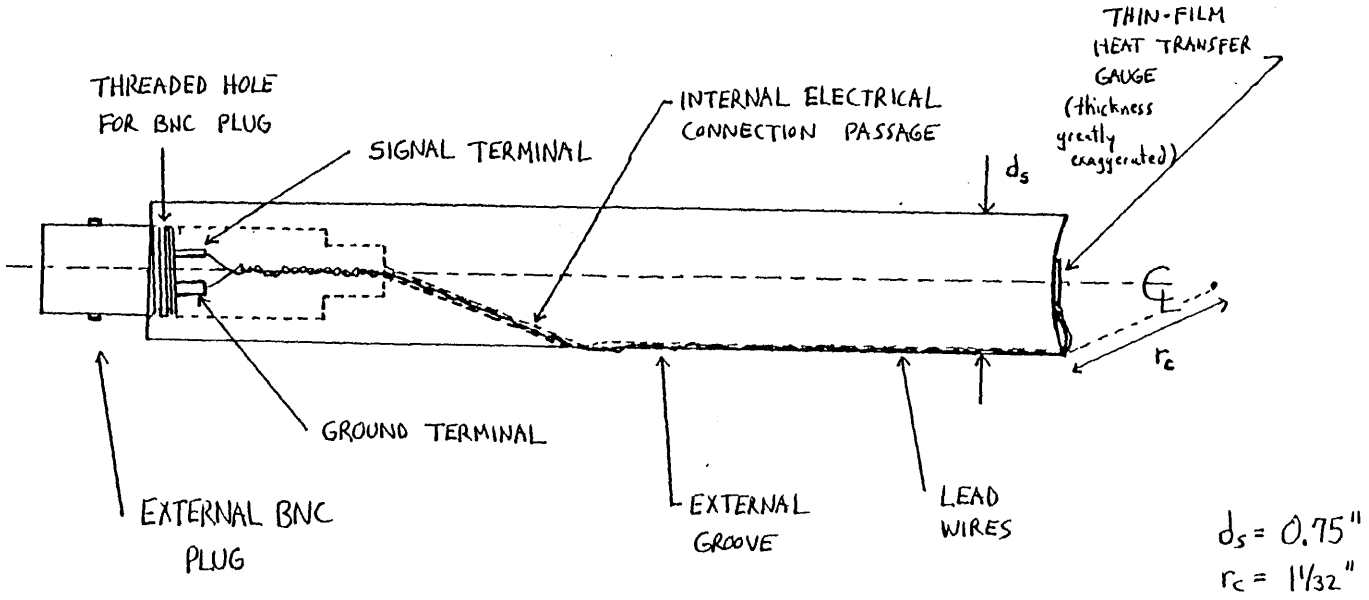

FIGURE 4.10: SINGLE-LAYER SENSOR SHOCK TUBE PROBE SUPPORT

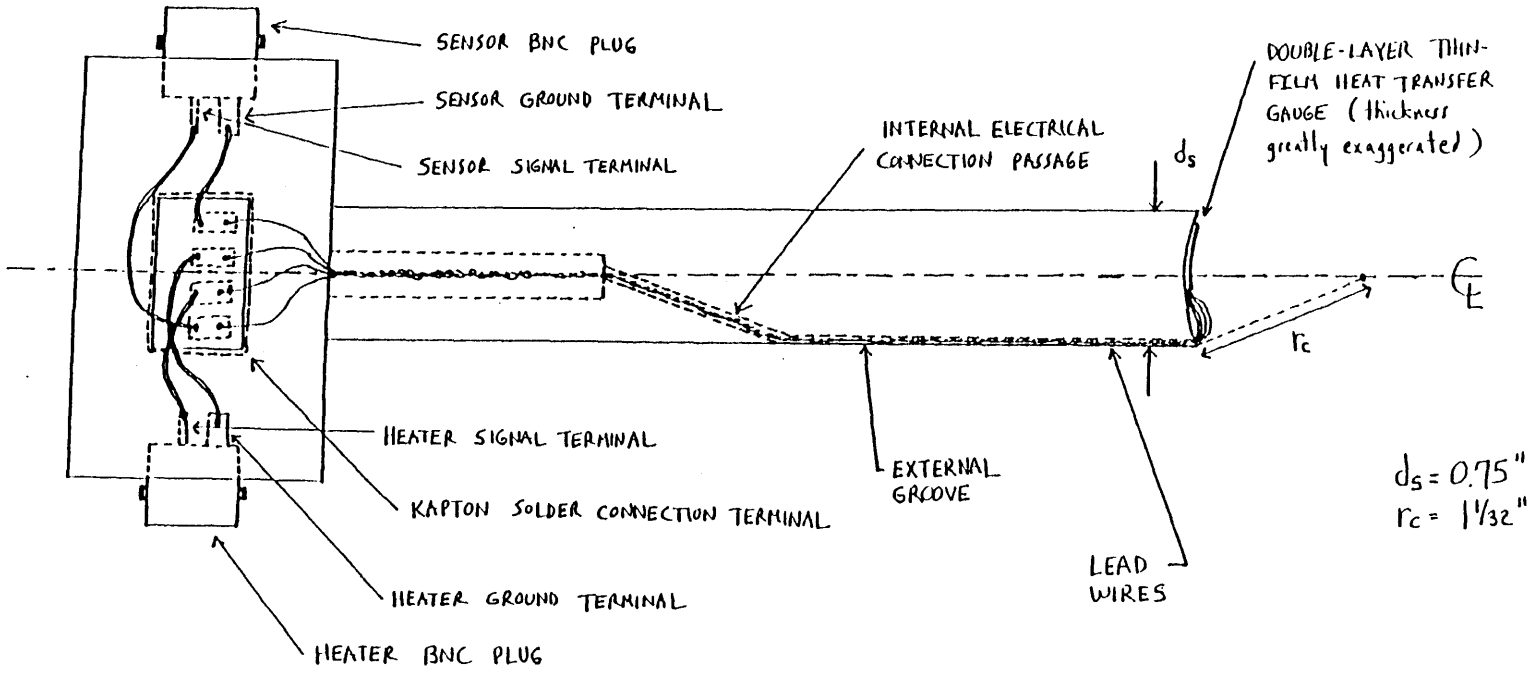

FIGURE 4.11: DOUBLE-LAYER SENSOR SHOCK TUBE PROBE SUPPORT

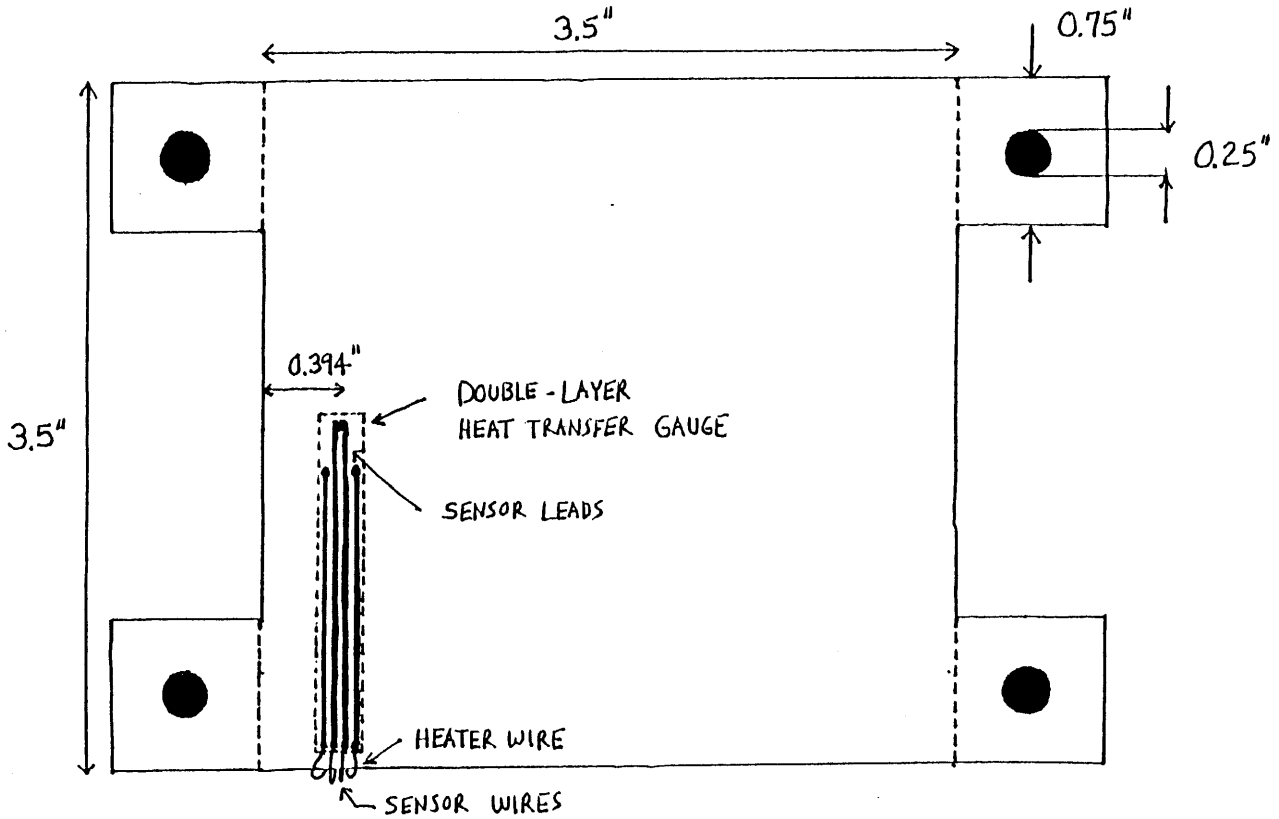

FIGURE 4.12: SUBSONIC WIND TUNNEL FLAT PLATE PROBE SUPPORT

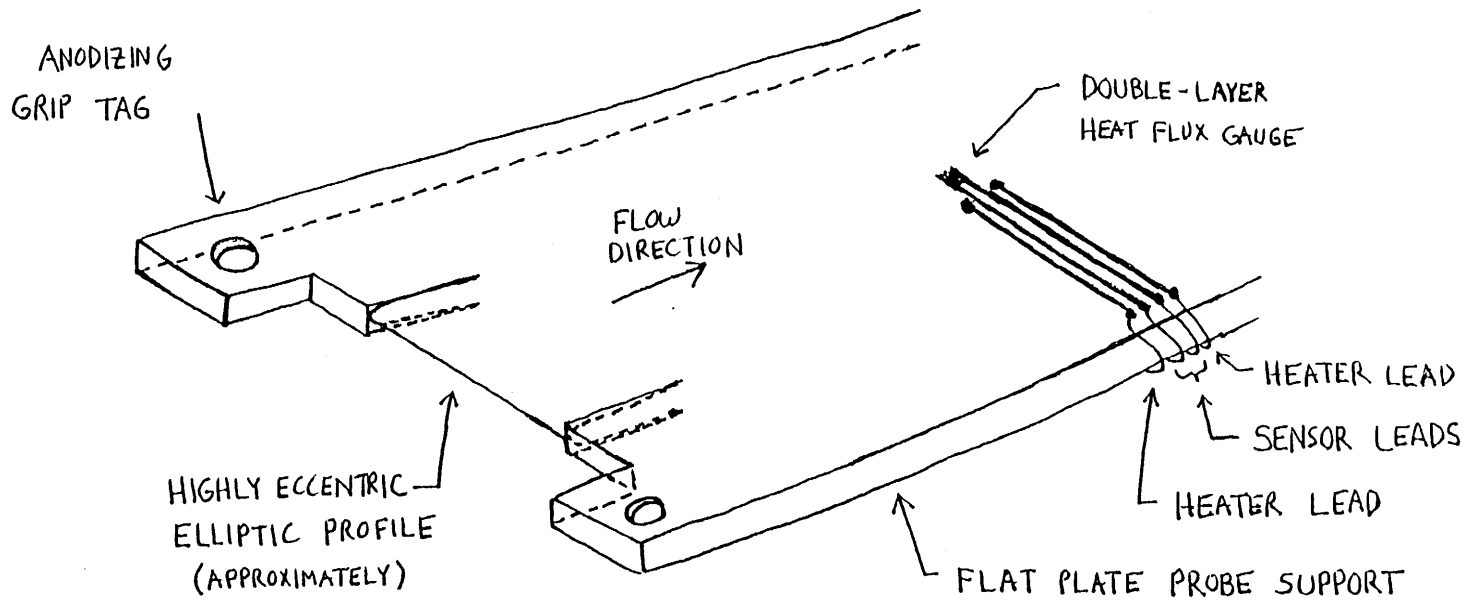

FIGURE 4.13: FLAT PLATE LEADING EDGE PROFILE GEOMETRY

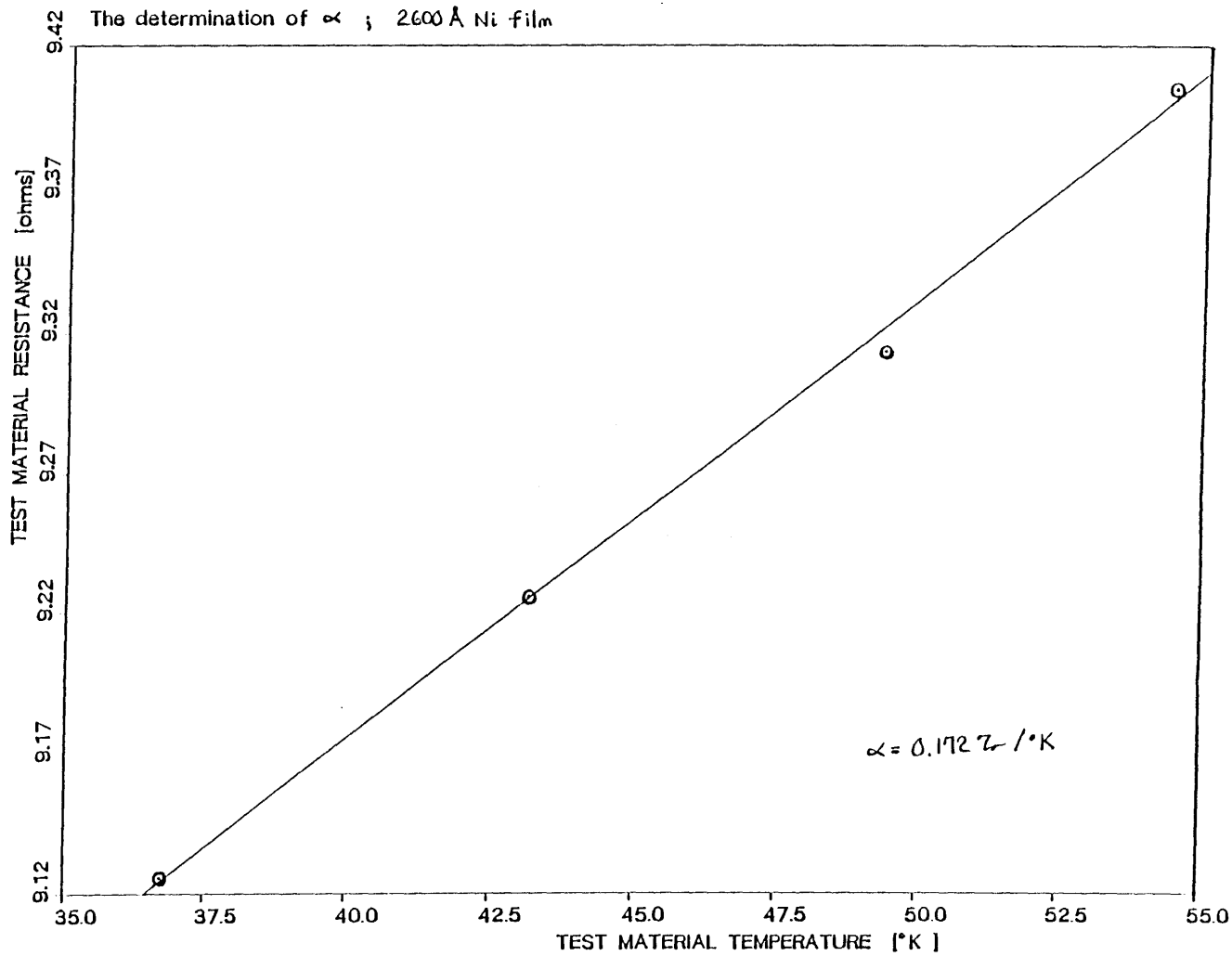

FIGURE 4.14: TEST MATERIAL RESISTANCE VS. TEST MATERIAL TEMPERATURE

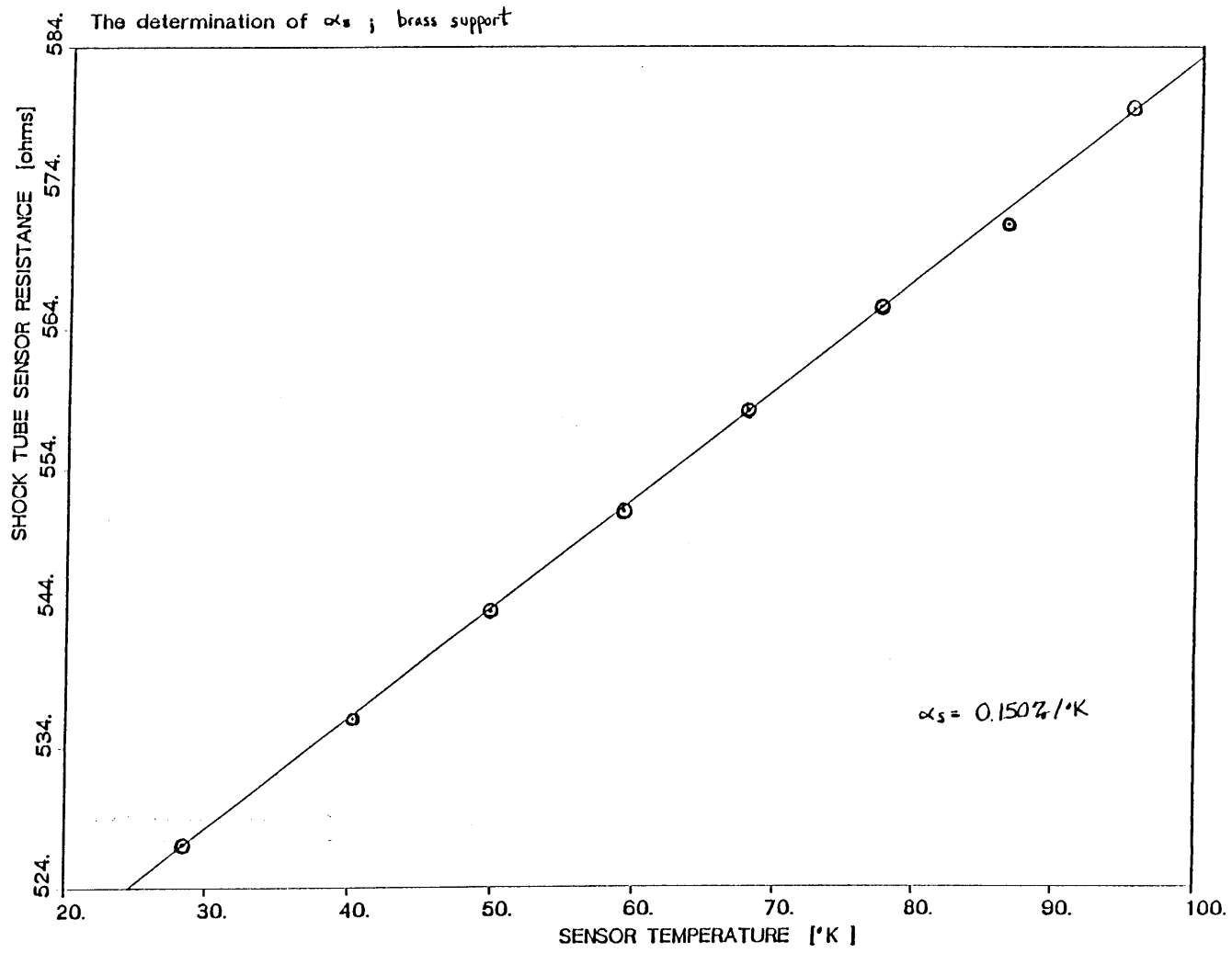

FIGURE 4.15: SENSOR RESISTANCE VS. SENSOR TEMPERATURE

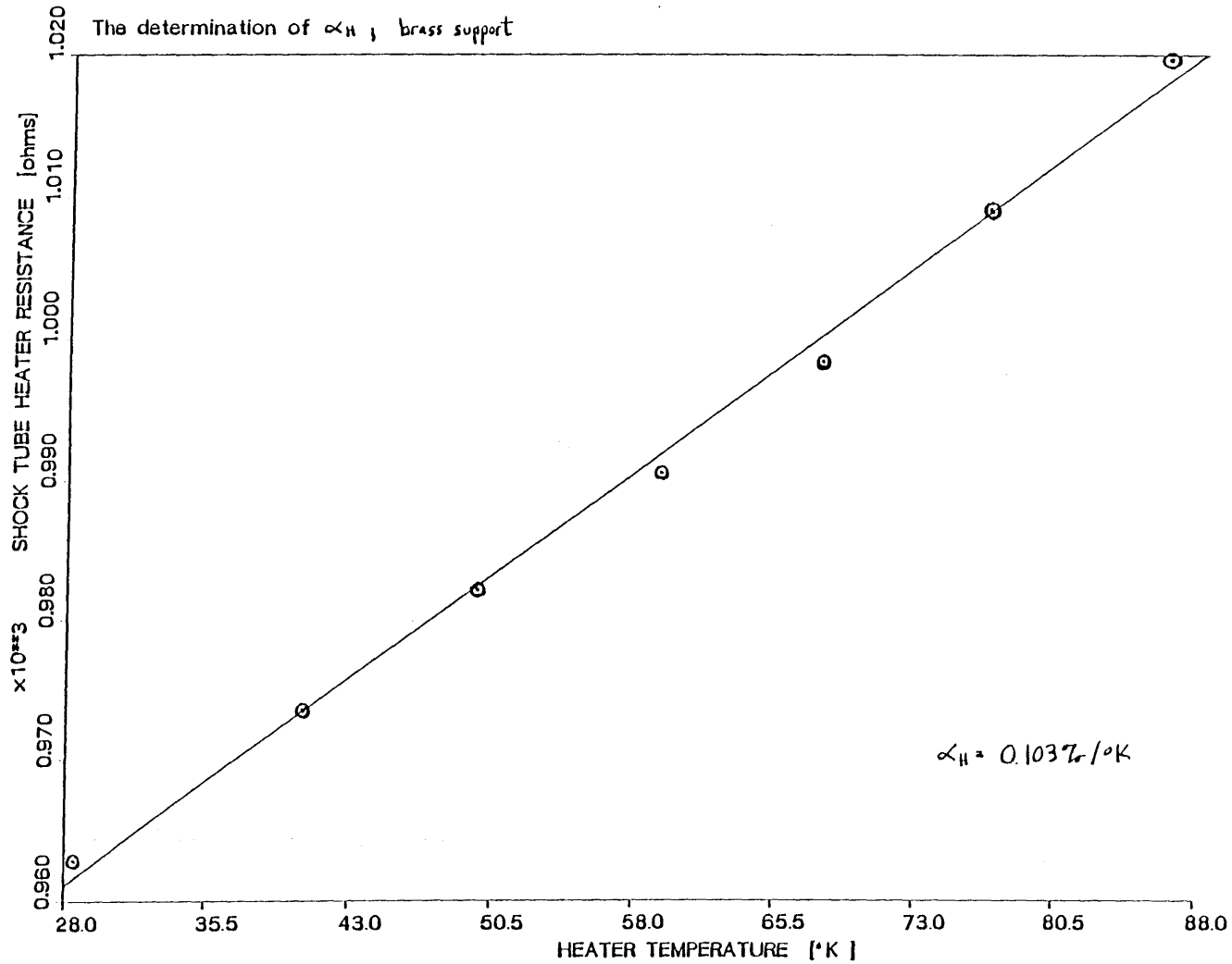

FIGURE 4.16: HEATER RESISTANCE VS. HEATER TEMPERATURE

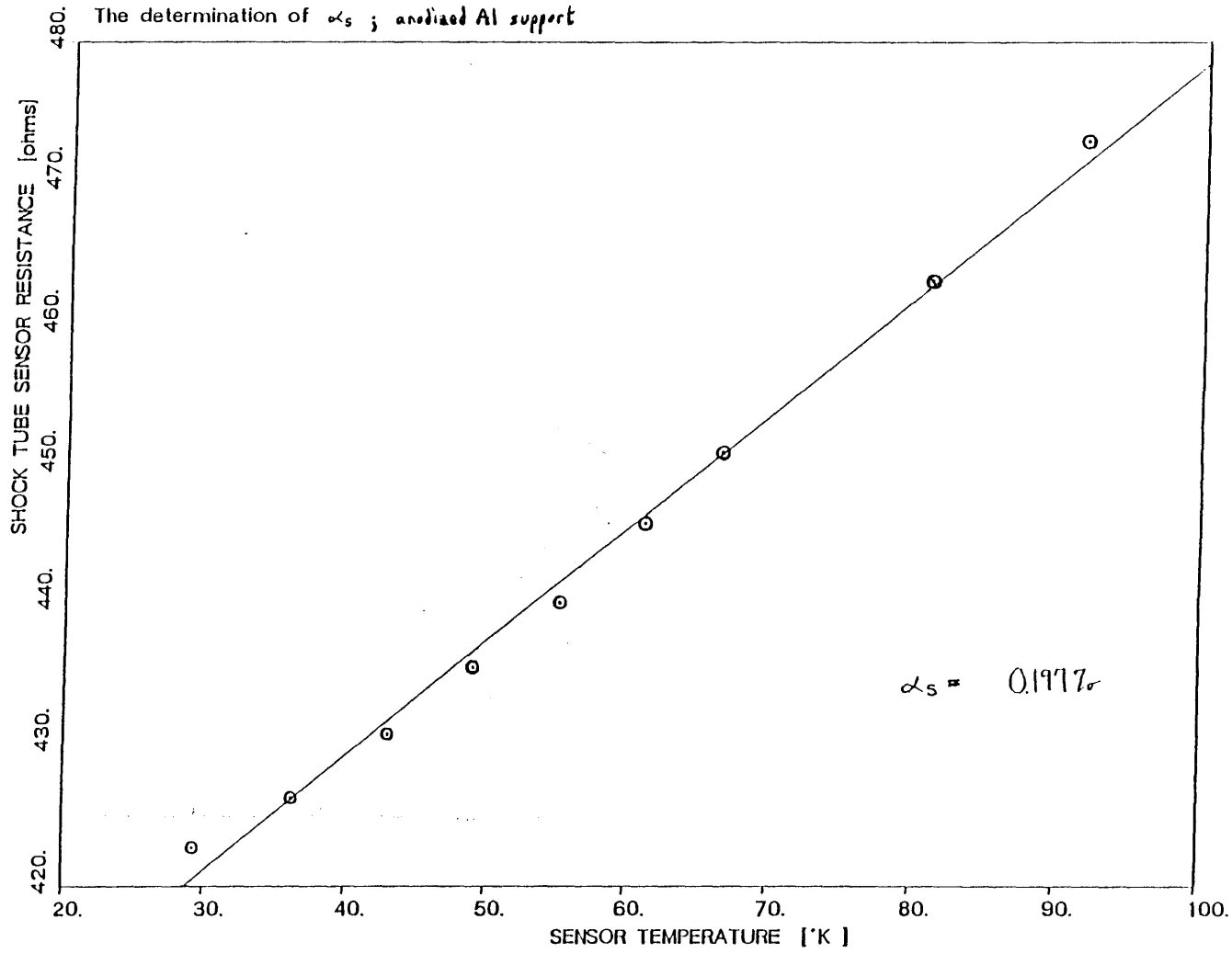

FIGURE 4.17: SENSOR RESISTANCE VS. SENSOR TEMPERATURE

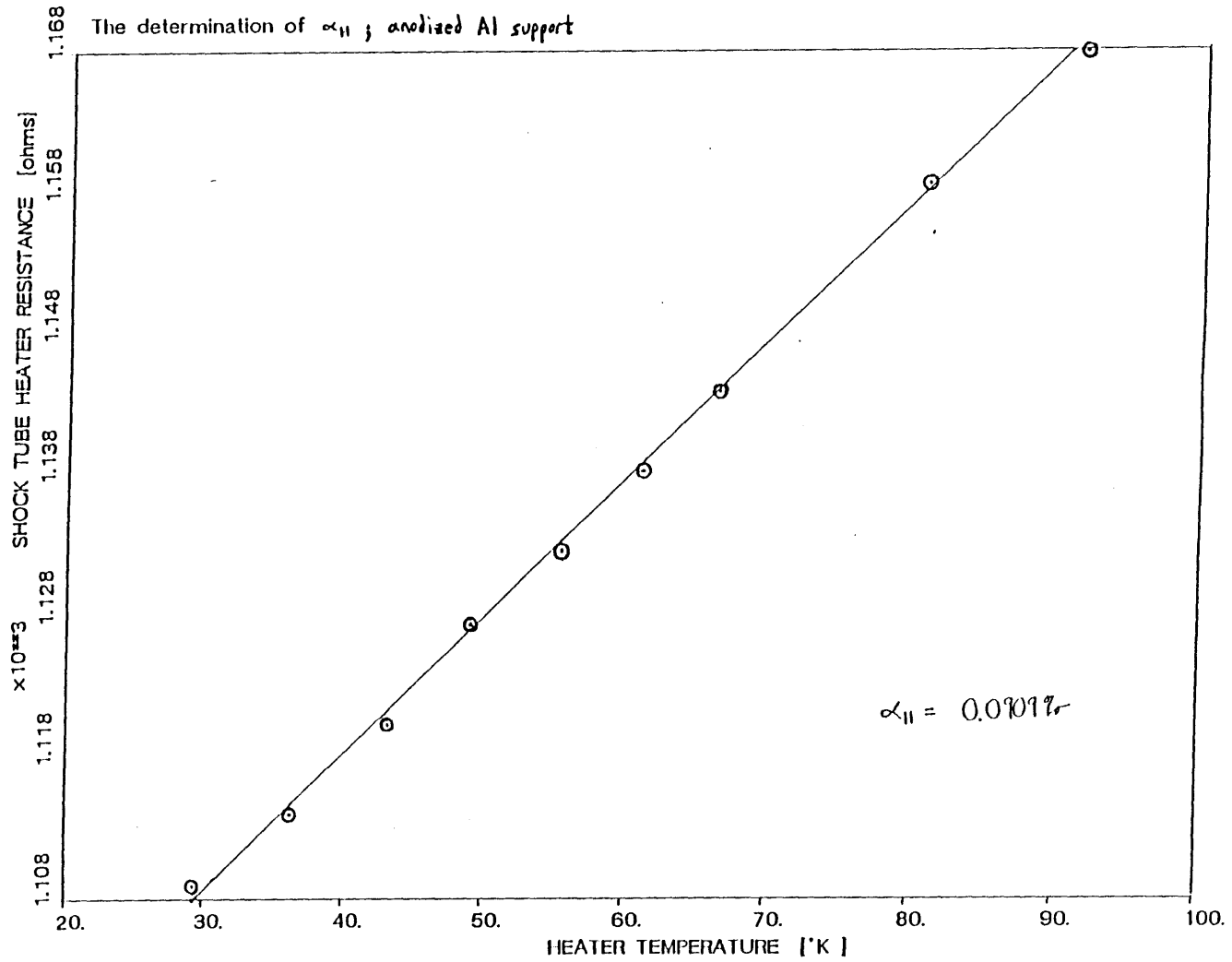

FIGURE 4.18 : HEATER RESISTANCE VS. HEATER TEMPERATURE

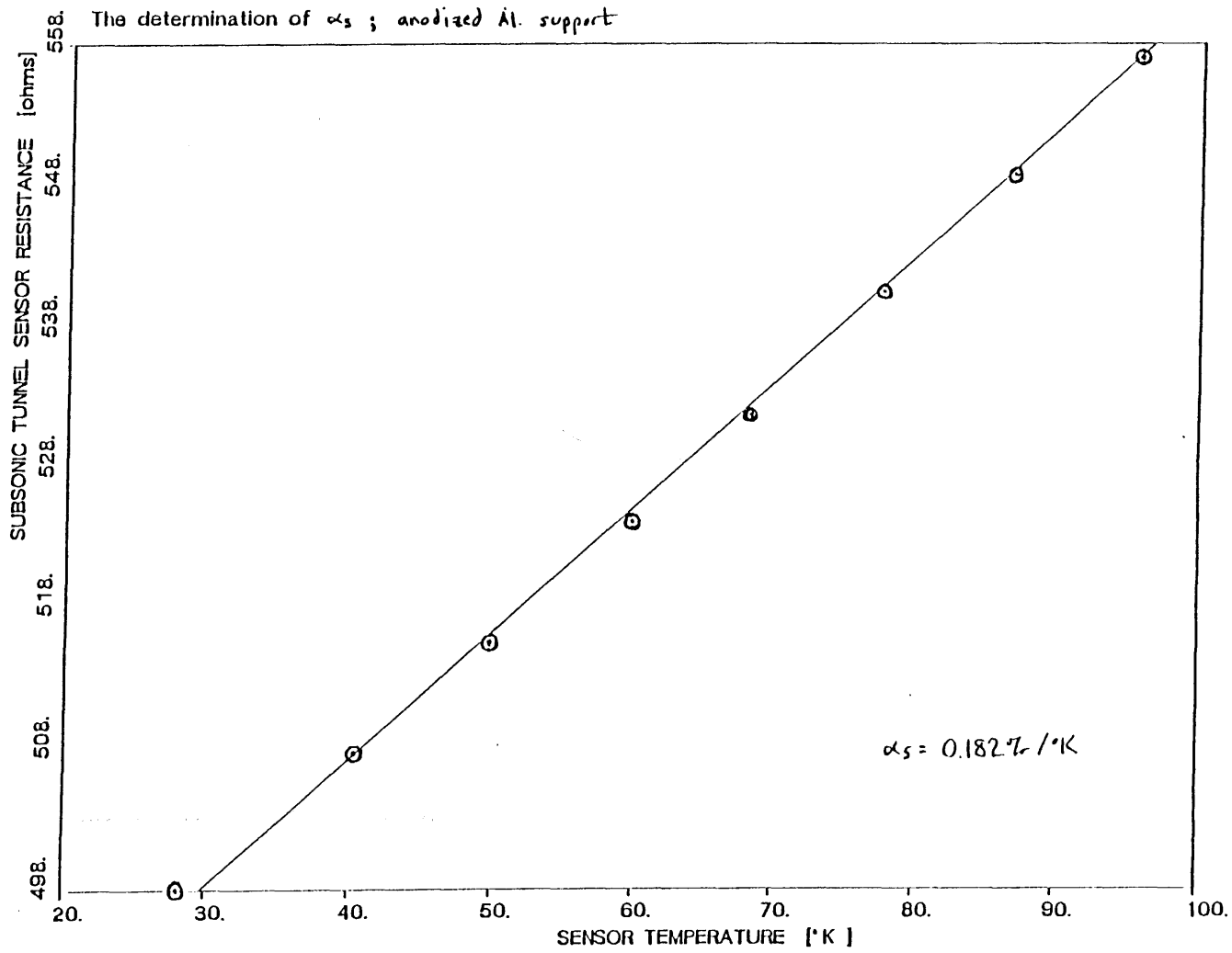

FIGURE 4.19: SUBSONIC TUNNEL SENSOR RESISTANCE VS. SENSOR TEMPERATURE

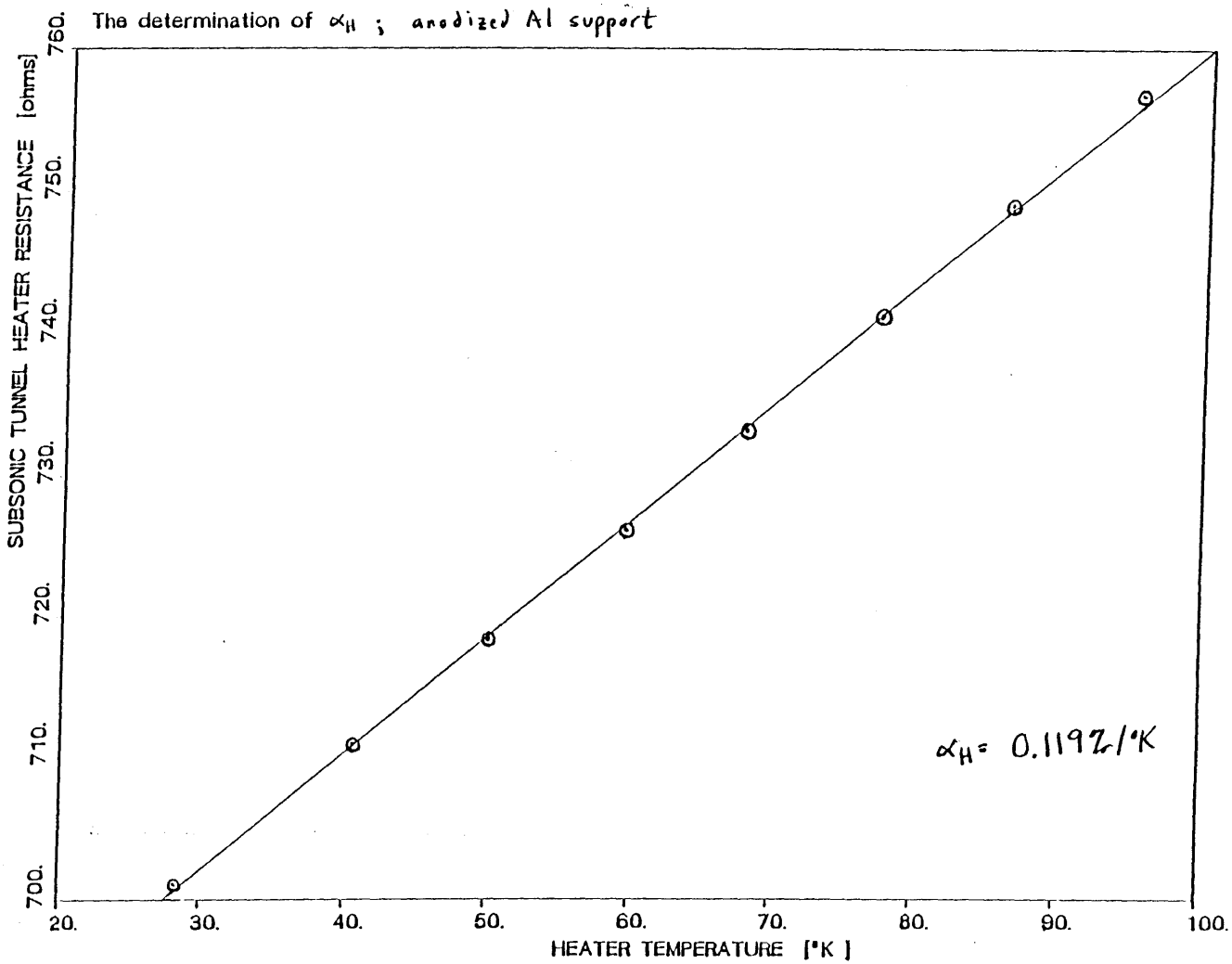

FIGURE 4.20: SUBSONIC TUNNEL HEATER RESISTANCE VS. HEATER TEMPERATURE

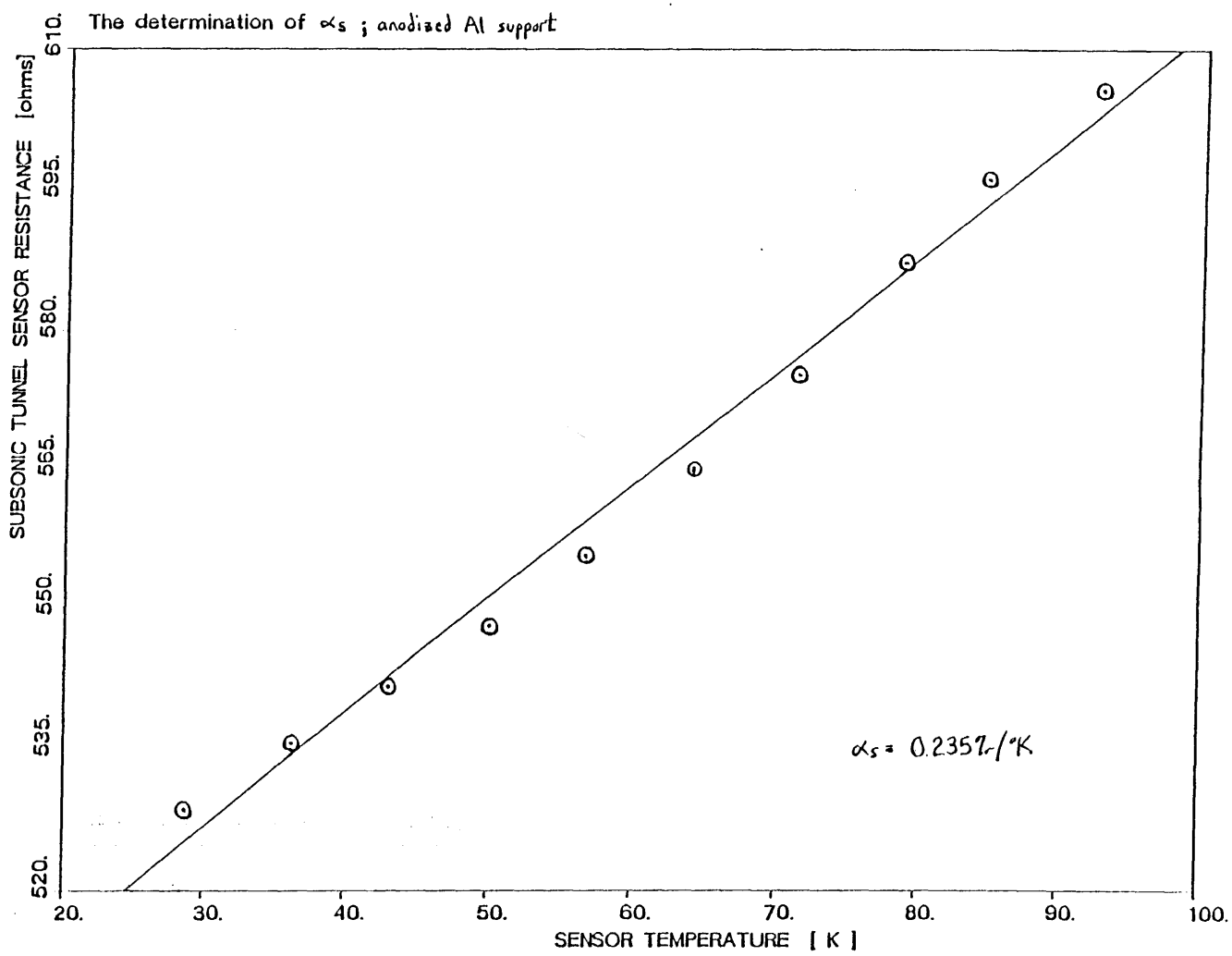

FIGURE 4.21: SUBSONIC TUNNEL SENSOR RESISTANCE VS. SENSOR TEMPERATURE

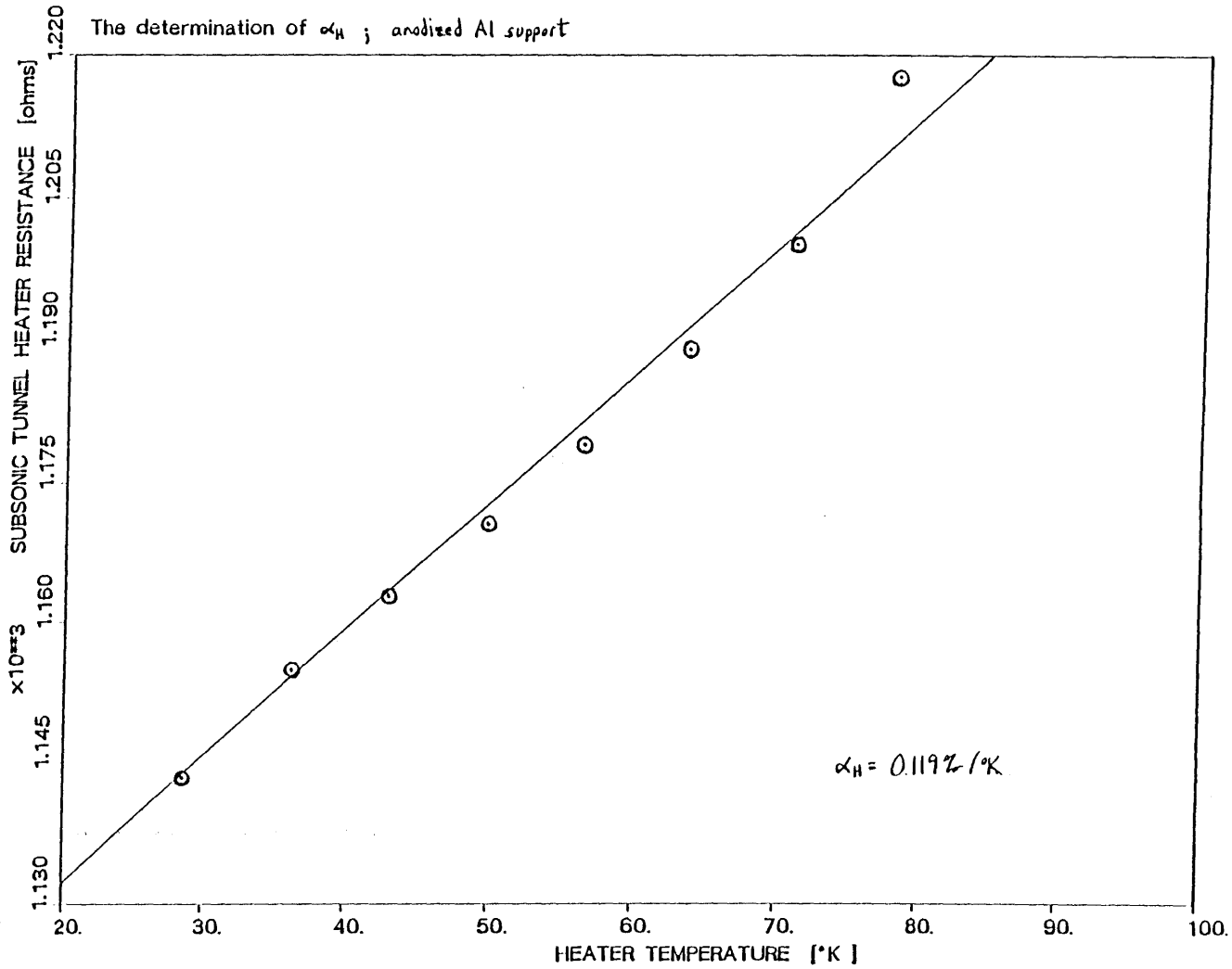

FIGURE 4.22: SUBSONIC TUNNEL HEATER RESISTANCE VS. HEATER TEMPERATURE

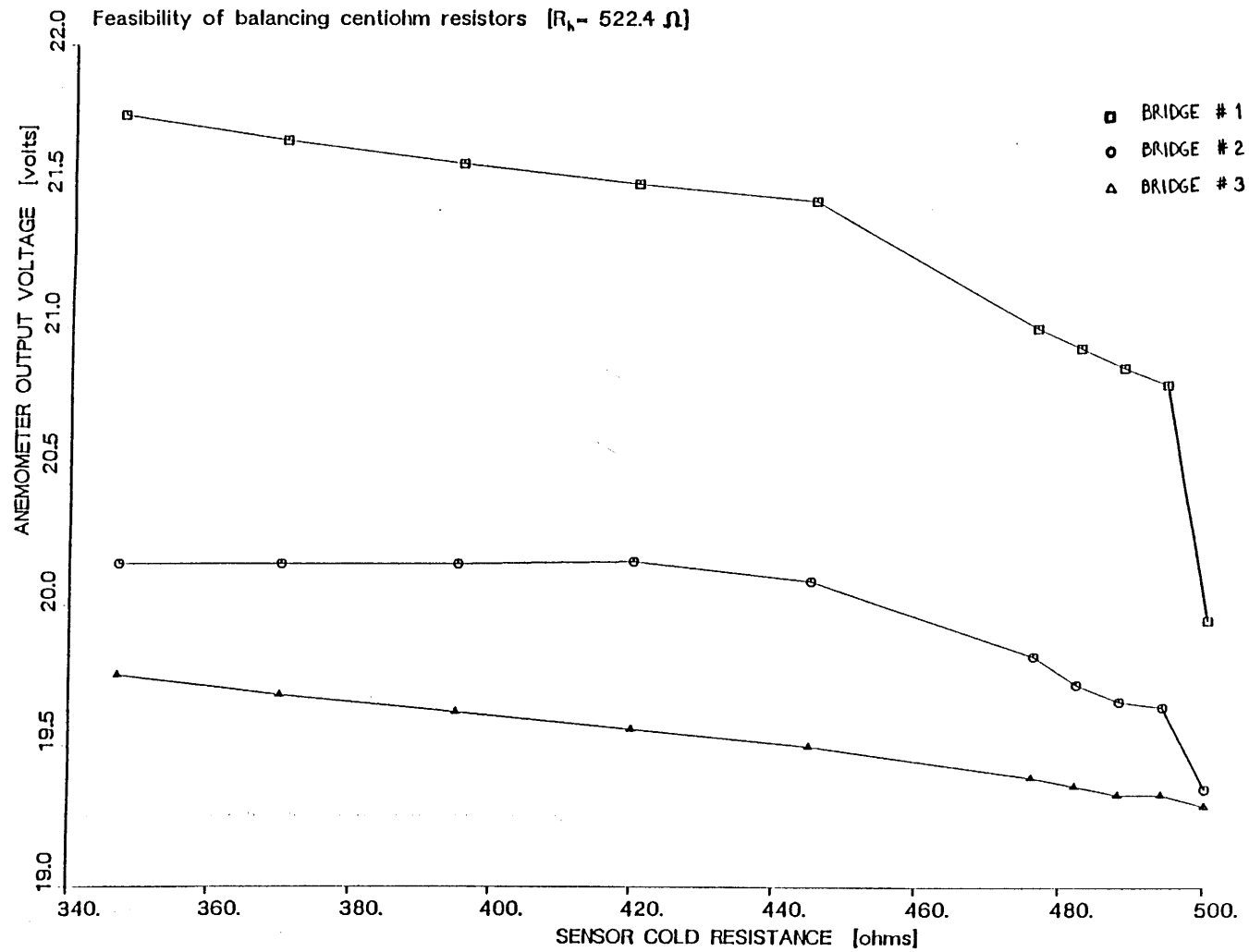

FIGURE 4.23: ANEMOMETER OUTPUT VOLTAGE VS. SENSOR COLD RESISTANCE

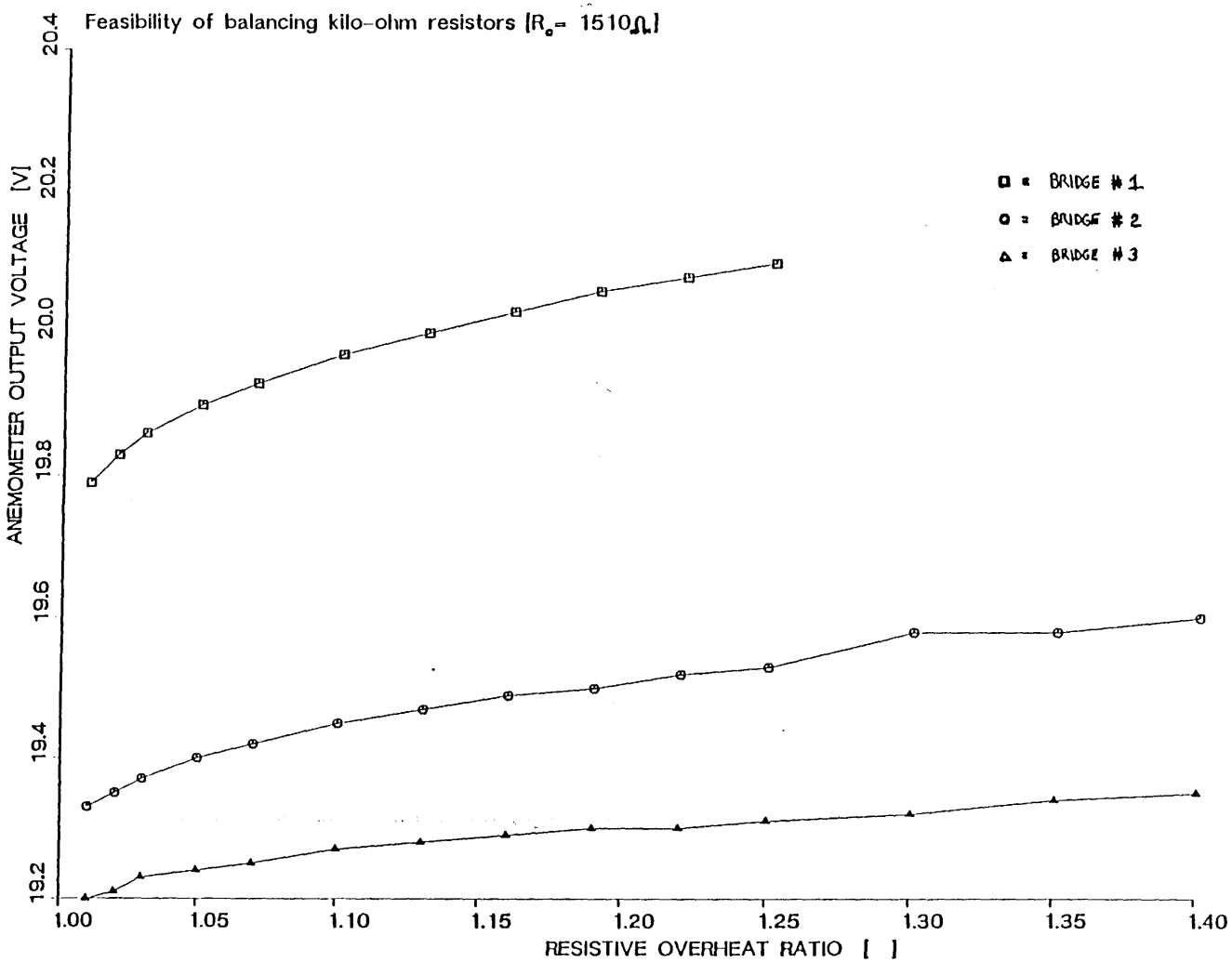

FIGURE 4.24: ANEMOMETER OUTPUT VOLTAGE VS. SENSOR OVERHEAT RATIO

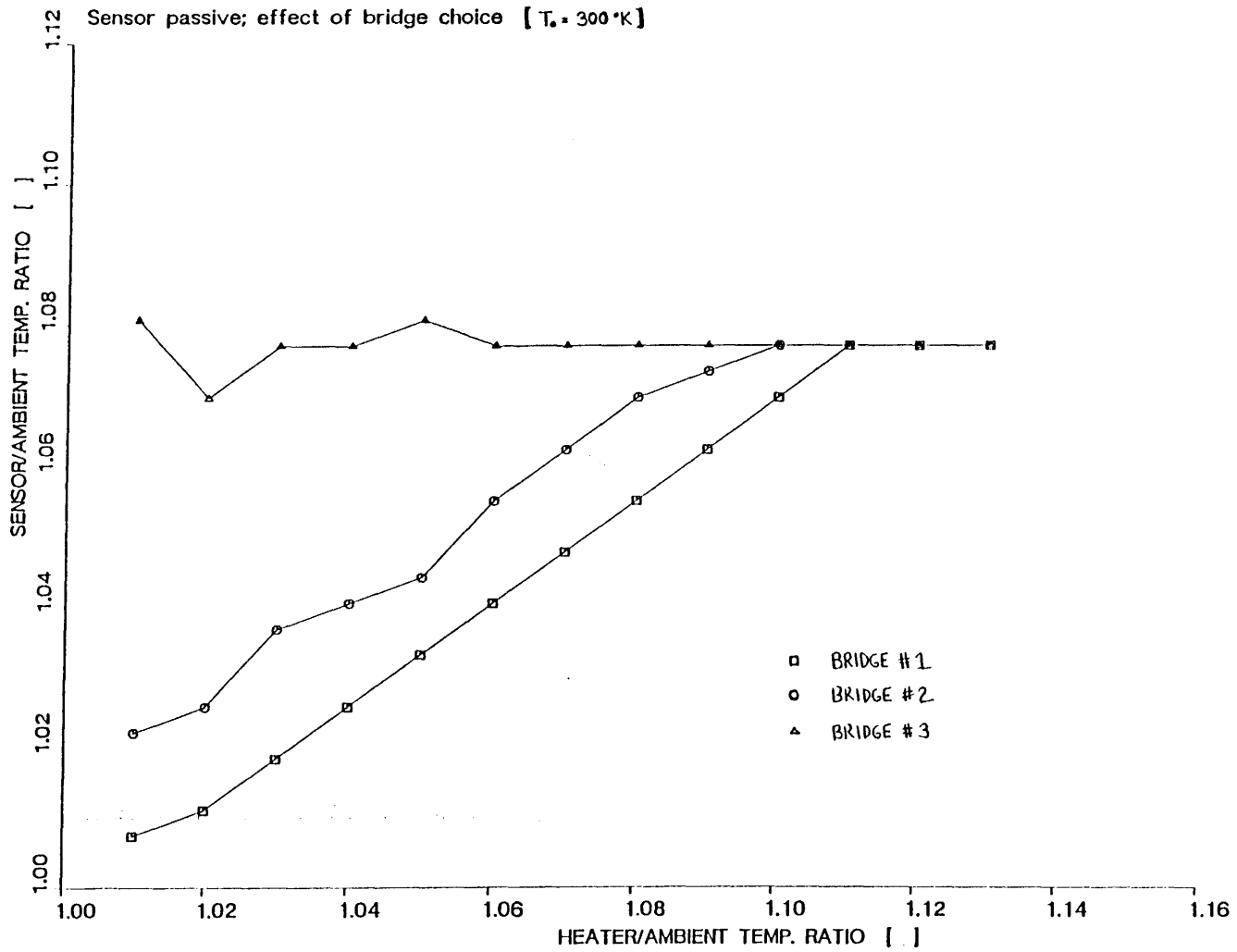

FIGURE 4.25: SENSOR/AMBIENT TEMPERATURE VS. HEATER/AMBIENT TEMPERATURE

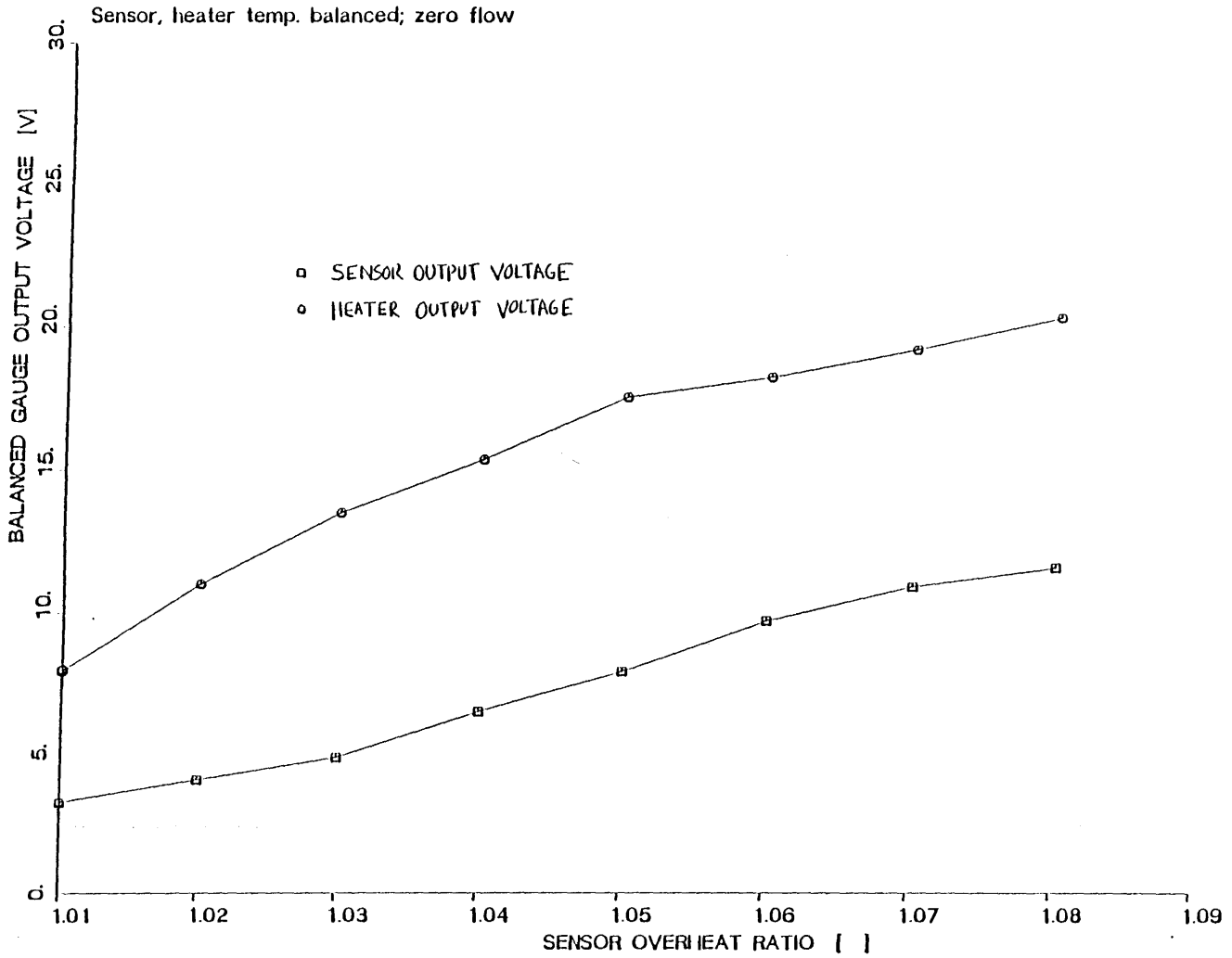

FIGURE 4.26: BALANCED-GAUGE VOLTAGE VS. SENSOR OVERHEAT RATIO

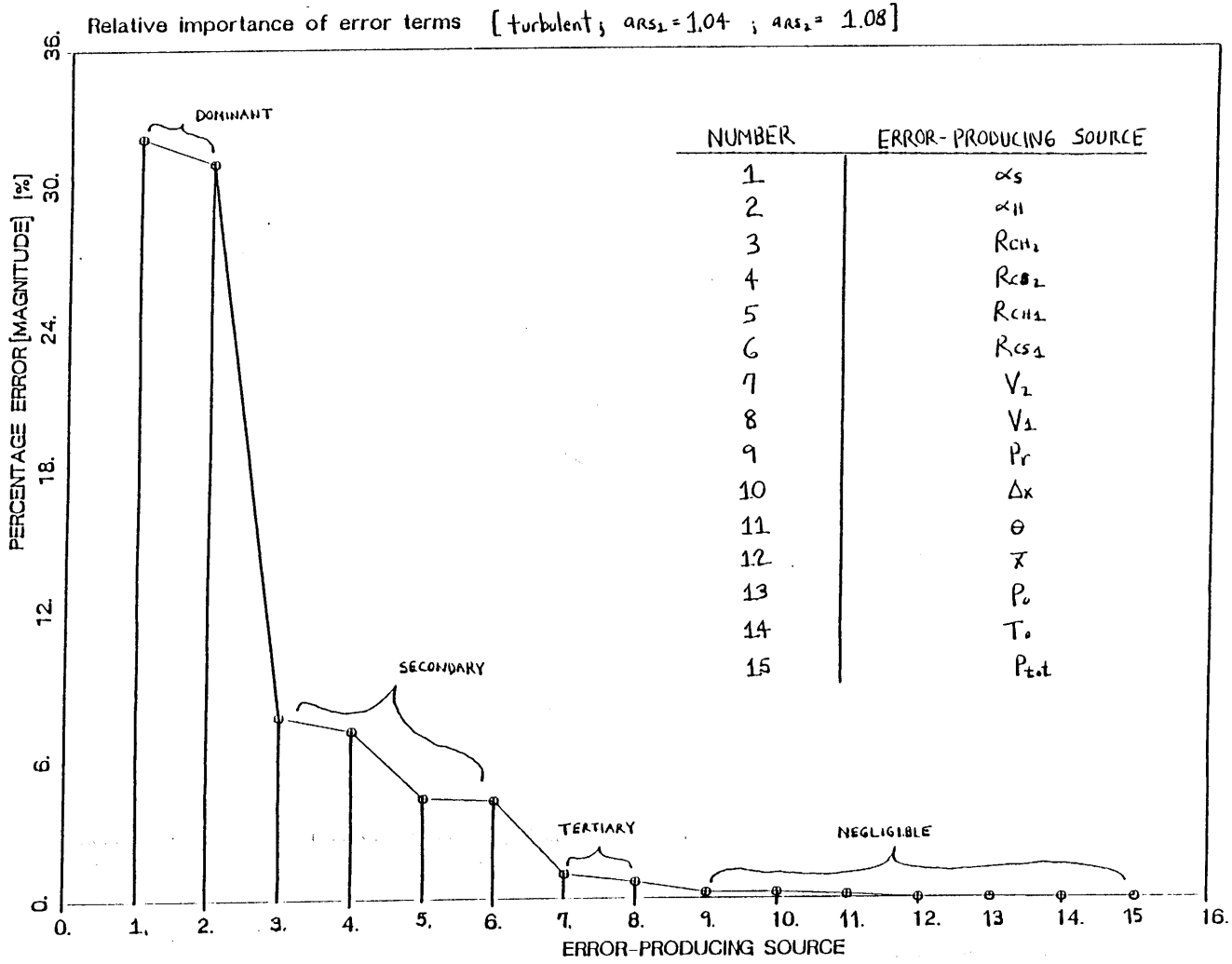

FIGURE 5.1: PERCENTAGE ERROR FOR ERROR-PRODUCING SOURCES IN SUBSONIC TUNNEL

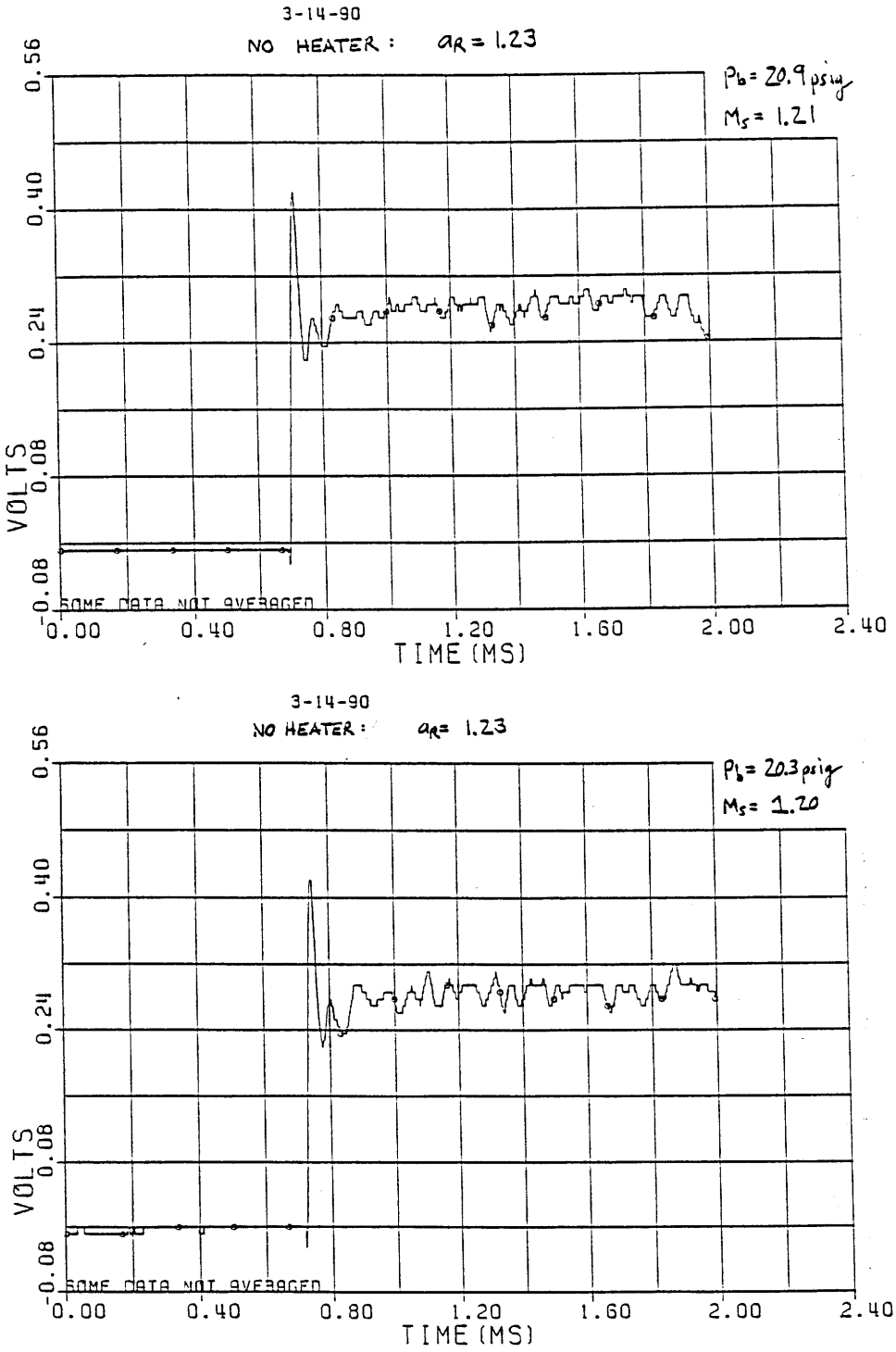

FIGURE 6.1: UNSTEADY VOLTAGE TRACES VS. TIME

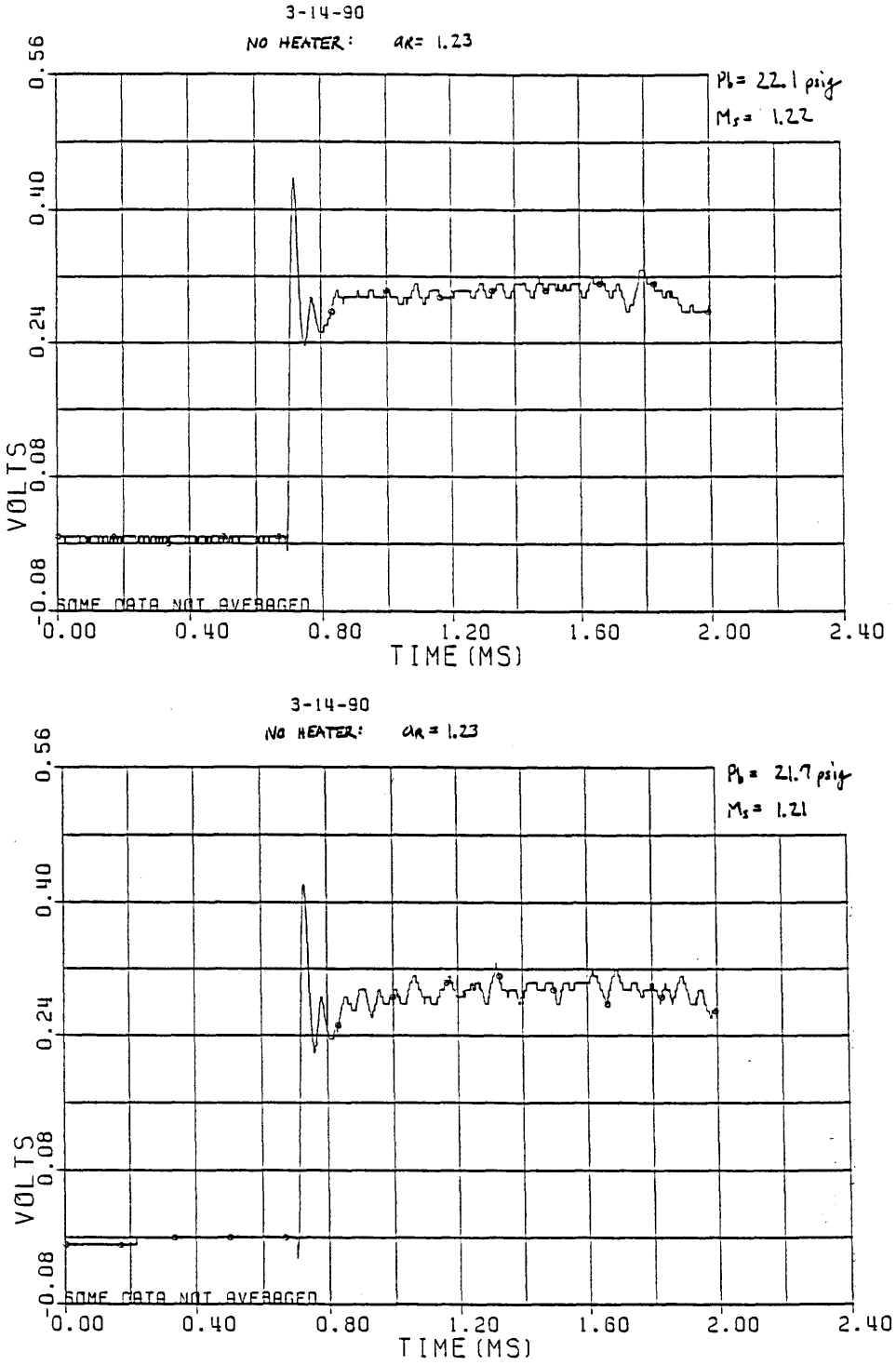

FIGURE 6.2: UNSTEADY VOLTAGE TRACES VS. TIME

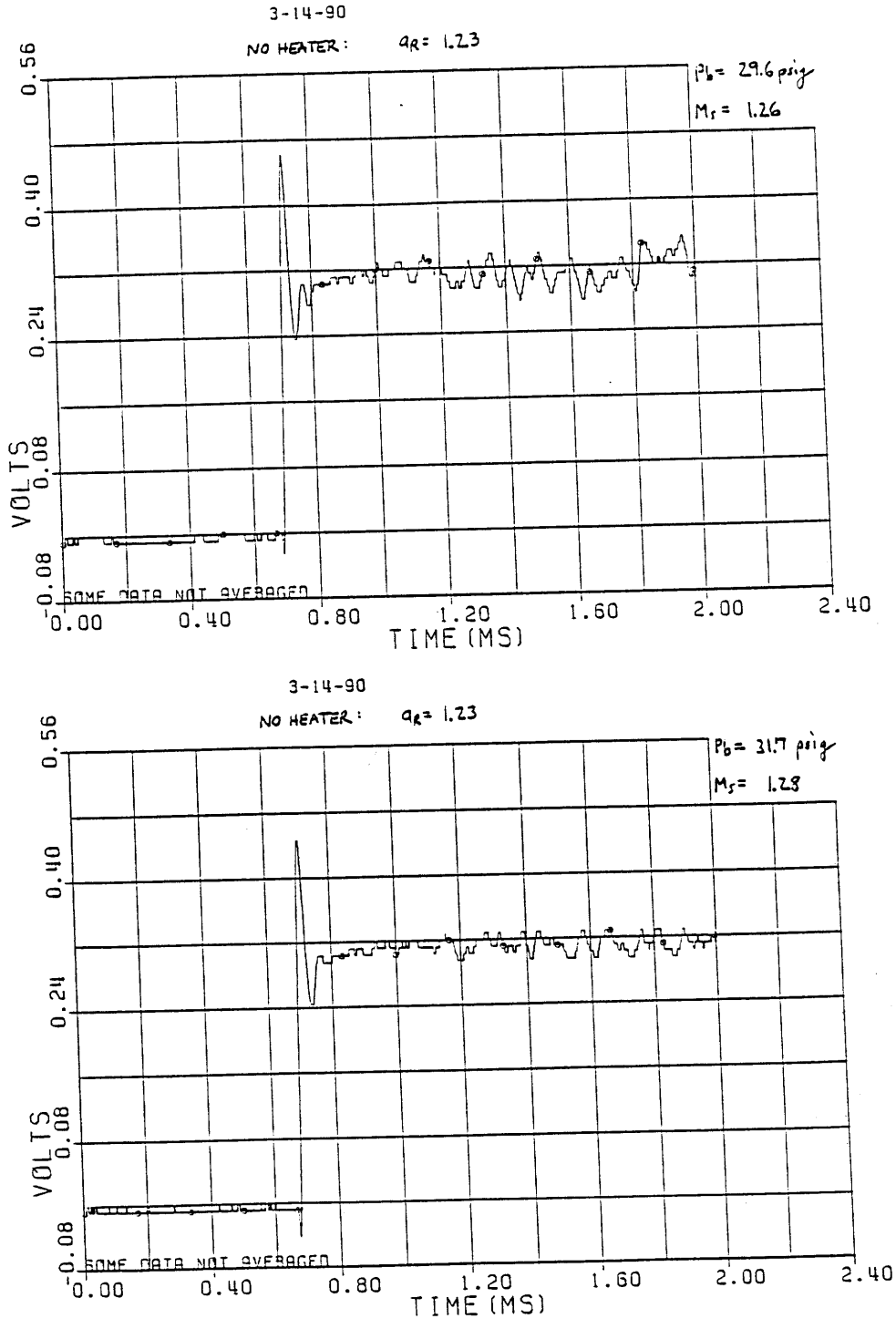

FIGURE 6.3: UNSTEADY VOLTAGE TRACES VS. TIME

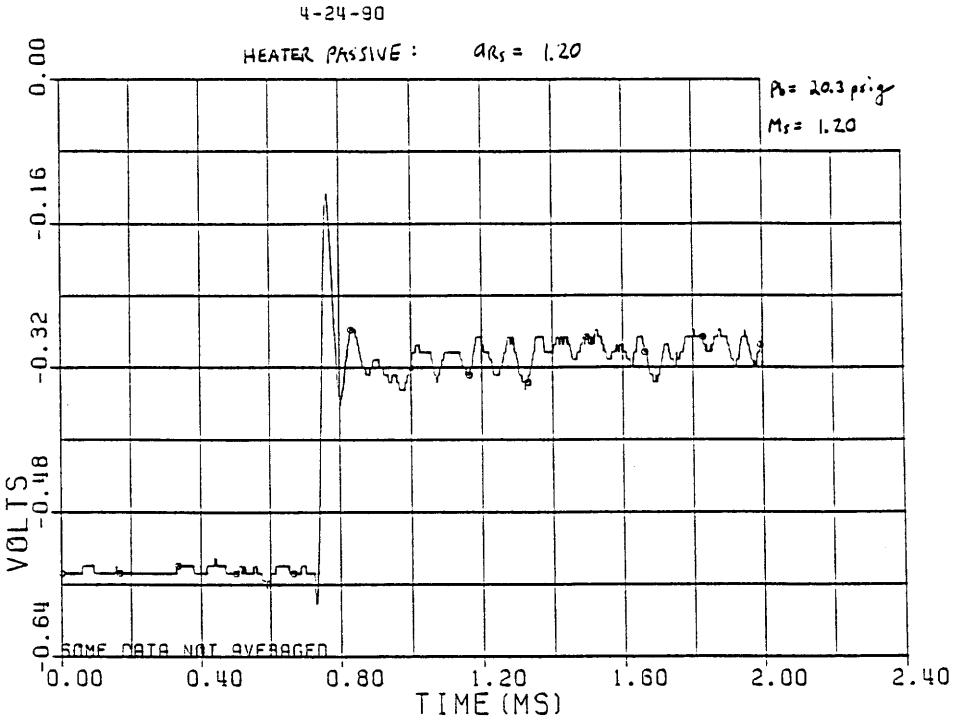

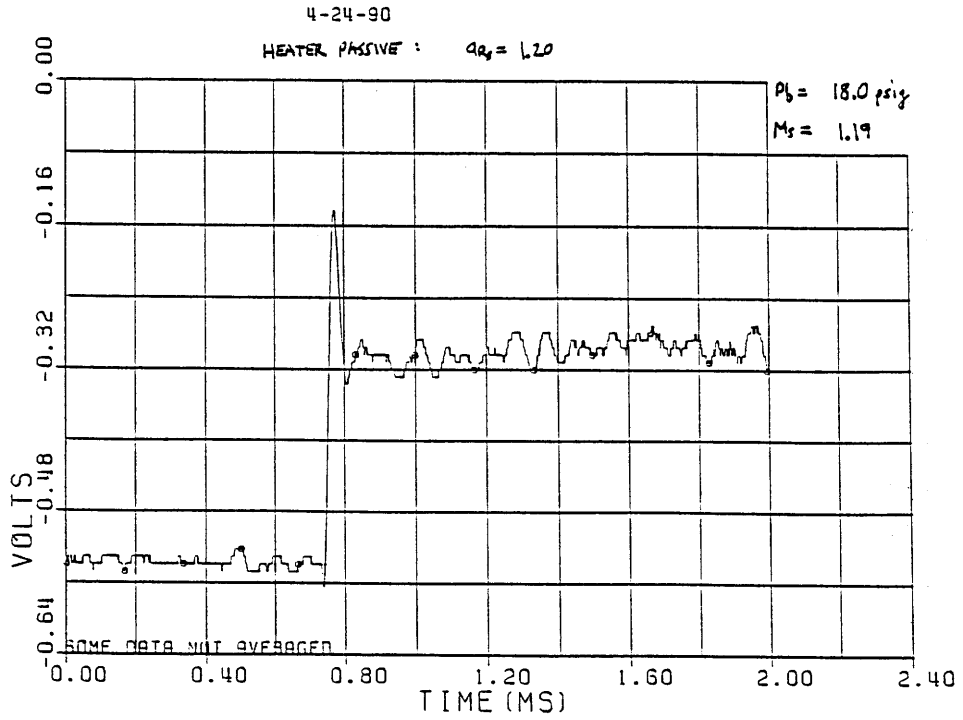

FIGURE 6.4: UNSTEADY VOLTAGE TRACES VS. TIME

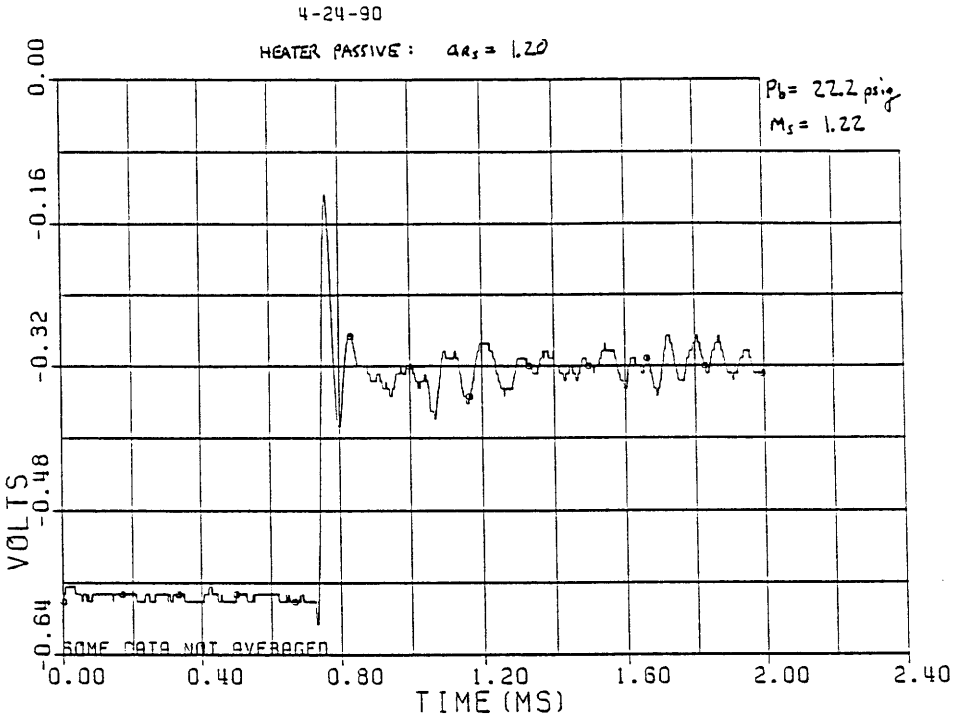

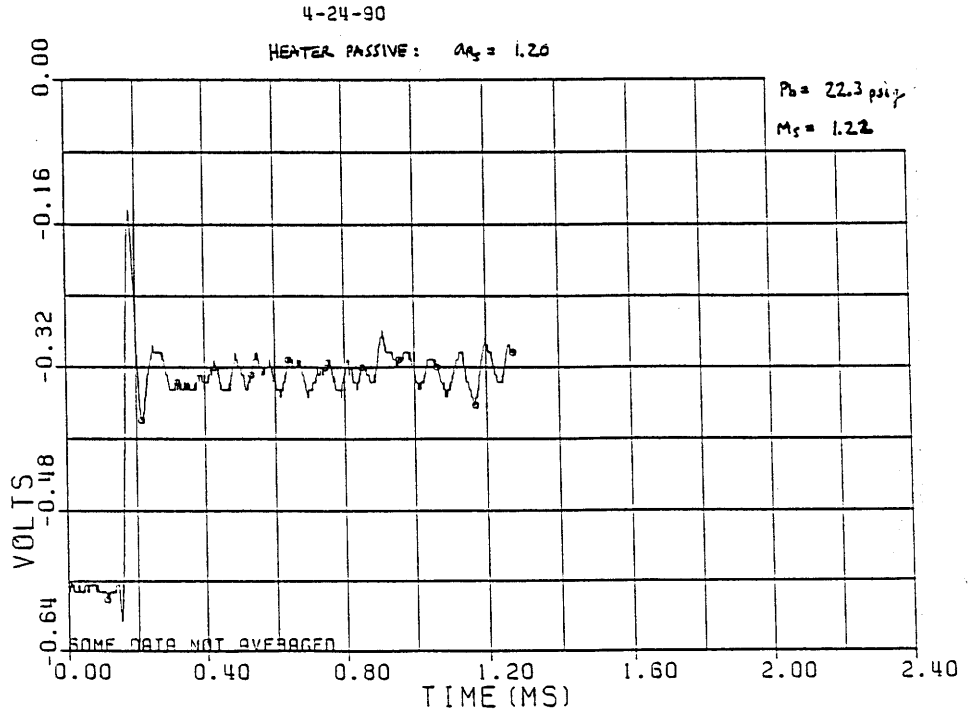

FIGURE 6.5: UNSTEADY VOLTAGE TRACES VS. TIME

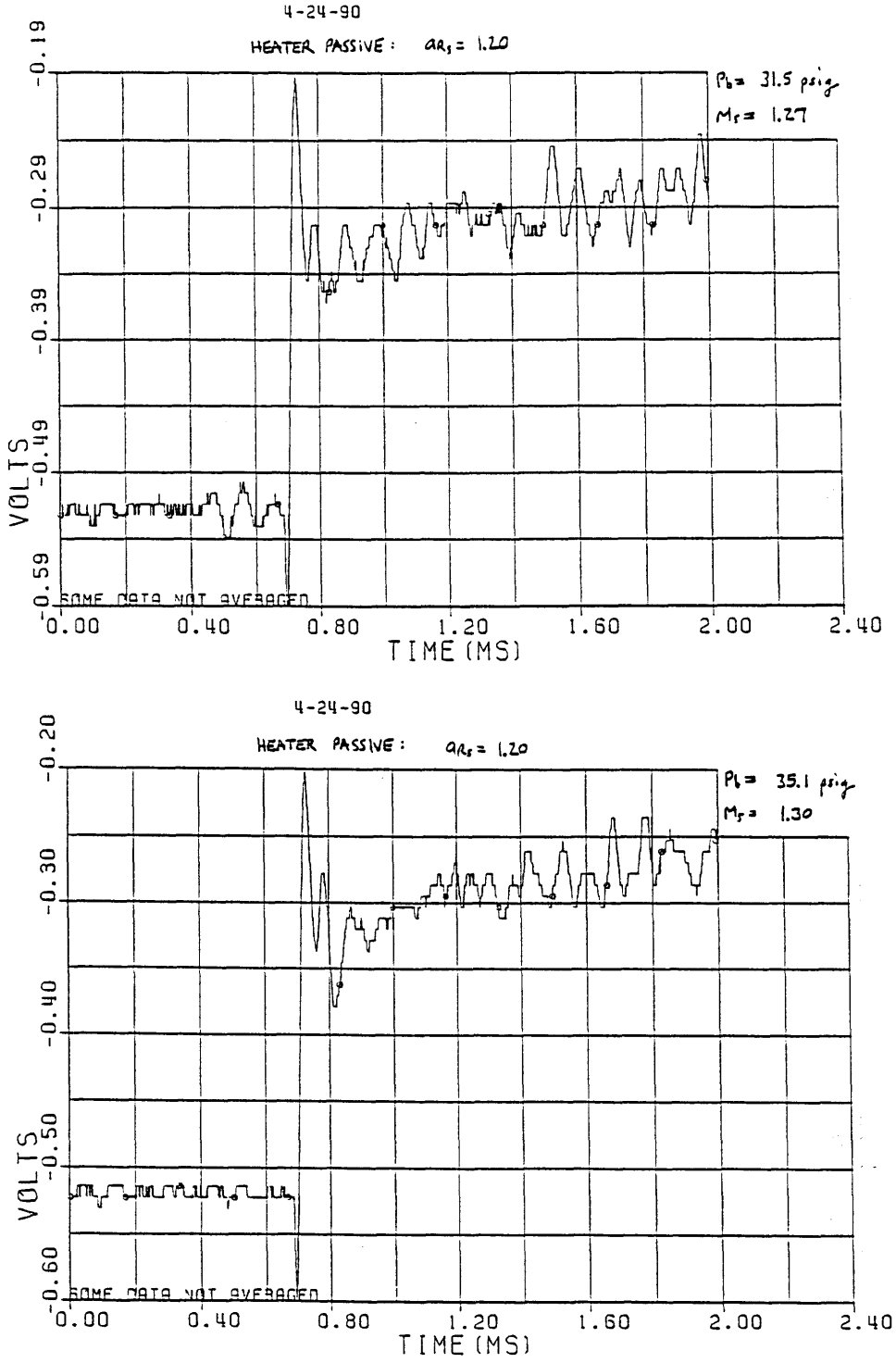

FIGURE 6.6: UNSTEADY VOLTAGE TRACES VS. TIME

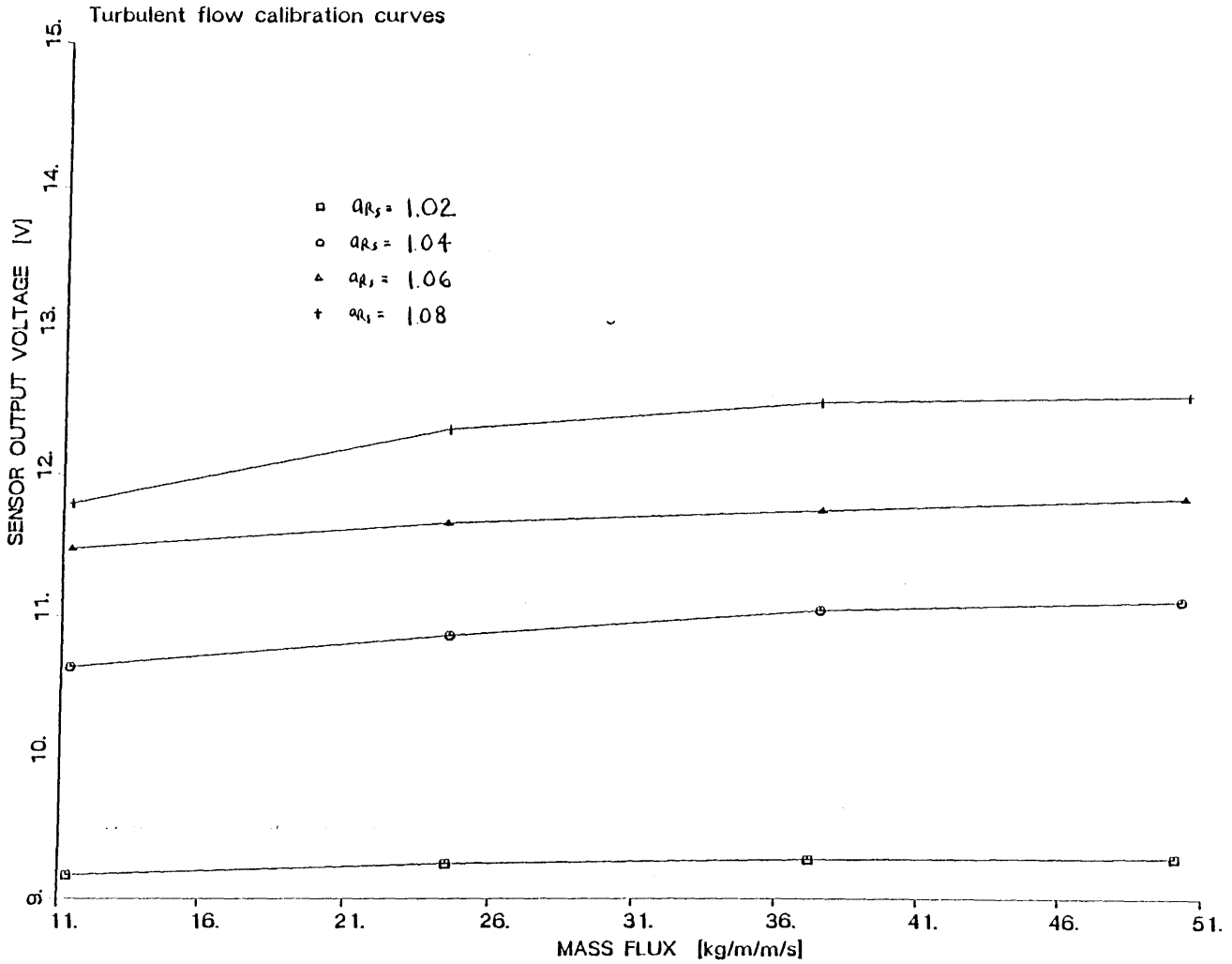

FIGURE 6.7: SENSOR VOLTAGE VS. MASS FLUX

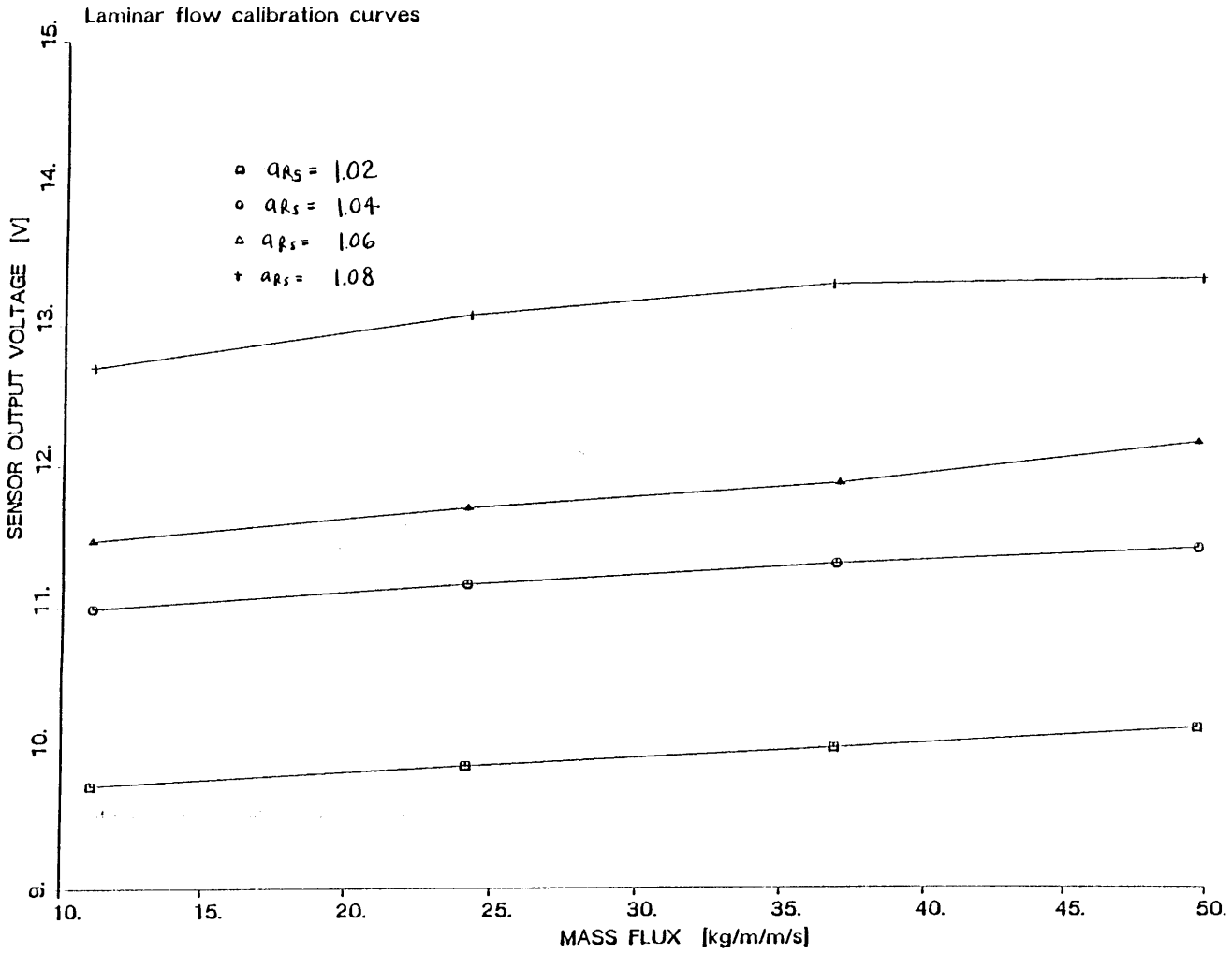

FIGURE 6.8: SENSOR VOLTAGE VS. MASS FLUX

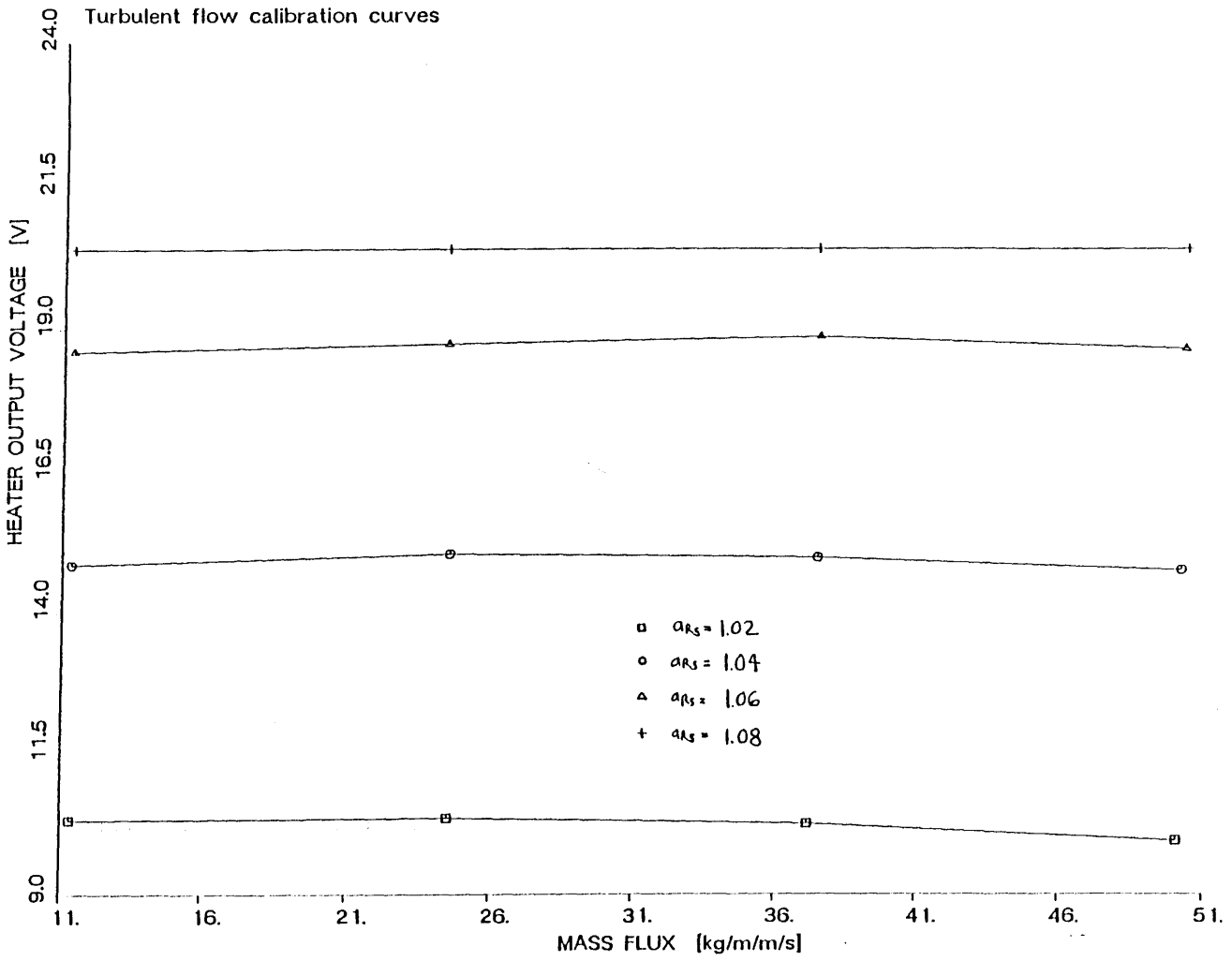

FIGURE 6.9: HEATER VOLTAGE VS. MASS FLUX

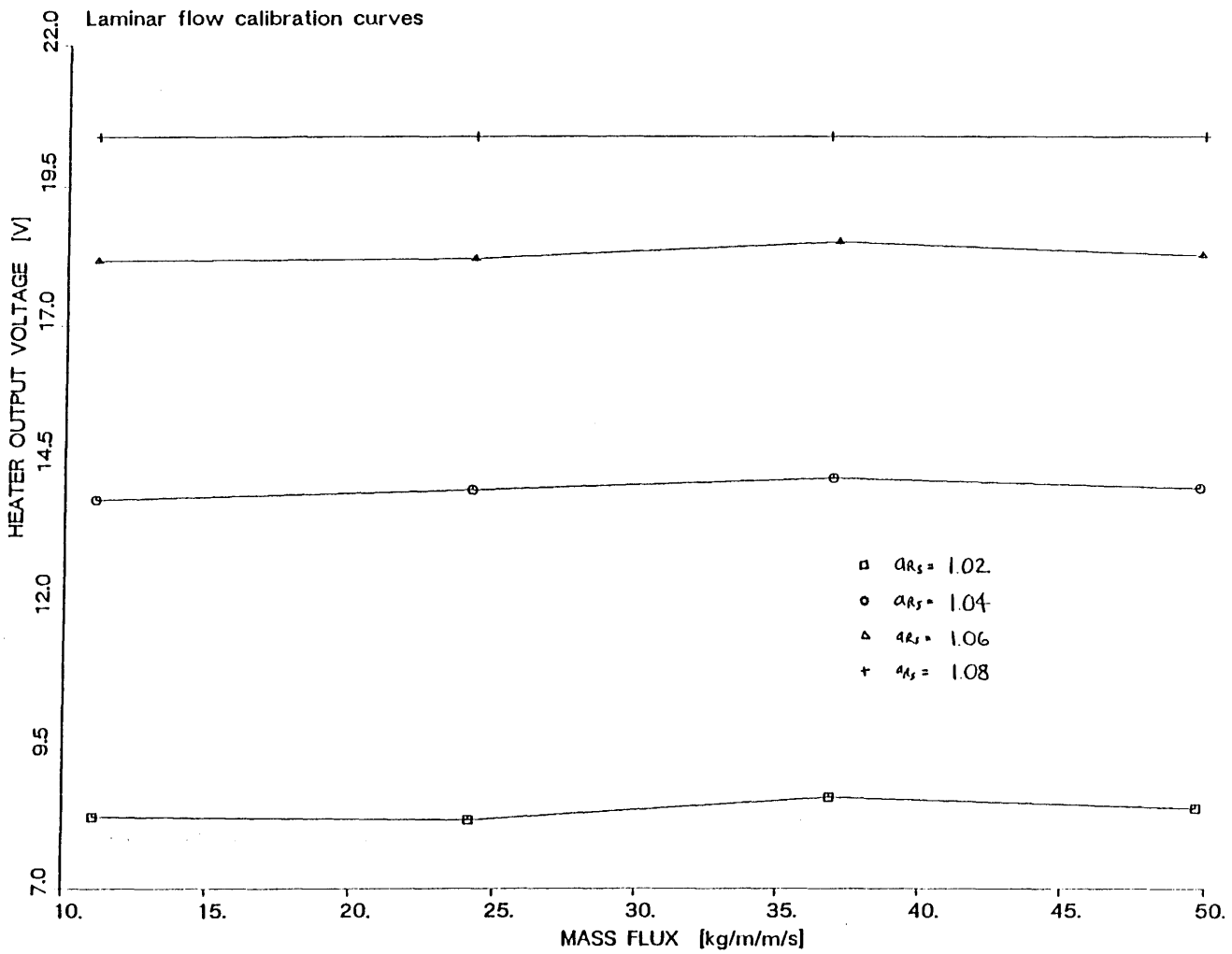

FIGURE 6.10: HEATER VOLTAGE VS. MASS FLUX

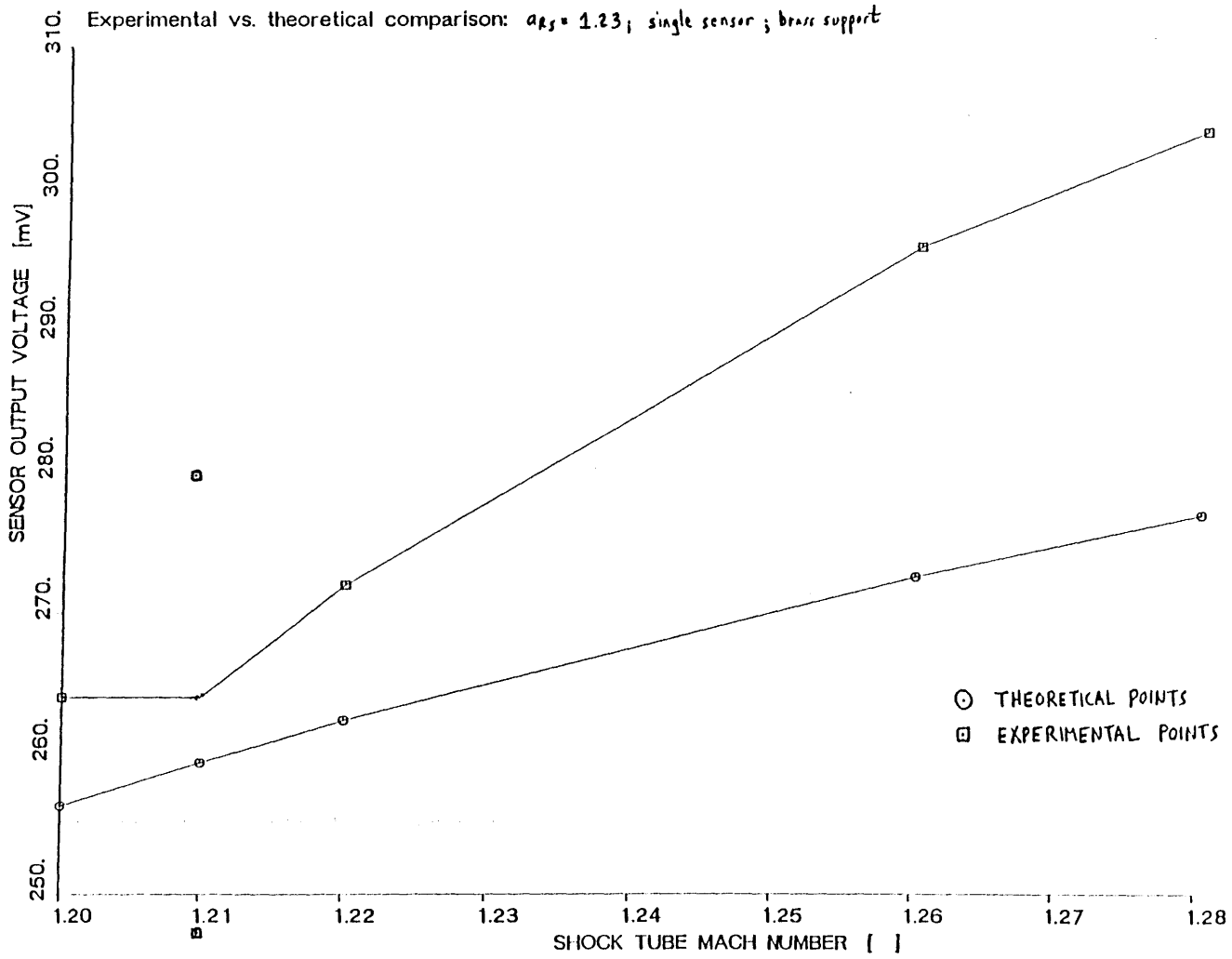

FIGURE 6.11: SENSOR VOLTAGE VS. MACH NUMBER

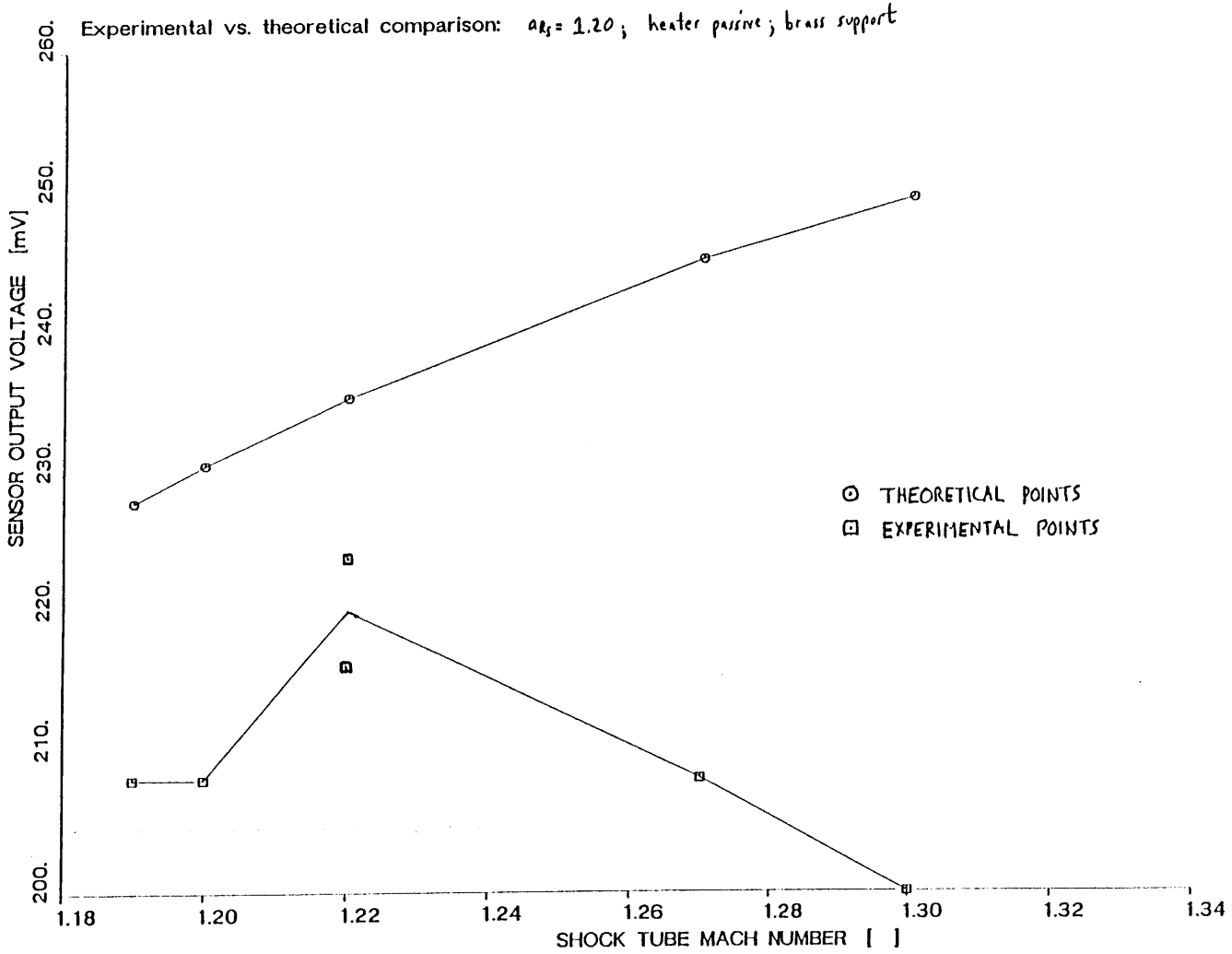

FIGURE 6.12: SENSOR VOLTAGE VS. MACH NUMBER

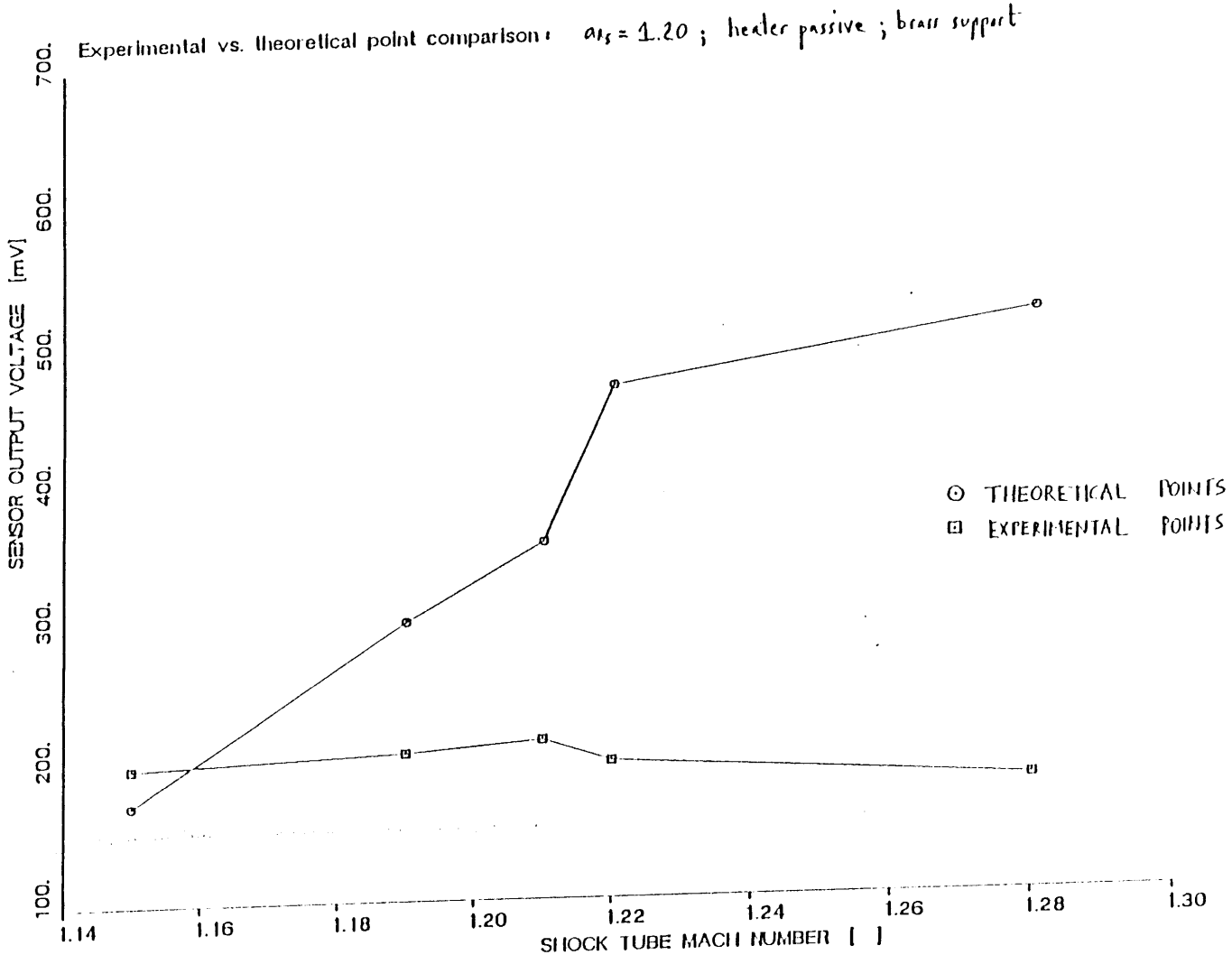

FIGURE 6.13: SENSOR VOLTAGE VS. MACH NUMBER

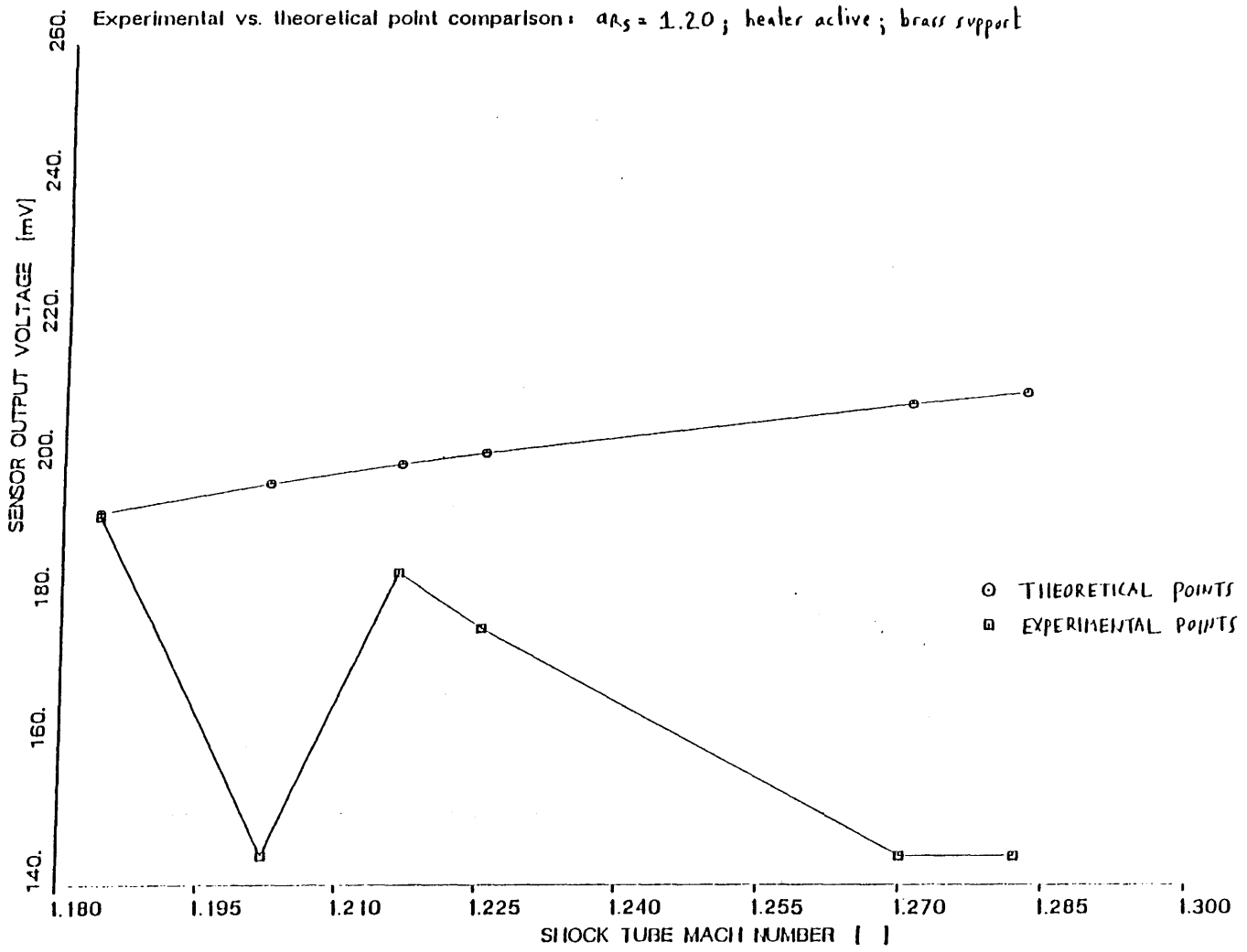

FIGURE 6.14: SENSOR VOLTAGE VS. MACH NUMBER

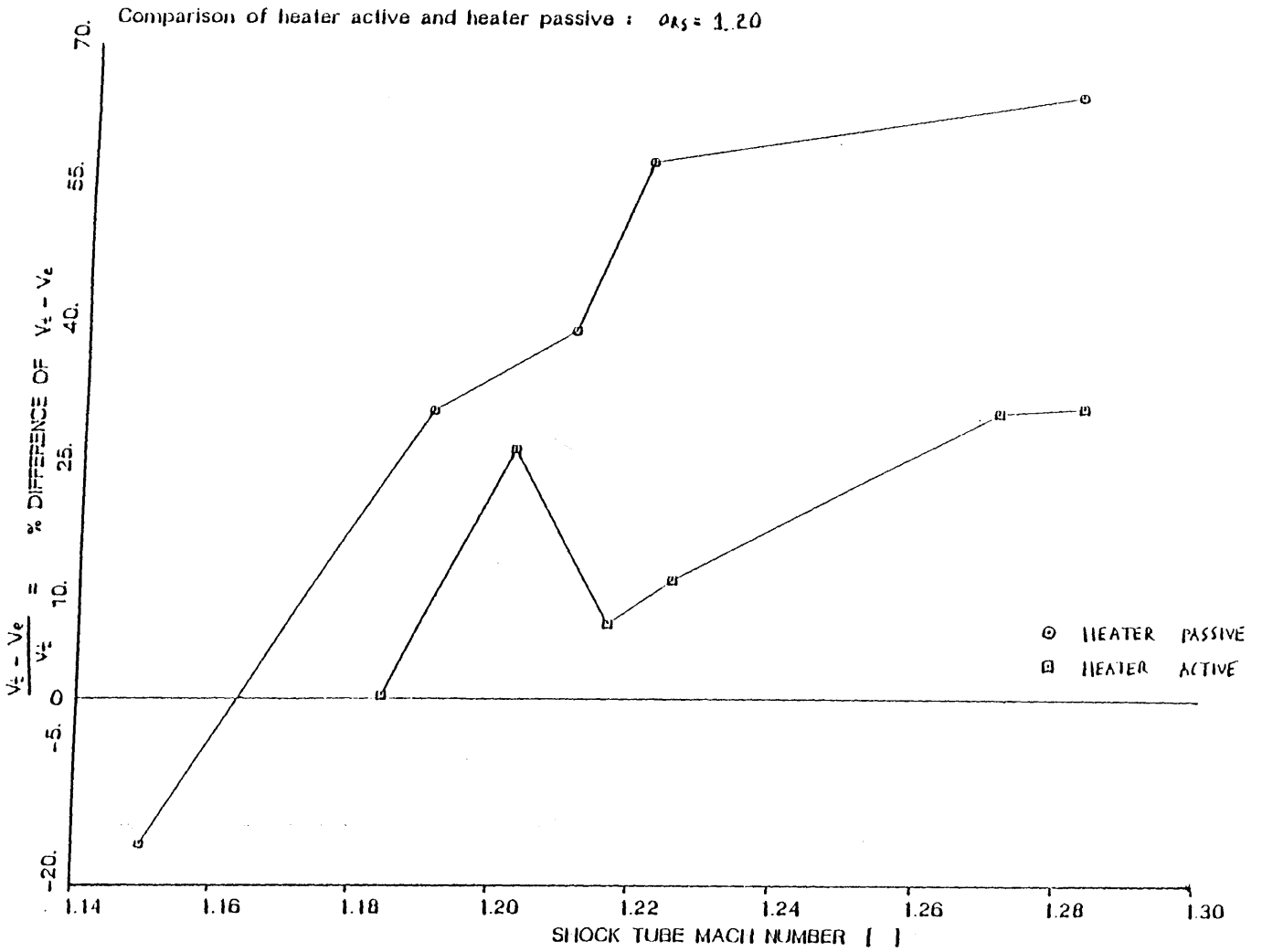

FIGURE 6.15: PERCENT DIFFERENCE OF THEORETICAL AND EXPERIMENTAL VOLTAGE ACROSS THE SENSOR

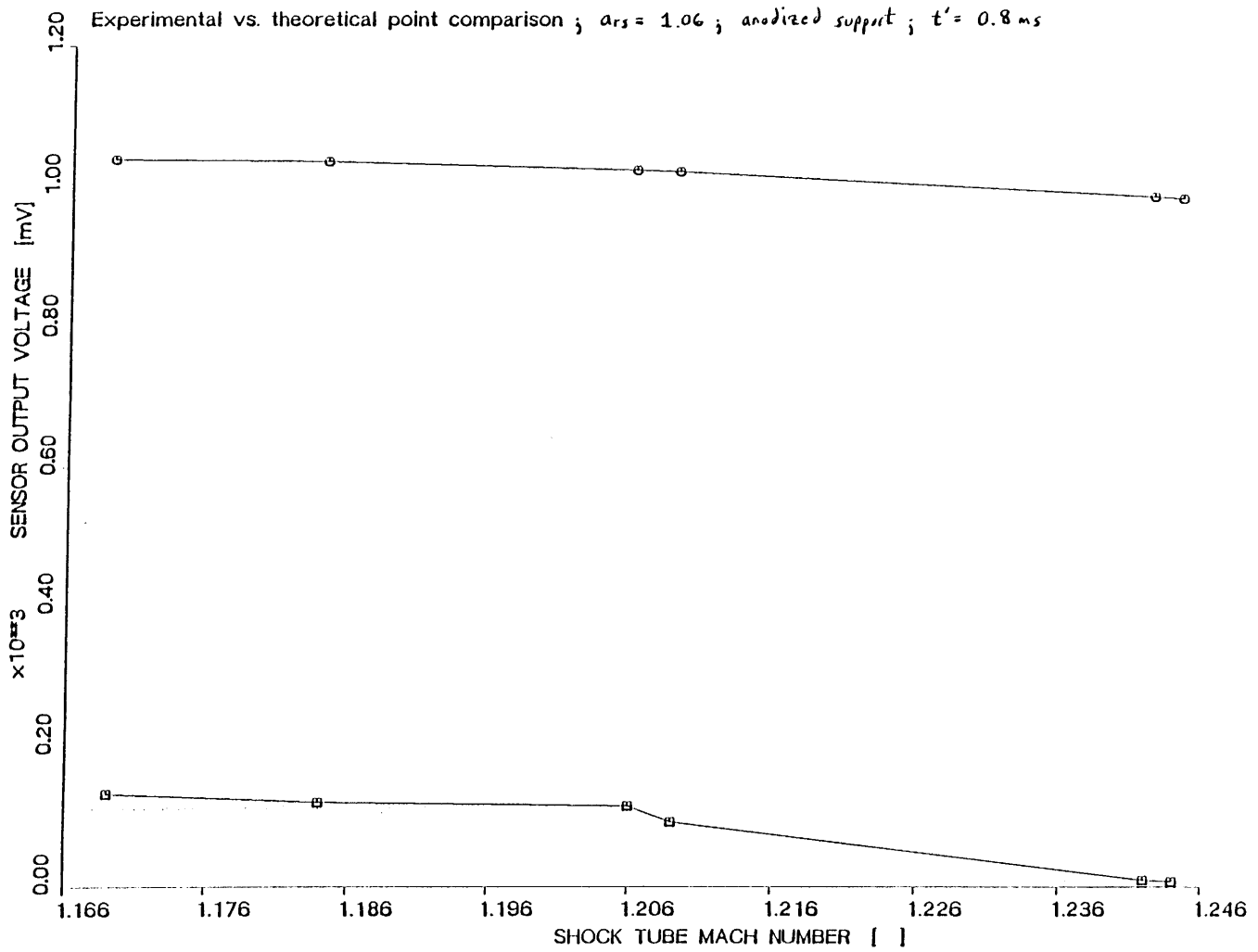

FIGURE 6.16: SENSOR VOLTAGE VS. MACH NUMBER

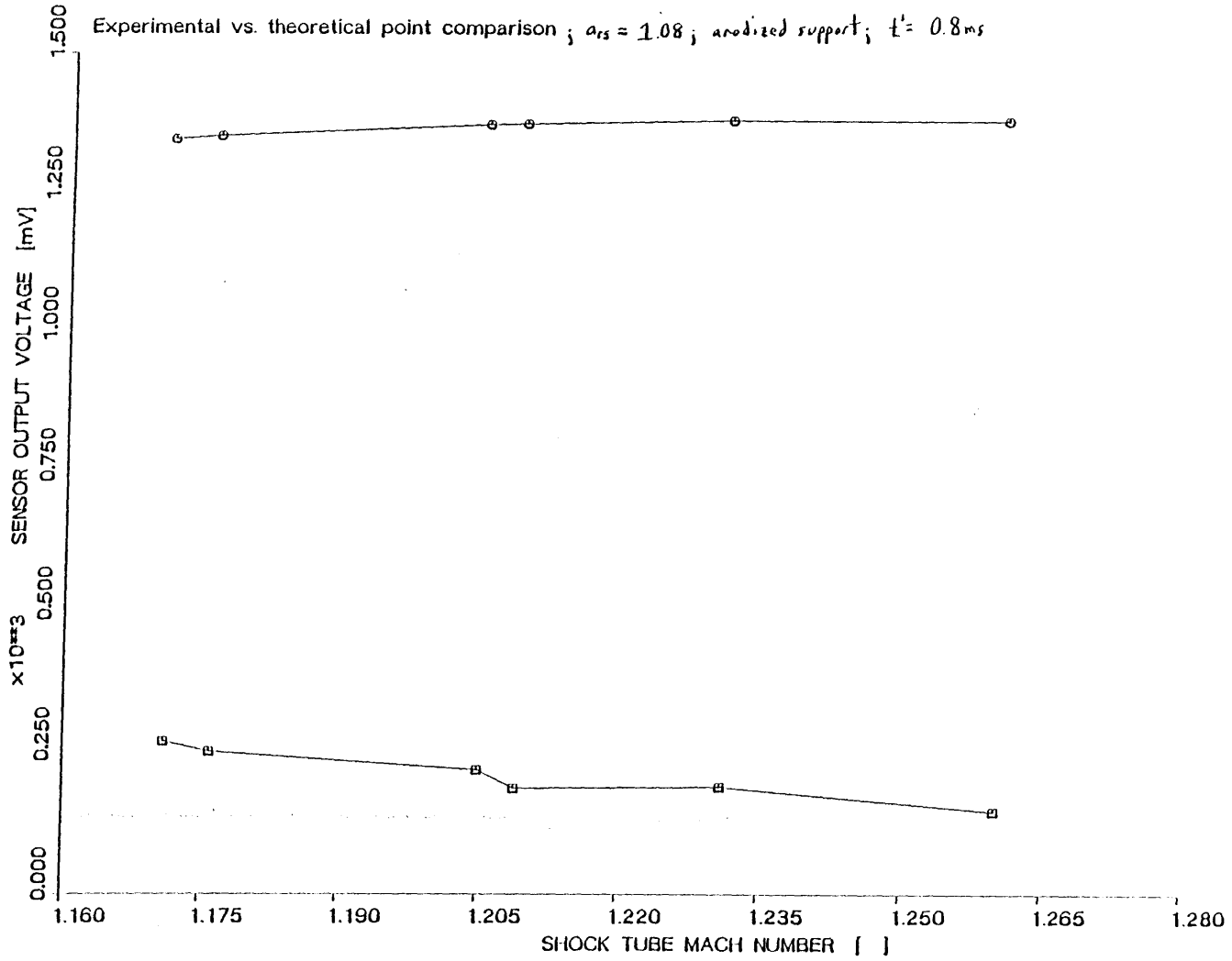

FIGURE 6.17: SENSOR VOLTAGE VS. MACH NUMBER

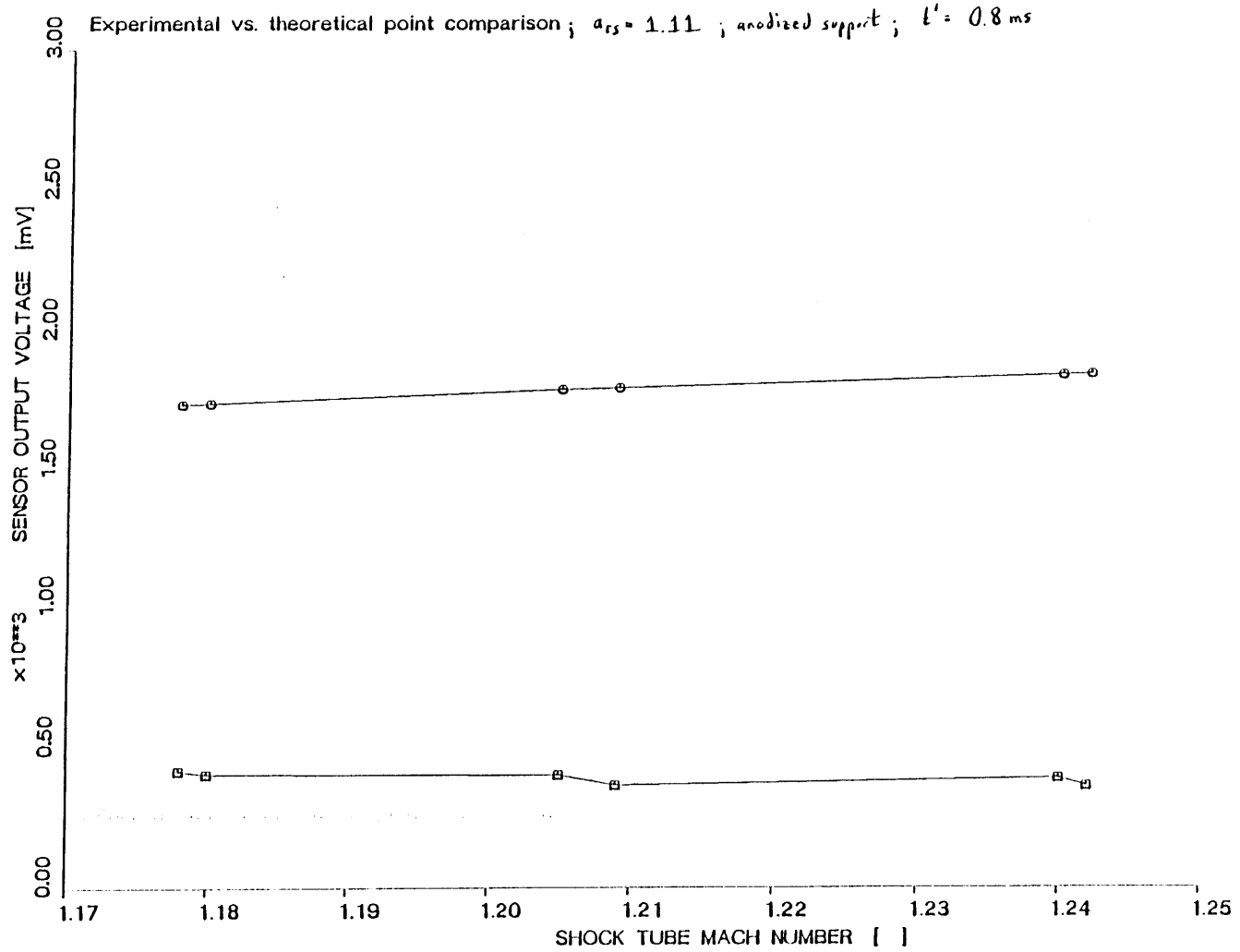

FIGURE 6.18: SENSOR VOLTAGE VS. MACH NUMBER

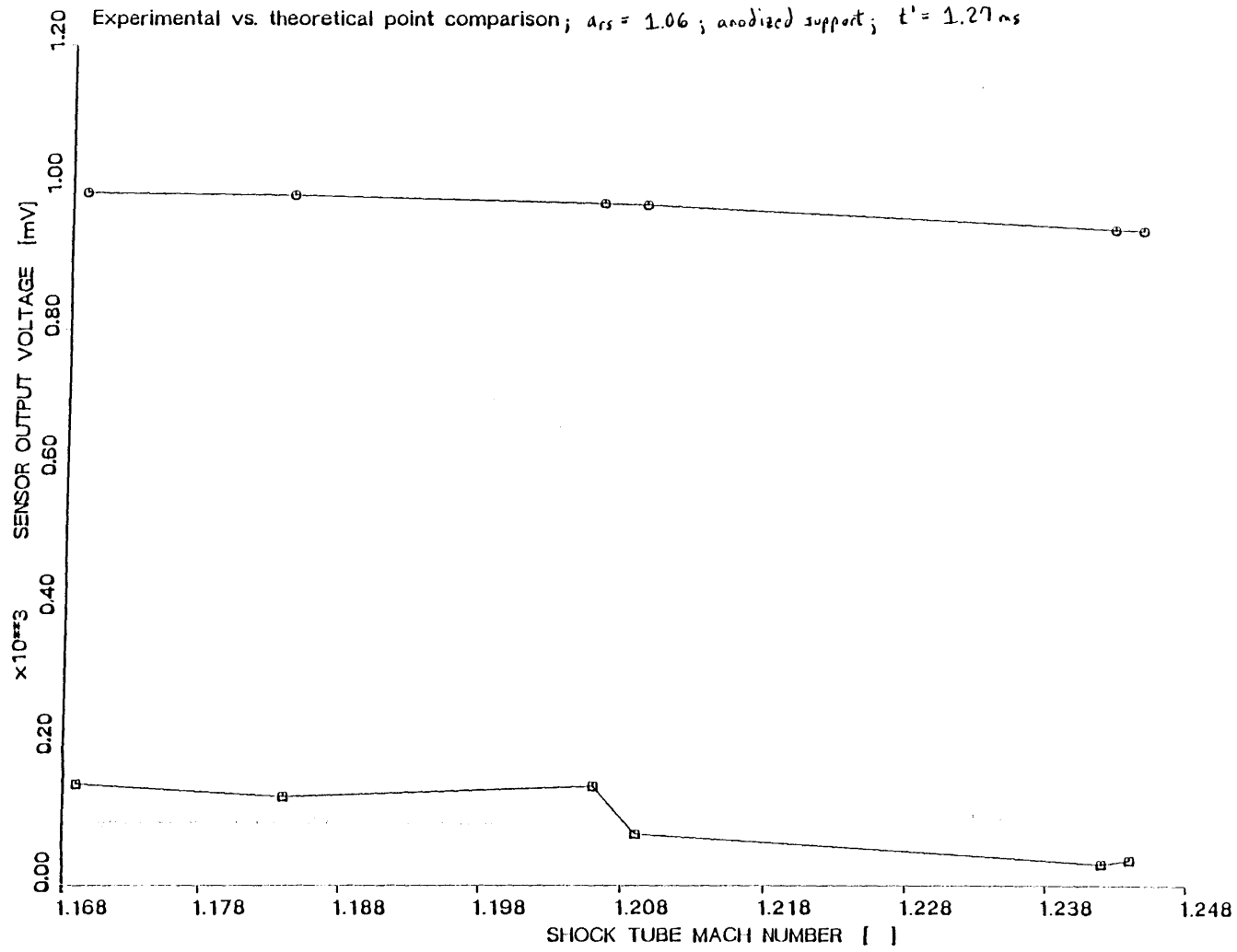

FIGURE 6.19: SENSOR VOLTAGE VS. MACH NUMBER

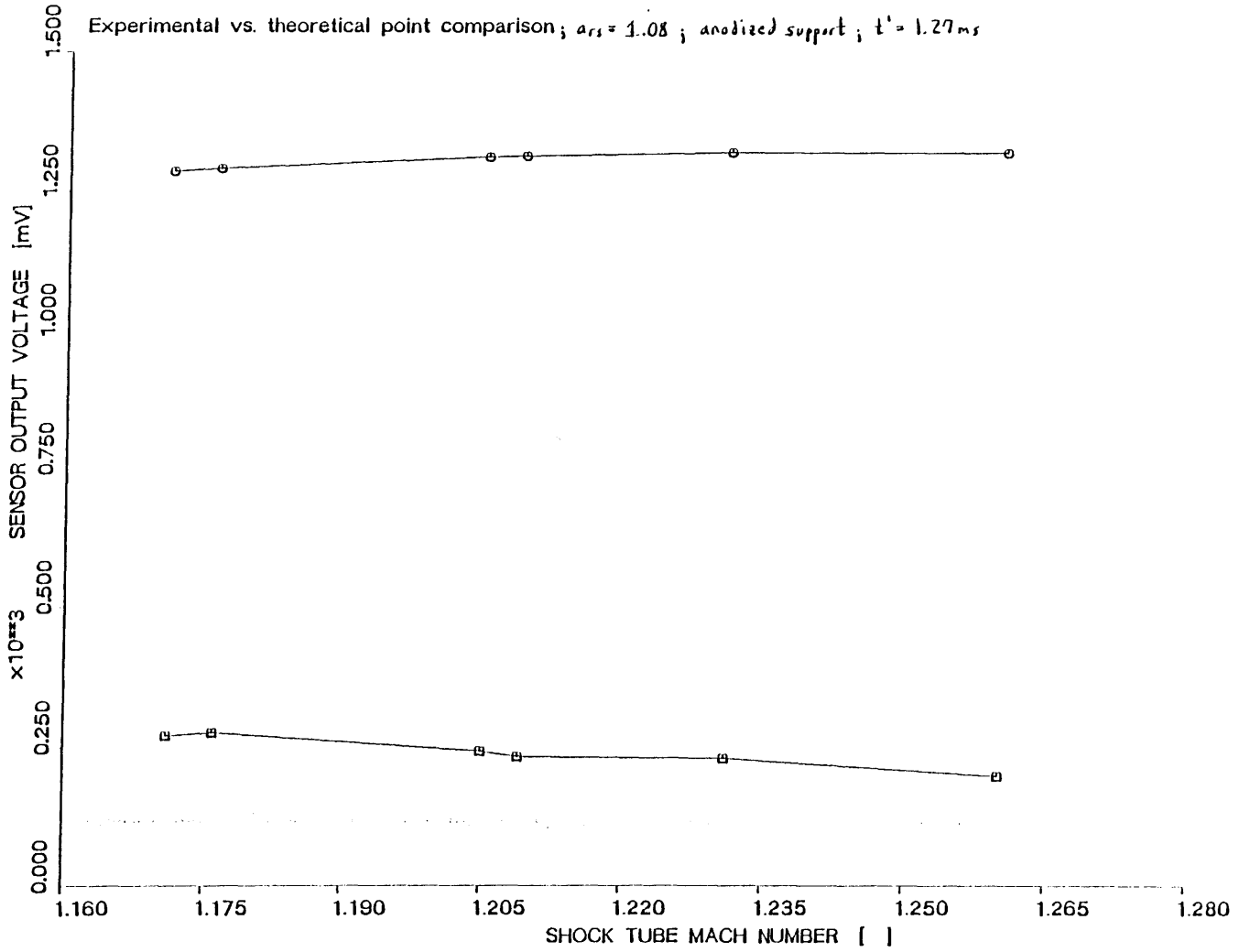

FIGURE 6.20: SENSOR VOLTAGE VS. MACH NUMBER

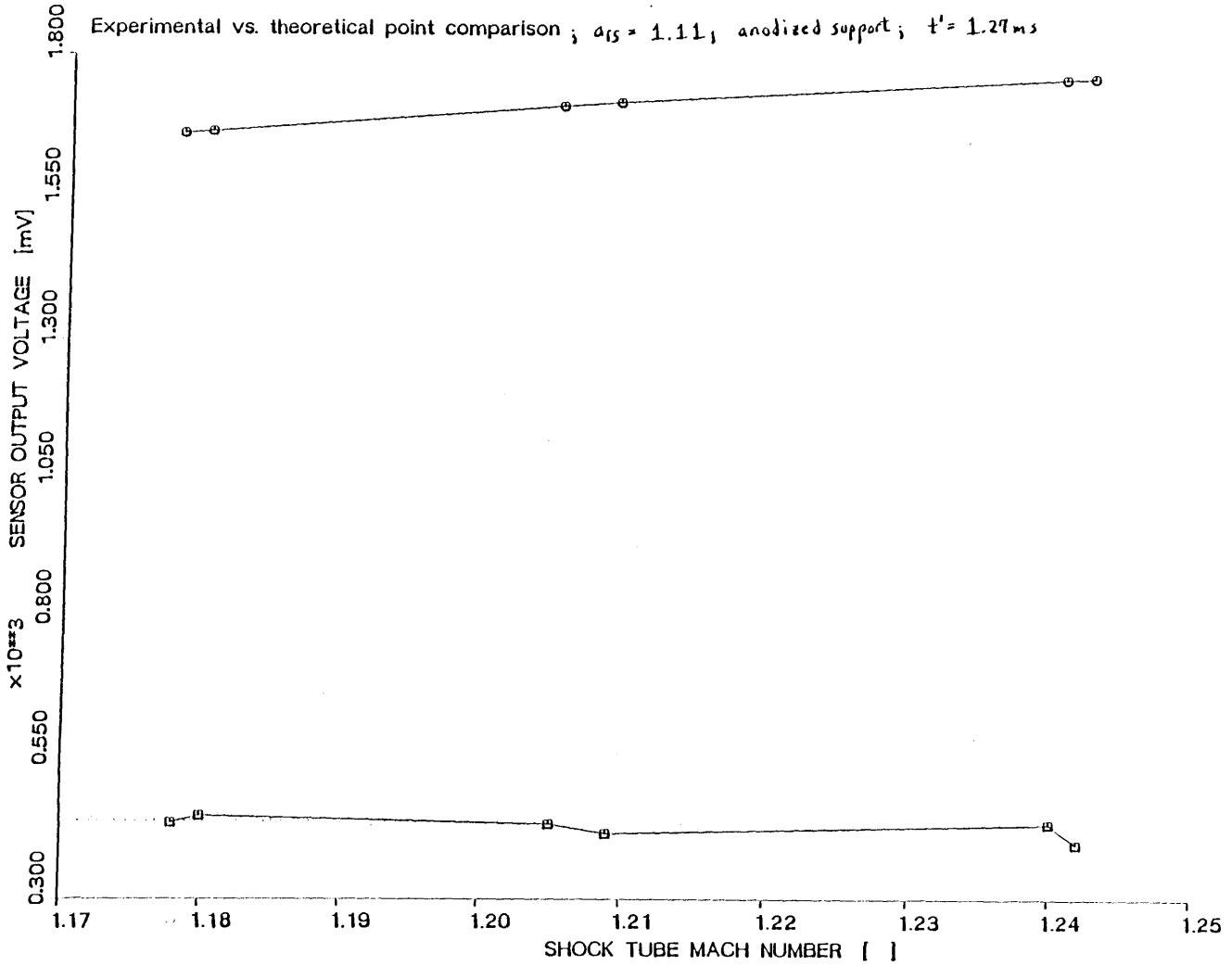

FIGURE 6.21: SENSOR VOLTAGE VS. MACH NUMBER

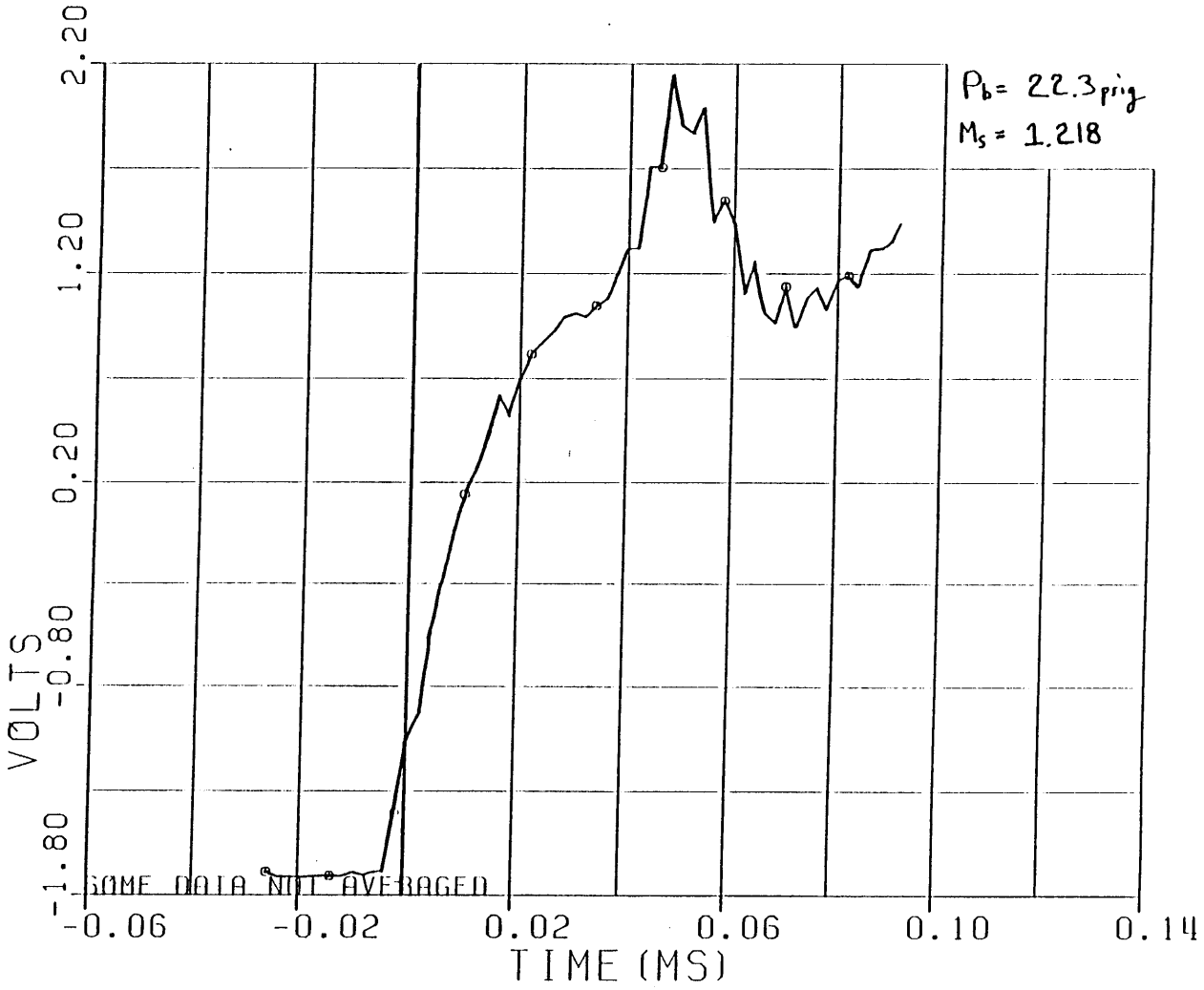

FIGURE 6.22: SHOCK TUBE PRESSURE PULSE: EXPANDED TIME SCALE

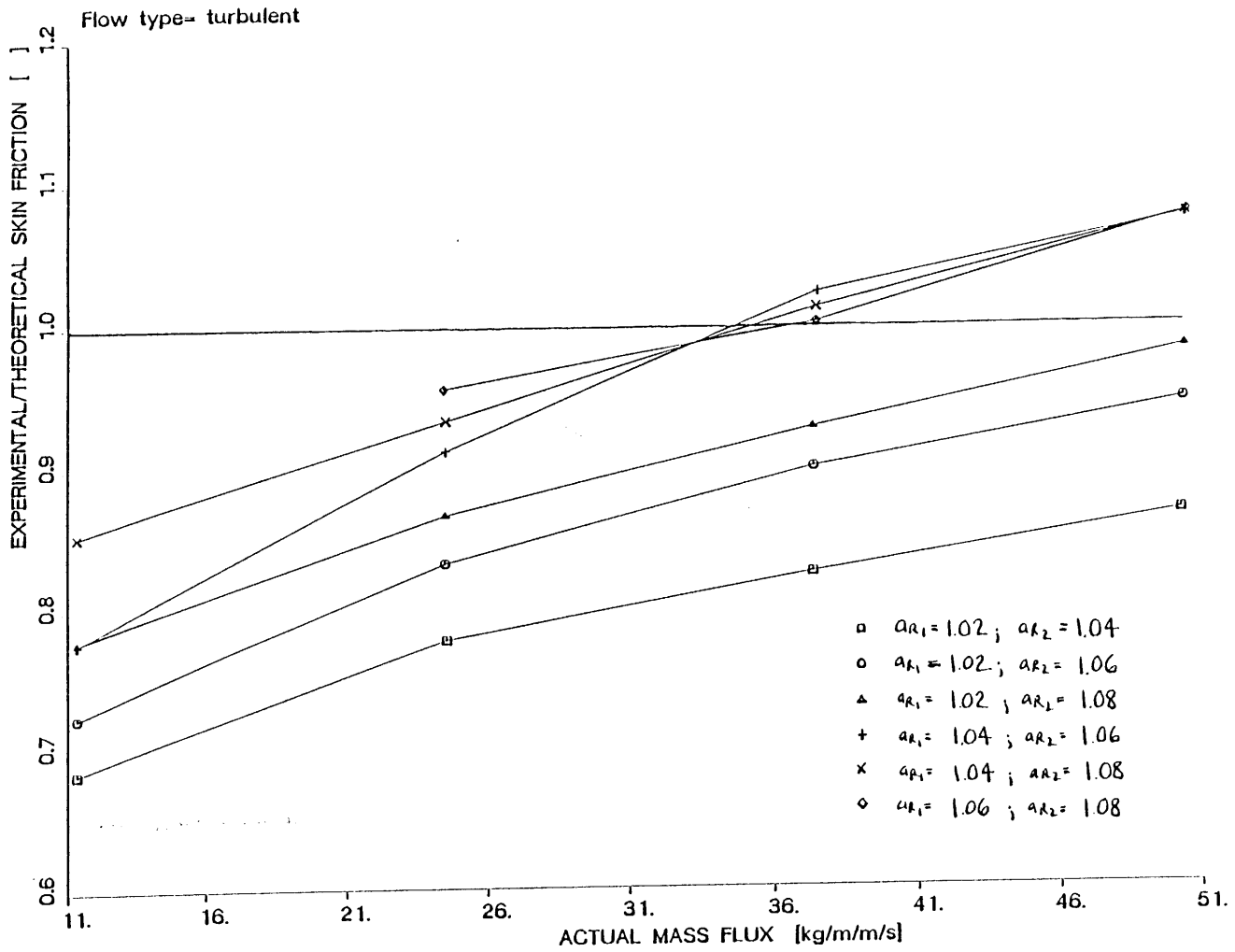

FIGURE 6.23: EXPERIMENTAL/THEORETICAL SKIN FRICTION VS. ACTUAL MASS FLUX

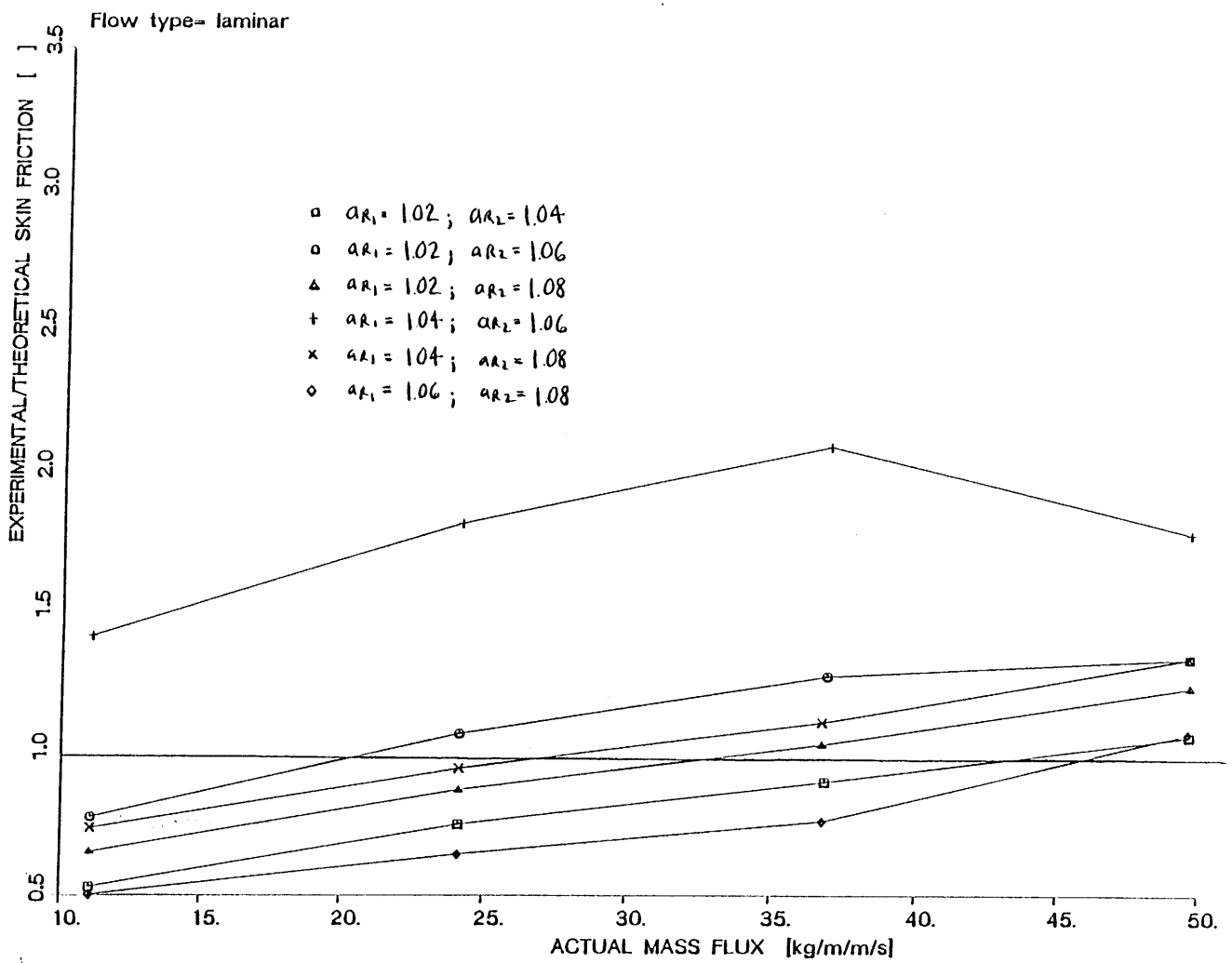

FIGURE 6.24: EXPERIMENTAL/THEORETICAL SKIN FRICTION VS. ACTUAL MASS FLUX

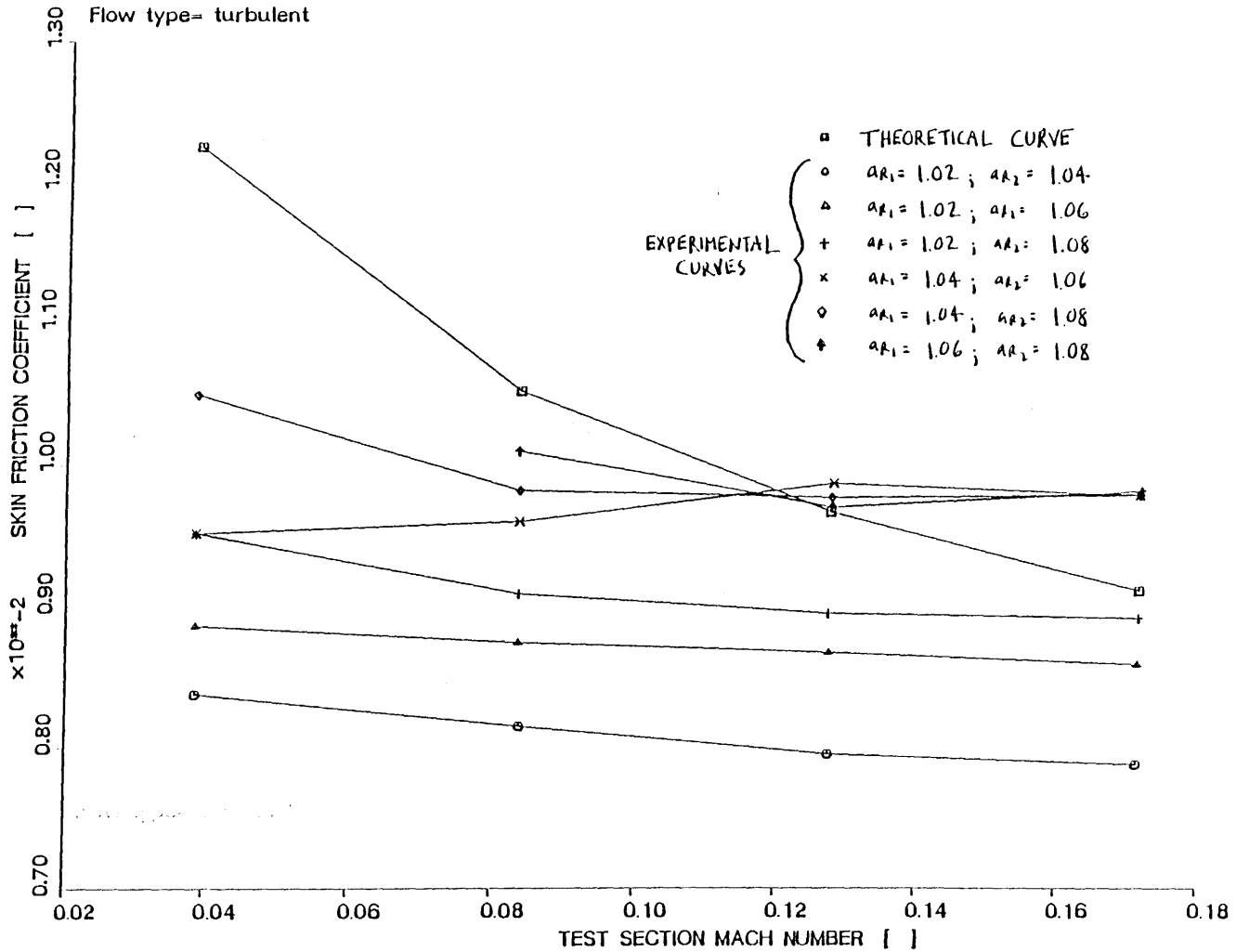

FIGURE 6.25: SKIN FRICTION COEFFICIENT VS. MACH NUMBER

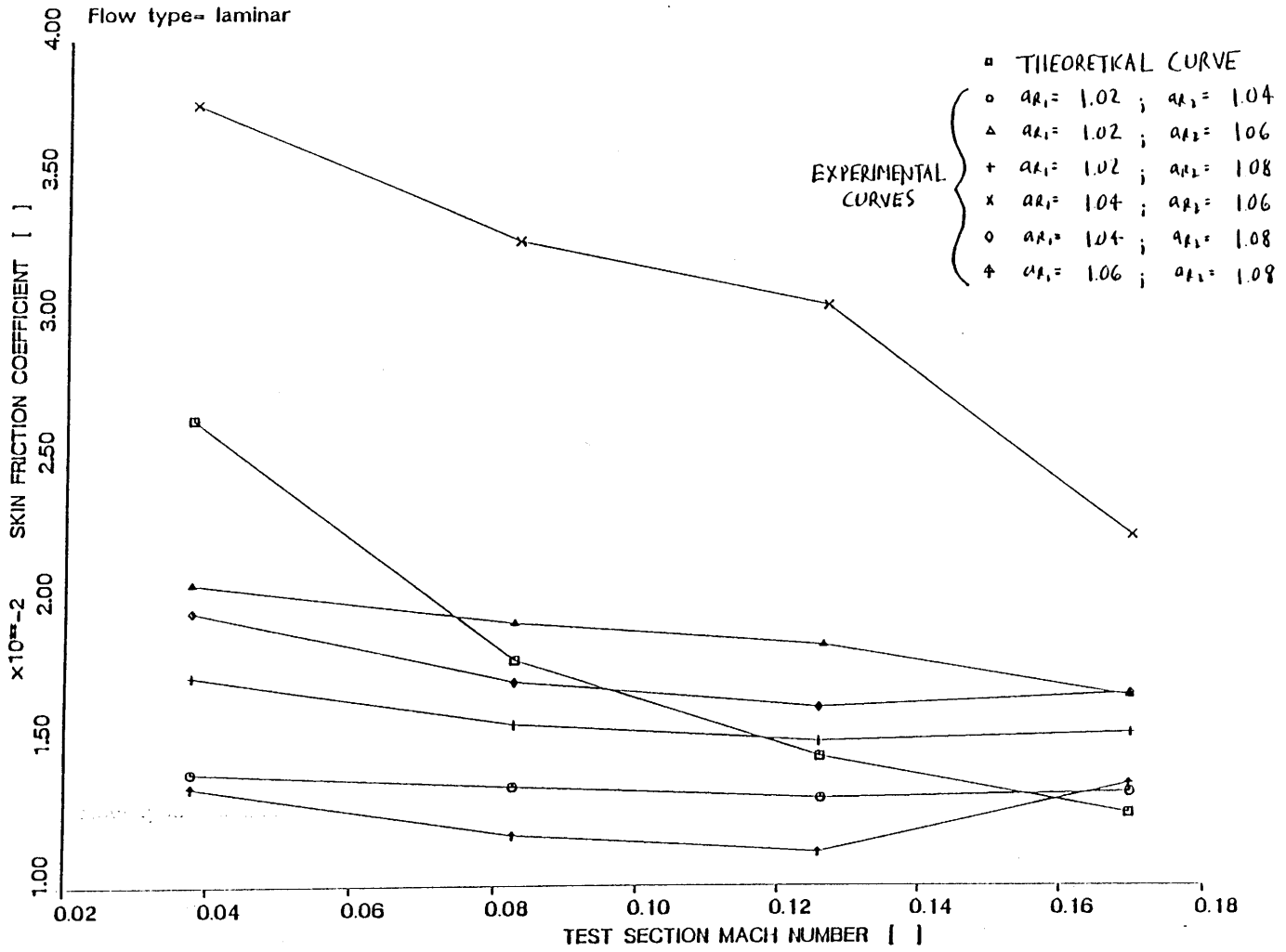

FIGURE 6.26: SKIN FRICTION COEFFICIENT VS. MACH NUMBER

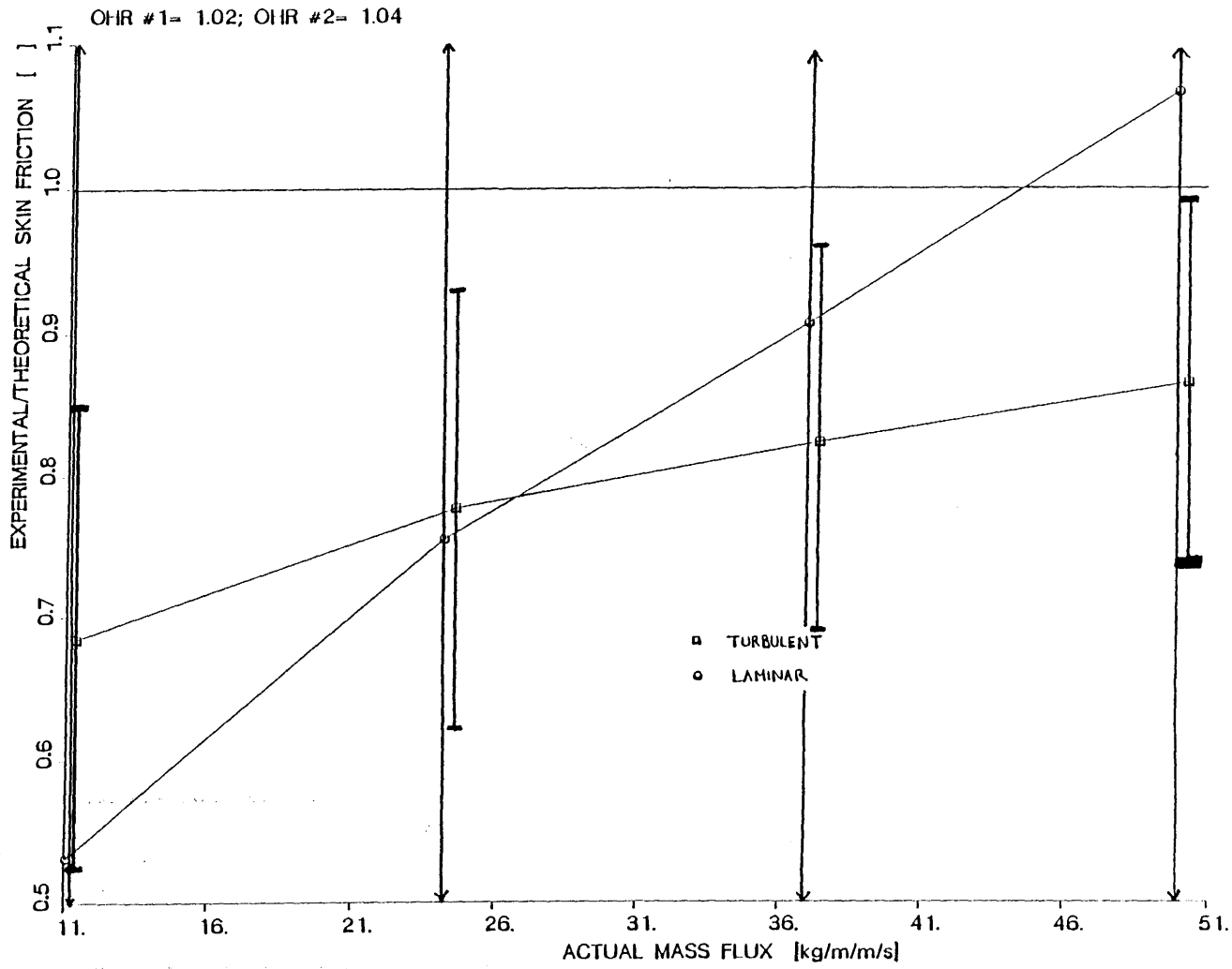

FIGURE 6.27: EXPERIMENTAL/THEORETICAL SKIN FRICTION VS. ACTUAL MASS FLUX

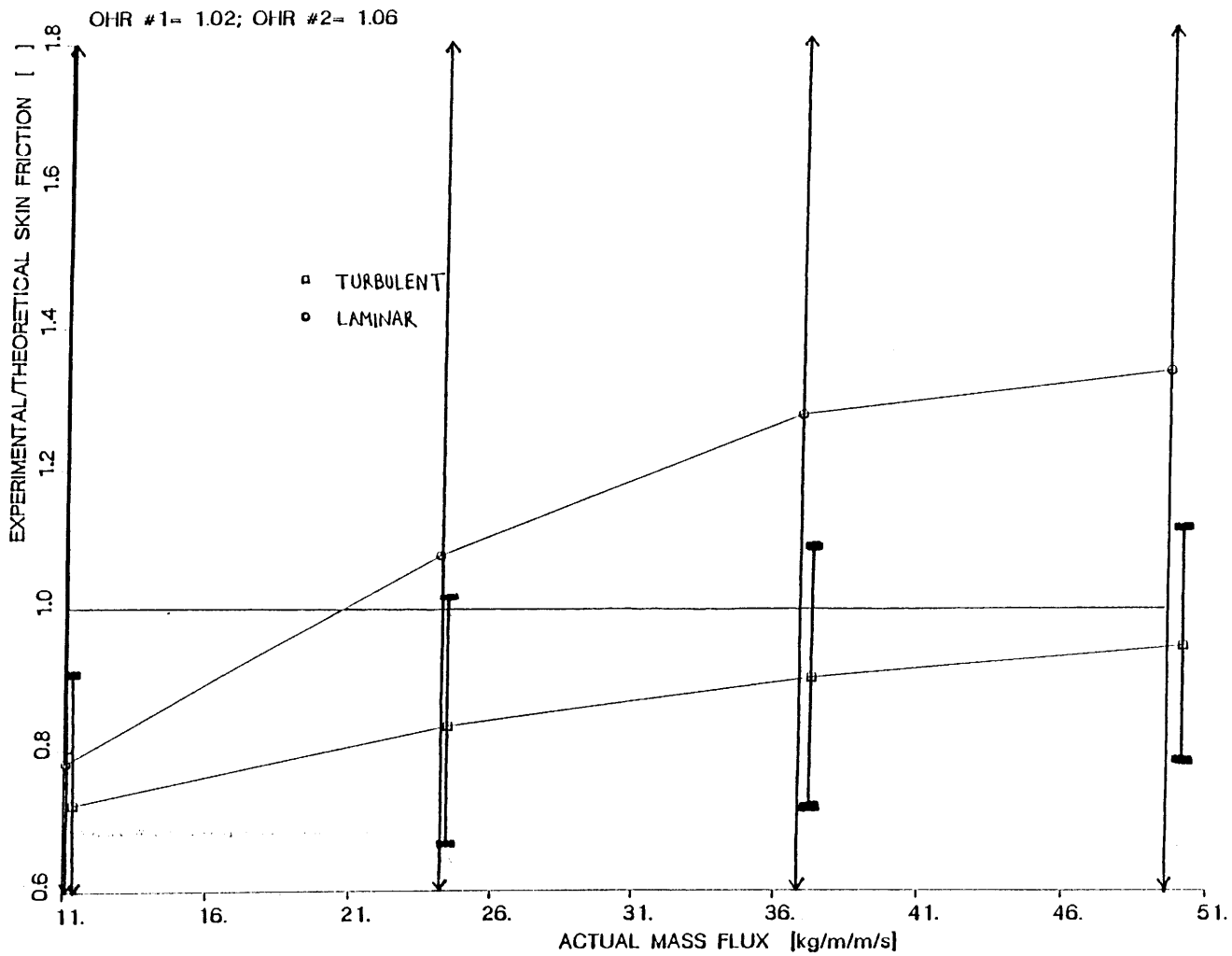

FIGURE 6.28: EXPERIMENTAL/THEORETICAL SKIN FRICTION VS. ACTUAL MASS FLUX

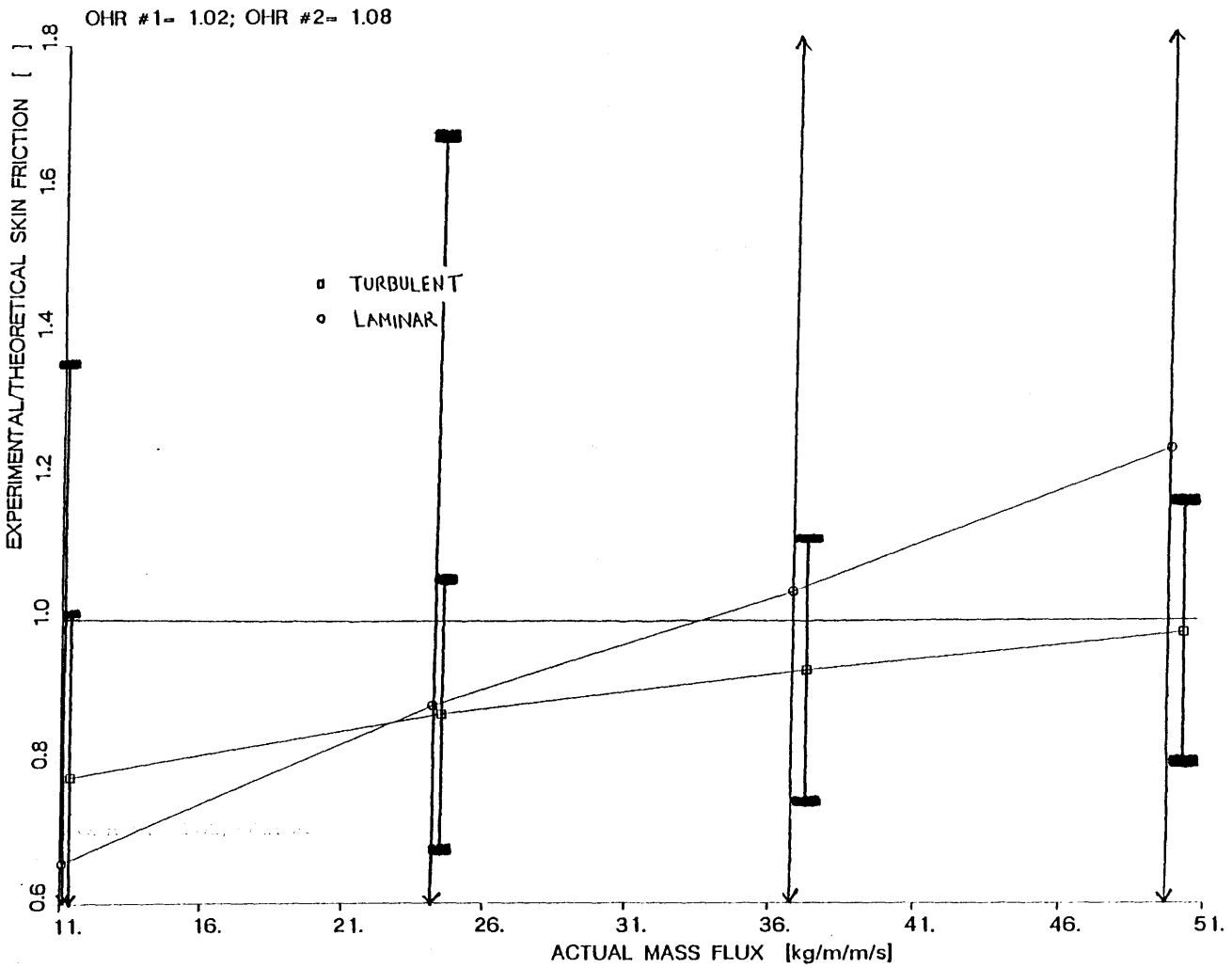

FIGURE 6.29: EXPERIMENTAL/THEORETICAL SKIN FRICTION VS. ACTUAL MASS FLUX

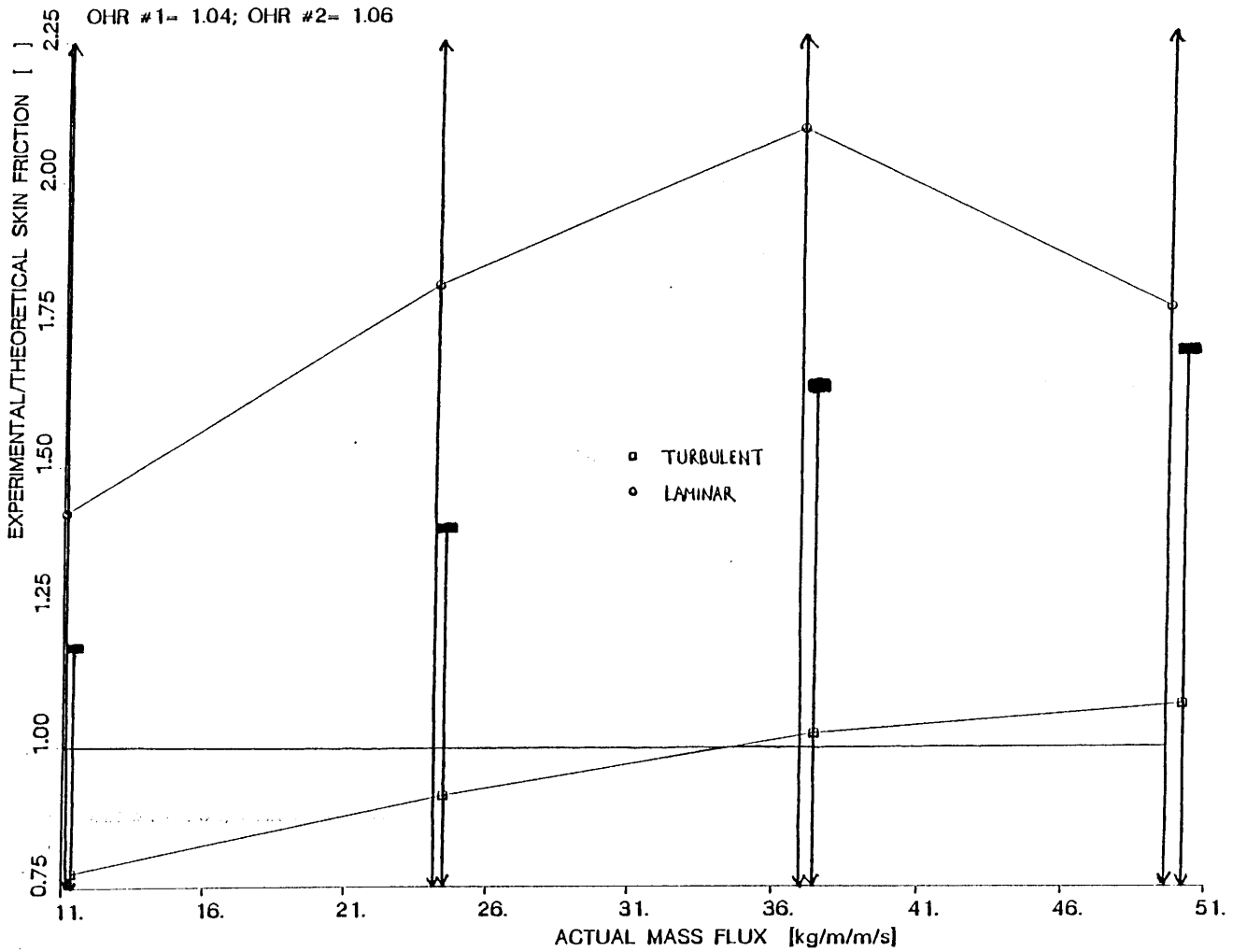

FIGURE 6.30: EXPERIMENTAL / THEORETICAL SKIN FRICTION VS. ACTUAL MASS FLUX

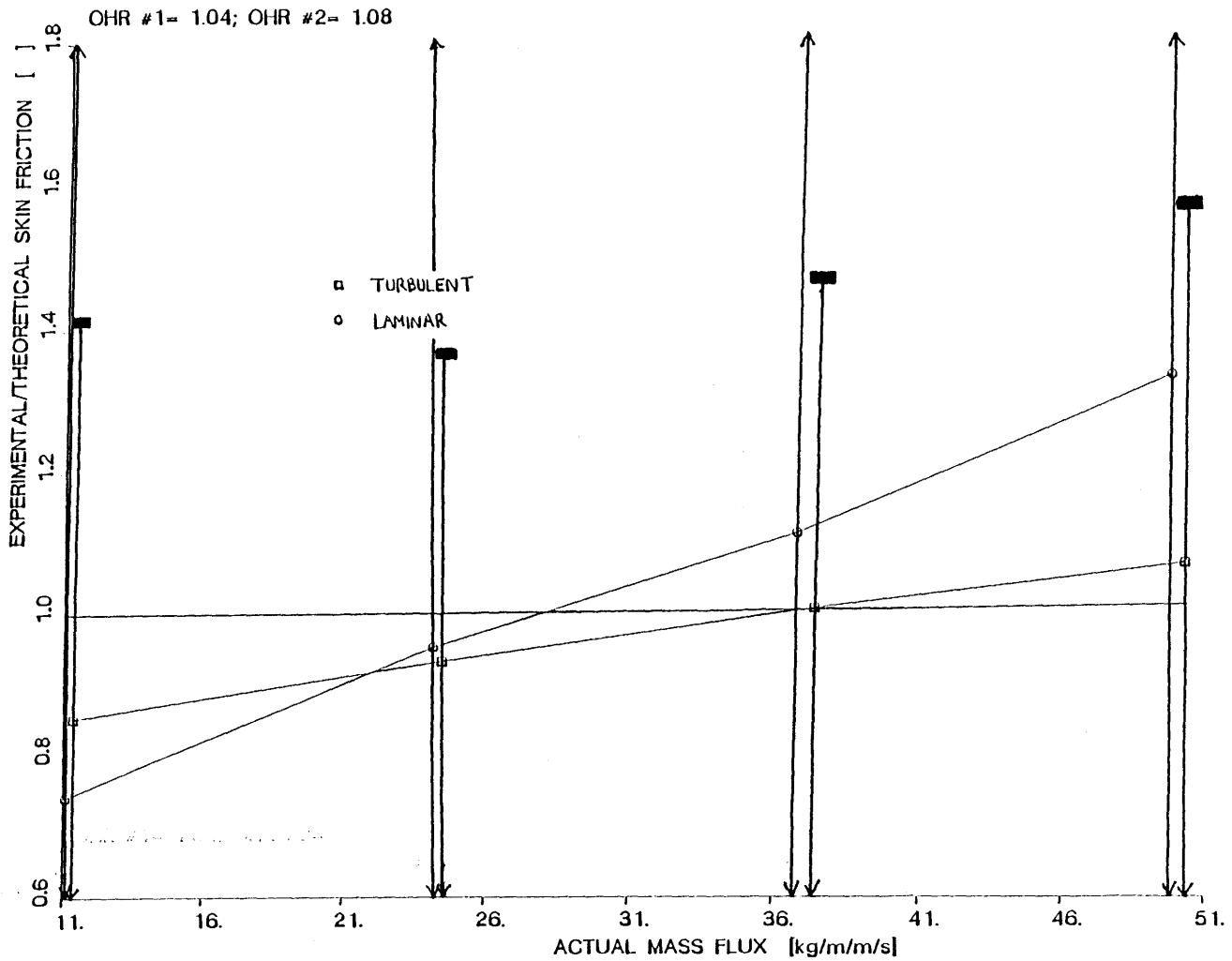

FIGURE 6.31: EXPERIMENTAL/THEORETICAL SKIN FRICTION VS. ACTUAL MASS FLUX

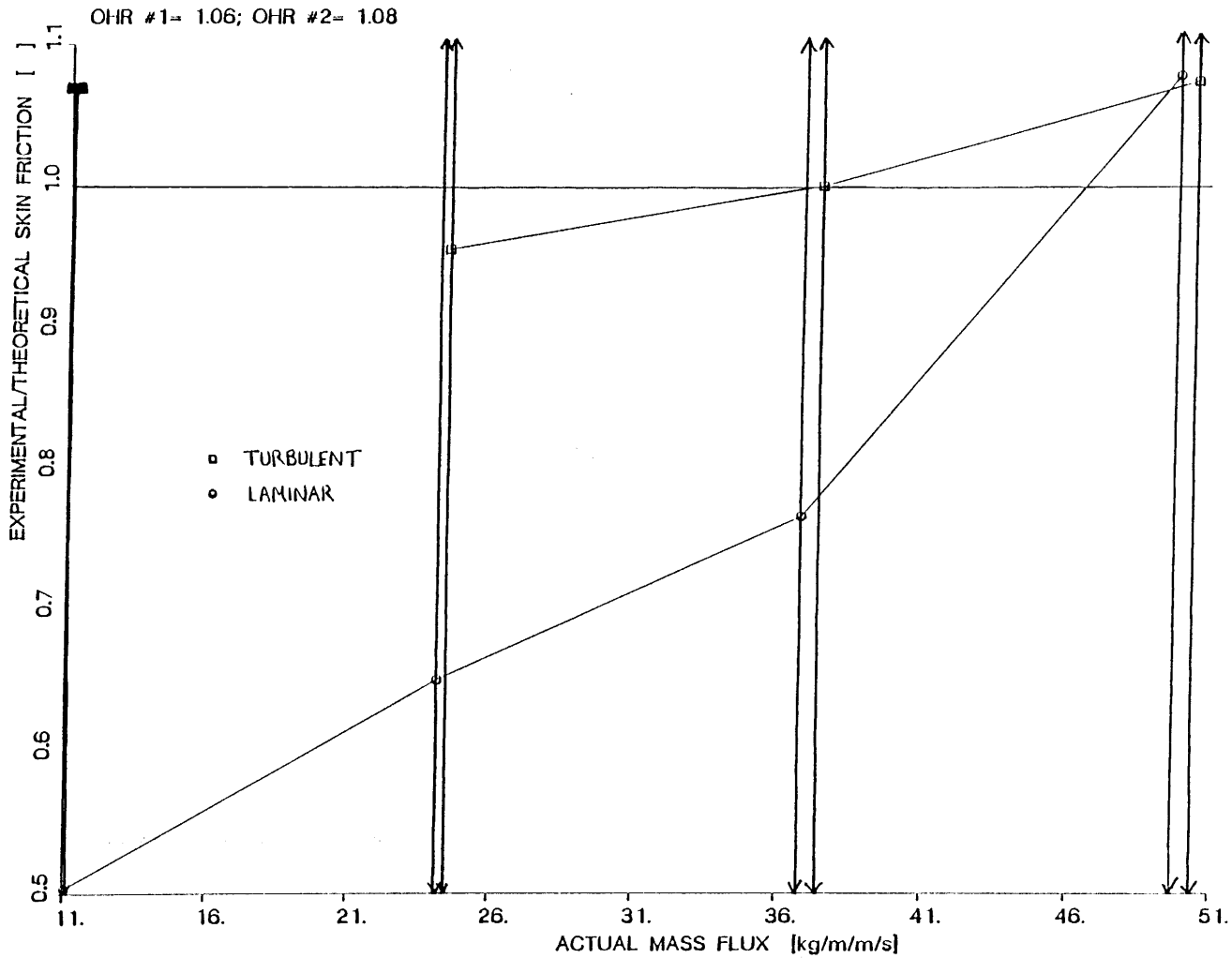

FIGURE 6.32: EXPERIMENTAL/THEORETICAL SKIN FRICTION VS. MASS FLUX

APPENDIX A

THERMAL TRANSPARENCY OF THE THIN FILM

It may be shown in a straight-forward manner that the thin-film's non-uniform temperature profile may be ignored. Therefore, models may be employed that neglect the actual heat conduction within and through the thin-film, treating the surface at the thin-film location as a constant-temperature boundary condition. Consider a region composed of a thin-film resistor with thickness t (region 1) and an insulating substrate of thickness B - t (region 2). Therefore, the problem to be solved is:

$$\frac{\partial^2 T_1}{\partial x^2} = -A \; ; \qquad 0 \le x \le t \tag{A.1}$$

$$\frac{\partial^2 T_2}{\partial x^2} = 0 \; ; \qquad t \le x \le B \tag{A.2}$$

subject to the following boundary conditions:

$$\frac{\partial T_1}{\partial x}(0) = 0 \tag{A.3}$$

$$T_2(B) = 0 \tag{A.4}$$

$$T_1(t) = T_2(t) \tag{A.5}$$

$$k_1 \frac{\partial T_1}{\partial x}(t) = k_2 \frac{\partial T_1}{\partial x}(t) \tag{A.6}$$

where A is the steady heat conducted within the thin-film gauge and can be written as follows:

$$A = \frac{i^2 R}{W L t k_1} \tag{A.7}$$

where i is the current through the sensor, R is the operating resistance of the sensor, W and L are the width and length, respectively, of the thin-film gauge, k_1 is the thermal conductivity of the thin-film, and t is the thickness of the thin-film. In addition, the hot resistance of the gauge can be written:

$$R = \frac{\rho L}{W t}\left[1 + \alpha(T_g - T_0)\right] \tag{A.8}$$

Finally, it seen that the the average temperature over the gauge must be equal to the temperature T_g, or:

$$T_g = \frac{1}{t}\int_0^t T_1(x)\,dx \tag{A.9}$$

Since the value of A is nominally constant, (A.1) and (A.2) can be integrated favorably:

$$T_1(x) = -\frac{1}{2}Ax^2 + ax + b \tag{A.10}$$

$$T_2(x) = cx + d \tag{A.11}$$

where the parameters a, b, c, and d are arbitrary constants of integration. Applying (A.3) to (A.10), (A.4) to (A.11), (A.6) to (A.10) and (A.11), and (A.5) to (A.10) and (A.11), the values for a, b, c, and d can be shown to be:

$$a = 0 \tag{A.12}$$

$$b = \frac{At}{2}\left[t + 2\delta \frac{k_1}{k_2}\right] \tag{A.13}$$

$$c = -At\frac{k_1}{k_2} \tag{A.14}$$

$$d = ABt\frac{k_1}{k_2} \tag{A.15}$$

The ambient temperature T_0 is now added back into the solutions obtained for T_1 and T_2, since T_0 was originally subtracted from the original problem. With this in mind, (A.12)-(A.15) may be combined with (A.10) and (A.11) to obtain the temperature profiles with x for the thin-film region and the substrate region:

$$T_1(x) = T_0 + \frac{A}{2}\left[\, t(t + 2\delta \frac{k_1}{k_2}) - x^2 \right] \tag{A.16}$$

$$T_2(x) = T_0 + At\frac{k_1}{k_2}\left[B - x\right] \tag{A.17}$$

Note the parabolic temperature profile within the thin-film gauge, as expected. Now the gauge temperature can be solved for in terms of the heat produced in the thin-film, by combining (A.16) with (A.9):

$$T_g = \frac{1}{t}\int_0^t \left[T_0 + \frac{A}{2}\left[t(t + 2\delta \frac{k_1}{k_2}) - x^2\right]\right] dx \tag{A.18}$$

$$T_g = T_0 + \frac{1}{3}At\left[t + 3\delta \frac{k_1}{k_2}\right] \tag{A.19}$$

Recalling the definition of the resistive overheat ratio:

$$a_r = \frac{R_{hot}}{R_{cold}} = 1 + \alpha(T_g - T_0) \qquad (A.20)$$

the equations (A.20) and (A.19) can be combined to give:

$$A = \frac{k_2 (a_r - 1)}{k_1 \alpha \delta t} \qquad (A.21)$$

The values of the heat conduction to the substrate for this model and a simplistic model can now be compared. The heat flux to the substrate can be written in general:

$$q_{cond} = -k_2 \frac{\partial T_2}{\partial x}(t) \qquad (A.22)$$

Applying (A.22) to (A.17) and utilizing (A.21), the following may be obtained for the conduction:

$$(q_{cond})_{\text{thin-film modelled}} = \frac{3 (a_r - 1) k_1}{\alpha \left[t + 3\delta \frac{k_1}{k_2} \right]} \qquad (A.23)$$

For a simplistic model, the conduction is easily shown to be:

$$(q_{cond})_{\text{thin-film ignored}} = \frac{k_2 (a_r - 1)}{\alpha \delta} \qquad (A.24)$$

Therefore, the relative effect of the thin-film can be seen by forming the ratio of (A.23) to (A.24). Calling this ratio Q:

$$Q = \frac{1}{1 + \frac{1}{3} \frac{k_2}{k_1} \frac{t}{\delta}} \qquad (A.25)$$

Therefore, more conduction is seen than is actually modelled with a simplistic assumption. However, the value is very slight due to the fact that $k_2 << k_1$, since kapton is an insulator and nickel is a

reasonable conductor, and that $t << \delta$, which is just a manifestation of the design used in thin-films. In particular, reasonable values for the parameters can be taken as follows:

$$k_1 = 5 \ \frac{W}{mK}$$

$$k_2 = 0.202 \ \frac{W}{mK}$$

$$t = 1000 \text{ Å}$$

$$\delta = 25 \ \mu m$$

With these values, the value for Q is 0.999946, effectively equal to one for the accuracy given here. Hence, for a steady calculation, the non-uniform temperature profile within the thin-film may be ignored.

APPENDIX B

OPTIMIZATION OF ELEMENT RESISTANCE FOR A GIVEN TOTAL GAUGE RESISTANCE

For the use of thin-film gauges, in order to assure the maximum sensitivity of the gauge, the sum of the lead and tag resistances should be kept to a minimum. One way to do this, previously mentioned, is to plate the leads and tags with a low resistance material, such as copper or gold. However, it is desirable to design the gauge so that the sensor resistance to total resistance ratio is maximized in case of a plate material failure. In reality, this analysis was performed before the plate process was discovered to be applicable. For a gauge with total resistance of 15 Ω, the element resistance can be written as follows:

$$(R_e)_0 = \frac{(R_T)_0}{1 + \lambda + \omega} \tag{B.1}$$

where $(R_e)_0$ is the cold resistance of the elements, $(R_T)_0$ is the cold resistance of the sensor (15 Ω), λ is the tag resistance divided by the element resistance (cold or hot), and ω is the lead resistance divided by the element resistance. Therefore, it is desired to maximize (B.1) with the choice of λ and ω. From a power balance of the sensor, it can be demonstrated that ω can be found as a function of λ. In particular, for a case with a_r= 1.5, a thin-film thickness of 1500 Å, α= 0.3 %/K, δ= 20 μm, ε= 50δ, i_{max}= 0.35 amp, δ_s= 25 μm, and k_s= 0.202 W/mK, the power balance equation gives the following expression for ω:

$$\omega(\lambda) = C\lambda - \sqrt{C\lambda\left[(C - 2)\lambda - 2\right]} - (1 + \lambda) \tag{B.2}$$

where C is defined as follows, for a given number of gauge elements n:

$$C \approx \frac{91.5}{n - 1} \tag{B.3}$$

From (B.1), it is seen that to maximize $(R_e)_0$ is the same as minimizing $(1 + \lambda + \omega)$. However, from (B.2), the expression $(1 + \lambda + \omega)$ can be written as a function of λ only:

$$1 + \lambda + \omega = f(\lambda) = C\lambda - \sqrt{C\lambda\left[(C - 2)\lambda - 2\right]} \tag{B.4}$$

To find the optimum λ, the quantity $\frac{\partial f}{\partial \lambda}$ must be calculated and set equal to zero. The λ then obtained by solving the equation represents the optimum choice for greatest sensitivity. The presence of an optimum is expected, for the power limitation imposes that the total surface area of the elements, tags, and leads be a constant. This allows for a gauge design with too high of resistance for the tags and too low a resistance for the leads, or vice versa, depending on the length to width ratios of the tags and leads. There should be an intermediate geometry that minimizes the sum of the tag and lead resistances, which is the same as maximizing the element resistance from (B.1). In fact, the optimum λ for this scenario is readily calculated from (B.4):

$$\frac{\partial f}{\partial \lambda} = 0 \Rightarrow \quad C - \frac{C\left[(C - 2)\lambda - 2\right] + C(C - 2)\lambda}{2\sqrt{C\lambda\left[(C - 2)\lambda - 2\right]}} = 0 \tag{B.5}$$

Manipulating (B.5):

$$\sqrt{C\lambda[(C-2)\lambda-2]} = \lambda(C-2) - 1 \qquad \text{(B.6)}$$

Squaring each side and cancelling terms:

$$(C-2)\lambda^2 - 2\lambda - \frac{1}{2} = 0 \qquad \text{(B.7)}$$

This is readily solved via the quadratic equation to give the optimum value of tag to element resistance:

$$\lambda_{opt} = \frac{1+\sqrt{0.5\,C}}{C-2} \qquad \text{(B.8)}$$

Combining (B.8) with (B.3), the optimum tag to element resistance ratio can be determined as a function of the number of gauge elements:

$$\lambda_{opt}(n) = \frac{(n-1) + 6.764\sqrt{n-1}}{93.5 - 2n} \qquad \text{(B.9)}$$

This expression is presented in Figure B.1. It is an increasing function of the number of gauge elements, as expected. By combining (B.9) and (B.2), the optimum lead to element resistance ratio (ω) can be obtained as a function of n. This is not presented here due to algebraic complexity. However, it can be noted that, for a given n, the value of ω is, within rounding errors, equal to the value of λ! Although at first glance this is a startling result, it makes perfect sense when the mathematics of the problem are focused on rather than the physics. Having obtained the expression for the optimum ω ($\omega_{opt} = \lambda_{opt}$), the optimum element resistance can be plotted as a function of the number of gauge elements. This presented in Figure B.2. Notice the severe penalty for increasing the value of n, although it is not as severe as an inverse square law. The values of the resistance of the tags and

leads are changed by changing the length to width ratio, consistent with the constraint that the total surface area remain constant. This optimization procedure may be used to design the most sensitive non-plated gauge possible for a given fixed total resistance.

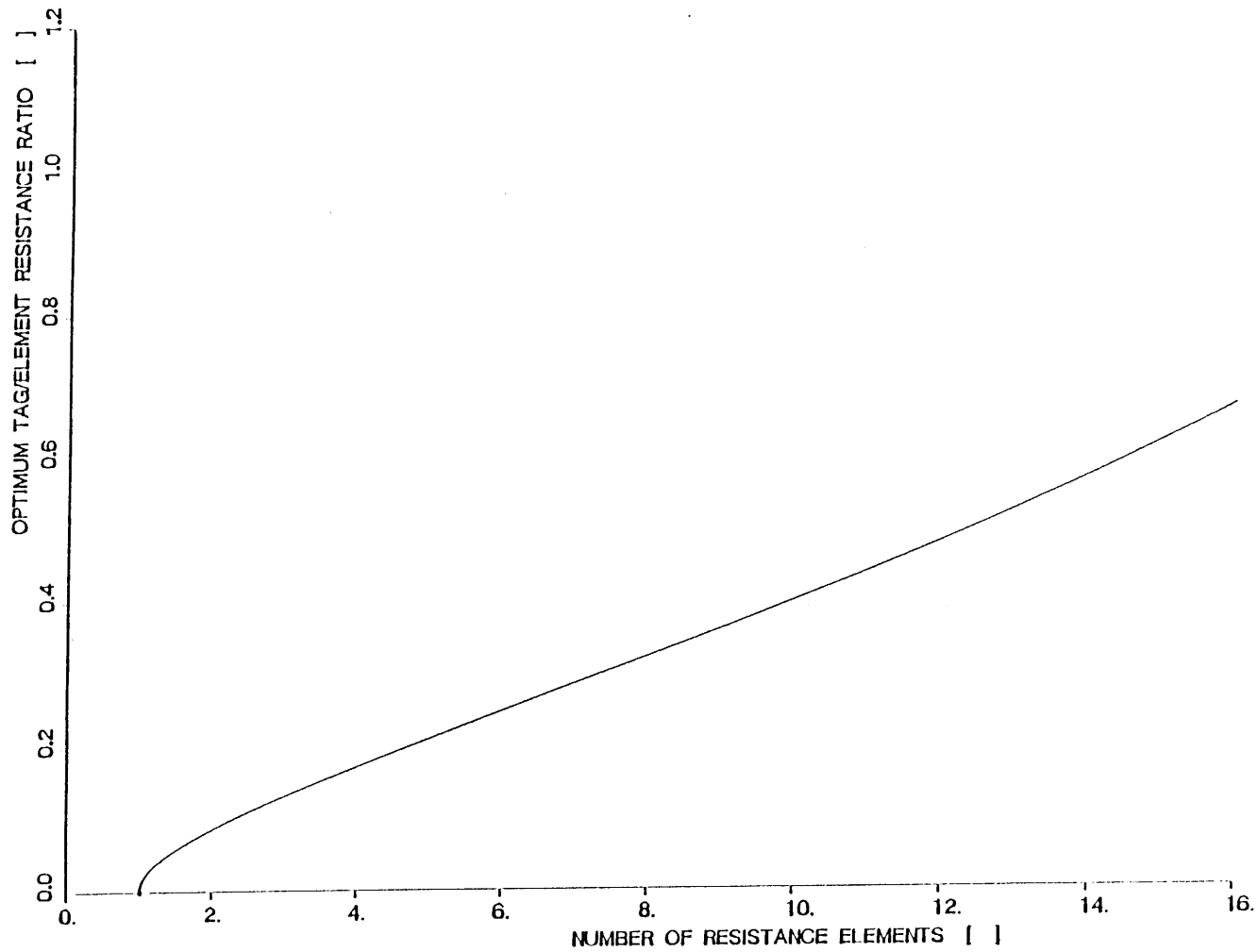

FIGURE B.1: OPTIMUM TAG/ELEMENT RESISTANCE RATIO VS. NUMBER OF ELEMENTS

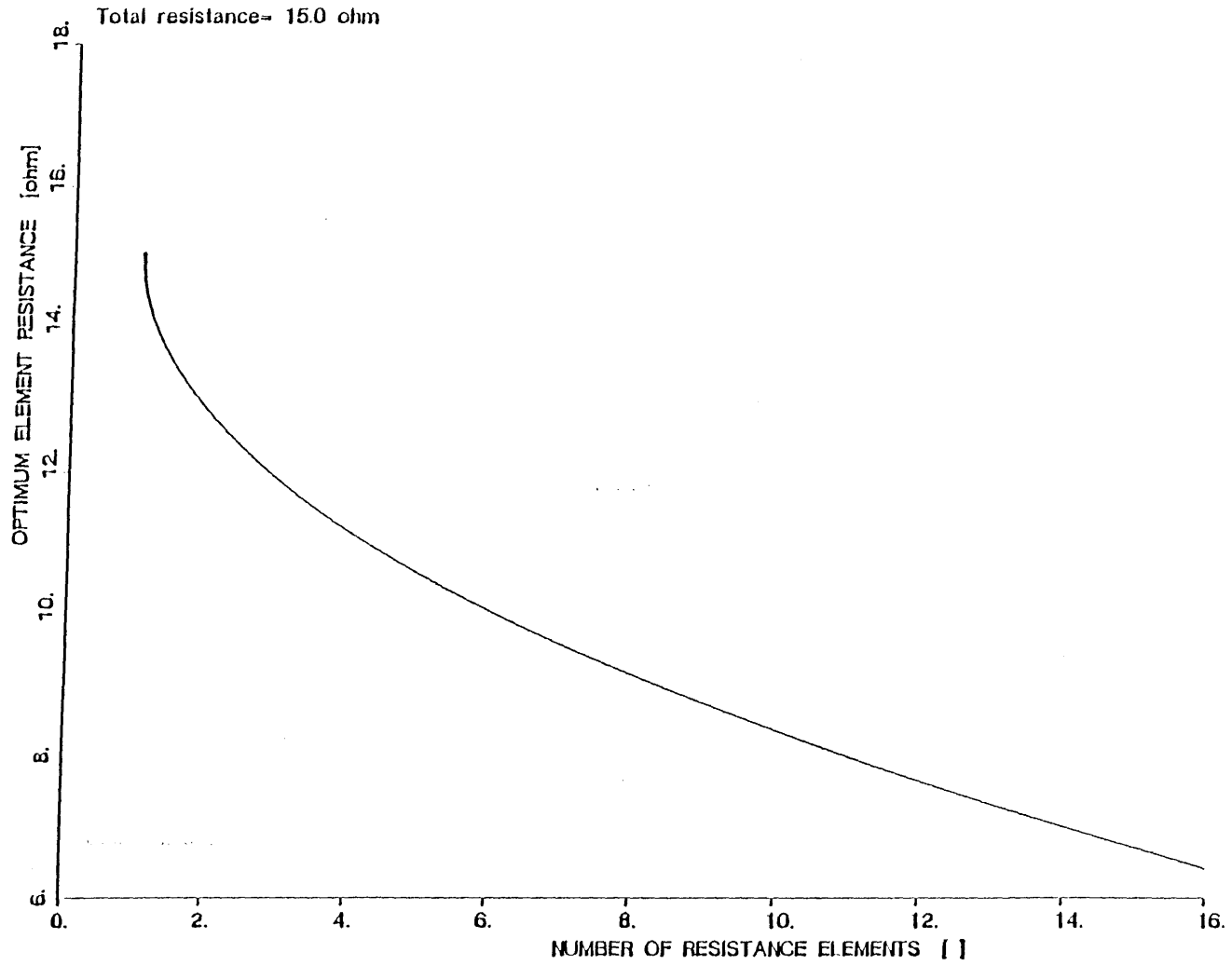

FIGURE B.2: OPTIMUM ELEMENT RESISTANCE VS. NUMBER OF ELEMENTS

APPENDIX C

TABLES OF FLOW PARAMETERS FOR THE TEN SHOCK TUBE RUNS

Presented below are the material, break pressure P_4 [psig], break pressure ratio P_4/P_1 [ ], shock pressure ratio P_2/P_1 [ ], shock Mach number M_1 [ ], predicted shock speed $(c_s)_{pred}$ [m/s], distance of shock travel Δx [m], shock transit time τ [ms], measured shock speed $(c_s)_{meas}$ [m/s], and the percentage error in the shock speeds [ ] for each trial of the ten shock tube data runs performed. Tables C.1-C.10 correspond to Runs #1-#10, respectively.

COMPARISON OF PREDICTED AND MEASURED SHOCK SPEEDS FOR THE SHOCK TUBE

Data Group # 1 : Shock tube familiarity testing

Trial # / Material	P_4 (psig)	P_4/P_1	P_2/P_1	M_1	$C_{s_{pred.}}$ (m/s)	Δx (m)	t (ms)	$C_{s_{meas.}}$ (m/s)	% error
1 Heavy Duty Al Foil	20.4	2.39	1.52	1.20	410	0.727	1.79	406	-0.98%
2 Heavy Duty Al Foil	24.2	2.65	1.60	1.23	421	0.727	1.74	418	-0.71%
3 Heavy Duty Al Foil	22.9	2.56	1.57	1.22	417	0.727	1.74	418	+0.24%
4 Heavy Duty Al Foil	22.2	2.51	1.56	1.22	416	0.727	1.76	413	-0.72%
5						0.727			
6						0.727			

COMPARISON OF PREDICTED AND MEASURED SHOCK SPEEDS FOR THE SHOCK TUBE

Data Group # 2 : Shock tube familiarity testing

Trial # / Material	P_4 (psig)	P_4/P_1	P_2/P_1	M_1	$C_{s_{pred.}}$ (m/s)	Δx (m)	τ (ms)	$C_{s_{meas.}}$ (m/s)	% error
1 Heavy Duty Al Foil	21.9	2.49	1.55	1.21	414	0.727	1.766	412	+0.48%
2 Heavy Duty Al Foil	22.9	2.56	1.57	1.22	417	0.727	1.758	414	+0.72%
3 Heavy Duty Al Foil	26.1	2.76	1.63	1.24	424	0.727	1.760	413	+2.59%
4 Heavy Duty Al Foil	22.9	2.56	1.57	1.22	417	0.727	1.758	414	+0.72%
5 Heavy Duty Al Foil	22.4	2.52	1.56	1.22	417	0.727	1.752	415	+0.48%
6						0.727			

COMPARISON OF PREDICTED AND MEASURED SHOCK SPEEDS FOR THE SHOCK TUBE

Data Group # 3 : Range of Diaphragm Materials

Trial # / Material	P_4 (psig)	P_4/P_1	P_2/P_1	M_1	$C_{s_{pred.}}$ (m/s)	Δx (m)	τ (ms)	$C_{s_{meas.}}$ (m/s)	% error
1 Thin Al Foil	7.1	1.48	1.21	1.09	373	0.727	1.932	376	-0.80%
2 Thin Al Foil	6.3	1.43	1.19	1.08	369	0.727	1.890	385	-4.34%
3 Heavy Duty Al Foil	23.2	2.58	1.58	1.22	417	0.727	1.728	421	-0.96%
4 Heavy Duty Al Foil	22.1	2.50	1.56	1.21	414	0.727	1.738	418	-0.97%
5 118 "V" 58F Cellophane	35.1	3.39	1.79	1.30	445	0.727	1.646	442	+0.67%
6 118 "V" 58F Cellophane	27.8	2.89	1.66	1.25	427	0.727	1.686	431	-0.94%

COMPARISON OF PREDICTED AND MEASURED SHOCK SPEEDS FOR THE SHOCK TUBE

Data Group # 4 : Single gauge; heat transfer data recorded

Trial # / Material	P_4 (psig)	P_4/P_1	P_2/P_1	M_1	$C_{s_{pred.}}$ (m/s)	Δx (m)	τ (ms)	$C_{s_{meas.}}$ (m/s)	% error
1 "K" HB-20 Cellophane	20.9	2.42	1.53	1.21	414	0.727	1.748	416	-0.48%
2 "K" HB-20 Cellophane	20.3	2.38	1.52	1.20	410	0.727	1.756	414	-0.98%
3 Heavy Duty Al Foil	22.1	2.50	1.56	1.22	417	0.727	1.734	419	-0.48%
4 Heavy Duty Al Foil	21.7	2.48	1.55	1.21	414	0.727	1.742	417	-0.72%
5 118 "V" 58F Cellophane	29.6	3.01	1.69	1.26	431	0.727	1.676	434	-0.70%
6 118 "V" 58F Cellophane	31.7	3.16	1.73	1.28	438	0.727	1.650	441	-0.68%

COMPARISON OF PREDICTED AND MEASURED SHOCK SPEEDS FOR THE SHOCK TUBE

Data Group # 5 : Single gauge; heat transfer data recorded

Trial # / Material	P_4 (psig)	P_4/P_1	P_2/P_1	M_1	$C_{s_{pred.}}$ (m/s)	Δx (m)	τ (ms)	$C_{s_{meas.}}$ (m/s)	% error
1 HST Cellophane	18.0	2.22	1.473	1.19	407	0.727	1.764	412	-1.23%
2 HST Cellophane	20.3	2.38	1.521	1.20	410	0.727	1.760	413	-0.73%
3 Heavy Duty Al Foil	22.2	2.51	1.560	1.22	417	0.727	1.758	414	+0.72%
4 Heavy Duty Al Foil	22.3	2.52	1.563	1.22	417	0.727	1.744	417	0%
5 118"V" 58F Cellophane	31.5	3.14	1.729	1.27	434	0.727	1.666	436	-0.46%
6 118"V"58F Cellophane	35.1	3.39	1.790	1.30	445	0.727	1.666	436	-2.02%

COMPARISON OF PREDICTED AND MEASURED SHOCK SPEEDS FOR THE SHOCK TUBE

Data Group # 6 : Double-layer gauge ; heater passive

Trial # / Material	P_4 (psig)	P_4/P_1	P_2/P_1	M_1	$C_{s_{pred.}}$ (m/s)	Δx (m)	τ (ms)	$C_{s_{meas.}}$ (m/s)	% error
1 "K" HB-20 Cellophane	14.0	1.95	1.385	1.15	394	0.727	1.822	399	-1.3%
2 "K" HB-20 Cellophane	18.9	2.29	1.494	1.19	408	0.727	1.790	406	+0.5%
3 Heavy Duty Al Foil	21.9	2.49	1.554	1.21	415	0.727	1.746	416	-0.2%
4 Heavy Duty Al Foil	22.0	2.50	1.557	1.22	416	0.727	1.730	420	-1.0%
5 123 "V" 58P Cellophane	32.1	3.18	1.739	1.28	437	0.727	1.670	435	+0.5%
6 123 "V" 58P Cellophane	32.1	3.18	1.739	1.28	437	0.727	1.656	439	-0.5%

COMPARISON OF PREDICTED AND MEASURED SHOCK SPEEDS FOR THE SHOCK TUBE

Data Group # 7 : Double-layer gauge ; heater active

Trial # / Material	P_1 (psig)	P_4/P_1	P_2/P_1	M_1	$C_{s_{pred.}}$ (m/s)	Δx (m)	τ (ms)	$C_{s_{meas.}}$ (m/s)	% error
1 "K" HB-20 Cellophane	17.8	2.21	1.470	1.18	405	0.727	1.788	407	-0.5%
2 "K" HB-20 Cellophane	20.2	2.37	1.520	1.20	411	0.727	1.752	415	-1.0%
3 Heavy Duty Al Foil	23.4	2.59	1.583	1.23	419	0.727	1.727	421	-0.5%
4 Heavy Duty Al Foil	22.1	2.50	1.558	1.22	416	0.727	1.736	419	-0.7%
5 123 "V" 58P Cellophane	32.7	3.22	1.750	1.28	438	0.727	1.660	438	0%
6 123 "V" 58P Cellophane	30.6	3.08	1.714	1.27	434	0.727	1.660	438	-0.9%

COMPARISON OF PREDICTED AND MEASURED SHOCK SPEEDS FOR THE SHOCK TUBE

$p_{RS} = 1.06$ Data Group # 8 : Double-layer gauge ; heater active; anodized support

Trial # / Material	$P_1 - P_0$ (psig)	P_4/P_1	P_2/P_1	M_1	$C_{s\,pred.}$ (m/s)	Δx (m)	t (ms)	$C_{s\,meas.}$ (m/s)	% error
1 "K" HB-20 Cellophane	15.9	2.082	1.429	1.169	400	0.302	0.742	407	-1.8%
2 "K" HB-20 Cellophane	17.7	2.204	1.468	1.184	405	0.302	0.734	411	-1.5%
3 Heavy-duty Al. Foil	21.2	2.442	1.540	1.209	413	0.302	0.728	415	-0.5%
4 Heavy-duty Al. Foil	20.7	2.408	1.530	1.206	412	0.302	0.732	413	-0.2%
5 123 "V" 58P Cellophane	26.0	2.769	1.632	1.242	425	0.302	0.702	430	-1.2%
6 123 "V" 58P Cellophane	26.4	2.796	1.639	1.244	425	0.302	0.701	431	-1.4%

COMPARISON OF PREDICTED AND MEASURED SHOCK SPEEDS FOR THE SHOCK TUBE

$a_{R_S} = 1.08$ Data Group # 9 : Double-layer gauge; heater active; anodized support

Trial # / Material	$P_4 - P_0$ (psig)	P_4/P_1	P_2/P_1	M_1	$C_{S\,pred.}$ (m/s)	Δx (m)	t (ms)	$C_{S\,meas.}$ (m/s)	% error
1 "K" HB-20 Cellophane	16.1	2.095	1.433	1.171	400	0.302	0.740	408	-2.0%
2 "K" HB-20 Cellophane	16.8	2.143	1.448	1.176	402	0.302	0.740	408	-1.5%
3 Heavy-duty Al. Foil	20.5	2.395	1.526	1.205	412	0.302	0.720	420	-1.9%
4 Heavy-duty Al. Foil	21.2	2.442	1.540	1.209	413	0.302	0.720	420	-1.7%
5 123 "V" 58P Cellophane	24.4	2.660	1.602	1.231	421	0.302	0.707	427	-1.4%
6 123 "V" 58P Cellophane	28.9	2.966	1.685	1.260	431	0.302	0.690	438	-1.6%

COMPARISON OF PREDICTED AND MEASURED SHOCK SPEEDS FOR THE SHOCK TUBE

$a_{R_S} = 1.11$ Data Group # 10 : Double-layer gauge; heater active; anodized support

Trial # / Material	$P_4 - P_0$ (psig)	P_4/P_1	P_2/P_1	M_1	$C_{s\,pred.}$ (m/s)	Δx (m)	t (ms)	$C_{s\,meas.}$ (m/s)	% error
1 "K" HB-20 Cellophane	17.3	2.177	1.459	1.180	404	0.302	0.737	410	-1.5%
2 "K" HB-20 Cellophane	17.0	2.156	1.452	1.178	403	0.302	0.740	408	-1.2%
3 Heavy-duty Al. Foil	20.5	2.395	1.526	1.205	412	0.302	0.720	420	-1.9%
4 Heavy-duty Al. Foil	21.2	2.442	1.540	1.209	414	0.302	0.720	420	-1.4%
5 123 "V" 58P Cellophane	26.1	2.776	1.634	1.242	425	0.302	0.700	431	-1.4%
6 123 "V" 58P Cellophane	25.7	2.748	1.626	1.240	424	0.302	0.698	433	-2.1%

APPENDIX D

VOLTAGE TRACES FOR SHOCK TUBE RUNS #6-#10

Presented below are the voltage traces for shock tube Runs #6-#10 in Figures D.1-D.15. Figures D.1-D.3 represent the data points for Run #6. This case is nominally the same as Run #5. As before, the highest Mach number traces (Figure D.3) display a gradual rise in voltage after the passage of the shock. The voltage dip precisely at the moment of shock passage increases with increasing Mach number as well, diminishing the trend of increasing voltage jump across the shock with increasing M_s. The reason for this voltage dip may be a local separation of the boundary layer or an unmodelled heat transfer process. An argument shall be presented for the former explanation subsequently. Comparing the voltage jump for a given Mach number between Run #5 and Run #6, it is seen that the voltage changes are comparable.

Figures D.4-D.6 represent the voltage traces for Run #7, which is identical to Run #6 except that now the heater is being actively controlled to be at the same temperature as the sensor. The reason for this operating condition is explained later during the theoretical modelling of the problem. Compared with Run #6, these voltage dips seem slightly less pronounced. The sensitivity to Mach number seems to have been reduced, as compared with the heater passive runs. Large noise spikes (due to laboratory background electromagnetic radiation) muddle the heat transfer signal throughout all six of the traces in this run. Since all electronic components in the experimental setup were already shielded from background noise, no further action could be taken to minimize stray electromagnetic signals.

Figures D.7-D.9 represent the voltage traces for Run #8. Particularly at this low overheat value, there is a quite large voltage dip at the shock passage point. This voltage dip is more pronounced as the Mach number increases. All plots display a rise in output voltage following the shock passage, contrary to theoretical predictions. Due to the pronounced voltage dip, the voltage change across the shock decreases with increasing Mach number, also in contradiction with theory. In general, it is seen that lower overheat values give less satisfactory predictions for the voltage change across a shock than higher overheat ratios.

Figures D.10-D.12 display the six data trials for Run #9, identical to Run #8 except that the overheat ratio of the sensor is 1.08, not 1.06. Again , we see that voltage dips are present and are more prevalent at larger Mach numbers, but they are much smaller than for Run #8. As before, the trend of voltage change across the shock with Mach number is reversed from what is expected. The voltage increases, for each of the six traces, after the passage of the shock (again, as before). Compared with Run #8, a corresponding Mach number for Run #9 gives a larger voltage jump across the shock, consistent with theory since the overheat ratio is greater.

Finally, Figures D.13-D.16 represent the six voltage traces for Run #10, which is similar to Run #9 and Run #8 except that the overheat ratio is now 1.11. All trends cited above hold here as well: (1) voltage dips are present, much smaller than in Run #8 or #9, and get larger with increasing M_s; (2) voltage increases for each trace after the passage of the shock; (3) voltage change across shock is much higher for a given M_s than for the lower overheat ratio cases; and (4) voltage jump increases with Mach number are not seen, inconsistent with theory. Although in some respects incorrect, the runs #8-#10 seem to form a consistent data group within themselves.

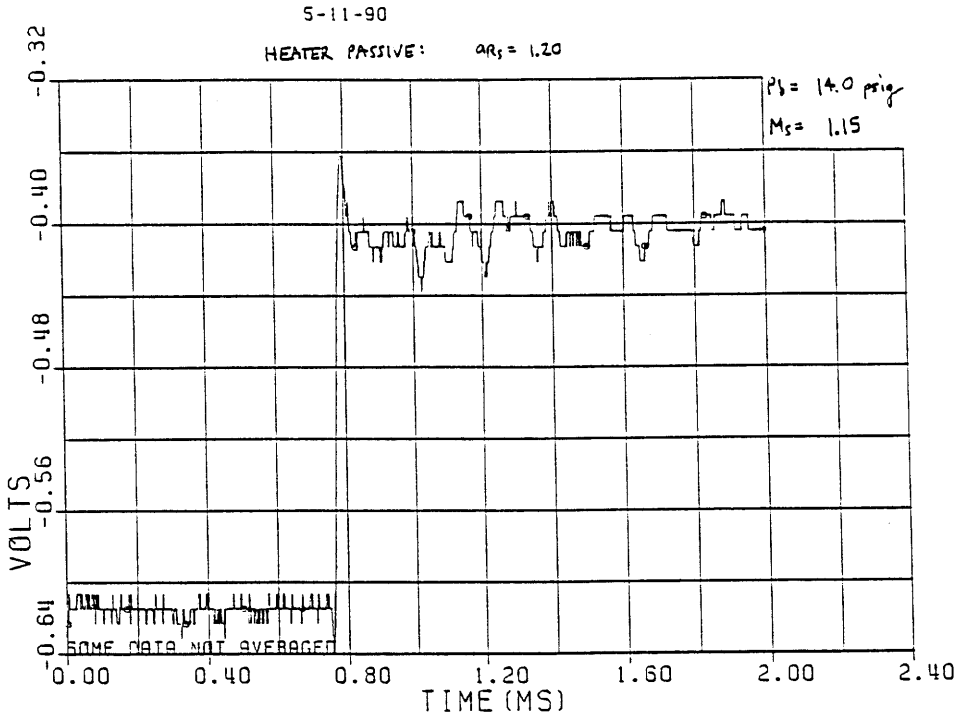

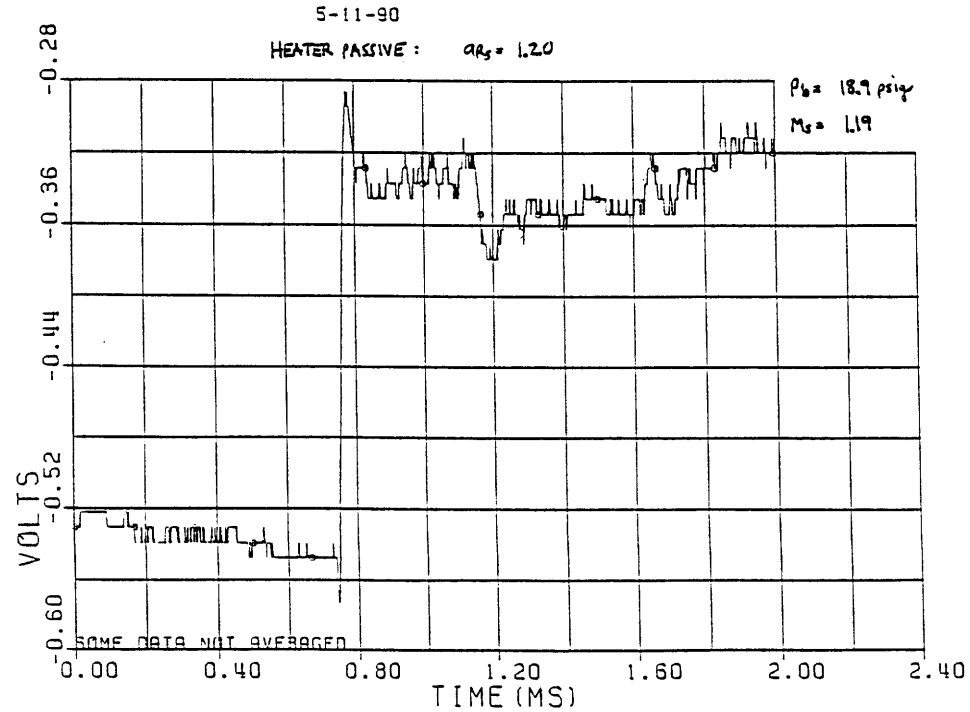

FIGURE D.1: UNSTEADY VOLTAGE TRACE VS. TIME

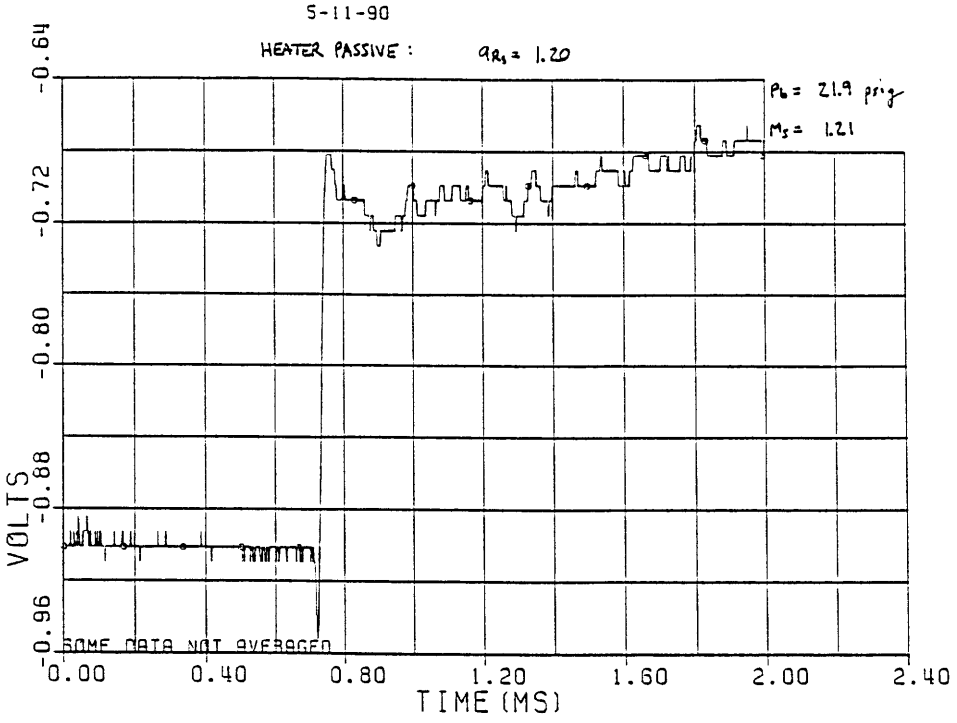

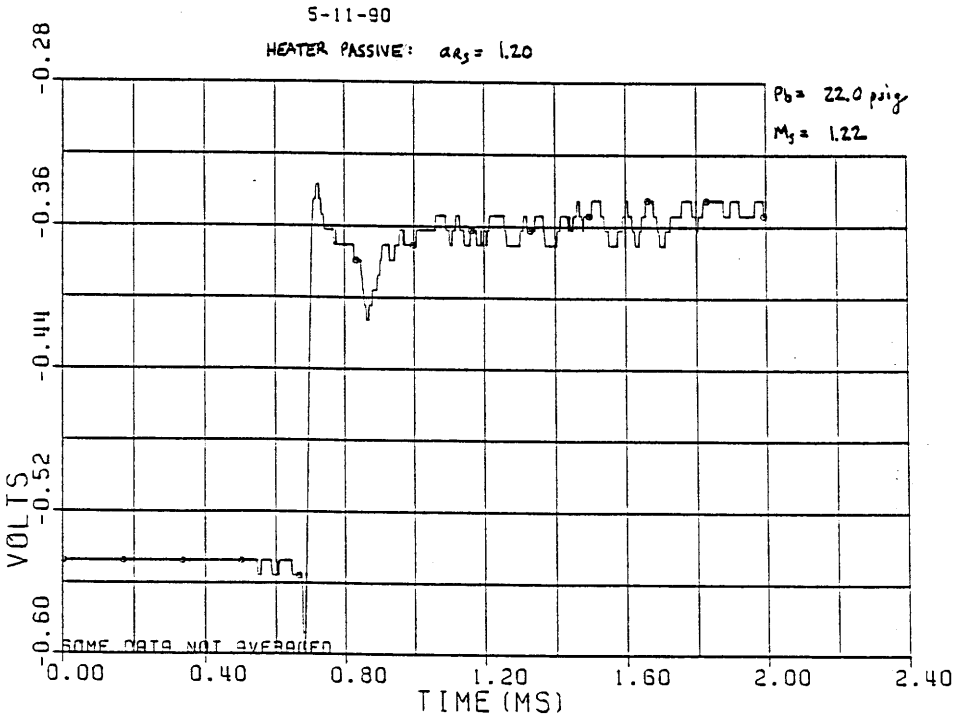

FIGURE D.2: UNSTEADY VOLTAGE TRACE VS. TIME

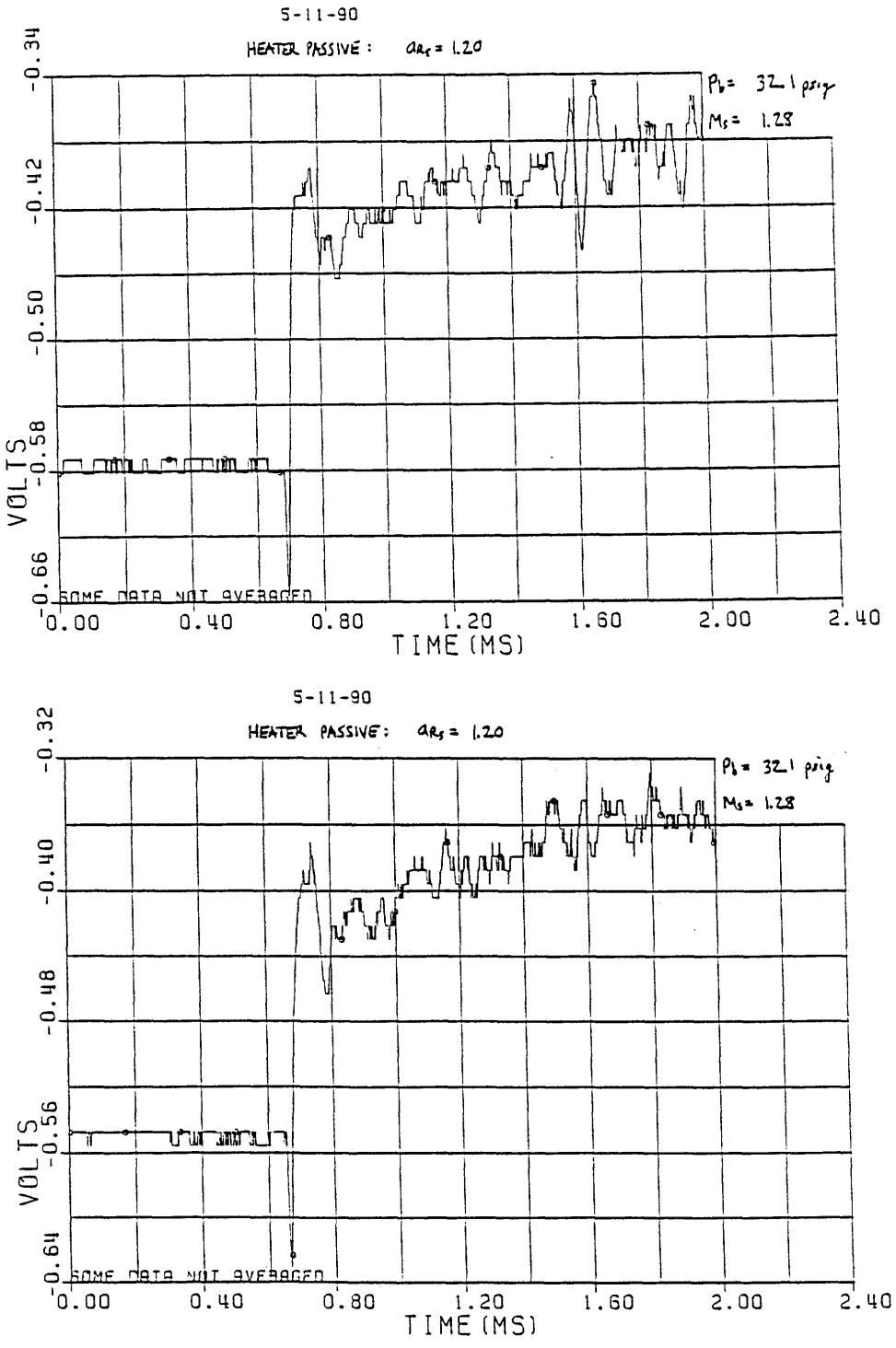

FIGURE D.3: UNSTEADY VOLTAGE TRACE VS. TIME

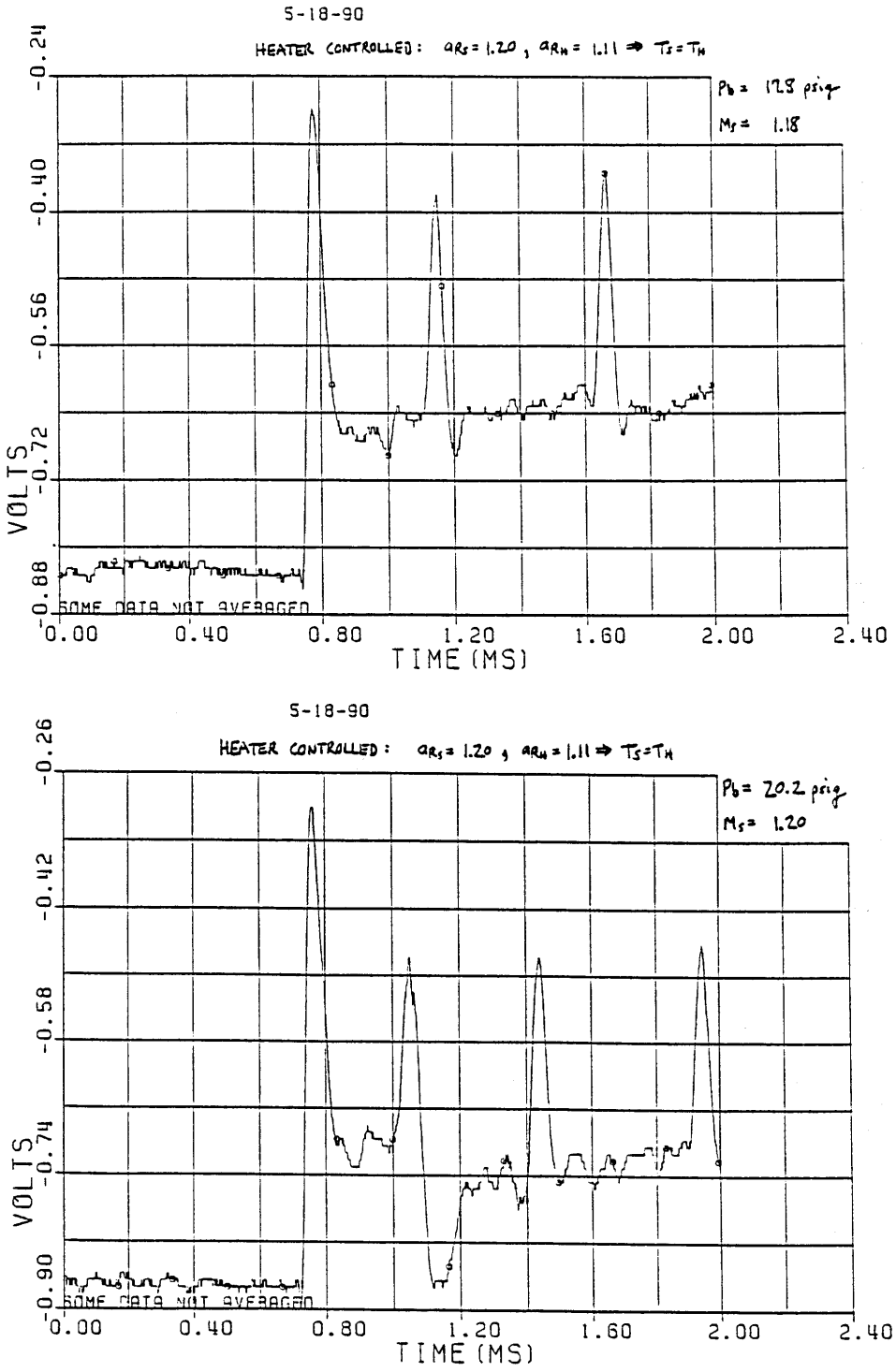

FIGURE D.4: UNSTEADY VOLTAGE TRACE VS. TIME

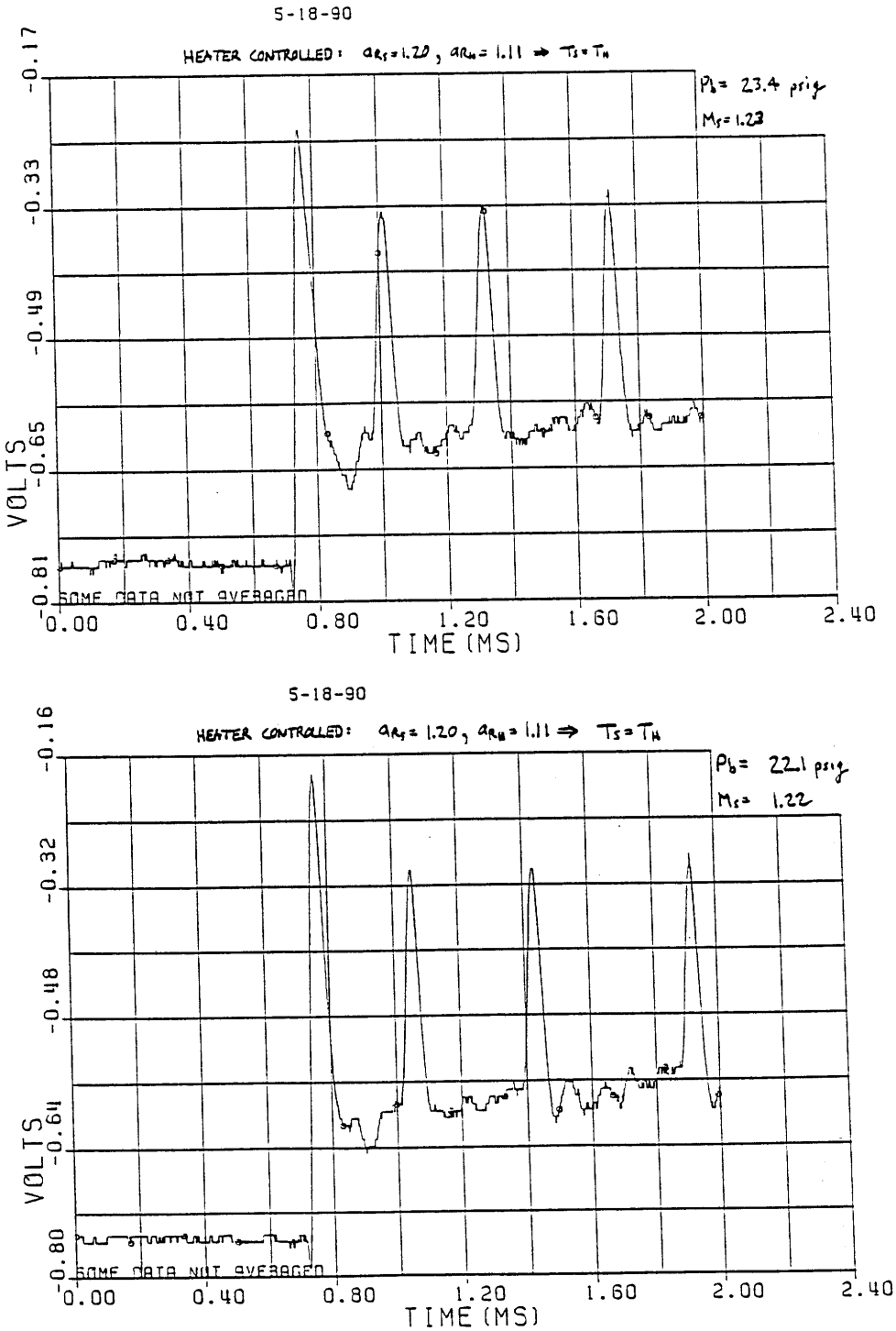

FIGURE D.5: UNSTEADY VOLTAGE TRACE VS. TIME

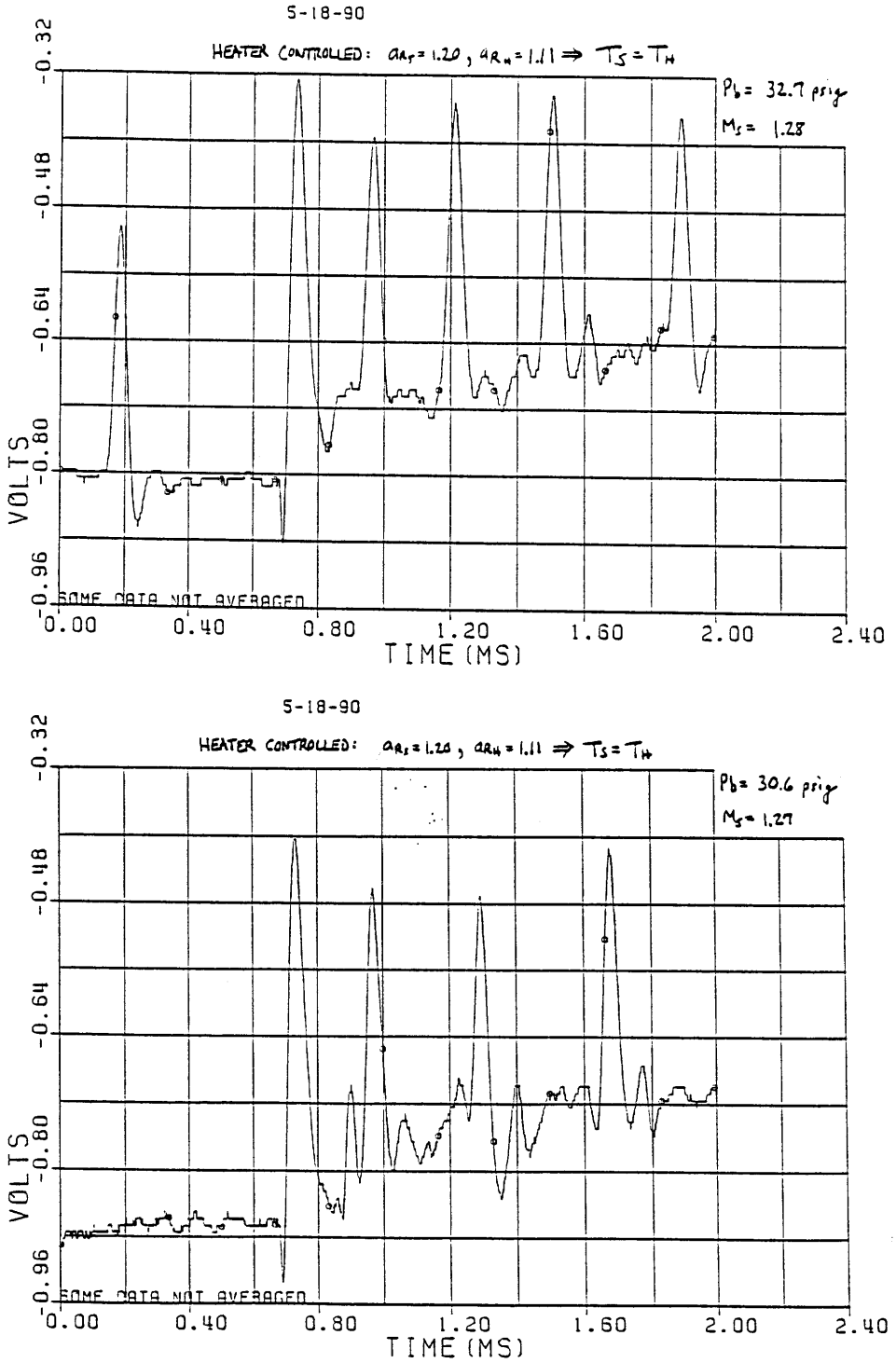

FIGURE D.6: UNSTEADY VOLTAGE TRACE VS. TIME

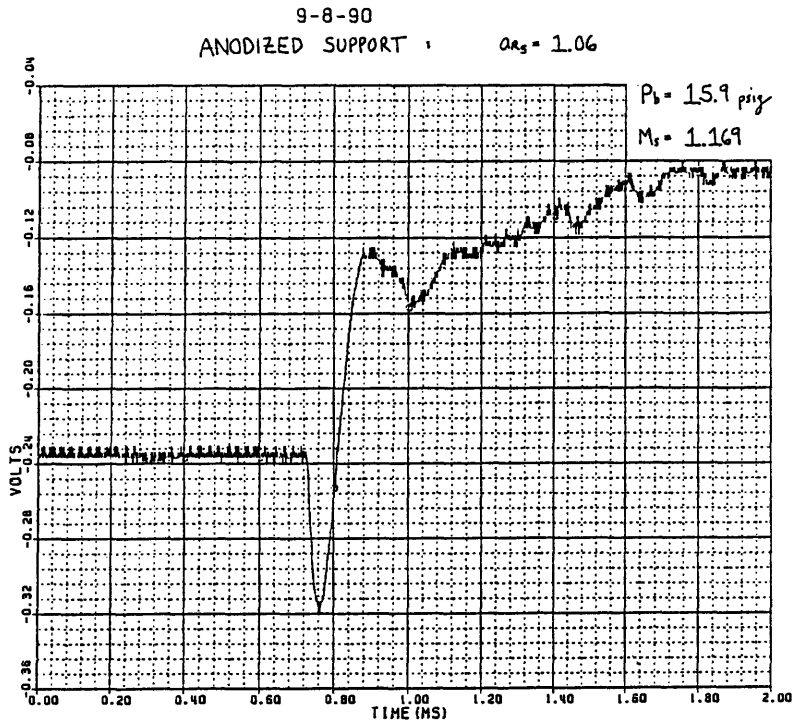

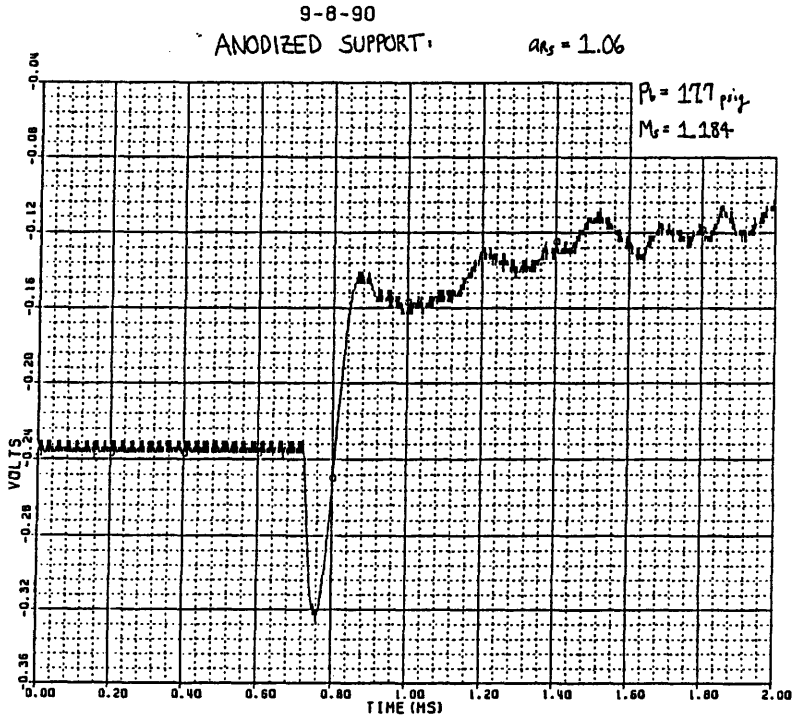

FIGURE D.7: UNSTEADY VOLTAGE TRACE VS. TIME

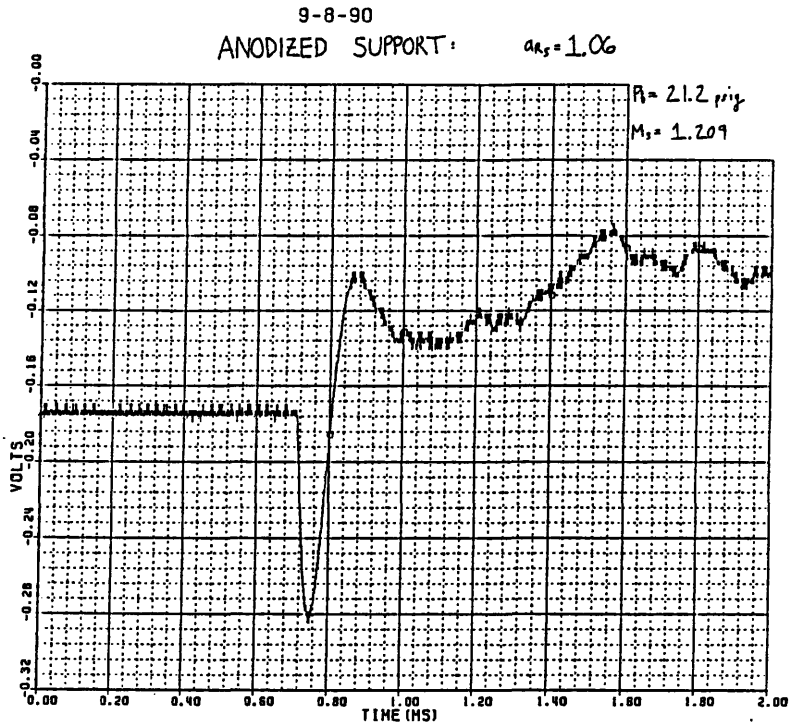

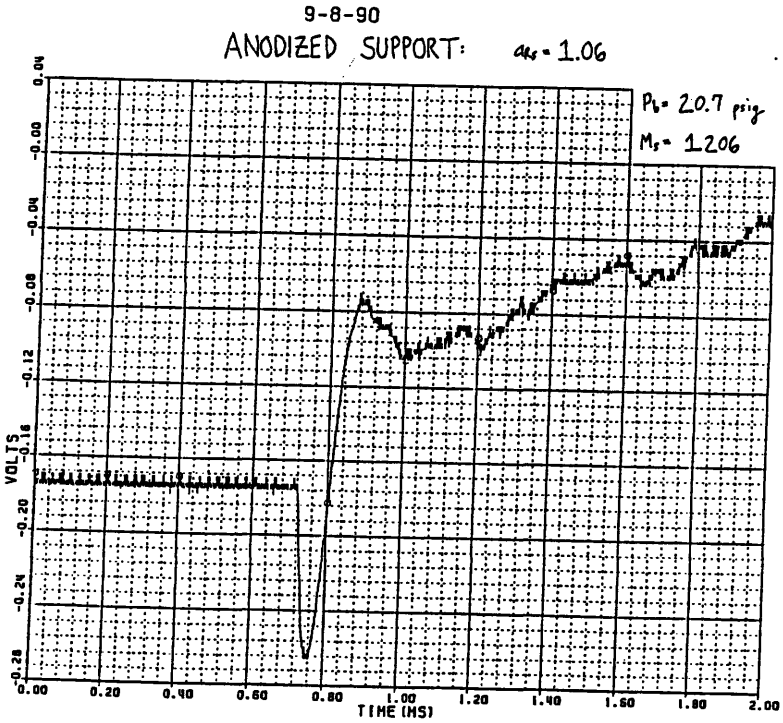

FIGURE D.8: UNSTEADY VOLTAGE TRACE VS. TIME

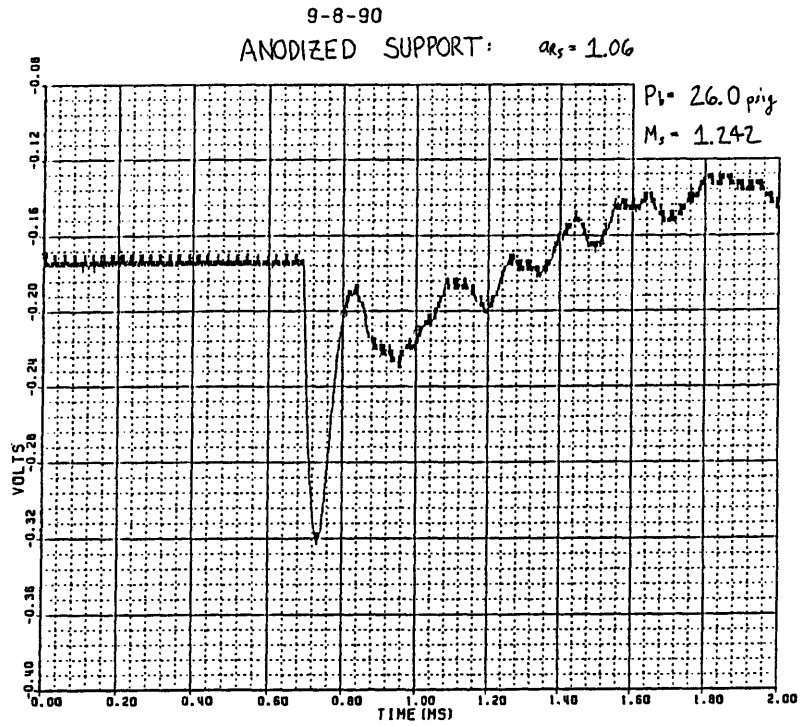

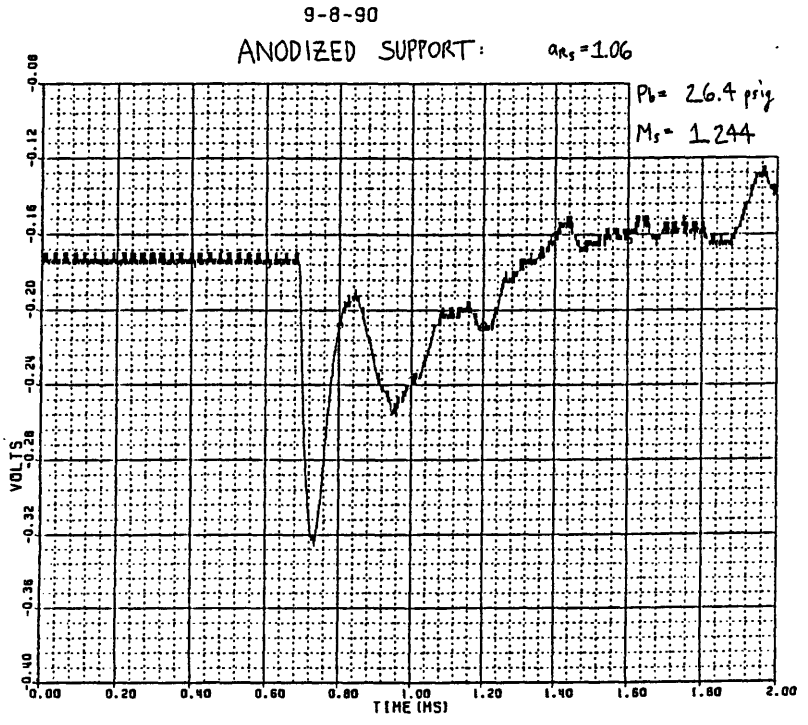

FIGURE D.9: UNSTEADY VOLTAGE TRACE VS. TIME

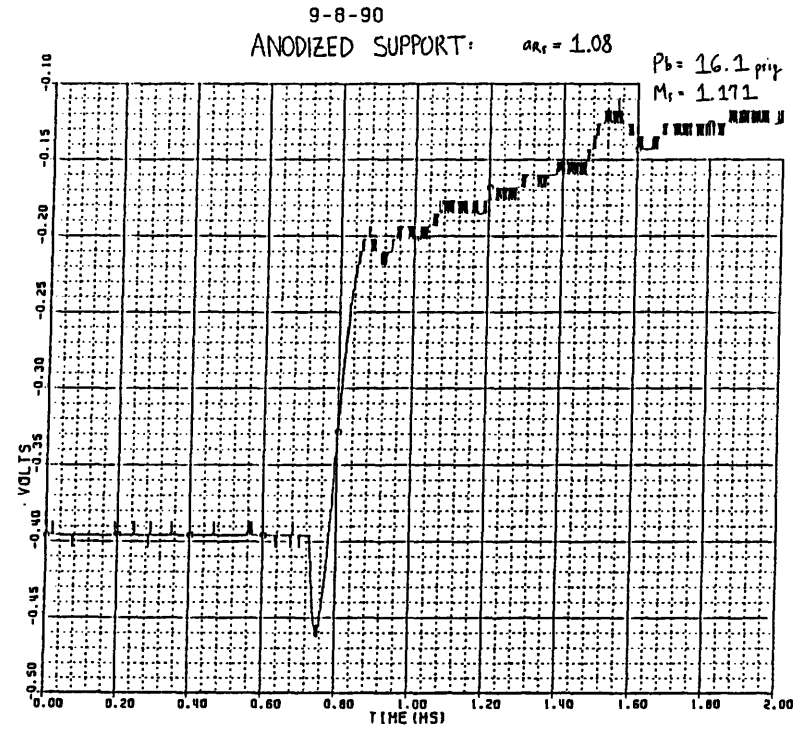

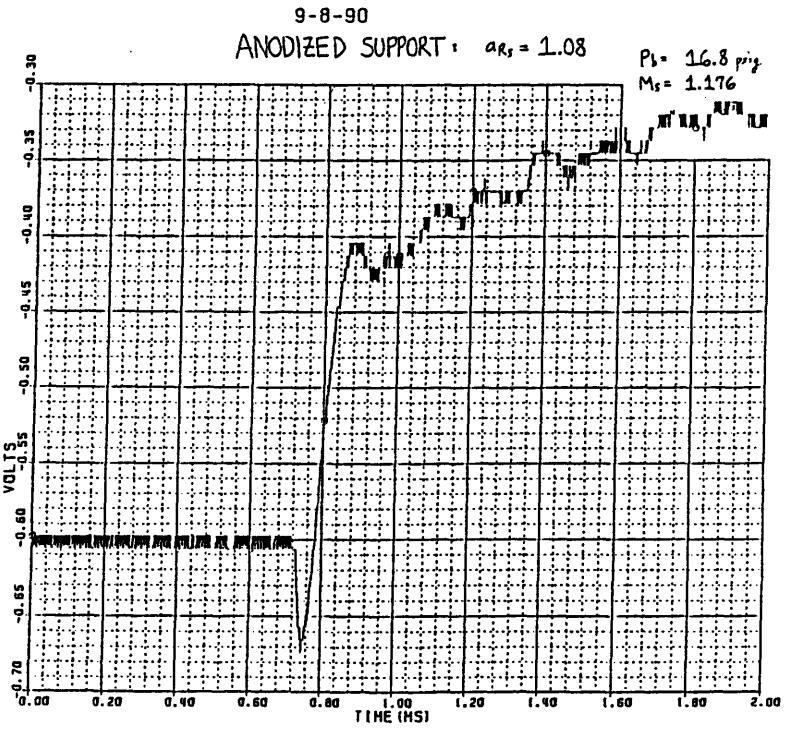

FIGURE D.10: UNSTEADY VOLTAGE TRACE VS. TIME

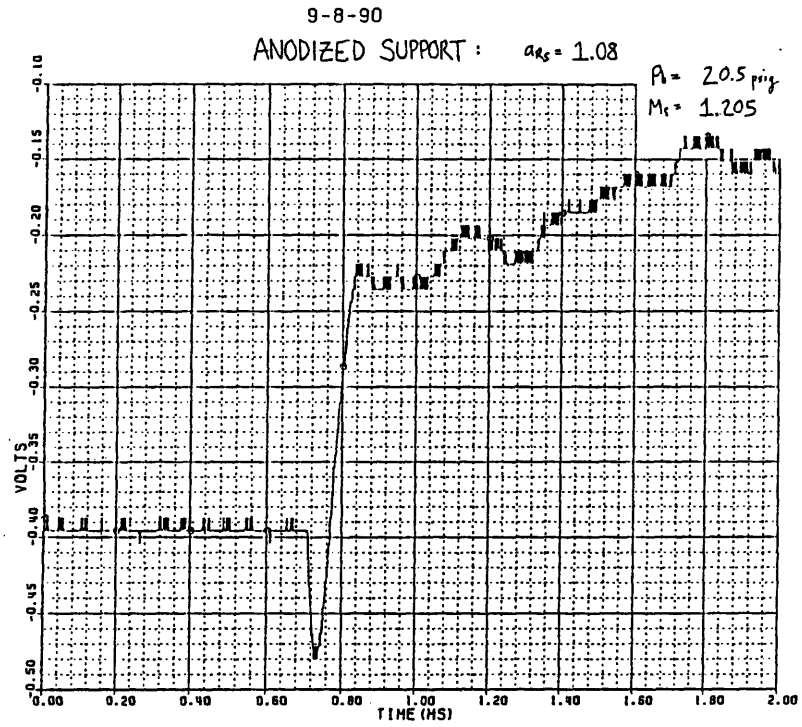

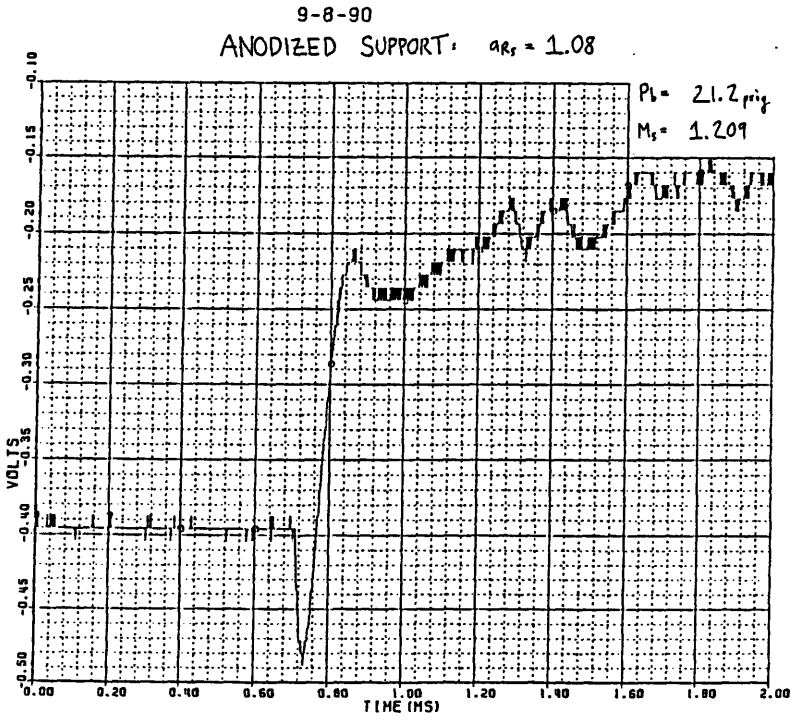

FIGURE D.11: UNSTEADY VOLTAGE TRACE VS. TIME

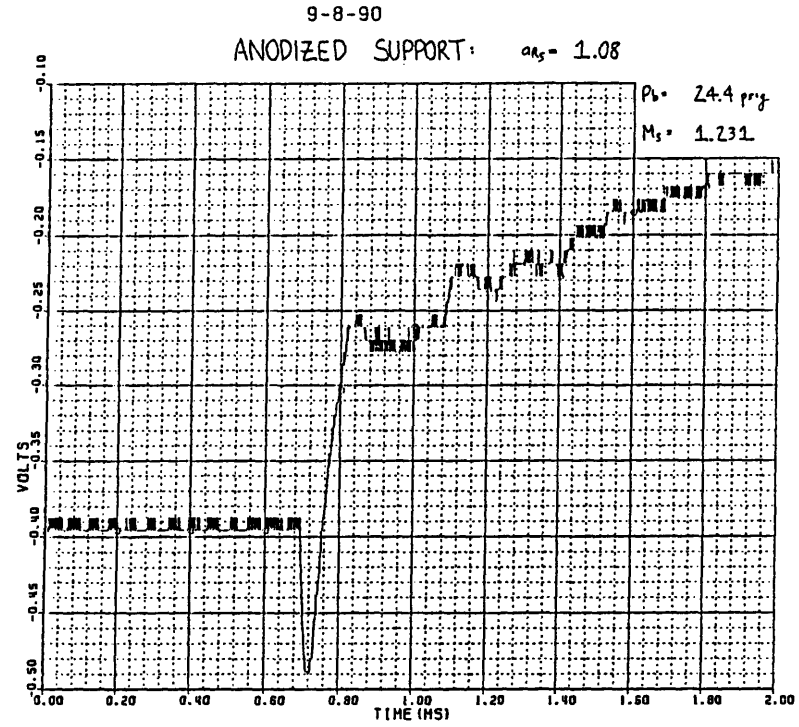

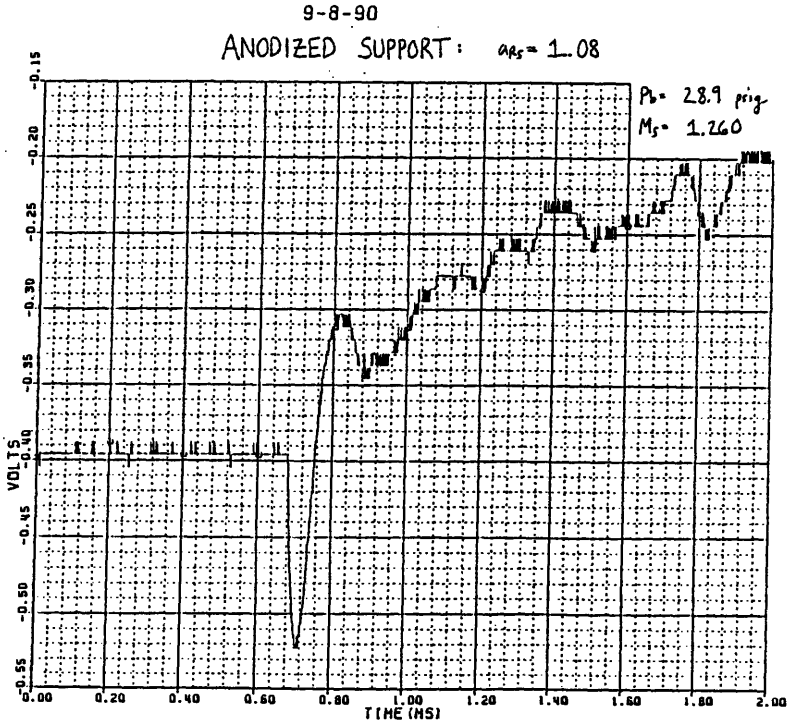

FIGURE D.12: UNSTEADY VOLTAGE TRACE VS. TIME

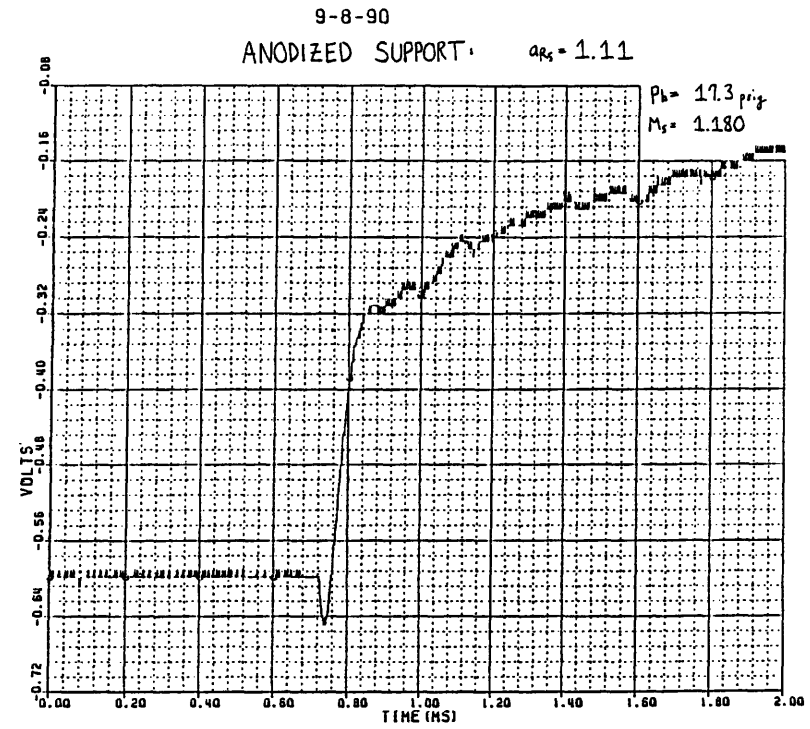

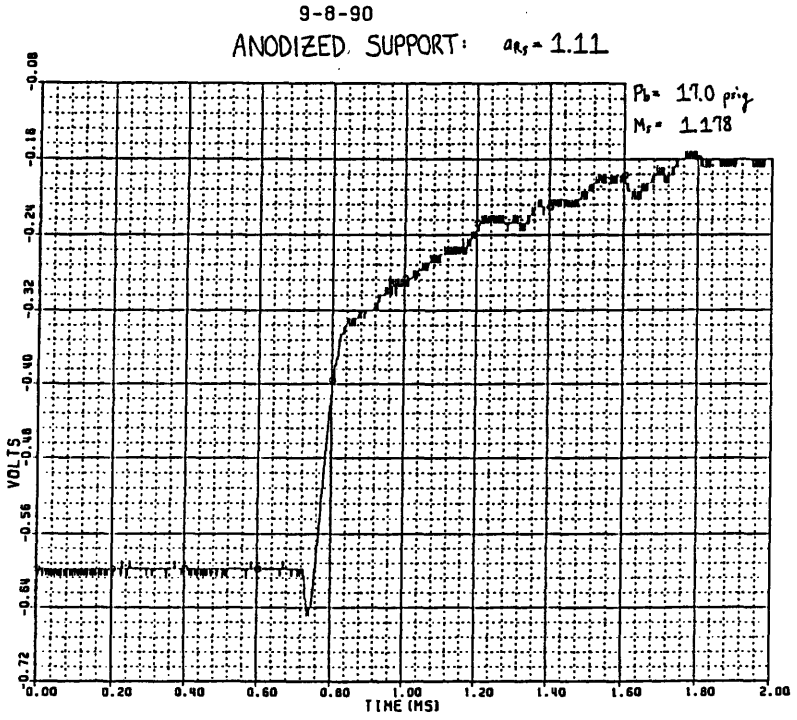

FIGURE D.13 : UNSTEADY VOLTAGE TRACE VS. TIME

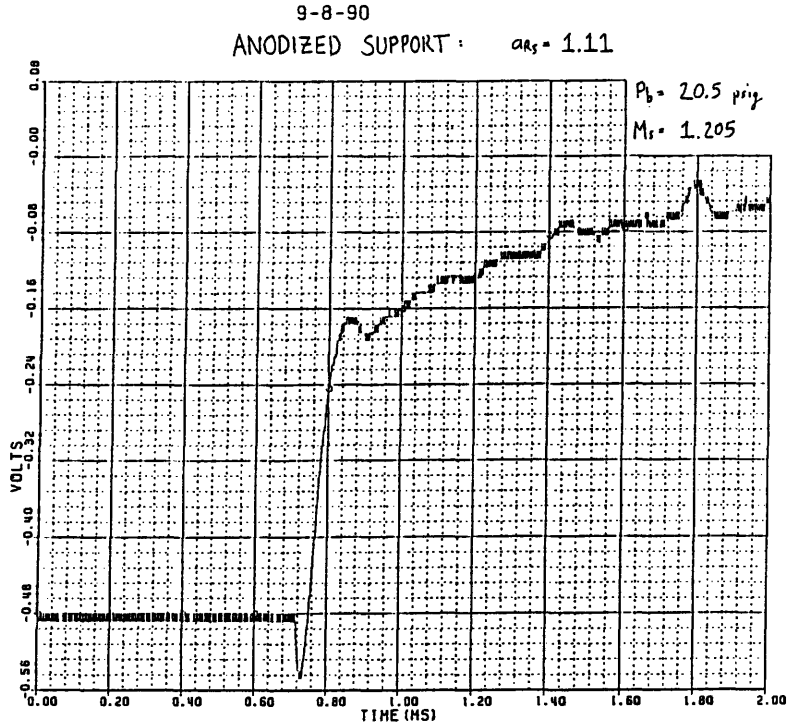

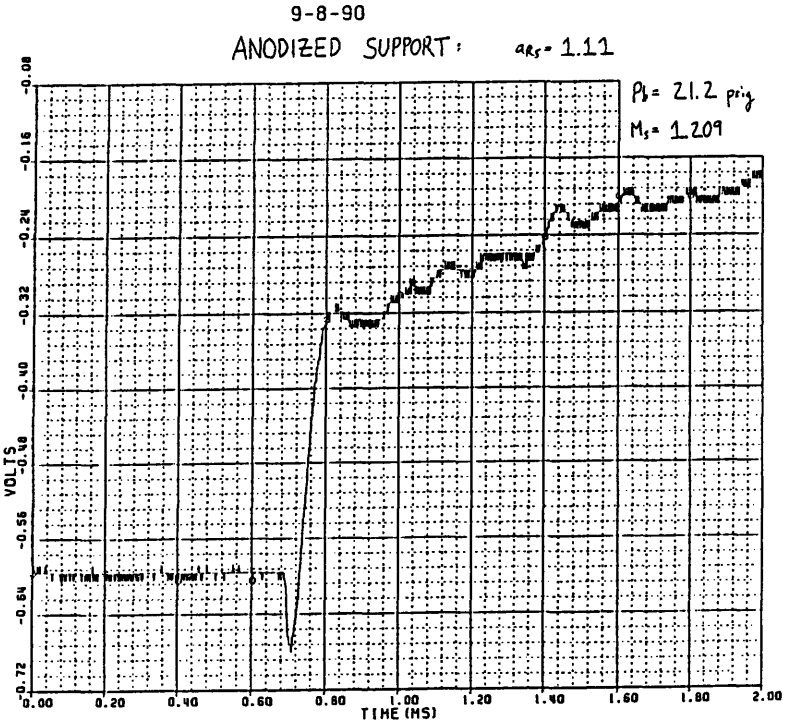

FIGURE D.14: UNSTEADY VOLTAGE TRACE VS. TIME

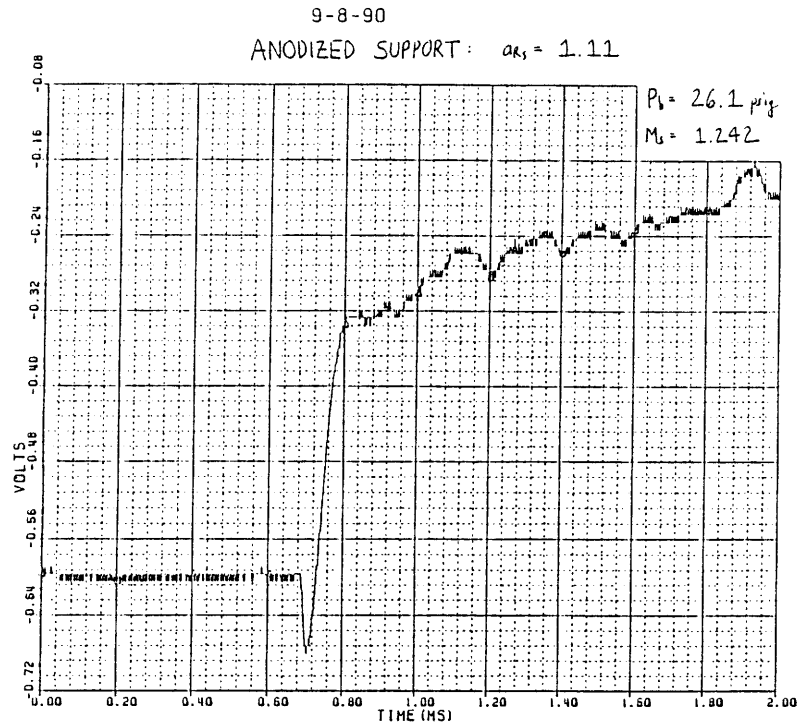

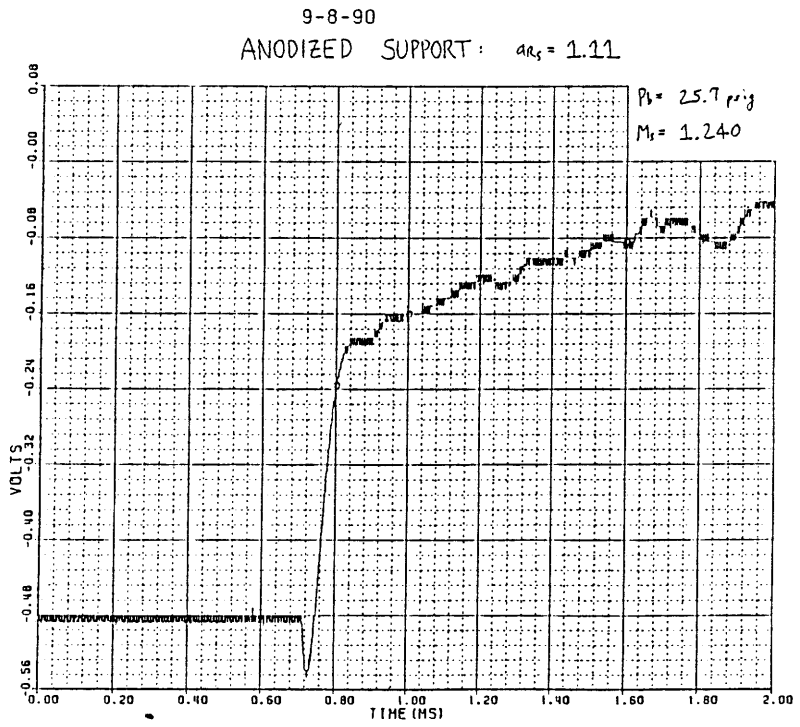

FIGURE D.15: UNSTEADY VOLTAGE TRACE VS. TIME